Order-disorder competition in the $Sc_2VO_{5+\delta}$ system. Review and experimental pursuit of $A^{3+}{}_2VO_5$ and $Sc_2VO_{5+\delta}$-inspired solid phases

By

Dmitry Vrublevskiy

A Thesis submitted to the Faculty of Graduate Studies of

The University of Manitoba

in partial fulfilment of the requirements of the degree of

DOCTOR OF PHILOSOPHY

Department of Chemistry

University of Manitoba

Winnipeg

Abstract

This work was motivated by the proclivity of oxygen-deficient metal oxides to enable oxide transport at high temperatures. This property depends on the composition and metal-oxygen connectivities within the structure and requires vacant crystallographic sites. The project initially focused on non-conducting derivatives of oxygen defect fluorites $AO_{2-\delta}$, namely split-cation A_2BO_5-type superstructures, but eventually turned into a broader experimental and theoretical investigation of formation regimes and metal-oxygen connectivities of these phases and, to a degree, their structural competitors – $A_2B_2O_7$ and $A_4B_3O_{12}$.

At the core of this work is the defect fluorite superstructure $Sc_2VO_{5+\delta}$ with tunable δ. It belongs to the structurally diverse yet scarce A_2VO_5 family of compounds. The high-temperature tetragonal polymorph t-$Sc_2VO_{5+\delta}$ is predominantly ordered – cation-ordered and oxygen-vacancy-ordered, and its vanadium sublattice is charge-ordered. Doping of the vanadium sublattice with commensurate cations Ge, Ti, Sn, and Cr replaced either $V^{3+\ldots4+}$ or V^{5+} in it in proportion to the octahedral ionic size of the dopant, also affecting δ and the average cation ordering. Increasing the content of the dopant led to formation of competing phases – $Sc_2B_2O_7$ and $Sc_4B_3O_{12}$, which are also discussed.

The low-temperature cubic polymorph c-$Sc_2VO_{5+\delta}$ is fully disordered on average but partially ordered on the local scale, insofar as its vanadium sublattice accumulates smaller V^{5+} species. This cubic phase can be oxidatively obtained from either its tetragonal polymorph or a cation-disordered bixbyite $Sc_2VO_{4.5}$, in both cases inheriting the average ordering scheme of its precursor. Key phases were investigated with a tandem of *ex-situ* and *in-situ* average and local structure probes, such as X-ray and neutron powder diffraction, X-ray absorption near-edge structure spectroscopy, and X-ray and neutron total scattering. Results led to a discussion on the evolution of coordination and connectivities in the cation sublattices, oxygen driven phase transitions, limit of oxygen concentration, oxide vacancy structure, the crucial role of the cation radius in phase formation, and the order-disorder interplay. Discussed vanadates with 2:1 and 1:1 stoichiometric ratio of A^{3+} and aliovalent vanadium were compared across their joint phase diagram and discussed with the help of stability maps.

Acknowledgments

I would like to express due gratitude to my supervisor Prof. Mario Bieringer for his profound erudition, patience, wit, and unprecedentedly contagious scientific enthusiasm. With them he successfully re-ignited and maintained my interest in the field of solid-state chemistry, confidently pulled me out of multiple rabbit holes in this field, and helped me methodically navigate past the proverbial Scyllas and Charybdises of graduate research (which so far has been the most pleasant time of my life, or at least before I collected the first feedback to this thesis). My thanks also go to Dr. Joey A. Lussier for his immense investment of time and intellectual effort in my research and for his eagerness to brainstorm. I would further like to extend my thanks to my graduate committee for much needed discussions, advice, and collaborations: Drs. Christopher R. Wiebe, Can-Ming Hu, H. Georg Schreckenbach, Yurij Mozharivskyj, Viktor Nemykin, as well as to Drs. Cole Mauws, Wojciech A. Sławiński, Andrew P. Grosvenor, and Jeremiah C. Beam, members of the Bieringer lab – Brooke, Jenny, Astley, Jonah, Dana, and Brandon, and other past and present University of Manitoba staff – especially Ravinder and Lesa.

I am also grateful for multiple opportunities to visit world-class national laboratories and collect top-quality X-ray[A] and neutron[B] data for my research[C] – a truly fascinating experience. In particular, I would like to thank the beam scientists Drs. George Sterbinsky (9-BM @ APS ANL), Tianpin Wu (9-BM), Saul Lapidus (11-BM), Olaf Borkiewicz (11-ID), Yue Meng (16-ID "HPCAT"), Wenqian Xu (17-BM), Andrey Yakovenko (17-BM), Zou Finfrock (20-BM), Debora Meira (20-BM), Joerg C. Neuefeind (BL-1B "NOMAD" @ SNS ORNL), Michelle Everett (BL-1B), Jue Liu (BL-1B), Ashfia Huq (BL-11A "POWGEN"), Melanie Kirkham (BL-11A), and Cheng Li (BL-11A).

For the insights into the nits and grits of diffraction and spectroscopic techniques and data analysis, I am grateful to the organizers of the 4th Summer School "Modern Methods in Rietveld

[A] On-site and mail-in synchrotron experiments presented in this work used resources of the Advanced Photon Source, a U.S. Department of Energy (DOE) Office of Science User Facility operated for the DOE Office of Science by Argonne National Laboratory under Contract No. DE-AC02-06CH11357.
[B] On-site and mail-in neutron experiments used resources at the Spallation Neutron Source, a DOE Office of Science User Facility operated by the Oak Ridge National Laboratory.
[C] I am grateful to the University of Manitoba for the UMGF award (2017-2021) and to the Manitoba Ministry of Education and Training for upgrading the UMGF to the MGF award (2017-2019).

Refinement for Structural Analysis" (2018), APS/IIT Virtual Summer XAFS School (2021), and the 4th US School on Total Scattering Analysis (2021), as well as Dr. Alan A. Coelho.

My gratitude likewise extends to my friends Dion and Alicia for radiating a great deal of support and care. And finally, I cannot thank enough my mother Anna for having encouraged my inquisitiveness, cheering for me at every stage of my education, and generally being a paragon of intelligence and composure I am doing my best to learn from. I find these traits useful both inside and outside the lab, especially when holding a blasting oxygen torch.

It is much easier to unwillingly evaporate all *p* elements I tried to work with than to recall all researchers and friends whose help should be rightfully acknowledged here. My gratitude is to those left unmentioned for this reason.

Table of contents

List of Tables

List of Figures

CHAPTER 1

Introduction

Solid-state chemistry is an old empirical science that recently underwent its Renaissance and has made invaluable contributions to contemporary technology[1]. Interestingly, and as opposed to chemistry of molecular materials, it still lacks full understanding of its own fundamentals. Due to this, predictions of structure-property, structure-reactivity, and structure-stoichiometry relations from the properties of elements and starting materials are hindered. To predict these relations and to understand how to access the needed phase or substantiate its instability are the prerequisite for the rational design of functional materials (sensors, catalysts, magnets, phosphors, conductors and insulators, etc.) and hence are of importance.

Fluorite-type metal oxides MO_2, where M^{4+} is a metal cation, are at the intersection of applied and fundamental parts of solid-state chemistry. As functional materials, oxide-based fluorites mostly found application as oxide ion conductors[2,3], are deemed as potential antiferroelectrics[4] and thermal insulators[5], and happen to be used as nuclear fuels[6]. On a fundamental level, they are crucial in understanding phase boundaries as well as formation, stability, and reaction mechanisms of solids[7]. Some properties of fluorites such as oxide ion conduction notoriously benefit from incorporation of an aliovalent cation (here A^{3+}) into the M site to produce $A_{1-x}B_xO_{2-x/2}$, which in a controllable way can take up or lose a small concentration (x/2) of oxide anions[3,8]. It is the latter property of the fluorite structure that inspired this work.

Central to this work is the family of compounds $A^{3+}{}_2B^{4+}O_5$[9] which is (for some family members) or can be (for many other family members) seen as a fluorite-derived series $A_2BO_{6-\delta}\square_\delta$, where $\square$ is an oxide vacancy. In this series, the former cation M^{4+} in the only crystallographic site splits into two cations: (1) redox-inactive trivalent A^{3+}, introducing into the structure a known and fixed amount of vacancies due to its lower charge, and (2) tetravalent B^{4+}. If B is redox-inactive or at least stable in its 4+ state, it allows for the fixed stoichiometry with respect to oxygen (δ =1) and stability of both the structure and the properties it possesses[10]. On the other hand, redox-activity of B might be beneficial as it enables finer control over δ through the means of topotactic chemistry, to be discussed later. Studying such structures will provide insights into the mechanisms behind phase formation, phase transitions, and phase competition.

Initially the A_2BO_5 family was anticipated from observing the pseudobrookite-type $A_{3-x}Ti_xO_5$ family of compounds[9,11] isomorphous to the anosovite Ti_3O_5. To-date, it exhibits incredible chemical and structural variety, including various titanates[12,13,14,15,16,17,18] (incl. Ti_3O_5[19,20,21]), germanates[22,23,24,25,26,27], vanadates[28,29,30,31,32,33,34] (incl. V_3O_5[35,36]), ruthenates[37,38], molybdates[39,40,41], rhenates[42,43,44,45,46], silicates[47,48,49,50], and carbonates[51,52,53] (listed for completeness). Across the A_2BO_5 phase diagram, the A^{3+} ion changes in size and in nature, i.e. diamagnetic (Ln, Y, Sc, In, Ga, Al,…), paramagnetic (V, Ti, Fe,…), and lone pair-bearing (Sb, Bi)[54,55,56,57,58,59]. **Fig. 1.1** illustrates the variety of the A_2BO_5 phases and the evolution of the unit cell volume *V/Z* across selected members of the series (*V* – unit cell volume, *Z* – number of unit formulas per unit cell). Despite the complexity of the figure (see legend to follow which cations form such phases), one clear trend is the overall increase in the unit formula volume with

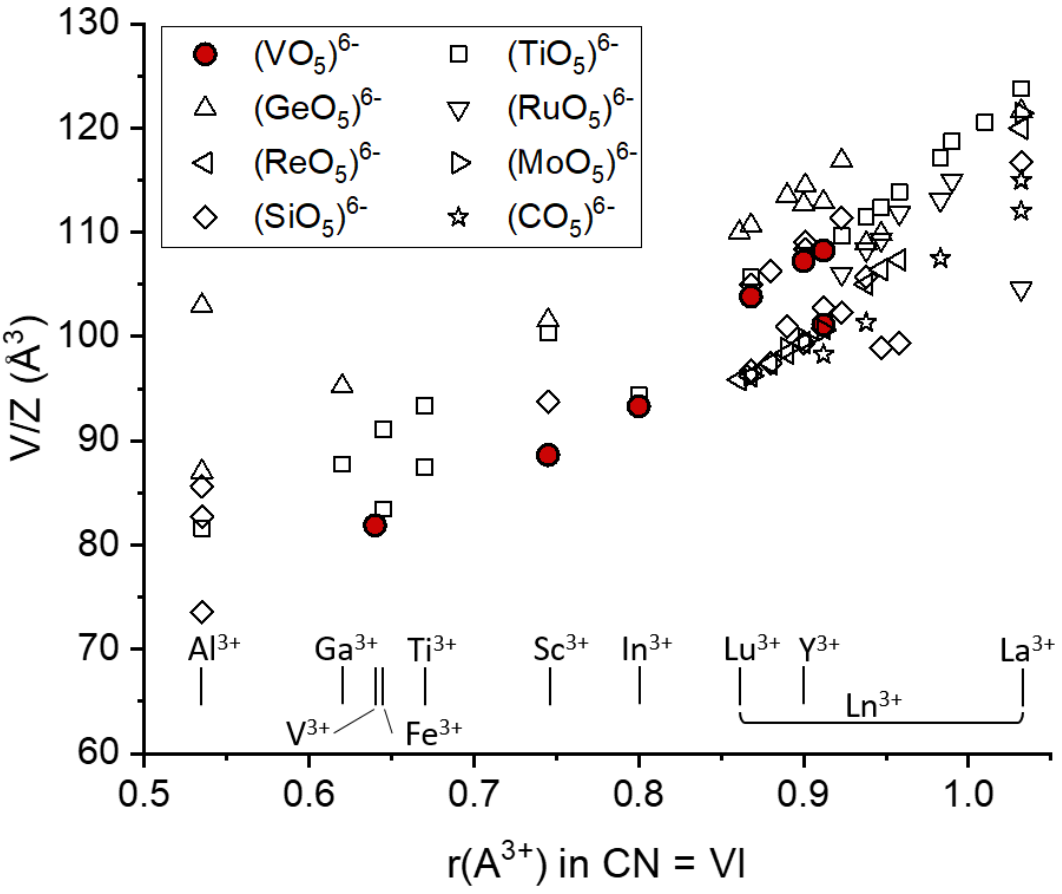

Figure 1.1. Selected A_2BO_5 phases. A^{3+} cations are listed on the bottom in ascending order of their ionic radii in the coordination number (CN) of six, while $(BO_5)^{3-}$ fragments are in the legend.

increasing ionic radius of A^{3+} cations. This plot becomes even more complicated if more parameters are included such as high temperature (incl. metastable products)[60], high pressure (incl. geological)[61,62,63], antisite[64] and site disordering [65,66], charge disordering[67], etc. The relative scarcity of A_2VO_5 phases with moderately abundant vanadium is surprising. The main reason is likely redox-activity of vanadium, which makes it hard to control in the solid state and limits its usage. Current work primarily focusses on vanadates due to its relative availability and a large number of oxidation states and ionic sizes that can be thermodynamically or kinetically stabilized, potentially promising a number of preparation routes and intermediate phases unavailable for at least titanates and germanates.

The few so far reported A_2VO_5 phases with stable A^{3+} cations were obtained by different methods and crystallize in different symmetries: In_2VO_5 (space group (SG): *Pnma*)[32,33]; Sc_2VO_5 (SG: $I\bar{4}$)[28,68,29,30,31]; R_2VO_5 (SG: $C2/c$ for R = Y, Yb, Dy and second $P2_1/c$ phase for R = Dy[34]). Orthorhombic In_2VO_5 was a product of high-temperature solid-state synthesis. Monoclinic R_2VO_5 phases are products of hydrothermal synthesis at much lower temperature. Tetragonal Sc_2VO_5 was first mentioned as a product of a direct solid-state reaction[28] and more recently identified as an impurity on a single crystal of $ScVO_4$ grown in oxidative atmosphere[29]. In both cases the product $Sc_2VO_{5+\delta}$ was by default considered oxygen-stoichiometric (δ=0), but later was proposed[30] and then confirmed[31] to have a range of δ, and a composition with δ = -0.15 was reported. Some other A_2VO_5 family members with multivalent A cations are known, such as Bi_2VO_5 (SG: $Pnma$[54], $I4/mmm$[69], $F222$ [70], $P2_122_1$[71]), Sb_2VO_5 (SG: $C2/\boldsymbol{c}$[55,72] and $Pmcn$ [56]), and V_3O_5, or V_2VO_5 (SG: $P2_1/c$, $P2/c$, and high-temperature – Cc[73,74,75,35,60,76]). Furthermore, an exotic Co_2VO_5 gas phase was found, but with no available structural details[77]. Finally, despite the fact that a full crystallographic description is absent from the Inorganic Crystal Structure Database (ICSD), the Ti_2VO_5 phase was reported (SG: $Cmcm$). It was synthesized by conventional solid-state techniques[78] as well as by controlled vapor deposition of metallic vanadium onto a TiO_2 substrate[79]. However, as vanadium seems to be in the 3+ state and titanium has a strong preference toward the 4+ state, this phase is rather a titanium-vanadium titanate $(VTi)TiO_5$. It then should be rather a member of the titanate family A_2TiO_5 often found as berdesinskiites (A = V[80]) or pseudobrookites (starting with A = Sc) [12,81,82]. Additionally, some cation-disordered polymorphs of the aforelisted cation-ordered phases have been reported crystallizing as defect cubic fluorites (space group $Fm\bar{3}m$), such as $Sc_2VO_{5+\delta}$ with δ somewhere between -0.5 (bixbyite with $V^{3+}{}_{VI}$) and

+0.5 (defect fluorite with V^{5+}_{VIII}) obtained by topotactic redox reactions[30,31] and Bi_2VO_5 prepared with mechanical activation but unfortunately lacking crystallographic description[83]. From this list, the structural variety of the A_2VO_5 phases can be due to a plethora of factors, such as A^{3+}/V^{4+} and A^{3+}/O^{2-} relative ionic radii, electronic structure, presence of the stereochemically active lone pair, type of bonding, etc., and also temperature and pressure. Redox activity of vanadium in these phases is another interesting property which can define the limits of structural stability (threshold of oxygen/vacancy concentration) and drive phase transitions when outside of this limit. Furthermore, tetravalent vanadium itself is a prerequisite for magnetism (the particular magnetic exchange path depends on its coordination environment) and an example of the stabilization of an intermediate oxidation state at high temperature. Studying the above is to embark on a quest to understand the fundamentals of phase formation and structure-property relations.

So far the most intriguing member of the A_2VO_5 family is the fluorite superstructure Sc_2VO_5[28,29,30,31]: it shows cation order between Sc and V and charge order between two types of vanadium – octahedral $V^{3+\ldots4+}$ and tetrahedral V^{5+}. While general comments on order-disorder and topotactic-reconstructive synthesis are made in ***Chapter 2***, the structure, synthesis, and redox behavior of Sc_2VO_5 are introduced in ***Chapter 3***. In ***Chapter 4***, other A_2VO_5 phases are compared to Sc_2VO_5. The chapter discusses the structure, ordering, and evolution of vanadium connectivities in A_2VO_5 phases as a function of the A^{3+} cation size and nature. A few overlooked A_2VO_5 phases are recruited into the family and a few hitherto existing members are suggested for exclusion. In ***Chapter 5***, Sc_2VO_5 is placed at the intersection of A_2VO_5 and Sc_2BO_5 phases, and connectivities in the B sublattices of the latter are discussed as a function of the size of the B^{4+} cation. Sc_2VO_5 is then used as a template for doping, and the role of the ionic radius of the dopants commensurate with V^{4+} ion in phase purity and site preferences is discussed. Competing phases of different stoichiometries become important in this discussion, and therefore a few frequently encountered competing structures are presented. ***Chapter 6*** introduces the cubic polymorph of Sc_2VO_5 and uses it as an example of order-disorder competition and contrast between average and local structure descriptions. ***Chapter 7*** summarizes the trends discussed in previous chapters. Via addressing the role of A^{3+} and V^{x+} cations in facilitating the structural variety of the A-V-O phase diagram, this chapter emphasizes the importance of predictions of phase formation based on the individual attributes of atoms and difficulties imposed by cation (dis-)ordering. ***Chapter 8*** suggests prospects for future work. Finally, the ***Appendix sections*** provide supporting information such as additional

figures, tables, as well as a list of used abbreviations and a list of key solid structures referred to in the text.

CHAPTER 2

Theory, materials, techniques

2.1. On topotactic and reconstructive solid-state synthesis

The rate-limiting step in solid-phase reactions is the diffusion of the material between crystallites of different reactants. To facilitate solid-state reactivity, the starting materials are ground in a mortar or a mill and often pelletized before heating. As a result of a solid-state reaction not only equal distribution of atoms or ions throughout the solid product is required, but also the (re-) establishment of long-range interatomic connectivities. Consequently, migration of material through the solid-solid grain boundary requires time (hours and days) and large thermal energy and hence high temperatures – typically well above 500 ºC; often resulting in thermodynamic products. It is known as conventional solid-state or conventional ceramic synthesis, or more pejoratively, the "shake-and-bake" or "heat-and-beat" method[84]. The advantages of this method are straightforwardness and stability of the final product, while disadvantages are:

(1) inability to target metastable phases or incorporate rational design of materials;

(2) long reaction time;

(3) potential presence of inhomogeneities after the first heating;

(4) reactivity of the material with the reaction container.

While (4) can be addressed by using levitation setups or precious-metal crucibles, (3) can be achieved by regrinding and reheating or using mechanical mills, improvements of (2) and especially (1) are incompatible with this technique or unwanted in it. In contrast with high-temperature reconstructive synthesis, lower-temperature topotactic synthesis can be tuned to target metastable phases. Topotactic ("framework preserving") process, or "reaction occurring in or on the crystal"[85], historically referred to oriented and correlated nucleation of a new phase (later excluded[86]) or substructure within a parent crystal via a phase transition or reaction[87,88]. Today the term implies manipulations on the more mobile sublattice/substructure of the solid material, while the more robust sublattice/substructure stays intact due to its stronger bonding. Topotactic manipulations on the sublattice include insertion and removal of single atoms into/from vacant positions[89] as well as creation and removal of 1D, 2D, and 3D substructures between the robust

layers of the host material[90] without rearranging the connectivities therein. On a fundamental level, topotactic processes are widely studied for perovskites[91], rutiles[92], fluorites[93], Ruddlesden-Popper phases[94], etc. to gain insight into the mechanisms of solid-state formation, reactions, and phase transitions[95]. On an applied level, they are used to give access to interesting properties, such as thermoelectric[96], superconducting[97], electrochromic[98], etc.

Throughout this work only one type of the topotactic process is entertained – topotactic insertion or removal of oxide ions in and out of the oxide-deficient anion sublattice.

2.1.1. The bixbyite-fluorite pair as an example of topochemically related structures

An example of a non-topotactic process is the formation of the bixbyite phase $ScVO_3$, while a telling example of a topotactic process is its reversible oxidation to the fluorite phase $ScVO_{3.5+\delta}$ (**Fig. 2.1**). In this pair of phases, a disordered cationic substructure of the bixbyite is obtained at high temperature (1100-1500 ºC, depending on the method), while additional oxygen can be introduced topotactically at much lower temperatures of 300-400 ºC[93,99,100]. Crystallographic structures partaking in these two reactions are important in this work; they are shown in **Fig. 2.1**.

A. The cubic bixbyite structure (named after the mineral bixbyite $(Mn_{1-x}Fe_x)_2O_3$ with small x) is shown in the figure in blue for Sc_2O_3 and green for $ScVO_3$. Bixbyite crystallizes in the space group $Ia\bar{3}$, #206 and has three crystallographic sites occupied. The two cation sites are 8*b* (¼, ¼, ¼) and 24*d* (*x*, 0, ¼); corresponding metal-oxygen polyhedra are shown separately in blue in the figure. The 48*e* site (*x*, *y*, *z*) is occupied by oxygen (brown balls) which bonds to central cations to form two distinct coordination geometries. Each cation is sixfold-coordinated and each polyhedron resembles a distorted cube with two missing corner-oxygens: along the body diagonal of the polyhedron (8*b*) or along its face diagonal (24*d*). Polyhedra are connected through shared oxygens (corner-sharing) or shared pairs of adjacent oxygens (edge-sharing).

B. The corundum structure of V_2O_3 (space group $R\bar{3}c$, #167) is named after the mineral corundum (Al_2O_3 with small addition of some 3d-metals) and is based on corner-sharing octahedra of oxygens around the metal cation in the 12*c* site (0, 0, *z*). Oxygen is in the 18*e* site (*x*, 0, ¼). The overall high-temperature reaction of Sc_2O_3 (blue) bixbyite with V_2O_3 (yellow) corundum is a non-topotactic process[99]. It results in $ScVO_3$ (green) which is a cubic bixbyite, similar to Sc_2O_3. High temperature ensures formation of a thermodynamically stable product

whose crystal structure depends on the ionic radii of constituting ions[101] and their stoichiometry[99]. The reaction mechanism can be interpreted as follows[102]: (1) diffusion of Sc (V) into the V (Sc) oxide until the corundum reaches its maximum concentration of Sc and (2) slow migration of corundum material into the bixbyite phase. The second step is non-topotactic, or reconstructive. In the final product $ScVO_3$, Sc^{3+} and V^{3+} cations are statistically distributed over both 8*b* and 24*d* sites, rendering the structure cation-disordered[100]. Randomization of cations is the consequence of the prevailing role of entropy at increased temperature as well as proximity (16%) of ionic radii – 0.745 Å for $Sc^{3+}{}_{VI}$ and 0.640 Å for $V^{3+}{}_{VI}$[103] – allowed by the bixbyite structure. More about disorder will be presented in the next subsection.

C. Fluorite structure type (green) is named after the CaF_2 structure; it crystallizes in space group $Fm\bar{3}m$ (#225). Its cations and anions occupy, correspondingly, 4*a* (0, 0, 0) and 8*b* (¼, ¼, ¼) sites generating a 1:2 stoichiometric ratio of cations to anions. Each cation bonds to 8 anions, which creates edge-sharing of metal-oxygen cubes. In the reaction in **Fig. 2.1**, the fluorite phase $ScVO_{3.5}$ is the product of topotactic insertion of oxygen (oxidation) into the vacancies in the bixbyite $ScVO_3$. Due to the decrease of the ionic radius of vanadium during its oxidation, the ionic size ratio between scandium and vanadium in the same 4*a* site of the fluorite

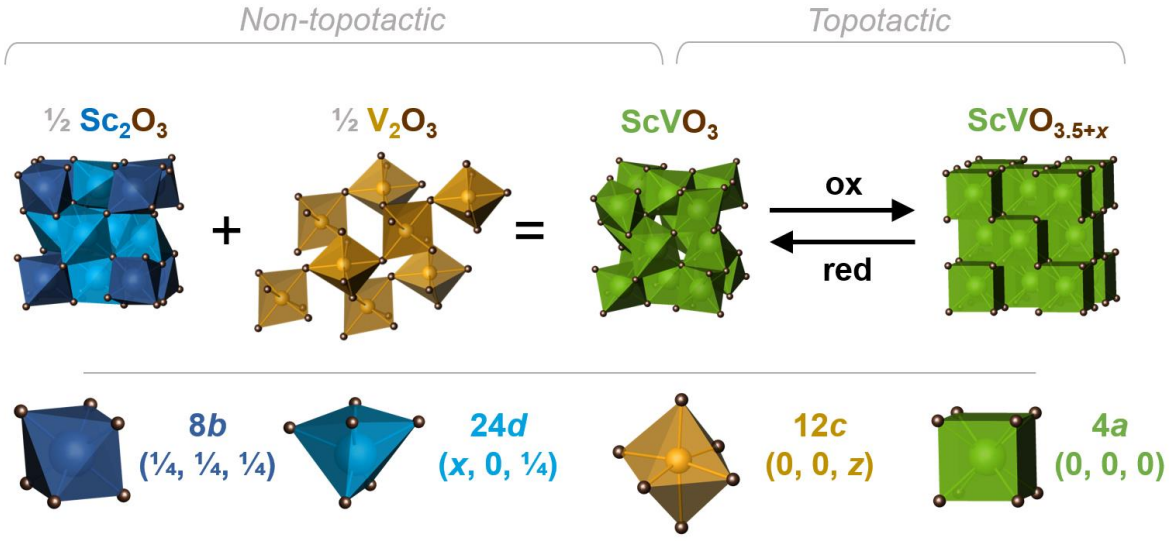

Figure 2.1. Polyhedral representation of a few relevant structures partaking in solid-state reconstructive (left) and topotactic (right) reactions. Sc and V coordination polyhedra are shown in blue and yellow, respectively, when separate and in green when indistinguishable. Brown spheres are oxygen. The bottom row shows coordination numbers, multiplicities, and coordinates of metals in the portrayed structures.

is larger than that in the bixbyite. This is despite supporting the same degree of cation disorder, as understood from the average structure probes. This concept will be further discussed and challenged in ***Chapter 6.***

2.1.2. Order and disorder for the example of the fluorite-bixbyite system

Cation (or anion) ordering, or site ordering, can be created when at least one of the two or more different cations (or anions) have strong site preferences. It is illustrated in **Fig. 2.2a** where two crystallographic sites and two sorts of ions populating them are schematically shown as baskets of colored balls. For example, in the zircon structure $ScVO_4$ (S.G. $I4_1/amd$, #141), Sc^{3+} and V^{5+} occupy, respectively, 4*a* (0, ¾, ⅛) and 4*b* (0, ¼, ⅜) sites only[104]. This corresponds to panel (1) in **Fig. 2.2a**. Alternatively, two ions A and B are considered site-ordered when, given the concentration of one of them (A) is too small to fill any of the sites completely, all ions A end up

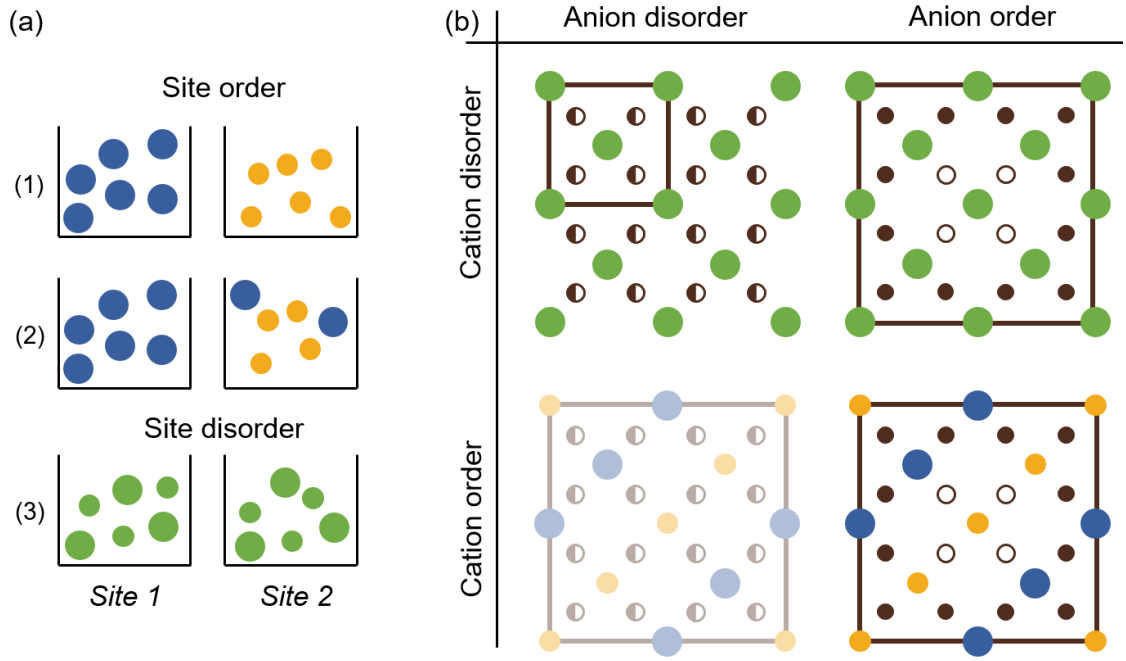

Figure 2.2. Schematic illustration of site ordering: (a) – schematics of cation ordering with crystallographic sites portrayed as baskets with balls – cations. Site preferences are counted as ordering; (b) – four cases of cation and/or anion ordering in a two-dimensional fluorite-like lattice. Cations are shown in blue and yellow when ordered and green when disordered. Anions and vacancies are brown and white when ordered and double-filled when disordered. Brown outlines in (b) are unit cells.

exclusively in one site. For example, in the spinel $Co_{1.2}V_{1.8}O_4$ (S.G. $Fm\bar{3}m$), V^{3+} sits in the site 16*c* (0, 0, 0) only, while cobalt shares the same site (Co^{3+}; 10% of it) and also occupies the site 8*b* (⅜, ⅜, ⅜) in the Co^{2+} state[105]. This scenario is depicted in panel (2) of the figure. Site preferences are usually driven by large discrepancies in ionic radii, electronic effects (associated with the ionic charge and geometry, i.e. ligand-field effects), ion-ion repulsion, etc. On the other hand, (anti-) site disorder arises when cations or anions are statistically distributed among the available sites, i.e. have no site preferences. For example, the bixbyite $ScVO_3$ is cation-disordered owing to its high formation temperature, and this disorder is maintained in the $ScVO_{3.5+x}$ fluorite – its topotactic oxidation product[93]. Such cation disorder corresponds to panel (3). **Fig. 2.2b** illustrates four scenarios of cation and anion ordering for the example of a schematic 2D projection of an oxide-defect fluorite structure and its so-called superstructures. The oxide-defect structure can be written as $ScVO_{3.5+x}\square_{0.5-x}$, where $\square$ denotes oxide vacancies. In the figure, oxide vacancies (○) and oxide-anions (●) are statistically disordered (◐) in the anion sublattice (top left). Simultaneously, Sc and V are also disordered in the only available cation site, as illustrated with colors: green colour (disorder) is a mixture of blue (scandium) and yellow (vanadium). Bixbyite $ScVO_3$ (top right) is cation-disordered as discussed above, also shown with the green color of cations. However, it is anion-ordered, as shown with systematically (not statistically) missing oxides (○) in the 16*c* (*x*, *x*, *x*) site – these vacancies are ordered with respect to oxygen in the 48*f* (●) site. Systematical (●/○) rather than statistical (◐) distribution of vacancies distorts the structure and results in a lower symmetry and the need to resort to a larger unit cell than in the fluorite parent structure, as illustrated with a larger box – supercell – around the bixbyite. The chemical difference between the top left and the top right scenarios is the concentration of oxygen which is smaller for the bixbyite (right). As will be shown with $Sc_2VO_{5+\delta}$ polymorphs in ***Chapter 3***, the non-topotactic alternative of the fully disordered fluorite is a fully ordered fluorite superstructure (bottom right) with systematically mixing oxides (○) and strong site preferences of scandium and vanadium. On average and similar to the bixbyite, this structure may also be oxygen-deficient with respect to the fluorite and can even be oxidized into it. The last case – anion disordering with cation ordering is far less probable than the other three scenarios, since typical highly charged cations (likely also different in sizes and charges from each other) will attract and hence order the surrounding anions.

Studying disordered oxide vacancies (◐) provides mechanistic insights into solid-state reactions and phase transitions and may facilitate the rational design of all-solid devices with applications

for energy conversion and storage. These applications include solid oxide fuel cells, electrolyzer cells, and electrochemical cells, carbon capture and storage systems, oxygen sensors, and others[3,106,107,108]. Apart from the fluorite structure introduced above[109,110,111], disordered oxide vacancies can be created in other oxide families and their derivatives (i.e. by doping or cation splitting[112]): perovskites[3,106,113], apatites[114], melilites[115], and others[116].

It should be noted that site disorder (ion-vacancy disorder and cation disorder) is not the only type of disorder. Disorder can also exist with respect to orientation of atoms or groups of atoms[117,118,119], compositional fluctuations[120], charge[121], magnetic moments[122], etc.[123]. Finding and controlling the degree of randomness in materials possessing these types of disorder is also within the field of rational design of functional materials.

2.2. Furnace setups used for lab-based solid-state synthesis

For high temperature non-topotactic synthesis, samples were prepared in resistively heated gas flow tube furnaces with mullite ($3Al_2O_3 \cdot 2SiO_2$) flow tubes – Carbolite (T_{max} = 1500 ºC) or Barnstead Thermolyne / Thermo Scientific (T_{max} = 1200 ºC), **Fig. 2.3a**. Cation-disordered frameworks were typically obtained at 1500 ºC in a flow of 3% H_2 (balanced Ar or N_2) to prevent

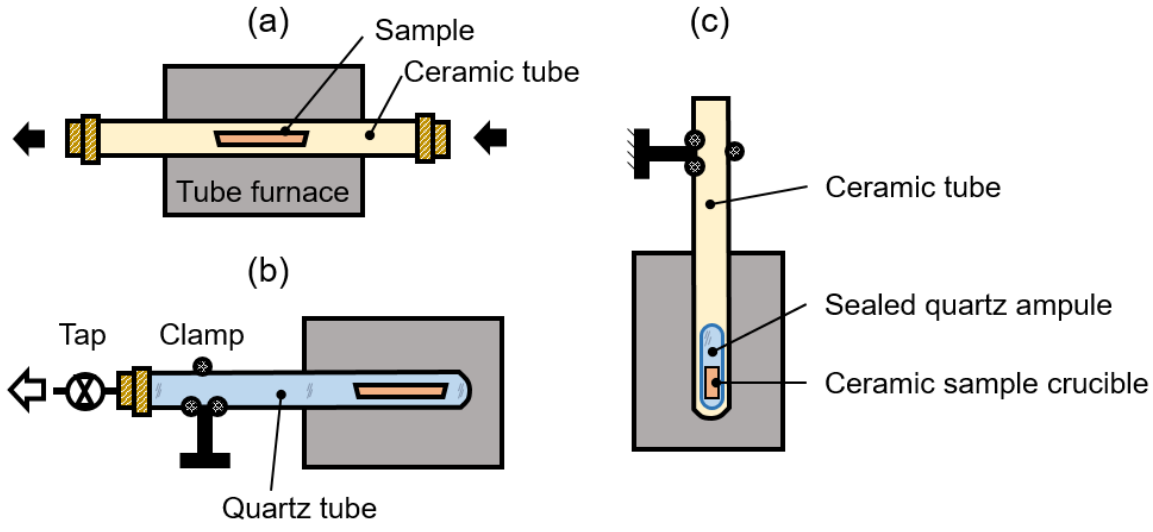

Figure 2.3. Some furnace arrangements for conventional solid state synthesis with gradual heating used in the work: (a) – a gas flow experiment, also usable with static air; (b) – a static vacuum setup with a tap; (c) – a static vacuum setup with the sample sealed into a quartz tube.

oxidation by atmospheric oxygen leaking into the tube through hot alumina. Lower-temperature reconstructive reactions as well as topotactic redox were done at 650-1200 ºC and 350-450 ºC, correspondingly.

For reactions in vacuum, a quartz insert with one sealed end was used according to **Fig. 2.3b**. The tube was evacuated prior to synthesis, and static vacuum was supported inside after closing the tap. Leakages were prevented by creating dynamic vacuum outside the tap. T_{max} was kept at or under 1100 ºC, which is below the softening point of quartz glass. For lower-throughput vacuum reactions, sample in a suitable alumina crucible was sealed under vacuum into an individual quartz tube in the natural gas/oxygen flame and then heated in the tube furnace. In rare cases where T_{max} was 1200 ºC, both the sealed sample and the ceramic inset of the tube furnace were arranged vertically (**Fig. 2.3c**) to mitigate the bending of the softened quartz walls under gravity.

Reconstructive redox synthesis with finer control of oxidation and reduction was carried out using the setup in **Fig. 2.4** involving a gas flow furnace and a longer quartz insert. In these experiments the furnace was typically preheated to 800 ºC in the flow of Ar to push out the air (a), then flushed with reactive gas (b), and only after that the preheated furnace was moved toward the

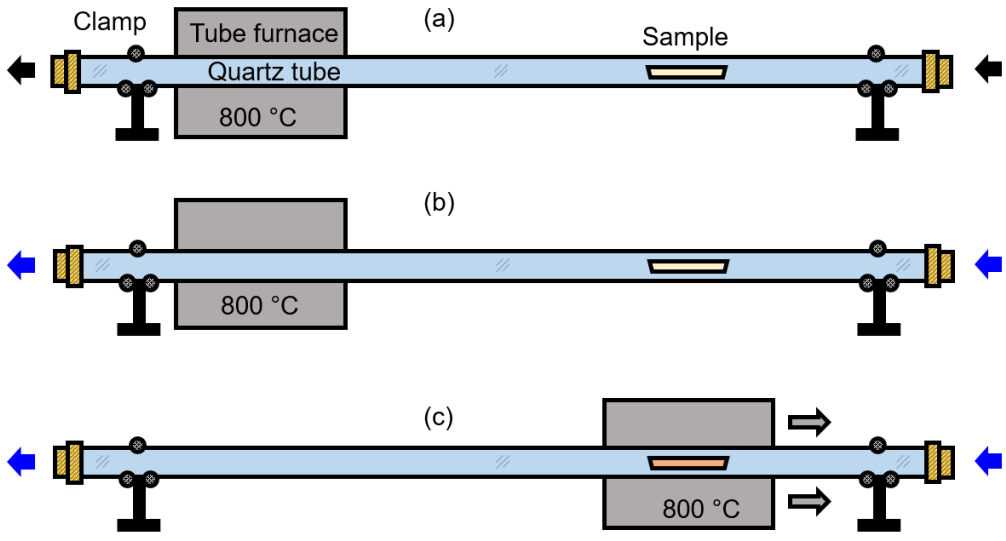

Figure 2.4. The "sliding furnace" setup for controlled oxidation/reduction of the sample with instant heating/cooling. Low-temperature polymorphs are skipped due to this three-stage process: (a) – flushing the setup with an inert gas in the direction sample→furnace; (b) – letting the oxidizing/reducing agent in; (c) – instant heating of the sample in the flow of the working gas.

sample for dwelling (c) against the flow of working gas. This configuration helped to stabilize higher-temperature phases which have stable competing lower-temperature polymorphs.

In all experiments, starting materials such as individual metal oxides were annealed if necessary and then ground in an agate mortar as acetone slurries. For large samples, ball-milling (Norton horizontal cylinder mill) with zirconia beads was used instead. Powders were then loaded into heat-resistant alumina combustion boats (McDanel, 99.8%) or ceramic crucibles of other shapes. For Sc-containing samples, platinum liner was often used at high temperatures (above 1200 ºC) to prevent formation of unwanted $Sc_2Si_2O_7$ from SiO_2 impurities in the boat. In solid-gas experiments (reduction or oxidation of solids), samples were typically loaded as loose powders. For solid-solid reactions, samples were pelletized using the PHI hydraulic press under a 7,000 pound load applied to a 13 mm (ID) die.

2.3. Chemicals used and preparation of key starting materials

The synthesis methods of further investigated samples for all experiments will be given when the corresponding experiment or synthesis is discussed, whereas below is the list of basic starting materials (and their preparation, when needed) from which the final samples were prepared.

(A) The starting material for preparation of vanadium (III) and (IV) oxides was V_2O_5, orange powder (Cerac, 99.9%). Loose powder was loaded in a ceramic boat and heated in a gas flow furnace overnight at 1100 ºC in pure H_2 flow (flushed with Ar before and after):

$$V_2O_5 + 2\,H_2 \rightarrow V_2O_3 + 2\,H_2O \qquad (2.1)$$

The resultant black powder of V_2O_3 crystallizes as a corundum type. To obtain VO_2, V_2O_3 was mixed in 1:1 molar ratio with V_2O_5 and heated at 1100 ºC in static vacuum (**Fig. 2.3b**):

$$V_2O_3 + V_2O_5 \rightarrow 4\,VO_2 \qquad (2.2)$$

Blue-grey powder of VO_2 crystallizes as a monoclinically distorted rutile (reversibly transitioning to the parent rutile type at 71 ºC[124]). The rutile structure is named after one polymorph of TiO_2 (light-beige/white) which was the source of Ti^{4+} of choice in this work. Prior to any experiments, TiO_2 from the shelf (Alfa Aesar, 99.995%) was annealed at 1000 ºC in air to convert

anatase impurities through an irreversible anatase-rutile phase transition[125]. Corundum-type Ti_2O_3 (black powder, Alfa Aesar, 99.8%) was the main source of Ti^{3+}; commercially available Ti_2O_3 accumulated a persistent impurity of Ti_3O_5 over time. An alternative source of Ti_2O_3 is a comproportionation reaction between Ti^{4+} and Ti^0 at 1500 °C[81] with 3% H_2 (bal. Ar) as an oxidation-preventing agent:

$$^3/_2\, TiO_2 + {}^1/_2\, Ti \rightarrow Ti_2O_3 \qquad (2.3)$$

where Ti is a dark-grey titanium metal powder (Alfa Aesar, 99.99%).

(B) Other starting materials used in synthesis were Sc_2O_3 (Synquest laboratories, 99.99%), Fe_2O_3 (Baker's Analyzed, ≤99.88%), Y_2O_3 (Alfa Aesar, 99.999%), In_2O_3 (Alfa Aesar, 99.994%), Yb_2O_3 (Alfa Aesar, 99.998%), Lu_2O_3 (Alfa Aesar, 99.99%), CrO_2 (Oakwood Chemical, unknown purity), MnO_2 (Alfa Aesar, 99.997%), GeO_2 (Alfa Aesar, 99.999%), ZrO_2 (Fisher Sci., un. pur.), SnO_2 (Alfa Aesar, 99.9%), NH_4VO_3 (Cerac, 99.9%), and Co_3O_4 obtained from old, partially reduced Co_2O_3 (Matheson Coleman & Bell, un. pur.) by heating it in air at 650 °C:

$$3\, Co_2O_3 \rightarrow 2\, Co_3O_4 + {}^1/_2\, O_2 \qquad (2.4)$$

All sesquioxides were preliminarily annealed in air.

More complex starting oxides were synthesized as follows. $ScVO_4$ (pale-yellow powder) was obtained by reacting Sc_2O_3 and NH_4VO_3 at 1100 °C in air:

$$Sc_2O_3 + 2\, NH_4VO_3 \rightarrow 2\, ScVO_4 + 2\, NH_3 + H_2O, \qquad (2.5)$$

$ScVO_3$ (brown powder) – by reducing $ScVO_4$ in pure H_2 flow at 1100 °C (although reduction at much lower temperature and with a milder reductant is also possible[126]):

$$ScVO_4 + H_2 \rightarrow ScVO_3 + H_2O, \qquad (2.7)$$

$Sc_2VO_{4.5}$ (brown powder) – by reacting Sc_2O_3 and V_2O_3 in 3% H_2 flow (bal. N_2 or Ar) at 1500 °C[99]:

$$Sc_2O_3 + {}^1/_2\ V_2O_3 \rightarrow Sc_2VO_{4.5}, \qquad (2.8)$$

(C) Standards for spectroscopy, if not mentioned above, were Cr_2O_3 (Fisher Sci., ≤ 99.7%), MnO (Sigma Aldrich, 99%), Mn_3O_4 (obtained by heating MnO at 1100 ºC in air), Mn_2O_3 (Cerac, 99.9%), Fe_3O_4 (Fisher Sci., unknown purity), Sc_2TiO_5 (cubic[127] and orthorhombic[12]), $Sc_2Ge_2O_7$[128], $YIn_{0.7}Mn_{0.3}O_3$[129], $Bi_{12}TiO_{20}$[130], and CoO (obtained via heating of impure Co_3O_4 from shelf at 950 ºC in air).

Phase purity of all materials was determined with lab-based X-ray powder diffraction.

2.4. Methods of analysis

The structure of the crystalline solids is central to this work. Crystallinity implies the same structural arrangement throughout the structure, achieved by translation of the same unit cell in all three dimensions with no gaps. Elucidation of such structures together with *in-situ* and *ex-situ* observation of their formation, decomposition, and phase transitions were carried out with average structure probes – powder X-ray diffraction and powder neutron diffraction. These probes provided an understanding of average crystal symmetry, average arrangement of ions, etc., as well as range of structural stability in real-time experiments. **Fig. 2.5** shows a 2D example of how the average structure (left) of a material under study (center) might look.

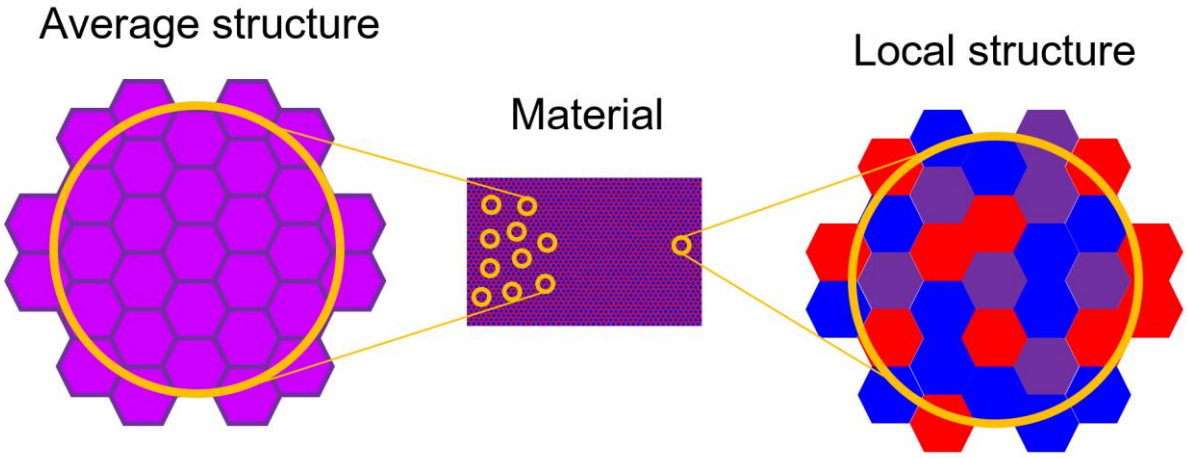

Figure 2.5. A schematic illustration of how different the crystalline structure (middle) might look under the average (left) and local (right) structure probes. Idea credit: Dr. Katharine Page.

However, physical properties and related structural peculiarities of solids are often defined on the scale of a single unit cell or even one polyhedron whose geometry might deviate from the average (averaged out) description. Hence, when necessary, local structure probes were also used – such as pair distribution function analysis and X-ray absorption near-edge structure spectroscopy. They supplied local or "average local" information, namely bond distances, charge speciation, etc. Right panel of **Fig. 2.5** shows how the local peculiarities of the same 2D structure of the same material might look different from the average structure, and even the choice of the unit cell might differ. The main techniques used for probing both average and local structure in this work are covered in the next sections.

2.4.1. Diffraction. X-ray powder diffraction (XRD)

Solid matter coherently scatters electromagnetic radiation when the size of the scatterers (i.e. atoms, but also the distances between them) are commensurate with the wavelength of the incident radiation. This condition is used in diffraction-based structure-probing techniques and especially for solids with long-range ordering of scatterers. The wavelength of the used radiation (X-rays in this section, but also neutron beams and electron beams) is on the order of 1 Å. Under the approximation that a wave scatters only once ("kinematical diffraction"), the correspondence between the wavelength of the incident and diffracted beams **λ**, interatomic distance $\mathbf{d}_{hkl}$ (distance between the planes *hkl* of equivalent scatterers in the solid), and the angle of incidence/diffraction **θ** can be written as follows and is called Bragg's law:

$$n\lambda = 2d_{hkl}sin\theta \qquad (2.9)$$

with ***n*** – order of diffraction (conventionally 1) and Miller indices ***h***, ***k***, and ***l*** denote sets of planes cutting the *a*, *b*, and *c* axes of the unit cell in points 1/*h*, 1/*k*, and 1/*l*, respectively. The one-dimensional case of Bragg's diffraction is schematically shown in **Fig. 2.6**, where two parallel beams scatter from the ions in the equivalent planes of the crystal lattice at an angle θ, equal to the angle of incidence. It can be geometrically derived that one beam (bottom) lags behind the other one (top) by a quantity $2d_{hkl}\sin\theta$. When this quantity amounts to an integer number of wavelengths, which happens at a particular value of θ, constructive interference is observed among diffracted

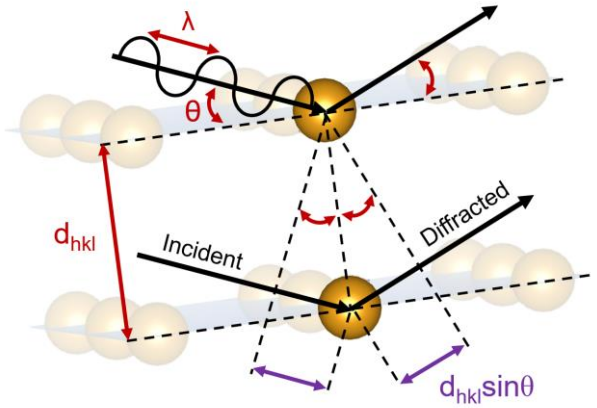

Figure 2.6. Illustration of Bragg's law. Ions are not to scale.

beams; importantly, the more scattering planes (the more crystalline the sample) – the sharper the resulting peaks. Superimposed on the resulting constructive interference pattern is a phase- and θ-dependent function ***f*** called the spherical atomic scattering factor or form factor, characterizing the scattering power of the electron cloud around a given ion. The form factor is the largest when there is no phase difference among diffracted beams, which in the X-ray diffraction experiment happens to correspond to the smallest incident angle due to more interactions between X-rays and the density of the electron cloud (which can be imagined as more concentrated close to the center and radially decaying outward). Scattering factors for a few ions relevant to this work are plotted in **Fig. 2.7a** as a function of $Q = \frac{2sin\theta}{\lambda}$ in accordance with the following equation[D]:

$$f\left(\frac{sin\theta}{\lambda}\right) = \sum_{i=1}^{4} a_i e^{\frac{-b_i sin^2\theta}{\lambda}} + c, \qquad (2.10)$$

where $\boldsymbol{a_1 \ldots a_4}$, $\boldsymbol{b_1 \ldots b_4}$, and ***c*** are tabulated coefficients[131]. It can be seen that scattering factors for vanadium and scandium, neighboring in the periodic table, and those of trivalent and pentavalent vanadium are virtually indistinguishable. It is also seen that all three are vastly different from oxygen, which allows for sufficient X-ray contrast between oxygen and mentioned metals in their oxides. In **Fig. 2.7b** a powder X-ray pattern of a cubic fluorite $Sc_2VO_{5+\delta}$ is shown with indexed diffraction peaks which correspond to diffraction planes illustrated on the right. Notably, the

[D] This function was said to be accurate at lower diffraction angles, while at higher angles another function is more accurate[305].

relation exists between Miller indices (*hkl*) used to denote the planes and interplanar distances d_{hkl}, which for a cubic system with a lattice parameter ***a*** (= *b* = *c*) takes the following form:

$$\frac{1}{d_{hkl}^2} = \frac{h^2+k^2+l^2}{a^2}. \qquad (2.11)$$

For less symmetric crystal systems, similar equations can be found elsewhere[132]. Since this relation shares *d* with Bragg's law, by iteration it is possible to find lattice parameters of an unknown single-phase sample directly from the diffraction pattern collected at a known wavelength. In general, the diffraction angle axis carries the information about the unit cell parameters (*a*, *b*, *c*, α, β, γ) as well as wavelength used, sample transparency, and some characteristics of the equipment. By contrast, the vertical axis – the intensity – carries the information about the atomic coordinates within the unit cell, concentration, atomic displacement, and also some parameters of the equipment. These and the previously mentioned form factor contribute to the structure factor $\boldsymbol{F_{hkl}}$ which describes the profile of a peak (see **Fig. 2.7b**):

$$F_{hkl} = \sum_{j=1}^{n} g_j \cdot t_j(\theta,\lambda) \cdot f_j(\theta,\lambda) \cdot e^{2\pi i(hx_j+ky_j+lz_j)}, \qquad (2.12)$$

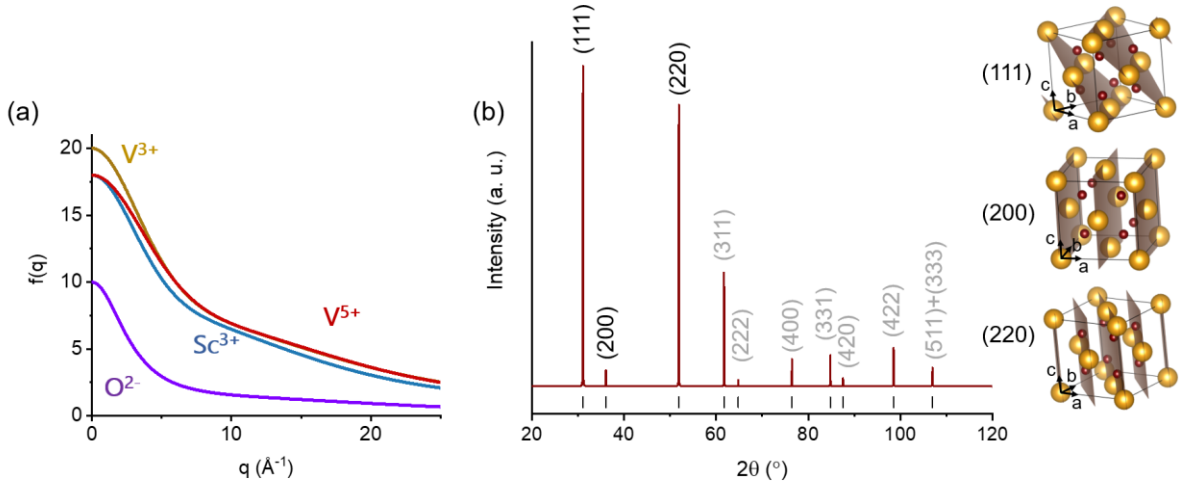

Figure 2.7. Atomic scattering factors of a few species relevant to this work (a) and an example of the X-ray diffractogram of a fluorite where the correspondence is shown between the Miller indices (labels on the peaks) and scattering planes within the fluorite structure (b).

where $\boldsymbol{n}$ is the number of atoms in the unit cell (including those already accounted for by the symmetry), $\boldsymbol{g}$ is the occupancy (shows by how much the site is occupied with the $\mathbf{j^{th}}$ atom), $\boldsymbol{t}$ is the displacement of the j^{th} atom (predominantly due to thermal vibrations), $\boldsymbol{x}$, $\boldsymbol{y}$, $\boldsymbol{z}$ are the coordinates of the j^{th} atom, and imaginary unit i indicates the vector nature of the structure factor. The absolute value of the peak structure factor F_{hkl} contributes to the peak intensity $\boldsymbol{I_{hkl}}$ as follows:

$$I_{hkl} = S \times M_{hkl} \times LP_{\theta} \times A_{\theta} \times T_{hkl} \times E_{hkl} \times |F_{hkl}|^2, \qquad (2.13)$$

where $\boldsymbol{S}$ is the scale factor (crudely – the number of registered scattered photons), $\boldsymbol{M_{hkl}}$ is the peak multiplicity (the number of symmetry-equivalent peaks appearing at the same value of θ, i.e. with the same sum of $h^2+k^2+l^2$, which depends on the crystal system), $\boldsymbol{LP_{\theta}}$ is the Lorentz-polarization factor (depends on the geometry of the diffraction experiment), $\boldsymbol{A_{\theta}}$ is the sample absorption, $\boldsymbol{T_{hkl}}$ is the preferred orientation factor which accounts for non-random distribution of families of scattering planes in the sample, $\boldsymbol{E_{hkl}}$ is the extinction coefficient (compensates for the errors introduced by the aforementioned kinematical diffraction approximation). The peak intensity

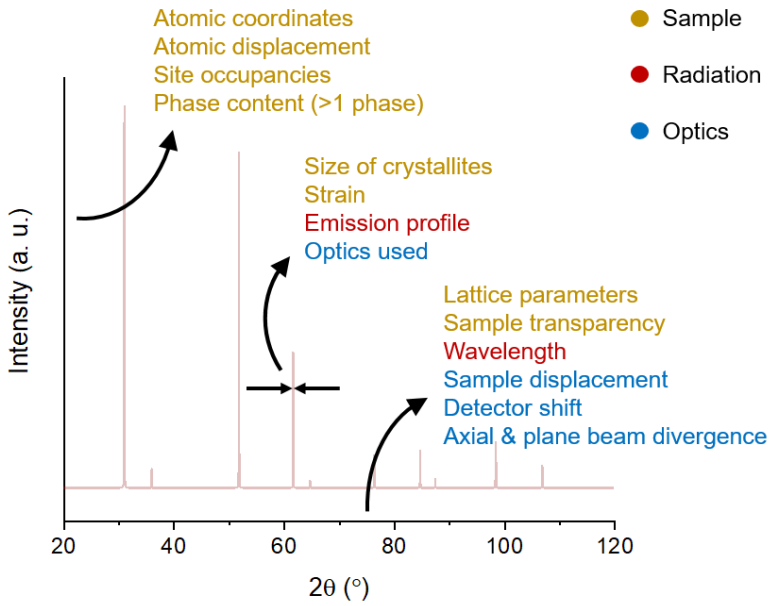

Figure 2.8. A color coded list of sample-, radiation-, and setup-related parameters one can obtain from refining intensity-, angle-, and peak-shape-related parameters in a Rietveld refinement against diffraction data.

contributes to the calculated (as opposed to observed) intensity in a point $\boldsymbol{Y_{i,c}}$ as described by eq. 2.14:

$$Y_{i,c} = b_i + \sum_{l=1}^{k} S_l \sum_{j=1}^{m} I_{l,j} y_{l,j}(x_{l,j}) \qquad (2.14)$$

where ***b*** is the background intensity of a point, ***S*** is the scale factor, ***y(x)*** is some peak profile function (see below), ***k*** is the number of phases in the sample, and ***m*** is the number of peaks in the pattern.

2.4.1.1. Rietveld refinement

The position, intensity, and even width of the diffraction peaks provide information about the sample, the equipment, and the emission as briefly summarized in **Fig. 2.8**. Depending on what is known about the experiment, this information can be used, confirmed, or obtained in a Rietveld refinement[133] of the structure against the powder diffraction data. This method was used as a final method of analysis of powder diffraction data throughout this work, meaning that the Rietveld method should be used after some certainty on the phase content of the analyte has already been achieved via phase identification, and the fine details of unit cell dimensions, atomic coordinates, phase content, etc. are missing. The method concerns the whole pattern (not separate peaks) and is based on least square minimization. The experimental powder diffractogram is fitted with a calculated profile, and the model is changed until the best agreement is achieved between the calculated pattern and the experimental data:

$$\Delta = \sum_{i=1}^{n} \frac{1}{Y_{i,obs}} \left(Y_{i,obs} - Y_{i,c}\right)^2 + C, \qquad (2.15)$$

where $\boldsymbol{Y_{i,obs}}$ is the experimental intensity in a point, $\boldsymbol{Y_{i,c}}$ is the calculated intensity (see eq. 2.14), and **C** is a non-mandatory set of physical and chemical restraints such as fixed stoichiometry, fixed interatomic distances, etc. The peak function *x(y)*, to be overlaid on the emission profile, can take many forms; in Rietveld analysis throughout this work a pseudo-Voigt function *PV(x)*[134] was usually used which is a linear combination of the Gaussian *G(x)* and Lorentzian *L(x)* peak shape functions:

$$PV(x) = \eta G(x) + (1-\eta)L(x) = \frac{2\eta}{FWHM_G}\sqrt{\frac{ln2}{\pi}}e^{-4ln2\cdot x^2} + \frac{2(1-\eta)}{FWHM_L}\cdot\frac{1}{\pi(1+4x^2)}, \quad (2.16)$$

where **η** is a refinable mixing parameter ($0 < \eta < 1$) and ***FWHM*** is the breadth of the peak, or its full width at half-maximum. The FWHM evolution as a function of diffraction angle is described as

$$FWHM_G = \sqrt{U\cdot tg^2\theta + V\cdot tg\theta + W}, \quad (2.17)$$

$$FWHM_L = {}^{X}/_{cos\theta} + Ytg\theta, \quad (2.18)$$

with independently refinable parameters ***U***, ***V***, ***W*** (three Caglioti parameters[135]), ***X*** (related to crystallite size), and ***Y*** (related to microstrain).

The refinement procedure involves several cycles of iteration, during which minimization of Δ is achieved and assessed with the help of figures of merit. In this work, the two most popular figures of merit were used, namely goodness of fit (GOF) $\boldsymbol{\chi^2}$ and weighted profile residual $\boldsymbol{R_{wp}}$:

$$\chi^2 = \frac{\Delta}{n-p}, \quad (2.19)$$

$$R_{wp}(\%) = \sqrt{\frac{\Delta}{\sum_{i=1}^{n} Y_{i,obs}}}\cdot 100\%, \quad (2.20)$$

where ***p*** is the number of independently refined parameters.

Throughout this work, two software suites were used for Rietveld refinement – FullProf[136] (v.5) and Topas[137] (v.5 and v.7).

2.4.1.2. Generation of X-rays

X-ray photons can be generated when fast moving electrons change their kinetic energy. In a frequently used laboratory setup, these electrons are generated inside a sealed ceramic or quartz tube like the one schematically shown in **Fig. 2.9a**. On a larger scale, X-rays can be produced in electron accelerators – synchrotrons, as shown in **Fig. 2.10**. Synchrotron X-rays are 10^{10}-10^{15} times

more brilliant than sealed X-ray tubes, meaning they produce many more photons per unit area and per useful photon energy.

(A) A sealed X-ray tube contains an electrically heated cathode (usually made of tungsten) and a water-cooled anode (often Cu, also can be Mo, Ag, etc.). When heated, the cathode loses some of its electrons, and tens of kilovolts between the anode and the cathode sends these electrons toward the anode[132]. The core electrons of the anode material are knocked out, and their place is taken by the electrons from any of the subsequent shells of the same atom, driven by the need to lower the energy of the now excited electronic state. Generation of the commonly used Kα radiation (L→K) is shown in **Fig. 2.9b**, where the newly formed K-vacancy is populated at the

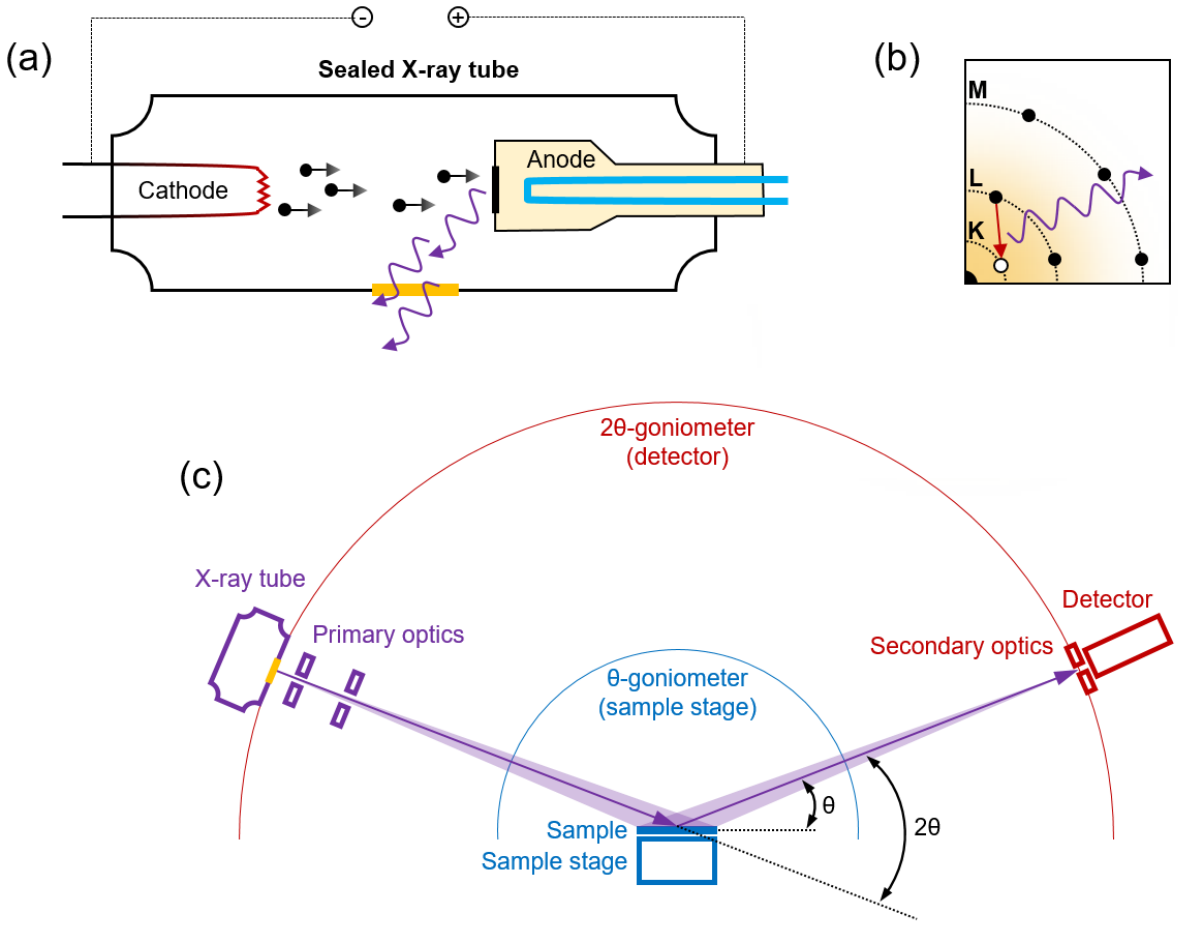

Figure 2.9. A few schemes related to X-ray diffraction: (a) – sealed ceramic X-ray tube (black – electrons, purple – X-rays, yellow bar – Be window); (b) – generation of Kα X-rays; (c) – goniometer circles of a Bragg-Brentano X-ray diffractometer with purple, blue, and red parts pertaining to X-ray tube (and its X-rays and incident optics), sample stage (and its goniometer), and detector (and its goniometer and optics).

expense of the L-shell, which produces $K\alpha_1$ or $K\alpha_2$ radiation depending on the electron spin. This radiation leaves through an X-ray transparent beryllium window and passes through the X-ray optics. See **Fig. 2.9c** for the reflection geometry predominantly used in this thesis (also known as θ-2θ configuration of Bragg-Brentano geometry). Various metal slits and masks are used to shape the divergent X-ray beam and the convergent diffracted beam, while filters and monochromators are used to remove other emission lines. In the setup predominantly used throughout this thesis, the sample stage and the detector block were situated on the goniometer arms rotating them in the plane of the figure by the angles θ and 2θ, correspondingly. The sample stage rotated the sample to achieve more homogeneous representation of all its available atomic planes in the beam. As opposed to reflection geometry, in transmission geometry (not shown, but occasionally used in the thesis) the beam is focused on the sample and passes through it. It is more sensitive to the material of the sample holder and varying path lengths through the sample and hence needs an absorption correction. On the other hand, it allows for θ-independent intensities of the diffraction peaks, whereas the divergent beam of the Bragg-Brentano geometry tends to cover different sample areas as a function of θ.

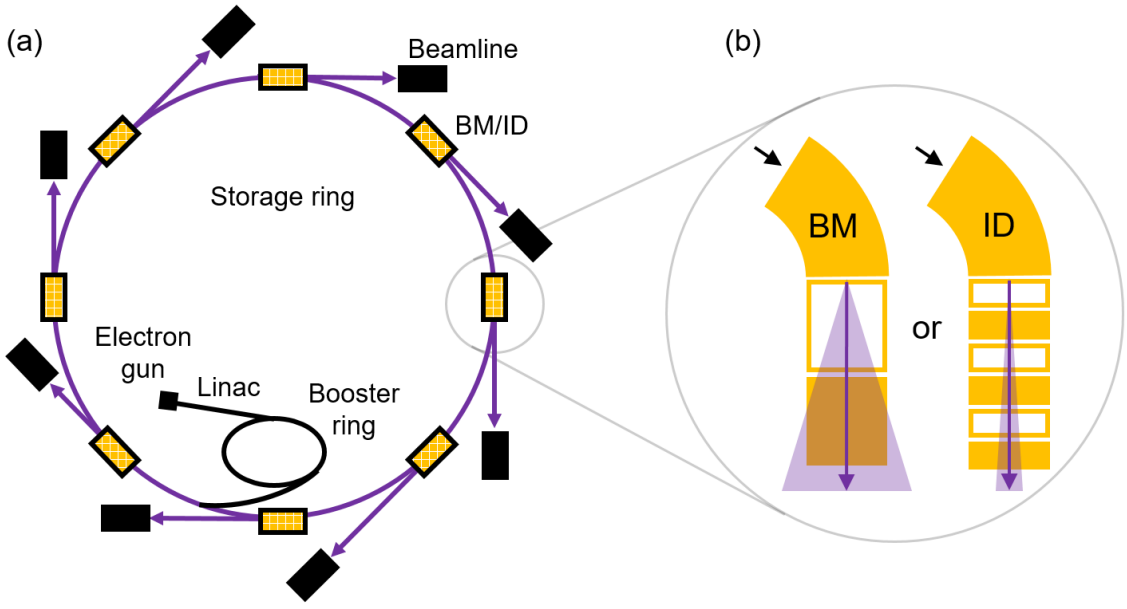

Figure 2.10. A schematic illustration of a synchrotron. Inset shows a half of a magnet which can be either a bending magnet or an insertion device. White and yellow parts are magnets of the opposite polarities. For both magnets the width of the resulting X-ray beam is shown with a purple cone.

(B) Synchrotrons are giant ring-shaped electron accelerators (**Fig 2.10a**). Similar to X-ray tubes, the process starts with generating electrons by heating a cathode inside the electron gun. As-generated electrons are then linearly accelerated in a magnetic field of the linac, injected into an energy-boosting inner ring to gain speed to just under the speed of light, and then injected into a larger outer ring (purple in the figure). The X-ray generation process hinges on the loss of energy of accelerated electrons each time they deviate from their initial trajectory. In contemporary synchrotrons, the losses are induced by passing the electrons through bending magnets (BM, 2nd generation) and insertion devices of the undulator type (ID, 3rd generation). Both devices are a sequence of magnets of opposite polarity, the more magnets – the narrower the produced photon band will be (**Fig 2.10b**) owing to more constructive interference events among the as-generated X-rays[138,139]. Trajectories of generated X-rays are tangential to the outer ring and lead to individual laboratories – beamlines – each having their own optics (apertures, mirrors, slits, etc.) and other equipment (furnaces, gas systems, cryostats, etc.) suitable for a particular set of scientific objectives. An average synchrotron is more brilliant than the average laboratory instrument and has higher resolution, but its main advantage is the tunability of the wavelength.

2.4.1.3. Sample preparation for XRD and experiment conditions

A. Room-temperature diffraction for both phase identification and Rietveld analysis was carried out on three lab-based powder diffractometers used at different stages of this work:

- PANalytical X'Pert Pro with Bragg-Brentano geometry (reflection mode) with Cu $K\alpha_{1,2}$ radiation; $\lambda(K\alpha_1) = 1.540598$ Å, $\lambda(K\alpha_1) = 1.544426$ Å. The usual set-up involved 0.04 rad soller slits, 1º divergent slit, 10 mm mask, 2º antiscatter slit, 3.4 mm receiving slit, Ni foil for blocking Kβ radiation, and an X'Celerator strip detector (128 microstrips altogether covering 2.122 º area). Usual step size was 0.0167 º, and collection time varied depending on the purpose of the scan. The sample stage was rotated at 1 Hz. Line profiles and peak positions were confirmed with corresponding NIST standards like LaB_6 SRM 660a and Si SRM 640b, respectively. Powdered samples were mounted as acetone slurries on 30 mm zero-background silicon disks.
- Bruker D4 Endeavor, with the same geometry and radiation profile but equipped with a point detector. Typical step size was 0.02º. Powdered samples were either mounted as ethanol slurries or sprinkled over a thin layer of grease on poly(methyl methacrylate) 52 mm disks.

- Huber G670, operating in transmission geometry with CuKα_1 radiation, achieved with a Ge monochromator, and a Guinier camera-type detector. Typical resolution was 0.005º. Powdered samples were mounted as acetone slurries onto polyester films clamped to an oscillating sample stage.

B. In-lab high-temperature *in-situ* powder diffraction was carried out on the PANalytical X'Pert Pro (above) equipped with a HTK-2000 (Anton Paar GmbH) furnace. Samples were mounted directly onto the 1 cm wide Pt strip as acetone slurries. The furnace allows heating up to 1300 ºC in different gas atmospheres.

C. Room-temperature high-resolution powder X-ray synchrotron diffraction data were measured on beamline 11-BM[140] (Advanced Photon Source) at Argonne National Laboratory. It covers a range of λ = 0.34-1 Å and 2θ = 0.5 - 130º, and has 12 analyzer crystal detectors ($LaCl_3$)[141]. Detectors with discriminatory analyzers and a monochromator (Si cut along (111) plane) ensure high-resolution (under $1.4 \cdot 10^{-4}$ $\Delta Q/Q$ for 11-BM) and signal-to-noise ratio, while their number (12) and the sample-changing robot allow for faster data collection and high throughput. The instrument works in transmission geometry where the beam is focused on a cylindrical sample.

11-BM data were used for experiments in ***Section 3.1.1*** and ***Chapter 6***. For preparation, powdered samples were loaded in 0.8 mm Kapton capillaries and protected with wax plugs from both sides. Data were collected at room temperature (RT) for 1 h at λ = 0.412831 Å in the 0.5-50º range and had 0.0001º step size.

D. High-temperature *in-situ* synchrotron powder diffraction with high-flux was carried out at the rapid-acquisition beamline 17-BM[142] (Advanced Photon Source) at Argonne National Laboratory. It uses the transmission geometry, in conjunction with a 2D detector for rapid data collection and a Si (311) monochromator for single wavelength selection. It operates in a range of λ = 0.24-0.46 Å and 2θ = 0.8 - 17º with a binned step size of 0.0064º. Powdered samples were loaded into thin quartz capillaries allowing a flow of working gas through them and heated below the softening point of quartz.

For the experiments in ***Section 3.2***, samples were heated up to 900 ºC with 5 to 100 ºC/min steps depending on the experiment. Atmospheres used were He, 3.5% H_2 (bal. He), O_2, ≈10 ppm O_2 (in N_2), or air flow. Data were collected with 12 s exposure time at λ = 0.72768 Å in the 1-45.3 Å range and had 0. 01772º step size.

Integration of resulting 2D images (an example is schematically given in the left panel of **Fig. 2.14** below) was done in GSAS-II[143], and some intensity corrections were done with 2DFLT[144] where necessary.

2.4.2. Neutron powder diffraction (NPD)

Neutron diffraction is another average structure probe, similar to X-ray diffraction in principle but different in the nature of interaction and hence layout and size of the instrument and particular capabilities. For example, neutrons interact with the nucleons and unpaired electrons rather than outer shell electrons, which leads to (1) larger penetration depths, (2) possibility of magnetic structure determinations (not considered here), and (3) often beneficial contrast between some neighboring elements. Neutrons scattering is independent of the size and electron density of atoms. The bound coherent neutron scattering length $b_{j,coh}(\theta)$ is the neutron equivalent of the X-ray form factor and is diffraction-angle-independent. The structure factor equation changes accordingly (see eq. 2.12 for definitions of other symbols):

$$F_{hkl} = \sum_{j=1}^{n} g_j \cdot t_j(\theta,\lambda) \cdot b_{j,coh}(\theta) \cdot e^{2\pi i(hx_j+ky_j+lz_j)}. \qquad (2.21)$$

The scattering length characterizes the strength of the neutron – nucleus interaction and depends on the particular isotope, spin difference of the incident and target particles, etc. It can be coherent $\boldsymbol{b_{j,coh}(\theta)}$ or $\boldsymbol{b_{coh}}$ and incoherent $\boldsymbol{b_{j,incoh}}$ or $\boldsymbol{b_{incoh}}$ (scattering in all directions). For example, **Fig. 2.11** compares coherent scattering lengths of Sc, V, and O, averaged over their naturally abundant isotopes[145]. From the figure, all three elements can be easily distinguished due to vastly different scattering lengths. This is in contrast with **Fig. 2.7a**, where Sc and V are indistinguishable under X-rays, and O is a much weaker scatterer. Thus, XRD and NPD

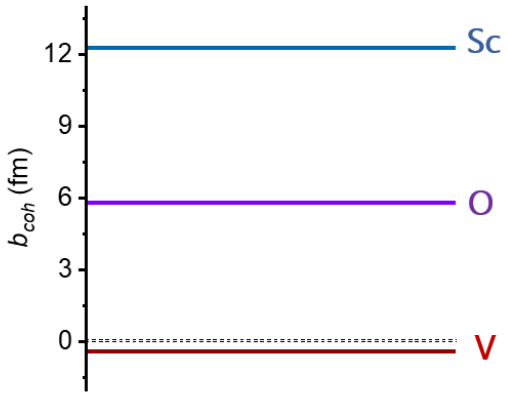

Figure 2.11. Neutron coherent scattering lengths of Sc, V, and O.

can be used as complementary probes. Another characteristic of interaction between neutrons and sample is the bound coherent scattering cross section $\boldsymbol{\sigma_c}$, which is the measure of the probability to be coherently scattered:

$$\sigma_c = 4\pi\overline{b_{coh}}^2, \qquad (2.22)$$

where the line on top of the symbol means its average value. However, when designing an experiment, more attention is paid to the cross section of the unwanted absorption, which is the "other side of the medal" of neutron-sample interaction:

$$\sigma_a = 2\pi\lambda\overline{Im(b_{tot})}, \qquad (2.23)$$

where $\boldsymbol{Im(b_{tot})}$ is the imaginary part of otherwise complex $\boldsymbol{b_{tot}}$, and b_{tot} itself is the total bound scattering length (coherent plus incoherent):

$$b_{tot} = b_{coh} + \frac{2b_{incoh}}{\sqrt{I(I+1)}} s \cdot I. \qquad (2.24)$$

Here, $\boldsymbol{s}$ is the spin of the incident neutron (s = ½) and $\boldsymbol{I}$ is the spin of the target nucleus[145]. Values of bound scattering lengths and cross-sections are tabulated.

2.4.2.1. Generation of neutrons

Larger penetration depths of neutrons imply the need for larger samples (which might be a nuisance) and operating in transmission geometry. Furthermore, the very generation of neutrons requires large facilities. There are two main types of neutron-generating facilities – nuclear reactors and spallation sources. Nuclear reactors generate neutrons through fission – radioactive decay of unstable U or Pu species, for example as follows:

$$^{235}_{92}U + {}^{1}_{0}n \rightarrow {}^{144}_{56}Ba + {}^{90}_{36}Kr + 2{}^{1}_{0}n + \gamma \qquad (2.25)$$

The resulting neutrons can (1) drive further fission via a chain reaction and (2) either be leaked out or used for research after moderation (the process of slowing them down). Neutrons obtained by fission have relatively low flux[132], and the reactor itself overheats rapidly. Higher flux can be obtained at spallation facilities, where neutrons are generated in pulses via collisions of constantly accelerated protons with a neutron-rich target out of which the neutrons are knocked out. **Fig. 2.12** shows the layout of the spallation Neutron Source at Oak Ridge National Laboratory (before the moderator) and the scheme of one particular beamline BL-11A "POWGEN" (after the moderator) [146,147] used in many neutron powder diffraction experiments below. The pulsed ion source (1 Hz) produces packets of hydride anions H^- which are easily accelerated and shaped into a beam by the linac magnets. The linac (linear accelerator) passes through a carbon foil which strips off both electrons from each H^- making it a proton H^+. The resulting protons are then injected into an accumulator ring. After more than a thousand rotations in the ring, pulses of protons are sent to the target (e.g. a body of mercury) to knock out its neutrons in a spallation event. Generated neutrons are collected into a beam and passed through a moderator (e.g. water or H_2) to reduce their speed and temperature[148]. After the moderator, neutrons are directed to the beamlines, each one having its own optical components (collimators, mirrors, etc.) and equipment (furnaces, cryostats, etc.) tailored for particular research conditions and objectives. Beamline BM-11A "POWGEN", used for most neutron diffraction experiments in the thesis, uses a set of bandwidth choppers – rotating disks – to achieve a reliably timed neutron beam covering a specific wavelength range[146]. The beam guide also contains supermirrors for total reflections of neutron back into the beam and preventing neutron absorption in the walls of the flight path. The sample is a loose powder, typically not less than 1 g in mass. The detector array consists of at least 40

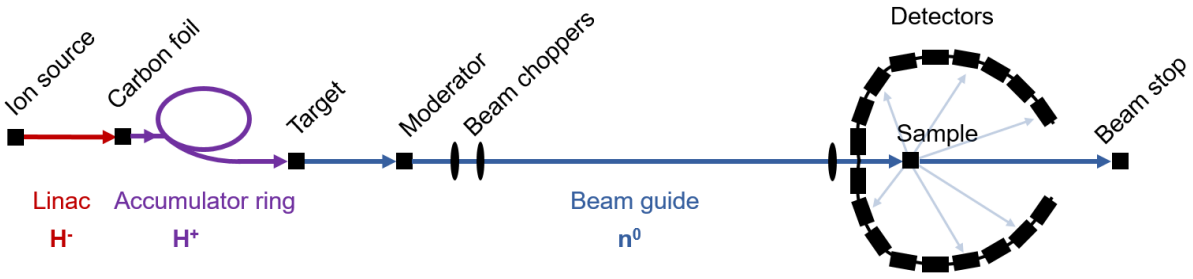

Figure 2.12. A schematic illustration of the spallation process and the powder neutron diffraction beamline BL-11A.

scintillator detector modules which surround the sample in three dimensions and cover a scattering range of $2\theta = 8\ldots170^{o}$ [147].

2.4.2.2. Time-of-flight

Pulse generation and wavelength (energy) selection translate into velocity selection: more energetic neutrons arrive faster at the detector[149]. The setup that discriminates among pulses based on arrival time is called the time-of-flight (TOF) technique. Combining the simple kinematic displacement equation, Bragg's law, and de Broglie particle-wave equation, a link can be established between the neutron TOF (τ) and the more familiar scattering angle (2θ):

$$\begin{cases} \boldsymbol{\tau} = \frac{L}{v} \\ \lambda = 2d \cdot sin\boldsymbol{\theta} \\ \lambda = \frac{h}{mv} \end{cases} \Rightarrow \boldsymbol{2\theta} = 2\arcsin\left(\frac{h\boldsymbol{\tau}}{2mdL}\right), \qquad (2.26)$$

where $\boldsymbol{L}$ is the beam guide length (60 m moderator to sample, 2-4.7 m sample to detector), $\boldsymbol{v}$ is the speed of neutrons, $\boldsymbol{d}$ is the interatomic distance, $\boldsymbol{\lambda}$ is the wavelength, $\boldsymbol{h}$ is Planck's constant (~$6.6261\cdot10^{-34}$ kg·m^2/s), $\boldsymbol{m}$ is the neutron's mass (~$1.6749\cdot10^{-27}$ kg). This relation is further adjusted when working with actual diffraction data from POWGEN:

$$\tau = Ad^2 + Cd + T, \qquad (2.27)$$

where $\boldsymbol{A}$ is an empirically derived constant (obtained from a Rietveld refinement on a standard), $\boldsymbol{T}$ is the zero point drift of the detector, and:

$$C = \frac{2mL\cdot sin\theta}{h}. \qquad (2.28)$$

When this quadratic equation needs to be solved with respect to d, a positive root is used for $A > 0$ and negative – for $A < 0$.

2.4.2.3. Sample preparation for NPD and experiment conditions

Samples for neutron diffraction were measured at BL-11A "POWGEN" or BL-1B "NOMAD" [150] (Spallation Neutron Source) at Oak-Ridge National Laboratory. At BL-11A, one to two grams of oven-dried powdered samples were loaded into 6.0 mm or 7.6 mm (ID) vanadium sample holders. Room-temperature scans (***Sections 5.3.3*** and ***6.1.2***) were taken over 1 to 2 hours at central wavelengths 1.5 Å or 2.665 Å, corresponding to *d*-spacing ranges 0.5-12.5 Å and 1.0-20.5 Å. *In-situ* experiments (***Section 3.1.1***) were conducted in a vacuum furnace in the temperature range from 30 to 1100 ºC with heating rates 2.5 ºC/min below 600 ºC and 0.75 ºC/min after. Data were collected at a central wavelength 2.665 Å and binned in 5 ºC increments. Data integration, reduction, and binning were performed in the Mantid software package[151]. At BL-1B (***Section 4.5.1***), under 300 mg of powdered sample was placed into a 3 mm (OD) quartz capillary. Room temperature data were collected with six detector banks in the wavelength range from 0.1 to 3 Å over 20 min total. The instrument was calibrated with $Ca_3Al_2Na_2F_{14}$.

2.4.3. Pair distribution function analysis (PDF)

Powder diffraction is among the best tools for structural analysis of long-range periodic structures as described in the two previous sections. Long-range periodicity provides enough scattering planes to observe the Bragg diffraction resulting in a description of an average crystal structure. However, analysis of long-range aperiodicities (e.g. in glasses) and short-range violations of periodicity, observed with increasing frequency in well-known ionic structures[152,153,154,155], requires a different probe. This probe is the total scattering described by the pair-distribution function (PDF) which produces a histogram of bond distances between each pair of ions[156] (**Fig. 2.13**). Apart from bond distances weighted by their abundance, information on structural disorder and the size of the probed cluster of ions can be extracted from PDF data as shown in **Fig. 2.14**. This information is available from the total scattering events including diffuse scattering (i.e. from the irregularly arranged scatterers) which are extinguished through destructive interference in Bragg scattering but prioritized in the PDF analysis. The pair distribution function $G(r)$ takes the following form[157,158]:

$$G(r) = \frac{2}{\pi}\int_{Q_{\min(\to 0)}}^{Q_{\max(\to\infty)}} F(Q)\sin(Qr)\,dQ = 4\pi r(\rho(r) - \rho_0) = 4\pi r\rho_0(g(r) - 1), \textit{(2.29)}$$

where ***r*** is the size of the probed cluster of ions, ***Q*** is the magnitude of the scattering vector (Q = 4πsinθ/λ), $\boldsymbol{\rho_0}$ is the density (number of ions per volume), ***ρ(r)*** is the atomic pair density consisting of ρ_0 and ***g(r)*** (which is the probability of finding two ions (say, *i* and *j*) at a distance *r* from each other), and ***F(Q)*** is the structure factor for total scattering: $F(Q) = Q(S(Q)-1)$ with ***S(Q)*** being the normalized structure factor found as follows for neutron PDF:

$$S(Q) = \left(\sum_{i=1}^{n} c_i\bar{b}_i\right)^{-2}\sum_{i,j=1}^{n} c_i c_j \bar{b}_i\bar{b}_j\left(1 + \rho_0\int_0^{\infty} 4\pi r^2(g_{ij}(r) - 1)\frac{sinQr}{Qr}dr\right). \quad \textit{(2.30)}$$

In the equation, ***n*** is the number of types of ions, $\boldsymbol{\bar{b}_i}$ **(**$\boldsymbol{\bar{b}_j}$**)** is the averaged (over all isotopes) coherent neutron scattering length of ion ***i*** **(*j*)**, and $\boldsymbol{c_i}$ **(**$\boldsymbol{c_j}$**)** is the relative content of ions *i* (*j*) in the sample. For X-ray PDF, Q-independent scattering lengths b_i are to be replaced with Q-dependent form factors f_i.

A PDF data refinement is carried out via the least square minimization routine following either a small-box or a big-box strategy. Small-box approach is known as the "real-space Rietveld" method, where a Rietveld-type analysis is applied to a marginally larger unit cell (e.g. see software PDFgui[159]). The other approach is the Reverse Monte-Carlo (RMC) routine, wherein atoms in random positions of a large starting configuration (>> 1 unit cell) are swapped, and different

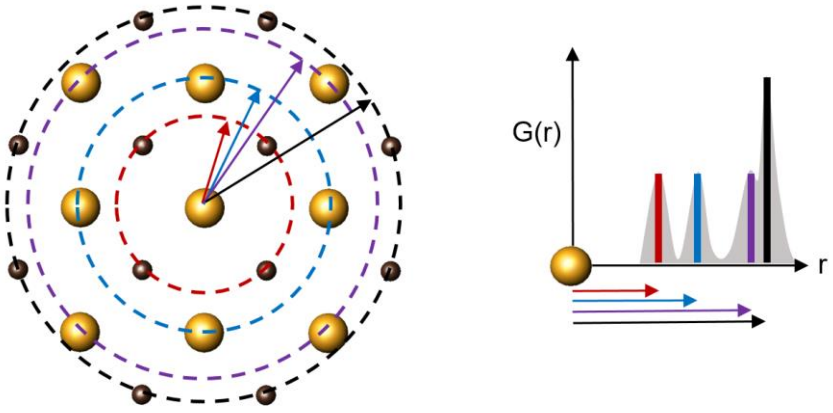

Figure 2.13. An illustration of the correspondence between interatomic distances and the number of nearest neighbors in a real structure (left) and the PDF profile in the G(r) space (right).

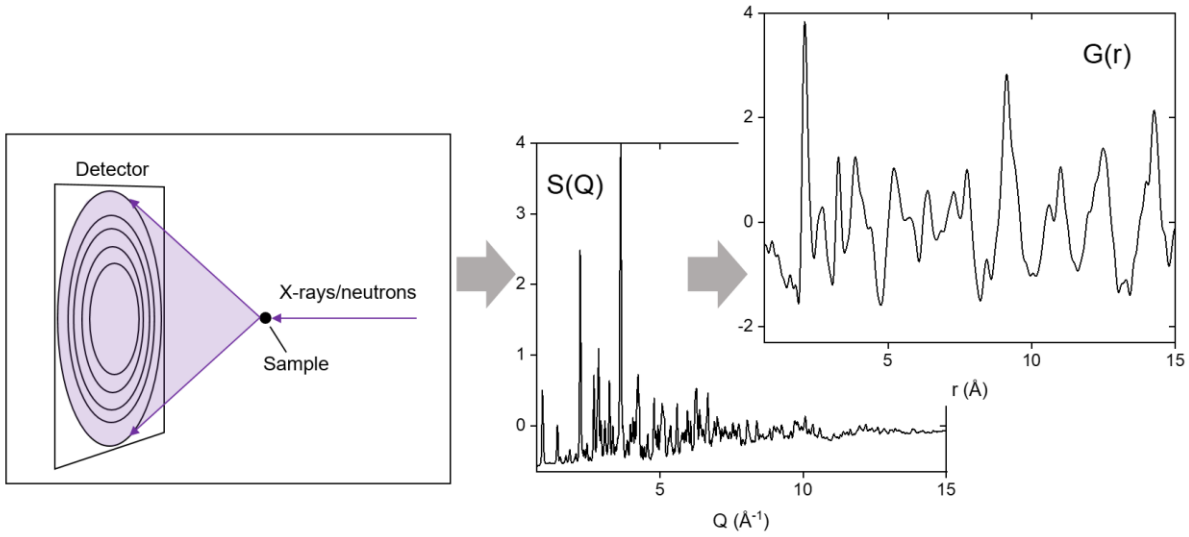

Figure 2.14. Stages of typical PDF data collection process: data collection with a 2D detector in a transmission geometry (left), data integration and normalization (middle), and extraction of the pair distribution function (right).

weights are assigned to "better" (allowed) and "worse" (too close to be allowed) moves[160]. In this work, big-box RMCProfile software[161] (v. 7) was used to refine Bragg scattering and total scattering data together (multi-histogram refinement) with the resulting goodness of fit summed over weighted GOFs of individual histograms.

2.4.3.1. Sample preparation for PDF and experiment conditions

Total scattering experiments are frequently carried out in transmission geometry, schematically shown in **Fig. 2.15**. The beam of X-rays or neutrons penetrates the sample and results in a scattered cone picked up by an area detector (left panel). While this step is common for all scattering experiments with the transmission geometry, such as neutron powder diffraction and rapid *in-situ* powder diffraction experiments in this thesis, the next step (right panel) is germane to PDF analysis only. The 2D image is integrated into a 1D S(Q) pattern which is then reduced to 1D G(r) pattern through a Fourier transform[162]. Along the way, calibration, background subtraction, scaling, and correction for absorption are done. The refinement in ***Section 6.2.2.*** also made use of two other related functions – total scattering structure factor and differential correlation function[158].

X-ray total scattering was performed at beamline 11-ID-B (Advanced Photon Source) at Argonne National Laboratory. All powdered samples (< 10 mg) in 0.8 mm (ID) Kapton capillary

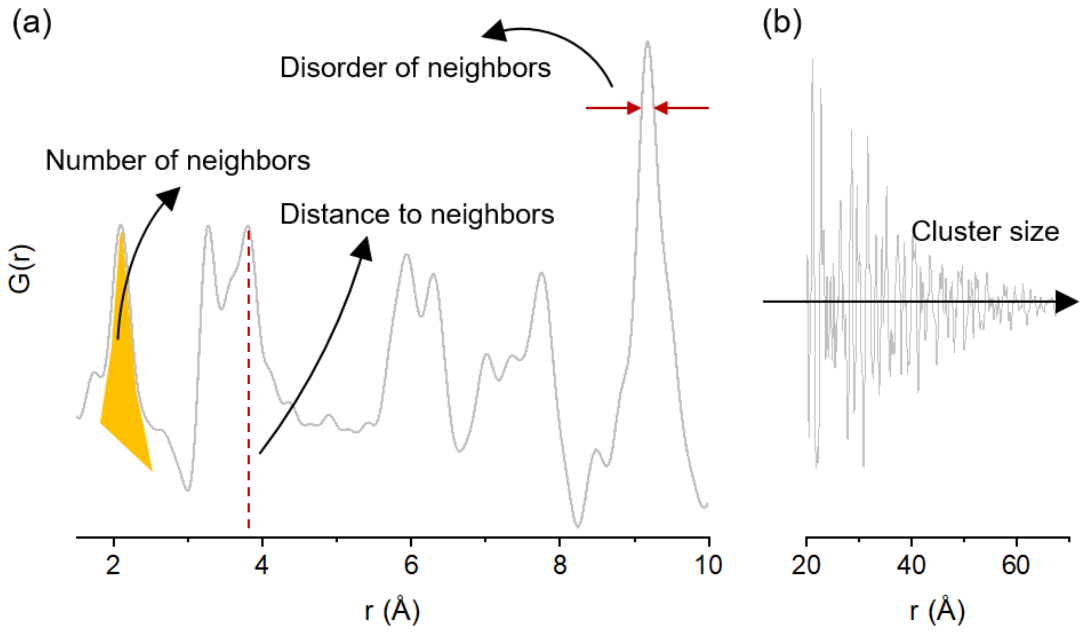

Figure 2.15. Sample-related parameters that can be obtained from the PDF data. Panel (a) is a small-r part of the dataset in panel (b).

tubes, plugged with wax from both sides, were measured at ambient conditions at a wavelength of $\lambda = 0.2113$ Å at a distance of 180 mm from the detector.

Neutron total scattering was performed at the beamline BL-1B "NOMAD"[150] (Spallation Neutron Source) at Oak-Ridge National Laboratory. Powdered samples (under 300 mg) were placed in 3 mm (OD) quartz capillary tubes sealed on one end and measured at ambient conditions at 0.5-3 m distance between the sample and six detector banks covering the *d*-spacing range 0.5-28 Å.

Quick simulations of X-ray and neutron PDF data and partials (selected atomic pairs) were done for visualization purposes in ***Section 3.1.1***. PDFgui[159] software suite was used which is based on the small-box approach. The multihistogram PDF data refinement was carried out in RMCProfile[161] (v. 7, in development; see results in ***Section 6.1***) on total scattering neutron and X-ray data as well as X-ray and neutron powder diffraction data, 13 histograms in total. Weights of the histograms were adjusted in the program StoG, supplied with the RMC Profile package. The starting configuration was an 8×8×8 supercell based on the NPD refinement of the average structure of cubic $Sc_2VO_{5.25}$, in the range between 1.5 Å and 20 Å. The supercell of $Sc_2VO_{5.25}$

contained 1366 Sc atoms, 682 V atoms, 3584 O atoms, and 512 O vacancies ("Va"). Disorder was modelled as Sc-V and O-Va swapping with 5% probability per move, where each move is a random shift of the atom. Data analysis was based on a cycle with $5.6 \cdot 10^6$ generated moves and $2.7 \cdot 10^6$ accepted moves. Twenty additional independent refinements were run to achieve better defined profiles of partial PDFs of individual atomic pairs. Structure visualization was done in VESTA[163] and OVITO[164].

2.4.4. X-ray absorption near-edge structure spectroscopy (XANES)

For semiquantitative elucidation of the oxidation states and coordination geometries of 3d and 4p metals in this work, X-ray Absorption Near Edge Structure Spectroscopy (XANES) was used. XANES is the lower energy regime of XAFS – X-ray Absorption Fine Structure Spectroscopy,

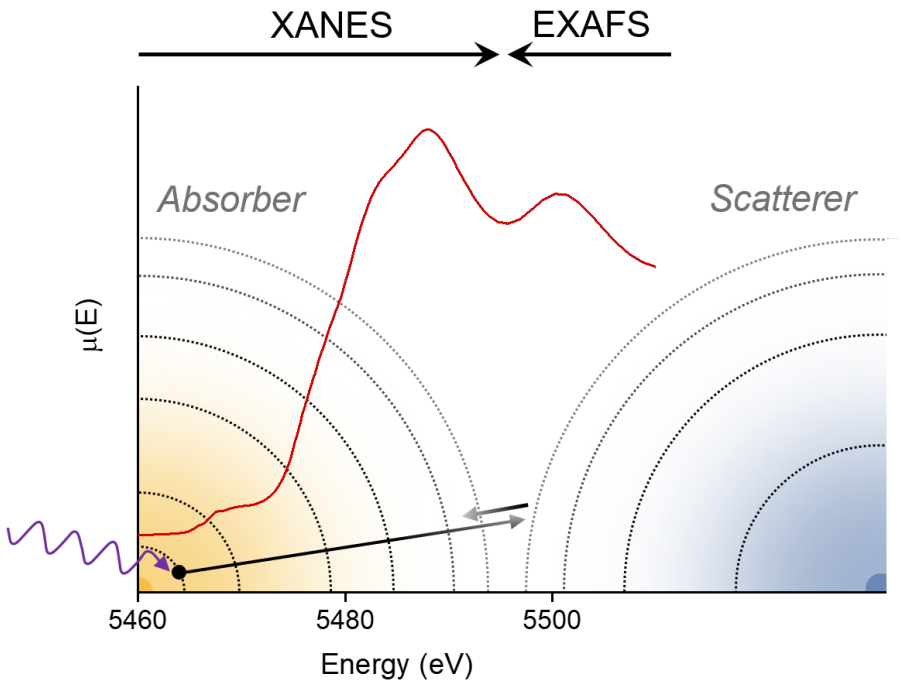

Figure 2.16. A XAFS spectrum of V_2O_3 (K edge, transmission mode) overlaid on a schematic representation of a photoelectron ejection event: energy of an X-ray photon (purple) is absorbed by a core electron (black) of the absorbing atom (yellow) and scattered off of a neighboring atom (blue). Promotion of the absorber's electron to the highest unoccupied electron state signifies the edge – the maximum absorption (say, p state); peaks at lower energies, if any, are due to occupation of lower-energy hybridized d and p states; curvature after the edge is from scattering of the photoelectron on neighboring atoms and interference with itself. Other electrons and scattering paths are not shown.

which is an element-specific X-ray spectroscopic technique probing the local environment around the absorbing atom. It is based on photoexcitation of its core electron and its interaction with neighboring atoms. A XAFS transmission spectrum (predominantly XANES) of V_2O_3 in **Fig. 2.16** has a step-like shape stemming from an electron excitation due to the absorption of an X-ray photon of characteristic energy commensurate with the binding energy. The global maximum of the spectrum is the absorption edge energy, and superimposed decaying sine curves following the edge are the extended fine structure (EXAFS) from the interference of the ejected electron with itself after scattering from neighboring atoms, including multiple scattering[165]. Both XANES and EXAFS are highly sensitive to bond distances, but while the refinement of the extended structure produces coordination environment and bond lengths *per se*, semi-quantitative XANES is a fingerprint of the coordination number, distortion of the coordination polyhedron, off-centering of the absorbing atom, its oxidation state, and the number of electrons in the receiving orbital.

XAFS is performed in either transmission or fluorescence geometry depending on the sample and X-ray hardness (e.g. less transparent sample measured at higher energy → fluorescence mode). The XAFS experiment setup with detectors for both modes is schematically shown in **Fig. 2.17**. In it, the collimated and monochromated X-ray beam (black arrows) hits the sample and is received by a multitude of detectors. The detectors allow measuring absorption ($\propto ln\frac{I_0}{I_t}$) and fluorescence ($\propto ln\frac{I_f}{I_0}$) as well as the reference signal aiding in calibration ($\propto ln\frac{I_t}{I_{ref}}$ or $ln\frac{I_0}{I_{ref}}$). The latter comes from a collision with a foil made of the material whose absorption edge is measured.

When the X-ray beam penetrates the sample, the effects of X-ray attenuation become important, such as elastic (Rayleigh), inelastic (Compton), and the photoelectric effect. The latter dominates the XAFS spectrum of the heavier elements. The measure of attenuation is the absorption coefficient μ, which takes the form:

$$\mu \sim \rho Z^4/E^3, \qquad (2.31)$$

where **ρ** is mass density, ***Z*** is atomic number, ***E*** is the X-ray energy, and the resulting **μ(*E*)** is the coordinate system in which all XANES spectra presented herein are plotted. At an element-specific value of *E*, a rapid increase in μ is observed associated with absorption of an X-ray photon by the core electron of the absorber (*Z*, ρ). This rapid increase peaks at the absorption edge. To promote the core photoelectron to the electronic state corresponding to the absorption edge (or any lower-

energy states if present), there should be available unoccupied final states of both appropriate energy and appropriate symmetry. In the 3d metals considered below and measured at their respective K absorption edges, the 1s electron (from a centrosymmetric s orbital) undergoes a transition to the molecular orbital of the p state (non-centrosymmetric), allowed under the selection rule for parity[166]. The rule states that only those electronic transitions are allowed which are accompanied by change in the orbital quantum number (thus forbidding s-s, p-p, etc.) and in parity (forbidding s-d, p-f) between the ground and the final electronic states. Consequently, XANES spectra of d metals in perfectly regular centrosymmetric geometry (e.g. octahedral) do not have pre-edge features. However, non-centrosymmetric geometry and distortions of the centrosymmetric geometry relax the rule giving rise to the pre-edge features like the ones at ~5465 eV in **Fig. 2.16**. This can be attributed to the larger overlap of the (n-1)d and np metal orbitals of appropriate symmetry, which adds a p character to the now hybridized molecular orbital of the final electronic state[167]. Together with the absorption edge when applicable, these pre-edge features were used to analyze coordination geometry and oxidation states of the metals through either (1) comparison of *E* and μ values with respect to those of standards or (2) linear combination fitting (LFC) of the pre-edge features of the analyte with the pre-edge features of standards. In general, both the intensity of the absorption features and their position in energy are telling of the bond distances[168]: shorter bonds result in higher intensity and higher energy, in particular leading to (1) higher pre-edge intensity (but lower edge intensity) for a smaller coordination number, (2) stronger distortion of the metal-oxygen polyhedron, possibly due to an (3) off-centered

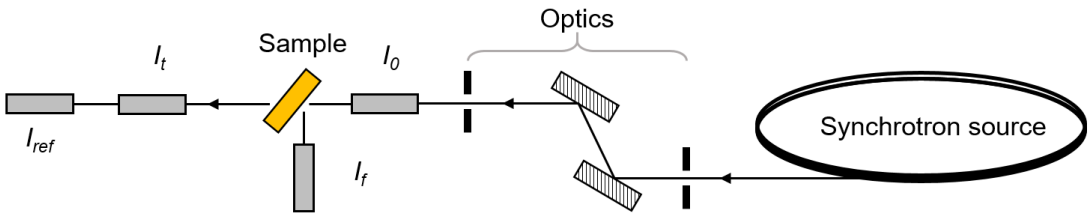

Figure 2.17. A schematic of a XAFS experiment. An X-ray beam of high brilliance passes through a set of slits, collimators, and monochromators before hitting the sample. In the setup, the incident (I_0), fluorescent (I_f), and transmitted (I_t) intensities can be measured with ion-chamber-type detectors. I_{ref} denotes the reference block which includes a foil made of the analyte material (for calibration purposes) and a detector.

cation[167,169], and to (1') lower pre-edge energy (higher edge energy) for the larger charge of the cation[170].

2.4.4.1. Sample preparation for XANES and experiment conditions

Room-temperature XAFS measurements (***Section 5.4***) were performed on pelletized samples prepared off-site. The calculated quantity of the analyte was mixed with polyethylene glycol PEG-10000 in 1:10-1:30 ratio, for two reasons: (1) to minimize the absorption of the X-ray beam, i.e. to let the beam pass through the sample, owing to the relatively low X-ray absorption by organic compounds; (2) as a good binding material, PEG helped to obtain pellets of high quality. Powders were pressed into 7 mm OD pellets under a 7,000 pound load and sandwiched in 20-slot 3D-printed sample-holder between two layers of thin (0.0035") polyimide Kapton tape with a silicone adhesive.

Samples for the *in-situ* measurements on vanadium compounds (***Section 6.2***) were mixed on-site with BN powder (an alternative to PEG) in 1:10-1:20 ratio (derived empirically), and packed into stainless steel sample holders with six sample slots each. Each holder was placed in the quartz tube inside the gas-flow electrical furnace connected to the gas manifold. Samples were heated in 20% oxygen (bal. He) flow to 400 ºC and then 600-950 ºC with 50 ºC increments, dwelt for 1-2 hours at each temperature depending on the sample, and scanned at least three times at each temperature. Data above 800 ºC were not used in this work due to encountering high-temperature redox processes involving vanadium in the sample, BN, and the sample holder, which affected the data. Room-temperature scans in ***Section 3.1.1*** were collected on samples in the same sample holders prior to heating and in the absence of gas.

The needed sample mass can be expressed as a sum of the desired masses of the analyte $\boldsymbol{m_{AN}}$ and attenuator $\boldsymbol{m_{PEG}}$ (or $\boldsymbol{m_{BN}}$) and for the *ex-situ* experiments was derived by iteration following eq. 2.31 for total absorption $\boldsymbol{\mu(E)}$ which should ideally be under 2.5 absorption lengths[171]:

$$\mu(E) = \frac{1}{A}\left(\sum_i \omega_i \mu(E_0+1)_{i_{AN}}\, m_{AN} + \sum_j \omega_j \mu(E_0+1)_{j_{PEG}}\, m_{PEG}\right), \qquad (2.32)$$

where $\boldsymbol{A}$ is the cross-section of the pellet in cm^2, $\boldsymbol{\omega_i}$ is the mass fraction of the $\boldsymbol{i^{th}}$ atom of the analyte or $\boldsymbol{j^{th}}$ atom of the attenuator, $\boldsymbol{m}$ is the unknown mass in mg, and $\boldsymbol{\mu(E_0+1)}$ is the element-specific

absorption taken 1 eV above the absorption edge energy $\boldsymbol{E_0}$. Formally E_0 is the inflection point of the XANES spectrum found roughly in the middle of the edge jump. For the edge jump itself, there is another condition to be accounted for when choosing m_{AN} – the jump should have a non-zero magnitude ($\boldsymbol{I_{E.J.}} > 0$):

$$I_{E.J.} = \frac{1}{A}\omega_1 \Delta\mu(E_0) m_{AN}, \qquad (2.33)$$

where subscript 1 refers to the element whose absorption edge is measured and $\boldsymbol{\Delta\mu(E_0)}$ is the absorption difference taken at energies 1 eV below and 1 eV above the absorption edge energy. Absorption coefficient and absorption energy values for calculations were taken from Hephæstus software, while normalization, calibration, and linear combination fitting of the obtained data were done in Athena software from the same suite[172].

2.4.5. Other methods of analysis and auxiliaries

2.4.5.1. Direct current (DC) magnetic susceptibility

DC magnetic susceptibility ($\boldsymbol{\chi}$) reflects the change in magnetization of the sample in response to the constant (hence DC) external magnetic field. Magnetization is proportional to the effective magnetic moment of the sample which, in the case of the spin-only magnetic moment, can be written as follows[173]:

$$\mu_{eff} = g\mu_B\sqrt{S(S+1)}, \qquad (2.34)$$

where $\boldsymbol{g} \approx 2$ is called the Landé g-factor, $\boldsymbol{\mu_B} = 9.274 \cdot 10^{-24}$ J/T is the Bohr-magneton (magnetic moment of one electron), and $\boldsymbol{S}$ is the total quantum spin number (the sum of individual spin numbers) which is the unknown in this equation. On the other hand, the magnetic moment can be determined as follows:

$$\mu_{eff} = \sqrt{\frac{3\,k_B C}{N_A}}, \qquad (2.35)$$

where k_B = 1.381·10^{-23} m^{2}kg/(s^{2}K) is the Boltzmann's constant, N_A = 6.022·10^{23} is the Avogadro constant, and C (emu·K/(mol·Oe)) is the Curie constant which for a paramagnetic material comes from the Curie-Weiss law (eq. 2.36):

$$\chi = \frac{C}{T-\theta}, \qquad (2.36a)$$

$$\frac{1}{\chi} = \frac{T}{C} - \frac{\theta}{C}, \qquad (2.36b)$$

where T (K) is the absolute temperature, θ (K) is the Weiss temperature, and magnetic susceptibility χ is the parameter measured in this method as a function of temperature. The sign of the Weiss temperature shows the type of the net magnetic coupling in the sample: <0 for antiferromagnetic coupling and >0 for ferromagnetic coupling. Both Curie and Weiss temperatures are determined from fitting the inverse magnetic susceptibility (eq. 2.36b). Since (1) the resulting Curie constant is the linear combination of Curie constants of all the magnetic species present and (2) the molar mass needs to be known to interpret the data (at the same time, it depends on the oxidation states of the paramagnetic species and hence is unknown), data interpretation requires constraints and chemical intuition.

Magnetic susceptibility in the paramagnetic scandium vanadate t-$Sc_2VO_{5+\delta}$ (see ***Section 3.1.1***) was measured on a Quantum Design Physical Property Measuring System – PPMS equipped with a vibrating magnetometer attachment. A sample of 12.0(1) mg in a quartz sample holder was measured in a 1,000 Oe static field between 4 and 330 K. The data were corrected for diamagnetic contributions from the sample environment and core electrons of the sample, using tabulated values[174].

2.4.5.2. Thermogravimetric analysis (TGA)

Thermogravimetric analysis allows measuring the change in mass of the sample with temperature and time. It is a sensitive microbalance equipped with electromagnets and a furnace therein. A flow of working gas can be supplied through the furnace to study the mass change during redox processes as well as to carry away unwanted gaseous products[166]. In this work, redox reactions of $Sc_2VO_{5+\delta}$ were studied. Four independent TGA experiments were conducted;

however, results were still inconclusive due to interference of the early onset of redox processes with water losses at low temperature, which obscured the starting point for mass calculations. However, some of the obtained data are still presented in ***Section 3.1.1***. Data were collected with TA Instruments Discovery SDT 650 between 25 and 1000 ºC with 7 ºC/min steps on ~100 mg of the powder in the flow of oxygen (oxidation) and 5 % hydrogen (reduction).

2.4.5.3. Bond valence sum analysis

In this work the bond valence sums (BVS) method was used as a way to derive the oxidation state of the metal ion from measured metal-oxygen bond distances. A bond valence can be thought of as the number of electrons participating in bonding, per bond[101]. BVS were calculated for metal-oxygen bonds based on refined or tabulated (in ICSD) bond distances in equilibrium $\boldsymbol{R_i}$:

$$BVS = \sum_i \exp\left(\frac{R_0 - R_i}{B}\right), \qquad (2.37)$$

where $\boldsymbol{R_0}$ is the reference bond length and $\boldsymbol{B}$ is some nearest neighbor-related coefficient, usually 0.37±0.05 Å [175]. Both values are tabulated [176,177,178,179]. Due to its exponential form, it implies that the strongest (weakest) contributions to it come from shorter (longer) bonds[180]. This method should be thought of as a good approximation rather than a precise calculation. Further, a global instability index (GII) was used[181] based on BVS calculations to assess the relative strain imposed on the atomic configuration by over- or underbonding of the central ion to its neighbors:

$$GII = \sqrt{\sum_{i=1}^{N} x_i (BVS_i - OS_i)^2}, \qquad (2.38)$$

where $\boldsymbol{N}$ is the number of crystallographic sites the metal center occupies, $\boldsymbol{BVS}$ is the bond-valence sum for this cation in the corresponding site, $\boldsymbol{OS}$ is its real oxidation state, and $\boldsymbol{x}$ is the concentration of this cation relative to the total number of cations in the unit formula or the unit cell.

2.4.5.4. Bond length and bond angle distortions

Relative bond length M-O distortions ($\boldsymbol{\Delta_{BL}}$) were calculated using the following equation[182]:

$$\Delta_{BL} = \frac{1}{n d_{av}} \sum_{i=1}^{n} |d_i - d_{av}|, \qquad (2.39)$$

where $\boldsymbol{n}$ is the number of M-O bonds $\boldsymbol{d_i}$ in the polyhedron and $\boldsymbol{d_{av}}$ is the average M-O bond length value. Relative bond angle O-M-O ($\boldsymbol{\Delta_{BA}}$) distortions were calculated similarly:

$$\Delta_{BA} = \frac{1}{m \alpha_{av}} \sum_{i=1}^{m} |\alpha_i - \alpha_{av}|, \qquad (2.40)$$

where $\boldsymbol{m}$ is the number of obtuse-only O-M-O bond angles $\boldsymbol{\alpha_i}$ in the polyhedron and $\boldsymbol{\alpha_{av}}$ is the average obtuse O-M-O bond angle value. In combination with bond lengths and energy shifts, distortions Δ_{BL} and Δ_{BA} were used for rationalization of near-edge and edge XANES features and prediction of metal oxidation states.

2.4.5.5. Structure information and visualization

Throughout this work, average and local crystallographic structures were visualized with ATOMS v. 5.1[183],VESTA v. 3.5.7[163], or OVITO v. 4.6[164] software suites. Published crystallographic data was accessed by means of the Inorganic Crystal Structure Database – ICSD[184], ACS SciFinder[185], or Pearson's Crystal Database - PCD[186].

CHAPTER 3

Tetragonal defect fluorite superstructure t-$Sc_2VO_{5+\delta}$

The ambient-pressure Sc-V-O phase diagram consists of corundums[99], fluorites[93], fluorite superstructures (bixbyites, doped pyrochlores, etc. [28,68,99,100,187,188]), and zircons[104,126]. The Sc:V 2:1 phases are of particular interest for order-disorder competition and solid state reaction pathway analysis[31]. This competition is illustrated in this chapter with a particular emphasis on the crystal structure and reactivity of the tetragonal polymorph and its place among other, structurally related scandium vanadates.

The disordered defect fluorite phase $Sc_2VO_{5+\delta}\square_{1-\delta}$ ($\square$ = oxide vacancies) shown in the center of **Fig. 3.1a** is related to the:

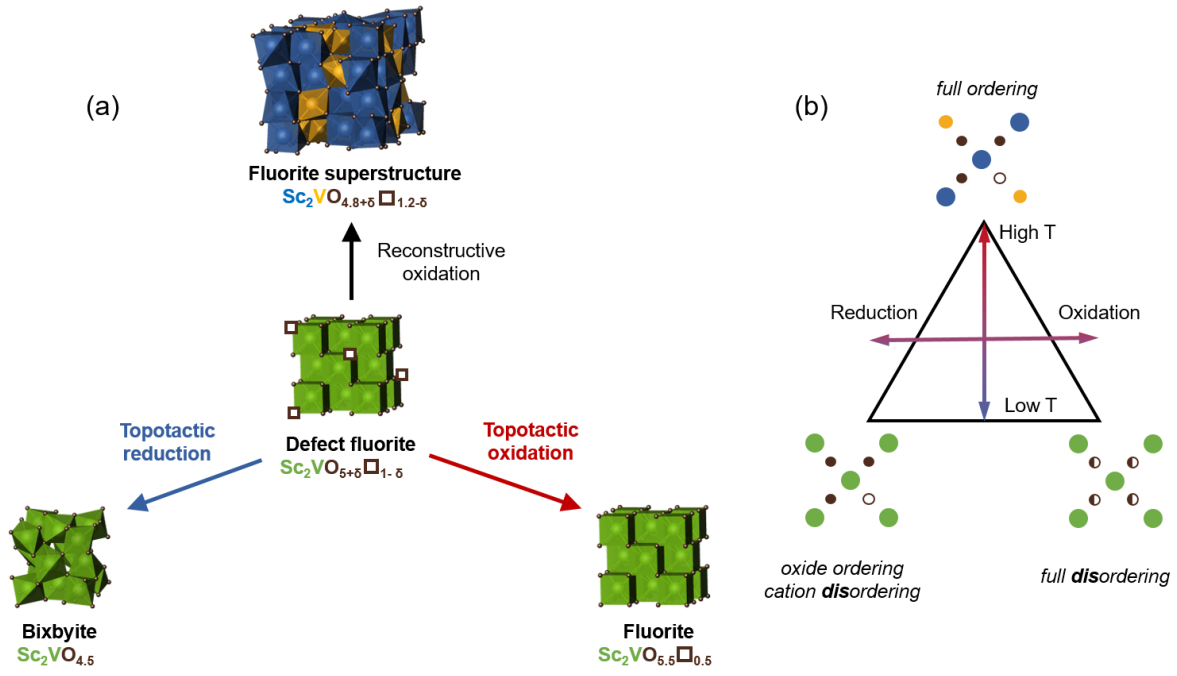

Figure 3.1. Order-disorder roadmap for Sc_2VO_{6-x} structures, centered on the defect fluorite: (a) – illustrating structures and reaction pathways between them; (b) – emphasizing general order/disorder relations. Blue = Sc, yellow = V, green = disordered Sc and V, brown = oxygen, white = oxide vacancy.

- cubic bixbyite $Sc_2VO_{4.5}$ via topotactic reduction (bottom left);
- cubic defect fluorite $Sc_2VO_{5.5}\square_{0.5}$ via topotactic oxidation (bottom right);
- tetragonal superstructure $Sc_2VO_{4.8+\delta}\square_{1.2-\delta}$ via reconstructive oxidation (top).

The defect fluorite structure $Sc_2VO_{5+\delta}\square_{1-\delta}$ with its tunable disordered point defects has the characteristics of a good oxide ion conductor[3]. This is in contrast to the other three phases for which it is not the case, since:

- the bixbyite, $Sc_2VO_{4.5}$, undergoes oxide vacancy ordering due to the large vacancy concentration (25% of the oxide sublattice);
- the fluorite $Sc_2VO_{5.5}\square_{0.5}$ has the smallest possible number of oxide vacancies (8.3%) due to the cation charge constraints ($O_{5.5}$ is the upper limit);
- the tetragonal fluorite superstructure $Sc_2VO_{4.8+\delta}\square_{1.2-\delta}$ is oxide vacancy ordered (20%) and cation ordered.

The phase transition from the disordered structure to an ordered structure at high temperatures is reminiscent of high-temperature ordering processes in solid electrolytes. Notably, vacancy ordering processes at operating temperatures can potentially limit oxide ion conduction in SOFCs.

Fig. 3.1b generalizes the relations between ordered and disordered fluorite-derived structures. Starting with a fully disordered fluorite structure (center) a low-temperature topotactic process leads to a cation-disordered product (bottom). The degree of cation order depends on whether this is a reduction or oxidation. In contrast, the high-temperature reconstructive process leads to an ordered product (top).

$Sc_2VO_{5+\delta}$ is a model system for the investigation of (1) the competing formation of poorly ion-conducting ordered phases; (2) following cation and charge ordering processes, and (3) non-stoichiometric compositions, $Sc_2VO_{5+\delta}$ ($\delta \neq 0$), which is in contrast to the other ordered A_2VO_5 phases.

3.1. Crystal structure of tetragonal Sc_2VO_5

In 1971 tetragonal $Sc_2VO_{5+\delta}$ was reported as a fully ordered and stoichiometric Sc_2VO_5 defect fluorite phase[28]. **Fig. 3.2**[68] illustrates the originally proposed cation ordering scheme consisting of cation slabs with sixfold V^{4+}, sixfold Sc^{3+}, sevenfold Sc^{3+} coordination, etc. In 2010 Cong *et al.*[29] published the single crystal structure of Sc_2VO_5 in space group $I\bar{4}$ (#82). The cation sublattice was

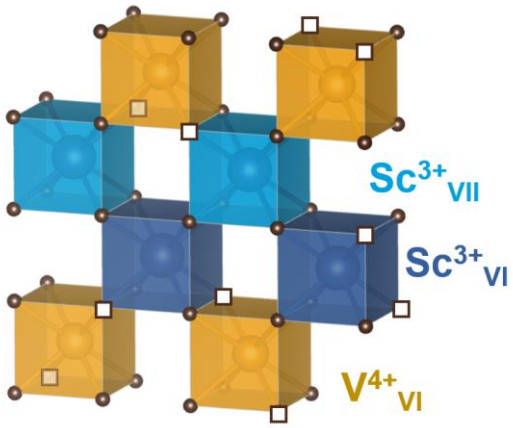

Figure 3.2. Idealized cation sublattice in the Sc_2VO_5 defect fluorite structure (one layer of cations is shown) by Pokrovskii *et al*. V^{4+}(VI) = yellow, Sc^{3+}(VI) = dark-blue and Sc^{3+}(VII) = light-blue, O^{2-} = brown, vacancies = white squares.

found to consist of 3 scandium sites (1 sixfold coordinated in 4*f* site and 2 sevenfold coordinated in 8*g* sites) and 2 vanadium sites – octahedrally coordinated in 8*g* site and tetrahedrally coordinated in 2*c* site. The hallmarks of Cong's description are:

(1) O_5 stoichiometry, and

(2) tetravalent vanadium in the octahedral and tetrahedral V-sites.

Notably, tetrahedral V^{4+} is rare and has been previously proposed only for a handful of solid oxides such as some A_2VO_5 (A = Y, Dy, Yb)[34] and A_2VO_4 (A = Sr, Ba)[189,190] phases. V^{4+} was also reported in minute concentration in a few doped and reduced zircons and garnets[191,192,193,194,195]. In these structures the $[V^{4+}O_4]^{4-}$ tetrahedra are sufficiently distorted to accommodate the larger V^{4+} ion. For comparison, **Fig. 3.3** shows relative distortions of V-O bond lengths (panel **a**) and O-V-O bond angles (panel *b*) within the vanadium-containing tetrahedra in the phases mentioned above. It can be seen that Sc_2VO_5 has the most geometrically regular $[VO_4]^{x-}$ tetrahedra among the A_2VO_4 phases[189,190] (shaded blue) and A_2VO_5[34] phases (shaded red). Bond angle distortions are also smaller in the 2*c* site of Sc_2VO_5 than in V-doped zircon $ZrSi_{0.98}V_{0.02}O_4$[196] and reduced garnet $Ca_2NaMg_2(VO_{3-\delta})_{12}$ with only tiny concentration of reduced V^{4+} species (structure details were taken from Nakatsuka *et al*.[197]). Based on the distortions it is suggested that V^{4+} is not in the 2*c* site. Instead V^{5+} is likely in this uniquely different and geometrically regular site in Sc_2VO_5. Here, the detailed structure of Sc_2VO_5 is presented using X-ray and neutron powder diffraction, XANES data and DC magnetic susceptibility. Based on these data we have concluded[31]:

(1) Sc_2VO_5 is non-stoichiometric $Sc_2VO_{5+\delta}$ with δ = -0.15 for as-synthesized samples;

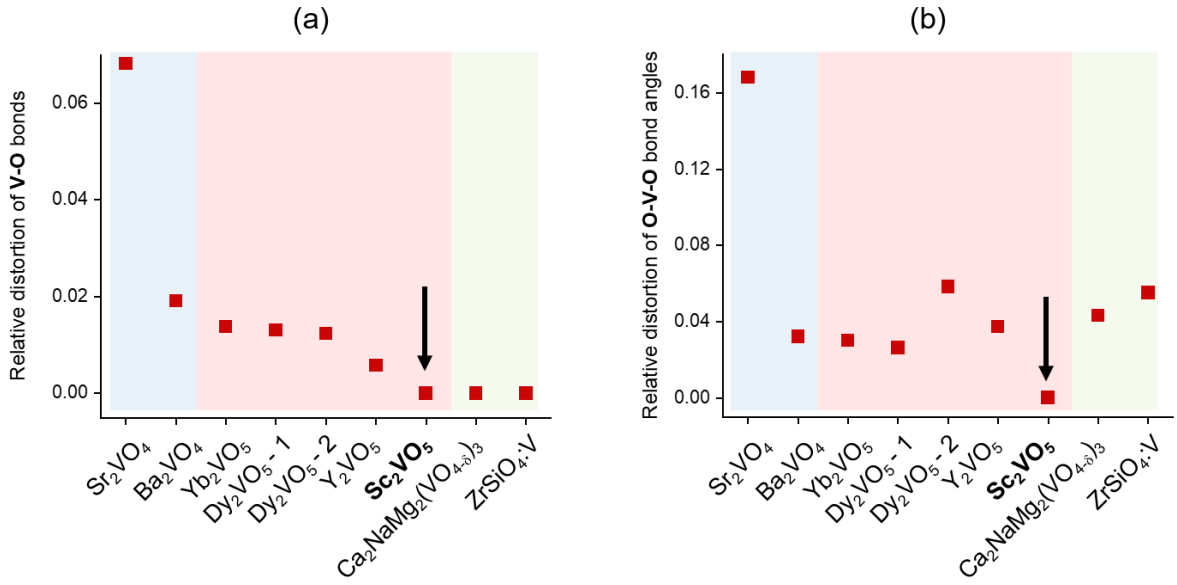

Figure 3.3. Relative distortions of V-O bond lengths (a) and O-V-O bond angles (b) in several phases reportedly containing tetrahedral V^{4+}. The arrows point at $Sc_2VO_{5+\delta}$ which has the least distorted vanadium polyhedron (site 2*c*). The 4+ oxidation state of tetrahedral vanadium in all structures to the left of $Sc_2VO_{5+\delta}$ is questioned later in the text.

(2) vanadium disproportionates and undergoes charge ordering;

(3) V^{5+} only occupies the 2*c* site with tetrahedral coordination;

(4) mixed $V^{3+\ldots4+}$ species occupy the 8*g* site with octahedral coordination;

(5) Sc^{3+} and $V^{3+\ldots4+}$ are 91.3(1.0) % ordered;

(6) the previously thought-to-be-octahedral ^{4f}Sc site is eight-fold coordinated when longer bonds (2.81 Å) are accounted for. This is important when addressing the relation of $Sc_2VO_{5+\delta}$ to the parent fluorite.

The detailed structure[31] is shown in **Fig. 3.4** (top) and contrasted against the previously reported description[29] (bottom). The following sections discuss the vanadium sublattice, ordering scheme, the synthesis and the relation of $Sc_2VO_{5+\delta}$ with other scandium vanadates.

3.1.1. Probing vanadium oxidation states in t-$Sc_2VO_{5+\delta}$

Determination of site specific vanadium oxidation states in t-$Sc_2VO_{5+\delta}$ is challenging due to the presence of 3 possible vanadium oxidation states and 5 potential cation sites. Thermogravimetric

analysis (**Fig. 3.5a**) clearly showed oxygen uptake and loss during oxidation and reduction, respectively. The oxidation did not go to completion within the measured temperature range. Low temperature DC magnetic susceptibility data (**Fig. 3.5b**) did not reveal any magnetic transitions but provided possible oxidation state distributions for vanadium. Those data are not conclusive on their own. X-ray absorption near-edge structure spectroscopy (**Fig. 3.5c,d**) is a local probe and revealed oxidation states and coordination environments. XANES data analysis strongly depends on the availability of appropriate standards. Only the combination of those methods allowed determining the oxidation states and overcoming their individual limitations.

The TGA data for the oxidation (red) and reduction (blue) experiments both show the initial loss of adsorbed water, which likely occurs simultaneously with topotactic oxidation and reduction of the structure. The reduction experiment results in fully reduced $Sc_2VO_{4.5}$ with all-V^{3+} at 1000 ºC (discussed further). The plateau between 400 and 700 ºC corresponds to $Sc_2VO_{4.99}$. Due to lack of a similar plateau in the oxidation data, it is unclear at what point $Sc_2VO_{4.99}$ appears. From the oxidation profile, after the water loss, the starting material undergoes several transformations as marked by steps at 400-800, 800-900, and ≥900 ºC. At 1000 ºC (encircled) its oxidation is still

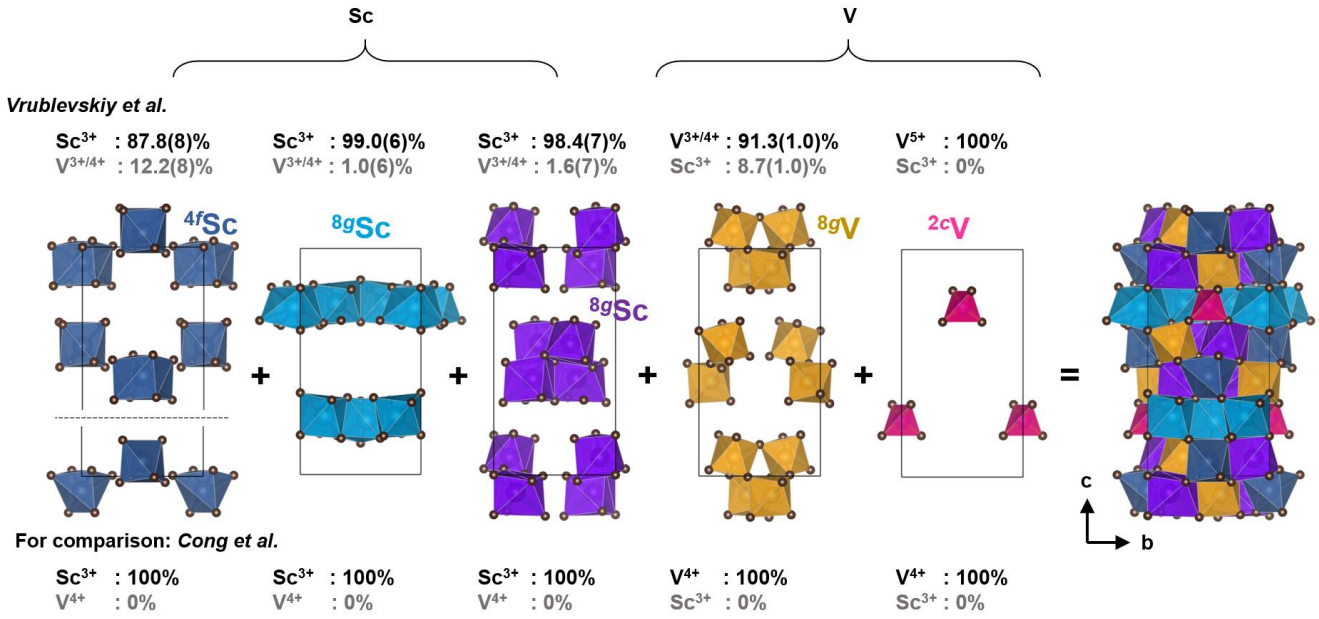

Figure 3.4. Detailed polyhedral representation of t-$Sc_2VO_{5+\delta}$ and its five cation sublattices. Site occupancies and oxidation states according to Vrublevskiy *et al*. are listed at the top (2021) and compared at the bottom with the structure by Cong *et al.* (2010).

incomplete, but the mentioned steps show important transitions and will be explored in ***Sections 3.2*** and ***3.3.***

The TGA data were not analyzed further. The following two subsections discuss DC magnetometry and XANES.

3.1.1.1. Magnetic susceptibility of t-$Sc_2VO_{5+\delta}$

The Curie-Weiss fit to the inverse DC susceptibility (**Fig. 3.5b**) revealed a Curie constant C_{total} = 0.64(1) emu·K/(mol·Oe). Keeping in mind that all three V^{3+}, V^{4+}, and V^{5+} species can be present in $Sc_2VO_{5+\delta}$, the Curie constant, *C*, is written as a linear combination of individual contributions:

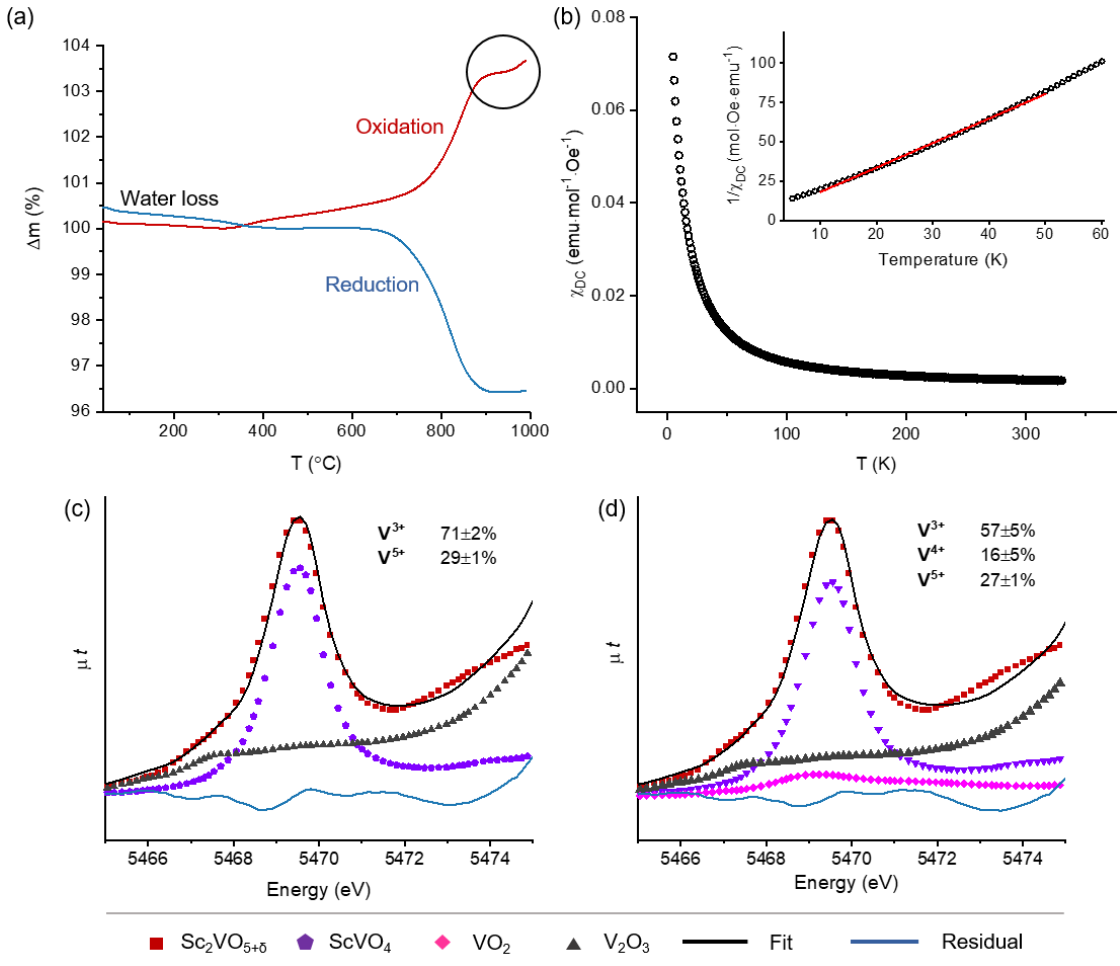

Figure 3.5. Results of TGA (a), DC magnetic susceptibility (b), and XANES (c,d) analyses probing the oxidation states of vanadium in $Sc_2VO_{5+\delta}$. See text for description.

$$C_{total} = (0.8 - x - y)\cdot C(V^{3+}) + y\cdot C(V^{4+}) + x\cdot C(V^{5+}) \quad (3.1)$$

where $C(V^{3+}) = 0.99$, $C(V^{4+}) = 0.37$, $C(V^{5+}) = 0$ emu·K/(mol·Oe) if the magnetic moment arises from the spins of unpaired electrons only and is confined exclusively to the 8*g* site, since the 2*c* site is assumed to be diamagnetic V^{5+} with C = 0 (see XANES and PDF below). Two scenarios were considered with $y = 0$ and $y \neq 0$, illustrated with **Fig. 3.6**. Only considering V^{3+} and V^{5+} results in $Sc_2(V^{3+}_{0.65}V^{5+}_{0.15})^{8g}(V^{5+}_{0.20})^{2c}O_{4.85}$. Charge balance suggests an oxygen deficiency of $\delta = -0.15$. **Fig. 3.7** compares oxygen concentrations as derived from DC susceptibility, XANES, and NPD/XRD analysis. When considering the potential presence of V^{4+}, the following composition is obtained: $Sc_2(V^{3+}_{0.56}V^{4+}_{0.24})^{8g}(V^{5+}_{0.20})^{2c}O_{4.82}$ with $\delta = -0.18$.

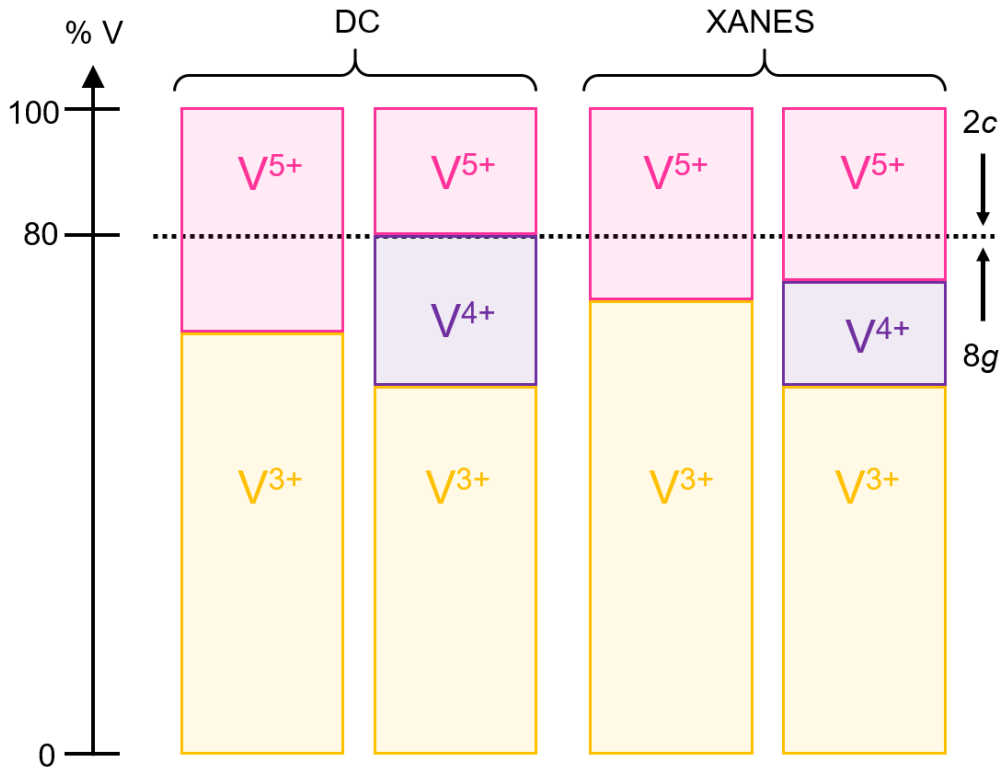

Figure 3.6. Several models of distribution of V oxidation states across the two sites (2*c* and 8*g*) from DC and XANES in t-$Sc_2VO_{5+\delta}$. Different V species are color coded. The dotted horizontal line separates the allowed concentration of vanadium in the two sites (2*c* and 8*g*).

3.1.1.2. XANES of t-$Sc_2VO_{5+\delta}$

Figs. 3.5c,d show the best two linear combination fits of the XANES pre-edge feature of $Sc_2VO_{5+\delta}$ (K absorption edge of V). Standards that produced the best fits were V_2O_3 ($V^{3+}{}_{VI}$), VO_2 ($V^{4+}{}_{VI}$), and $ScVO_4$ ($V^{5+}{}_{IV}$). The first fit (panel **c**) has 71(2) % of V_2O_3 and 29(1) % $ScVO_4$ and thus generates a model $Sc_2(V^{3+}{}_{0.71}V^{5+}{}_{0.09})^{8g}$ $(V^{5+}{}_{0.20})^{2c}O_{4.79}$ (**Fig. 3.6**) with $\delta = -0.21$ (**Fig. 3.7**). The fit slightly improves[E] upon inclusion of VO_2 as a $V^{4+}{}_{VI}$ standard (panel d), which generates the second model: $Sc_2(V^{3+}{}_{0.57}V^{4+}{}_{0.16}\ V^{5+}{}_{0.07})^{8g}$ $(V^{5+}{}_{0.20})^{2c}O_{4.85}$ with $\delta = -0.15$. Both XANES models suggest more than 20% of tetrahedral V^{5+} in the vanadium sublattice (more than the number of 2*c* sites), i.e. up to 1/8 of the 8*g* sublattice is V^{5+}. The dominant feature in the XANES data is modeled as $V^{5+}{}_{IV}$ but could also be due to uncoordinated V^{4+} caused by oxygen vacancies around the

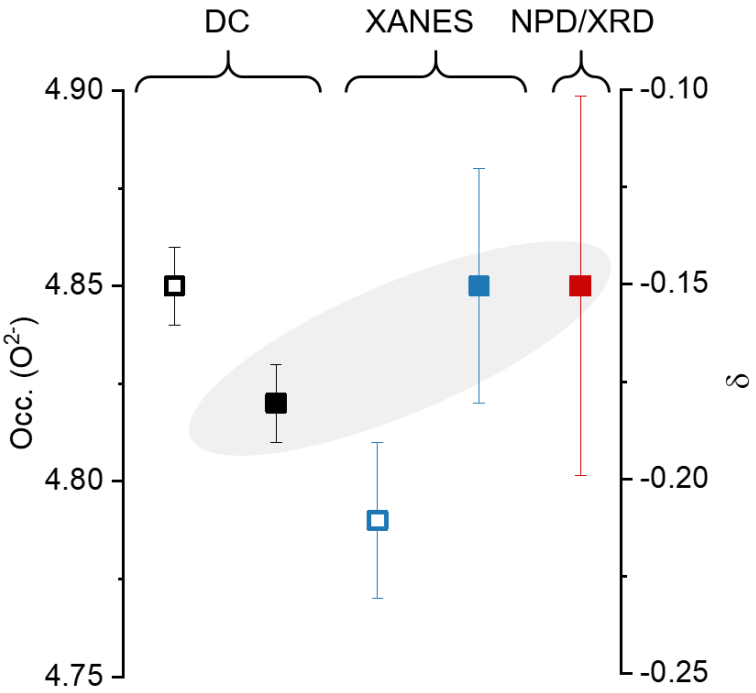

Figure 3.7. Oxygen concentration per unit formula (and δ) derived from DC magnetic susceptibilities, XANES, and NPD/XRD analysis of models 1 (□) and 2 (■). Grey area highlights the values obtained with the accepted model 2.

[E] Introducing the V^{4+} standard decreases χ^2 from 0.00222 to 0.00189, but most importantly it improves the fit around 5,469 eV.

vanadium 8*g* site. The strong correlation between a larger oxidation state and lower coordination on the pre-edge intensity precludes an unambiguous distinction.

3.1.1.3. XRD, NPD, PDF of t-$Sc_2VO_{5+\delta}$

The value $\delta = -0.15$ agrees the DC susceptibility and XANES data. The same value was obtained from a Rietveld refinement against synchrotron powder X-ray and neutron diffraction data (**Fig. 3.8**). The same refinement suggested 8.7(1.0) % site mixing among three Sc sites and the 8*g* vanadium site. Multiple refinement strategies were attempted for site mixing, such as Sc^{4f}-V^{8g}, Sc^{8g}-V^{8g}, Sc^{8g}- Sc^{8g} - V^{8g}, and Sc^{4f}- Sc^{8g} - V^{8g} exchanges. All attempts converged at the same value for the site mixing parameter. For all attempts the 2*c* site only contains vanadium. The V^{5+}(IV) size matches the 2*c* site dimensions, whereas the twofold larger Sc^{3+} (VI) ion exceeds the available space of the 2*c* site. This is further supported by the pair distribution function data and simulations in **Fig. 3.9** (neutron – top, X-ray – bottom). The relevant region of the data includes the shortest bonds such as V-O (1.7…1.9 Å; blue-shaded area), Sc-O (1.9…2.4 Å; red), and O-O (>2.4 Å; green). Notably, V-O pairs cannot be measured with neutron data due to the near-zero coherent neutron scattering length of vanadium. Therefore, any peak visible in the X-PDF data but missing in the N-PDF data can be assigned to V-O or V-V pairs (see blue line). The small distance agrees with V^{5+}-O bonds in the 2*c* site. The second X-PDF peak at 1.9 Å is absent in the neutron data and simulation corresponds to V-O bond distances in the 8*g* site. The largest peak in this range (2.1 Å) corresponds to the majority of Sc-O bond distances in its 8*g* and 4*f* sites. While V-O and Sc-O partials overlap after 1.9 Å, no scandium can be seen in the 2*c* site, which is in agreement with the Rietveld refinements.

3.1.1.4. Cation distribution and vacancy structure

The following cation distribution over all 5 sites is in agreement with all presented data and accounts for partial cation disorder, disproportionation and charge distribution[31]:

$$(Sc_{0.351}V_{0.049})^{4f}(Sc_{0.792}V_{0.008})^{8g}(Sc_{0.787}V_{0.013})^{8g}(V_{0.73}Sc_{0.07})^{8g}(V_{0.2})^{2c}O_{4.85}\square_{1.15}.$$

This expression can be simplified by focusing on vanadium oxidation states in the 2 vanadium sites:

$$Sc_2(V^{3+}_{0.57}V^{4+}_{0.16}\ V^{5+}_{0.07})^{8g}\ (V^{5+}_{0.20})^{2c}O_{4.85}.$$

Two observations can be made.

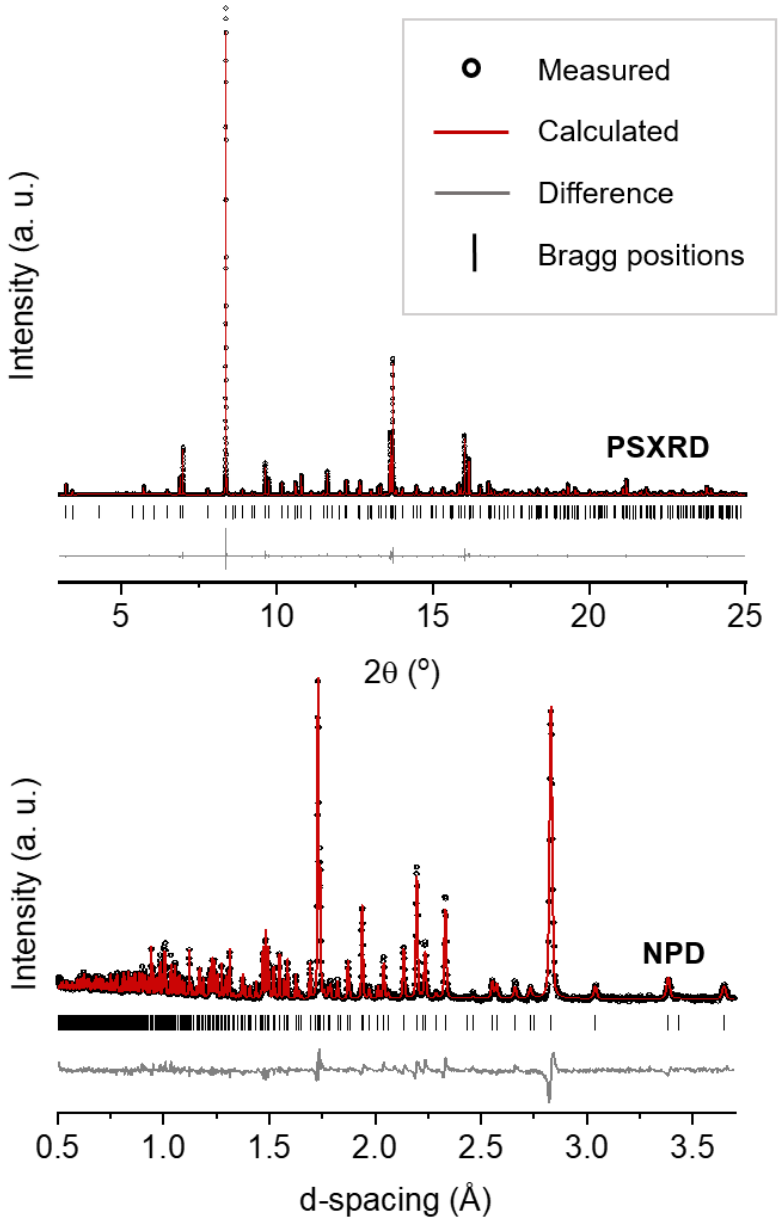

Figure 3.8. The plot of a two histogram Rietveld refinement against synchrotron powder XRD data (main panel) and neutron powder diffraction data (insert) on $Sc_2VO_{5+\delta}$.

Anions: The phase has 48.5 anions per unit cell. However, a fluorite superstructure with 30 cations per cell is expected to have 60 anions. The remaining 11.5 voids consist of 1.5 vacancies in the known anion sites and 10 additional voids elsewhere in the lattice. The former can likely be filled topotactically (***Section 3.2.3***), while the latter are expected to partake in the reconstructive transition to the cubic polymorph (***Sections 3.2.1*** and ***6.2.2***).

Cations: Rationalizing charge ordering is complicated by minor cation site mixing, since V^{3+} and V^{4+} ions can fit into any of the three scandium sites. It is proposed that due to their stronger repulsion from V^{5+}, V^{4+} species would prefer to substitute scandium in the 4*f* site which is the most distant site from the highly charged 2*c* site of vanadium. However, it is hard to prove. **Fig. A1-1** of ***Appendix 1*** shows V^{5+}-Sc^{3+} bond distances of which there are two or three different kinds. Each Sc^{3+} ion of three forms the longest bonds around one V^{5+} ion but the shortest bonds around the neighboring V^{5+} ion. If only the shortest V-Sc bonds are compared, Sc-1 in the 4*f* site forms the longest bonds among them (4.59Å). It is suggested to be the driving force for Sc-V mixing, and it agrees with the largest concentration of V (presumably V^{4+}) in the 4*f* site of scandium.

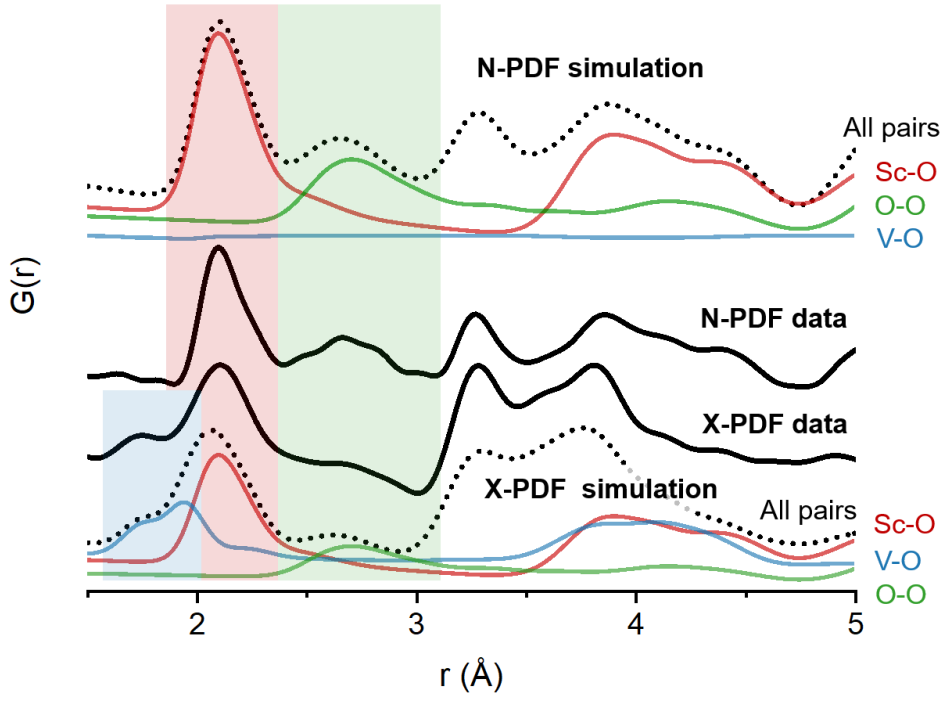

Figure 3.9. Neutron (top) and X-ray (bottom) PDF data for $Sc_2VO_{5+\delta}$ (black) and selected simulated pairs: Sc-O (red), V-O (blue), O-O (green), and all pairs together (dotted black). Shaded areas highlight important peaks: V-O (blue; only in X-PDF), Sc-O (red), and O-O (green). Neither of the metal-metal pairs contribute below 3 Å, hence Sc-Sc, Sc-V, and V-V simulations are not shown.

3.2. Structural relations and synthetic approaches

The tetragonal and ordered defect fluorite superstructure t-$Sc_2VO_{5+\delta}$ (synthesized as $Sc_2VO_{4.85}$) can be synthesized via multiple routes (**Fig. 2.2**). We identified several reconstructive and non-topotactic synthetic routes, namely oxidative, reductive, and inert (or mildly reductive) preparation methods. These preparation methods reveal the peculiar structure of t-$Sc_2VO_{5+\delta}$ and provide a better understanding of its relation to other scandium vanadates.

3.2.1. Oxidative synthesis and oxidative reactions of t-$Sc_2VO_{5+\delta}$ and c-$Sc_2VO_{5+\delta}$

Oxidative synthesis of single-phase t-$Sc_2VO_{5+\delta}$ was conducted in a flow of nitrogen with a trace amount of oxygen (5-15 ppm O_2 in N_2) at 800 ºC with the setup shown in **Fig. 2.4**[30]:

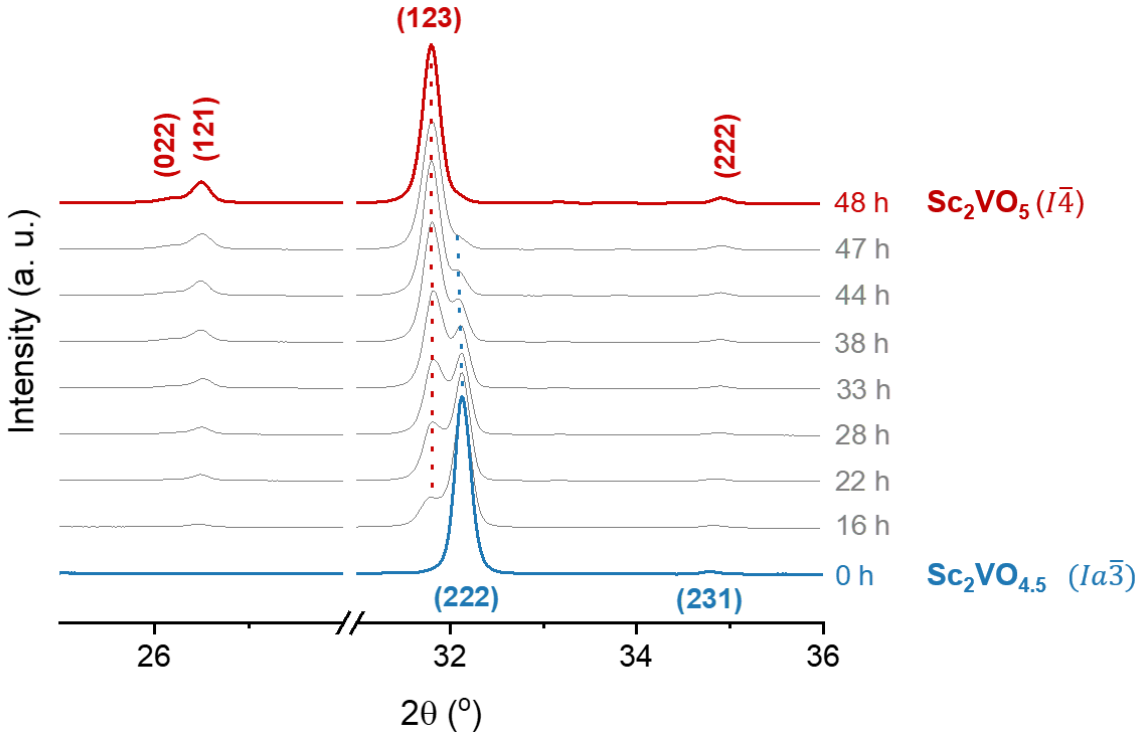

Figure 3.10. A stack plot of *ex-situ* powder XRD diffractograms (Cu Kα) illustrating the oxidation of the $Sc_2VO_{4.5}$ (blue) to tetragonal $Sc_2VO_{5+\delta}$ (red) in traces of oxygen.

$$Sc_2VO_{4.5} + \left(\frac{1+2\delta}{4}\right) O_2 \rightarrow Sc_2VO_{5+\delta} \qquad (3.2)$$

The starting material is a cubic bixbyite ($Ia\bar{3}$), brown in colour, synthesized following eq. 2.8 [99]. The XRD pattern stack plot (**Fig. 3.10**) shows the disappearance of starting bixbyite phase (blue pattern) while characteristic t-$Sc_2VO_{5+\delta}$ (red pattern) peaks emerge. No other intermediate phases were found in the synthesis. This reaction requires constant regrinding and monitoring with XRD. After each heating the upper (oxidized) layer of the sample was black (end product), while the bottom layer was brown (starting material), and further dwelling led to overoxidation of the black layer (toward yellow $ScVO_4$) rather than conversion of the brown layer into t-$Sc_2VO_{5+\delta}$. To expose the yet underoxidized bottom layer to oxygen and to prevent t-$Sc_2VO_{5+\delta}$ from overoxidation, it was essential to stop the reaction and break up the top layer. Notably, since t-$Sc_2VO_{5+\delta}$ in the top layer passivated the starting material underneath, the tetragonal phase can be considered a poor oxide ion conductor.

Lowering the oxidation temperature to 350-400 ºC, oxidation of the same starting material yields a fully disordered cubic defect fluorite c-$Sc_2VO_{5+\delta}$[30]. The oxidation process is shown in **Fig. 3.11** with a powder X-ray *in-situ* contour plot (filled contour plot). The (222) bixbyite peak disappears at 400 ºC and the (111) peak of the cubic fluorite appears and stays till 900 ºC. In this reaction, more oxygen is offered to the starting bixbyite, but overoxidation of vanadium in the fluorite to

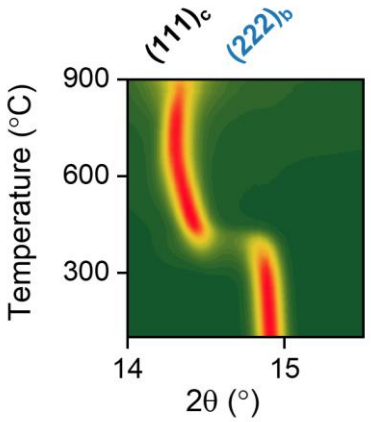

Figure 3.11. A fragment of the synchrotron powder XRD contour plot illustrating the oxidation of $Sc_2VO_{4.5}$ (blue Miller indices) to c-$Sc_2VO_{5+\delta}$ (black) in oxygen flow. λ = 0.72768 Å. Scattering intensity increases from green to red.

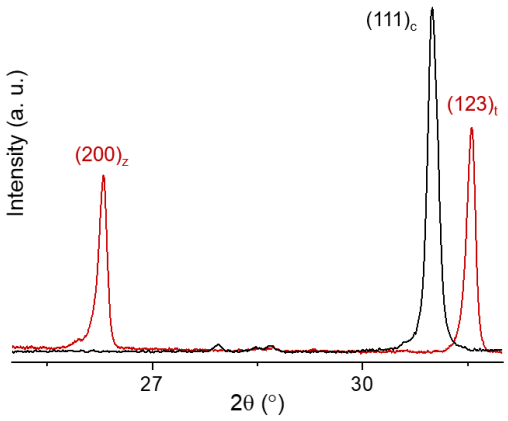

Figure 3.12. Fragments of XRD patterns of c-$Sc_2VO_{5+\delta}$ (black) and a mixture of t-$Sc_2VO_{5+\delta}$ and zircon $ScVO_4$ (red) after reacting c-$Sc_2VO_{5+\delta}$ in static vacuum.

all-V^{5+} ($ScVO_4$) and ordering of cations is avoided by using a lower temperature. Unlike the previous synthesis of t-$Sc_2VO_{5+\delta}$, formation of the cubic polymorph happens fast and does not require repeated mixing. Fast bulk oxidation of the material, rather than only surface oxidation, is indicative of high oxygen mobility in the cubic polymorph and hence its superior oxide ion conduction properties over the tetragonal polymorph.

The two polymorphs can be obtained from each other. In a separate experiment, tetragonal t-$Sc_2VO_{5+\delta}$ was obtained from c-$Sc_2VO_{5+\delta}$ at 1100 ºC in in a sealed quartz tube. The other major product of this reaction was $ScVO_4$, in 1:1 ratio with t-$Sc_2VO_{5+\delta}$. **Fig. 3.12** shows two XRD pattern fragments of the starting material (black) and the products (red). Reaction goes to completion, and the product is a mixture of $ScVO_4$ (peak at 26.3º), t-$Sc_2VO_{5+\delta}$ (contributes to the peak at 31.5º), and Sc_2O_3 (contributes to the same peak). Formation of t-$Sc_2VO_{5+\delta}$ is the result of high-temperature ordering of c-$Sc_2VO_{5+\delta}$, in particular antisite ordering of Sc and V and charge ordering of Sc^{3+}, $V^{3+...4+}$, and V^{5+}. $ScVO_4$ forms from the excess of V^{5+} in c-$Sc_2VO_{5+\delta}$. It is safe to assume that in the starting c-$Sc_2VO_{5+\delta}$: (1) it was V^{5+}-rich and (2) formation of $ScVO_4$ does not require oxygen – it is a process of Sc^{3+}-V^{5+} ordering and separation of Sc_2O_3 (surplus of Sc^{3+}). An oxygen-

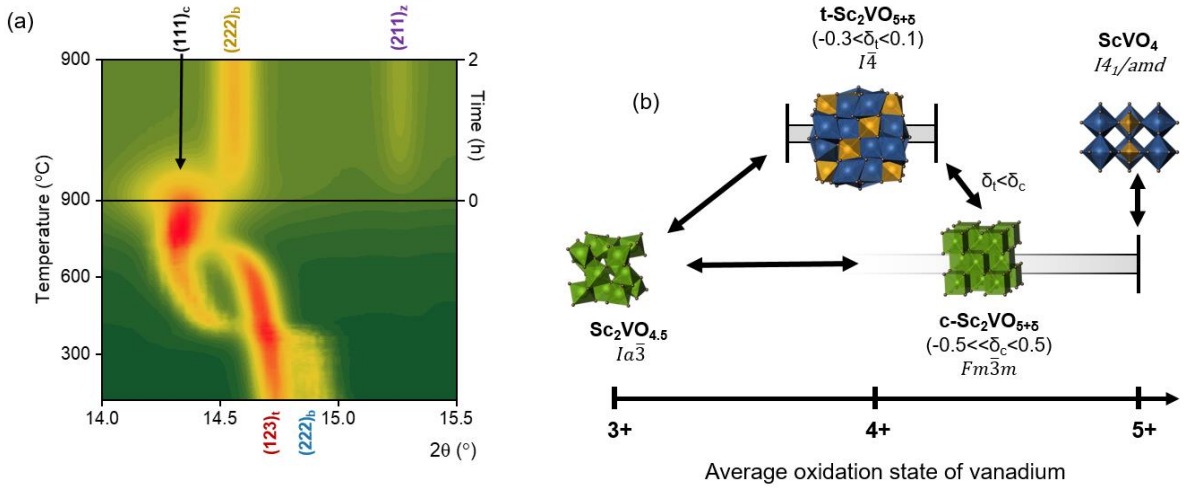

Figure 3.13. To the relations among $Sc_2VO_{4.5}$, c-$Sc_2VO_{5+\delta}$, t-$Sc_2VO_{5+\delta}$, and $ScVO_4$: (a) synchrotron powder XRD contour plot showing real-time oxidation of the 1:1 mixture of $Sc_2VO_{4.5}$ (blue indices) and t-$Sc_2VO_{5+\delta}$ (red) to c-$Sc_2VO_{5+\delta}$ (black) and decomposition to $ScVO_4$ (purple) and ½ Sc_2O_3 (yellow); (b) – structure-reaction map connecting the four vanadates. X axis is the oxidation state of vanadium, Y direction is cation ordering: Sc – blue polyhedra, V – yellow polyhedra, Sc/V disorder – green polyhedra. Grey bars illustrate the range of oxidation states which can be adjusted via topotactic redox.

stoichiometric fluorite c-Sc_2VO_5 ($\delta = 0$) with V^{4+} only is expected to order into pure t-Sc_2VO_5, while c-$Sc_2VO_{5.5}$ ($\delta = 0.5$) with V^{5+} only is expected to decompose into a mixture of zircon $ScVO_4$ and Sc_2O_3.

Converting the ordered tetragonal phase t-$Sc_2VO_{5+\delta}$ to the disordered cubic c-$Sc_2VO_{5+\delta}$ structure requires oxidation at 600-700 ºC. The contour plot in **Fig. 3.13a** shows oxidation of a 1:1 (molar) mixture of $Sc_2VO_{4.5}$ (blue) and t-$Sc_2VO_{5+\delta}$ (red) in oxygen flow. The most intense peaks of the starting materials at $2\theta = 14.7^o$ and 14.8^o disappear at 400 and 750 ºC, respectively, while the (111) peak of the cubic fluorite c-$Sc_2VO_{5+\delta}$ appears[30,31]. In fact, those are two distinct fluorite phases, to be distinguished in ***Chapter 6.*** Nevertheless, at 900 ºC both of them transition to $ScVO_4$ (purple) and ½ Sc_2O_3 (yellow). For the fluorite formed from t-$Sc_2VO_{5+\delta}$ it means a narrow temperature window of stability. This phase thus appears to be more of a kinetic product rather than thermodynamic.

All oxidative reactions discussed in this section are presented in **Fig. 3.13b**. The upper row of structures contains fully or predominantly ordered phases, and cation order in particular is highlighted with blue Sc polyhedra and yellow V polyhedra. The bottom row represents cation-disordered phases as illustrated with green cations (mixed Sc/V). Grey areas mark the ranges of oxidation states accessible topotactically and tolerated by the respective structures.

3.2.2. Reductive synthesis of t-$Sc_2VO_{5+\delta}$

Tetragonal t-$Sc_2VO_{5+\delta}$ can be obtained reductively from $ScVO_4$ with various vanadium oxides as side products[F]:

$$2ScVO_4 + \frac{3}{2}H_2 \rightarrow Sc_2VO_{5+\delta} + \frac{1}{2}VO_{(3-2\delta)} + \frac{3}{2}H_2O \qquad (3.3)$$

This reaction was run in 3% H_2 (balanced N_2) at 800 ºC. Judging by the color of the sample after heating, reaction happens on the surface, which requires constant regrinding of the final product mixture and monitoring with XRD. The stack of XRD patterns in **Fig. 3.14** suggests no

[F] Similar reductive synthesis was carried out not only in flowing hydrogen, but also via microwave synthesis on a graphite bed in air. Graphite pellet served as the sample crucible, the internal heater via the so-called Maxwell-Wagner polarization mechanism[306,307], and presumptively the reducing agent. This method is lower-throughput than reduction of $ScVO_4$ and produced a more contaminated sample, not shown here.

intermediate product between $ScVO_4$ (purple) and t-$Sc_2VO_{5+\delta}$ (red). Marked with blue arrows are

bixbyite phases which are the result of over-reduction of $ScVO_4$ (producing $ScVO_3$) and/or t-$Sc_2VO_{5+\delta}$ (producing $Sc_2VO_{4.5}$), disappearing with more thorough grinding. More importantly, the intermediate fluorite c-$Sc_2VO_{5+\delta}$ which was observed during controlled oxidation of t-$Sc_2VO_{5+\delta}$ in **Fig. 3.10**, was not found upon reduction. Two mutually exclusive scenarios are possible:

(1) reduction of $ScVO_4$ does not pass through the formation of a fluorite phase (be it $ScVO_{3+\delta}$ or c-$Sc_2VO_{5+\delta}$), or

(2) a fluorite phase forms but very rapidly reduces to a corresponding bixbyite in a topotactic process owing to high oxide ion conductivity in c-$Sc_2VO_{5+\delta}$.

The two scenarios are indistinguishable with the probes used: the second scenario can look like the first scenario. To reconcile the oxidative and reductive routes, the diagram in **Fig. 3.15** proposes that oxidation of $Sc_2VO_{4.5}$ to $ScVO_4$ passes through two local minima – deeper t-

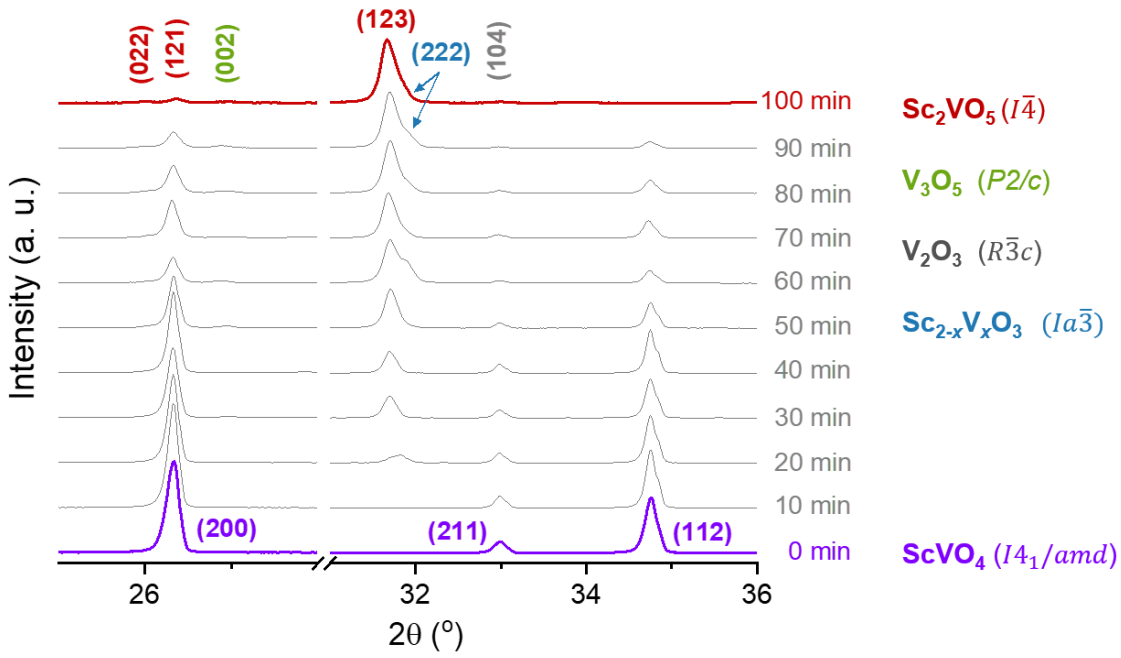

Figure 3.14. A stack of *ex-situ* powder XRD patterns showing slow reduction of $ScVO_4$ (purple) to t-$Sc_2VO_{5+\delta}$ in flowing dilute H_2 (3%, bal. N_2) with no intermediate scandium vanadates (a) and a speculation suggesting that c-$Sc_2VO_{5+\delta}$ can still be an intermediate in the $ScVO_4$ reduction if reduction goes through the shown energy profile.

$Sc_2VO_{5+\delta}$ (point A) and shallower c-$Sc_2VO_{5+\delta}$ (point B). The maximum (C) would likely be lower than the maximum (D), so that c-$Sc_2VO_{5+\delta}$ (B) can be stabilized on oxidation but not on reduction. In other words, once the supplied thermal energy is sufficient to overcome peak D during reduction, minimum B is easily skipped and maximum C is easily overcome. Given the complexity of the Sc-V-O phase diagram, related energy calculation is a project on its own and is beyond the scope of the current work.

As a side note, the discussed oxidation of $Sc_2VO_{4.5}$ in traces of oxygen (**Fig. 3.10**) and reduction of $ScVO_4$ in dilute hydrogen (**Fig. 3.14**) can be compared to the oxidation and reduction in excess oxidant/reductant. **Fig. 3.11** already showed how $Sc_2VO_{4.5}$ oxidizes to c-$Sc_2VO_{5+\delta}$ and then $ScVO_4$ in excess oxygen. Similarly, $ScVO_3$ can be oxidized to $ScVO_{3.5}$ (a fluorite) and to the same zircon $ScVO_4$[126]. Thus, an intermediate fluorite with 2:1 or 1:1 ratio of Sc:V forms oxidatively regardless of how much oxygen is offered. In contrast, reduction of $ScVO_4$ in excess hydrogen leads to $ScVO_3$ with no visible intermediates[126]:

$$ScVO_4 + H_2 \rightarrow ScVO_3 + H_2O \qquad (3.4)$$

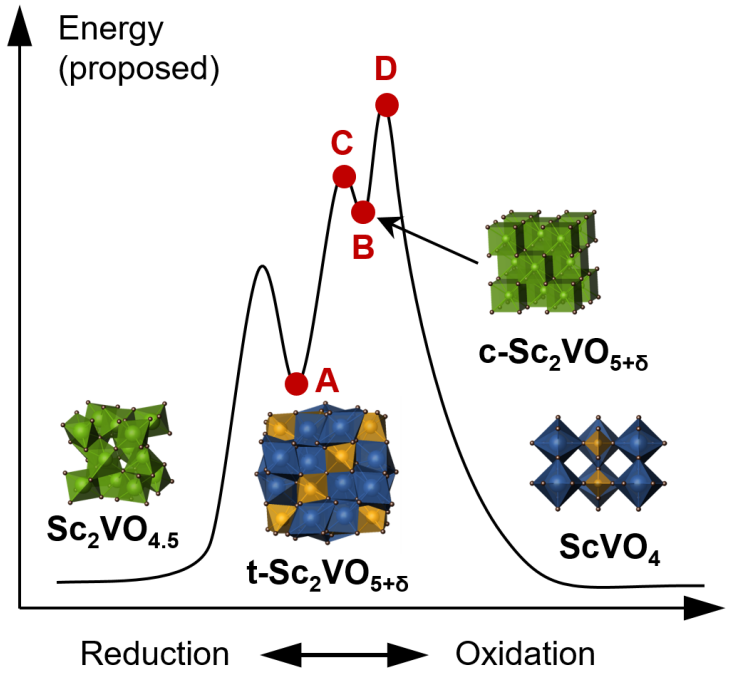

Figure 3.15. A proposed schematic energy profile suggesting that c-$Sc_2VO_{5+\delta}$ can still be an intermediate in the $ScVO_4$ reduction.

The case with 1:1 ratio of Sc:V can be also explained by a diagram similar to **Fig. 3.15**.

3.2.3. Direct synthesis of t-$Sc_2VO_{5+\delta}$. Disproportionation of vanadium

Tetragonal t-$Sc_2VO_{5+\delta}$ can be obtained directly from VO_2 and Sc_2O_3 in static vacuum according to this equation (δ=0 for simplicity):

$$Sc_2O_3 + VO_2 \rightarrow Sc_2VO_5 \qquad (3.5)$$

The reaction was done *in-situ* on a neutron diffractometer (**Fig. 3.16**), and full phase conversion occurred by 1100 ºC. The same reaction was carried out *ex-situ* at 1100 ºC with the setup in **Fig. 2.3b**, and the product of this synthesis was the sample investigated with XRD, NPD, PDF, TGA, XANES, and DC susceptibility measurements (**Figs 3.5, 3.7, 3.8**). This product was established to have δ = -0.15, i.e. it lost 0.15·O^{2-} per unit formula. This loss accompanies disproportionation of vanadium V^{4+} into $^{8g}V^{3+}$ (co-existing with remaining V^{4+}) and $^{2c}V^{5+}$, in the 8*g*:2*c* ratio of 4:1. The same equation can be rewritten to show the loss of oxygen:

$$Sc_2O_3 + VO_2 \rightarrow Sc_2VO_{5+\delta} - \frac{\delta}{2}O_2 \qquad (3.6)$$

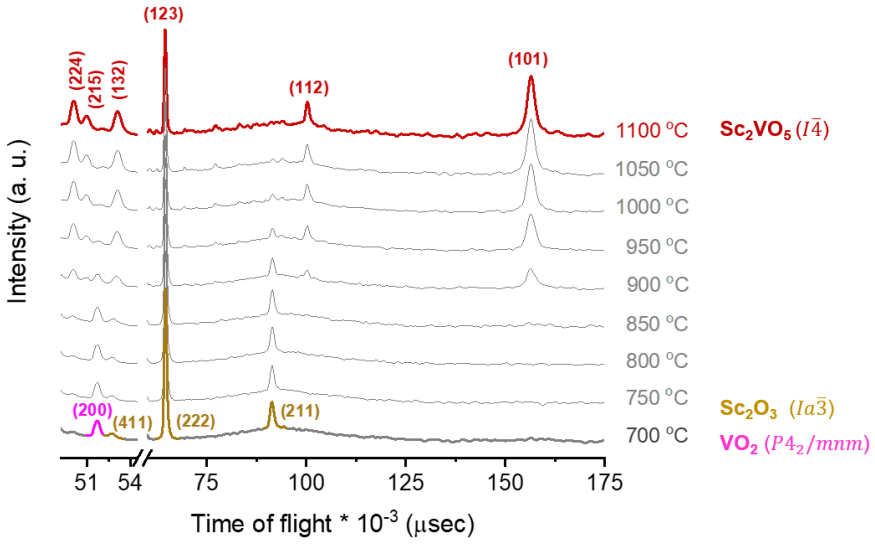

Figure 3.16. An *in-situ* stack-plot of NPD diffractograms showing real-time direct synthesis of t-$Sc_2VO_{5+\delta}$ (red) from VO_2 (magenta) and Sc_2O_3 (yellow).

An alternative approach was tried where *three* starting materials were reacted under the same conditions: $ScVO_3$ (source of V^{3+} targeting site 8*g* of vanadium), $ScVO_4$ (source of V^{5+} targeting site 2*c*), and Sc_2O_3 (major source of scandium). The overall equation can be written in a simplified form as:

$$\frac{1}{2}\,Sc_2O_3 + \frac{1}{2}ScVO_3 + \frac{1}{2}ScVO_4 \rightarrow Sc_2VO_5 \qquad (3.7)$$

Fig. 3.17a shows XRD patterns of the starting materials mixture and the final product of heating at 1100 ºC. Recalling the 4:1 ratio of reduced to oxidized vanadium in t-$Sc_2VO_{5+\delta}$, a single-phase product can be expected at a 4:1 ratio of $ScV^{3+}O_3$:$ScV^{5+}O_4$. However, this was not the case and the pure-phase product was obtained only with the ratio V^{3+}:V^{5+} = 9:11. This ratio is reasonably close to 1:1 which is equivalent to V^{4+} in VO_2. Various starting ratios $ScVO_3$:$ScVO_4$ were tried as shown in **Fig. 3.17b**. The purest product (ratio 9:11) is in red, with the nominal composition

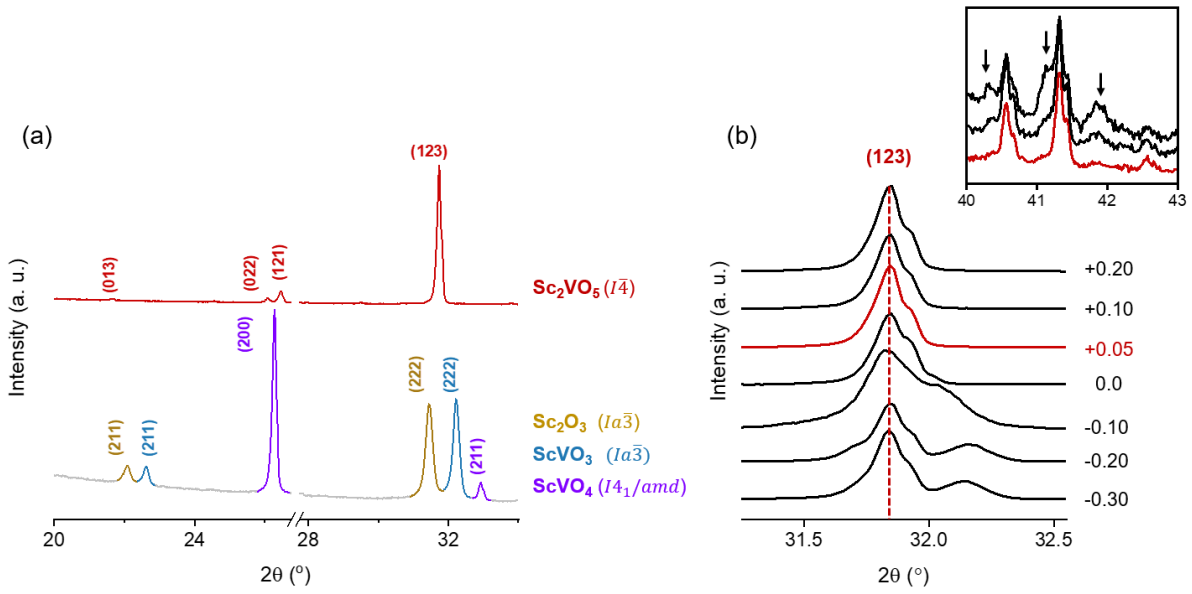

Figure 3.17. Fragments of XRD plots showing direct synthesis of t-$Sc_2VO_{5+\delta}$ *ex situ* in vacuum: (a) – its formation (red) from a mixture of Sc_2O_3 (yellow), $ScVO_3$ (blue), and $ScVO_4$ (purple); (b) – same, but with a varying ratio of $ScVO_3$ and $ScVO_4$. The one leading to the purest product is shown in red and corresponds to the *nominal* δ=0.05 in $Sc_2VO_{5+\delta}$. Insert zooms into the high-2θ region of patterns with $\delta > 0.05$ to show impurity peaks (arrows).

$Sc_2VO_{5.05}$ (nominal δ = 0.05). Other attempted compositions had nominal δ of -0.3 (ratio 4:1), -0.2 (7:3), -0.1 (3:2), 0 (1:1), +0.1 (2:3), and +0.2 (3:7); see revised equation 3.8:

$$\frac{1}{2}\, Sc_2O_3 + (1-x)\, ScVO_3 + (x)\, ScVO_4 \;\rightarrow Sc_2VO_{5+\delta}, \qquad (3.8)$$

where x = ½ + δ. Notably, product mixtures with nominal δ < 0.05 had bixbyite-type impurities (V^{3+}-rich), while at δ > 0.05 other unidentified impurities were found (likely V^{5+}-rich; see inset).

Both direct methods point at the requirement to start the synthesis with a larger average oxidation state of vanadium than anticipated in t-$Sc_2VO_{5+\delta}$. 99.7% proximity of t-$Sc_2VO_{5+\delta}$ unit cell volumes after reactions 3.6 and 3.8 and the value of δ = -0.15 after reaction 3.6 suggest reduction of the product. Reduction is likely driven by the charge ordering of vanadium between the 8*g* (reduced) and 2*c* (oxidized) sites required by the structure. Additional reduction due to the gradient of the oxygen partial pressure (sample *vs* environment) also cannot be excluded.

3.3. Topotactic redox of vanadium

The possibility for topotactically tuning δ in t-$Sc_2VO_{5+\delta}$ was reflected in **Fig. 3.13b** which suggested a range of oxygen stoichiometries in t-$Sc_2VO_{5+\delta}$. Based on the vanadium oxidation state in the vanadium 8g site, the composition theoretically ranges from $Sc_2V^{3+}_{0.8}V^{5+}_{0.2}O_{4.7}$ (δ = -0.3) with only V^{3+} in the 8*g* site to $Sc_2V^{4+}_{0.8}V^{5+}_{0.2}O_{5.1}$ (δ = 0.1) with only V^{4+} (and no V^{5+}). A sample of t-$Sc_2VO_{5+\delta}$ obtained via eq. 3.6 was studied with *in-situ* X-ray powder diffraction between room temperature and 500 ºC (**Fig. 3.18**). The unit formula volume increases during oxidation (**Fig. 3.18a**) and decreases during reduction (**Fig. 3.18b**), which is associated with the insertion and removal of oxygen ions into the oxide vacancies, correspondingly. Although the sample was a thin slurry on the heating element of the furnace and although the oxidation is topotactic (fast), it is possible that more grinding would allow more complete oxidation. In general, evolution of the unit cell in such redox experiments is governed by at least two competing processes: (1) increase/decrease of the radius of the redox-active cation (vanadium) and (2) uptake/release of oxide anions. For the Sc-V-O system it is expected that the unit cell volume increases upon oxidation primarily because the uptake of larger oxygen outcompetes the 9% contraction of V^{3+} to V^{4+} [93,99]. It is the opposite, however, for the system Y-Pr-O: the unit cell volume of $YPrO_{3+\delta}$

decreases on oxidation of much larger Pr^{3+} to Pr^{4+} [117,198]. Hence, the unit cell volume change is sensitive to the cation-to-anion size ratio. In principle, the two competing processes can compensate each other if a pair of cations with a smaller ratio than Y-Pr but larger than Sc-V can be found.

The experiment in **Fig. 3.18** was carried out well below 600 ºC to avoid the oxidation of t-$Sc_2VO_{5+\delta}$ to c-$Sc_2VO_{5+\delta}$ expected above 600-650 ºC. However, the same temperature range, and t = 460 ºC in particular, was high enough to reduce t-$Sc_2VO_{5+\delta}$ to $Sc_2VO_{4.5}$ (panel **c**) simultaneously with the topotactic reduction. Since this temperature range is usually sufficient to rearrange the anions but not the cations, the final bixbyite $Sc_2VO_{4.5}$ might retain the cation ordering scheme of its precursor t-$Sc_2VO_{5+\delta}$. An additional neutron experiment is required to corroborate this idea.

Notably, in **Fig. 3.18**, the uptake and release of oxygen was limited by the duration of the experiment. It is anticipated that the actual range of δ is much wider than the tuned concentration in this figure. It was partially explored in recent work by Richtik[127] where the limit of oxygen content was probed via doping the 8*g* site of $Sc_2VO_{5+\delta}$ with Ti^{4+}.

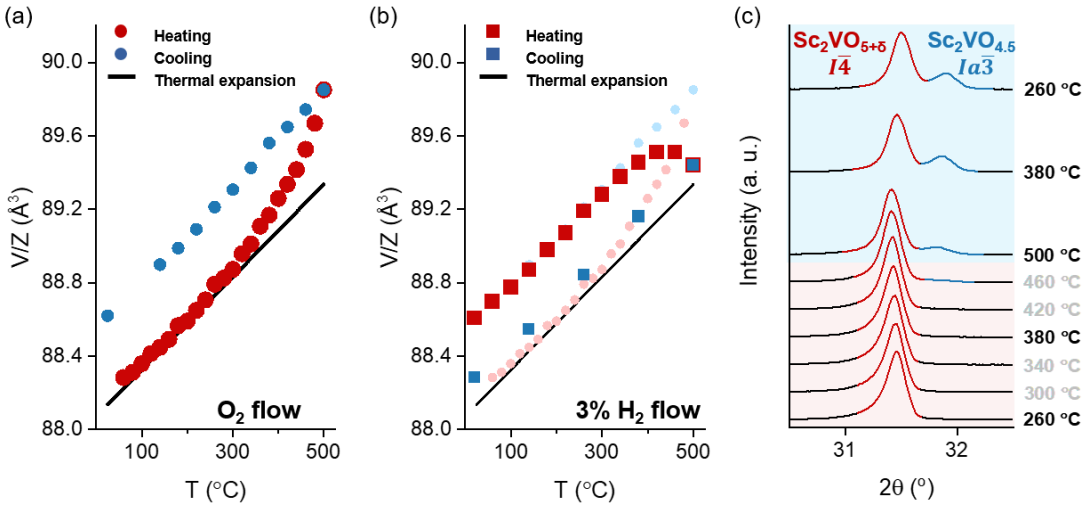

Figure 3.18. Topotactic redox of $Sc_2VO_{5+\delta}$ followed with *in-situ* XRD: (a) – evolution of the unit formula volume during oxidation on heating (red) and cooling (blue), associated with topotactic oxidation of V^{3+} toV^{4+} in the 8*g* site. The black line shows the thermal expansion; (b) – same on reduction, associated with reduction of V^{4+} to V^{3+} in the 8*g* site. Faded markers (oxidation) are used for reference; (c) – stack plot of XRD pattern fragments related to reduction, where red and blue shaded areas are heating and cooling, and red and blue peaks are (123) of $Sc_2VO_{5+\delta}$ and (222) of $Sc_2VO_{4.5}$. The latter manifests a competing reductive process whose onset is noticeable at ~460 ºC.

3.4. Conclusion

Charge ordering of vanadium is key to the formation of t-$Sc_2VO_{5+\delta}$ and distinguishes it from other A_2VO_5 phases. Under the conditions similar to direct synthesis of t-$Sc_2VO_{5+\delta}$, reaction of Sc_2O_3 with $V^{3+}{}_2O_3$ rather than $V^{4+}O_2$ results in the bixbyite structure ($Sc_2VO_{4.5}$) with exclusively sixfold metal-oxygen coordination and full cation disorder. It suggests that octahedral coordination of vanadium *per se* is insufficient to form t-$Sc_2VO_{5+\delta}$. Although the unit cell contains only two tetrahedral V^{5+} ions out of 30 cations, it is the Coulombic repulsion between these highly charged cations that drives the formation of t-$Sc_2VO_{5+\delta}$. In particular, the V^{5+} ions are at a maximum distance of 7.79 Å (along *b*) and 9.15 Å (mostly along *c*) from each other. In the oxidative synthesis, charge ordering is possible only after disproportionation of V^{4+} in VO_2, the extent of which is governed by the 4:1 ratio of 8*g*:2*c* sites. Since under the same conditions VO_2 alone (i.e. in absence of scandium) does not undergo disproportionation, formation of the $I\bar{4}$ structure might require Sc^{3+} ions which would further "dilute" highly charged V^{5+} ions and likely set the limit of their concentration in the unit cell. The structure also requires reduced vanadium species, otherwise the only ordered V^{5+}-bearing Sc-V-O system would be $ScVO_4$. Thus, although thermodynamically stable, t-$Sc_2VO_{5+\delta}$ exists as a subtle balance between the bixbyite $Sc_2VO_{4.5}$ and the zircon $ScVO_4$ (all three are *fcc*-based or -derived). It can be said to contain both of their structural motifs – $V^{3+}{}_{VI}$ / $Sc^{3+}{}_{VI}$ and $V^{5+}{}_{IV}$ / $Sc^{3+}{}_{VIII}$.

Having a sizable 16…28% difference of ionic radii in CN = VI, Sc^{3+} and $V^{3+\ldots4+}$ ions in t-$Sc_2VO_{5+\delta}$ are ~9% disordered in four out of five cationic sites. This antisite disorder might owe to charge disorder within the vanadium sublattice, whereby the structure would benefit from expelling highly charged V^{4+} ions from the 8*g* site of vanadium (adjacent to V^{5+}) into the most distant 4*f* site of scandium. Regardless of the mechanism, there seems to exist an opportunity to substitute larger scandium for a smaller ion commensurate with vanadium, and vice versa. This observation led to multiple attempts to selectively dope scandium sites or either of the two vanadium sites with commensurate ions. When doping scandium sites with even the smallest lanthanides (Lu, Yb, Ho), neither direct methods nor slow reduction of zircons resulted in a single-phase $I\bar{4}$ product. Unsuccessful attempts were made to incorporate other ions including of different charges (e.g. Cu^{+}) and composite charges (e.g. pair Ca^{2+}-Hf^{4+}). Resulting competing phases are not discussed further, and the only successful replacement of Sc^{3+} with In^{3+} via the

direct synthesis is mentioned in the following chapter, ***Chapter 4***. Notably, this chapter is mostly devoted to the other members of the A_2VO_5 family which can be thought of as the instances of full replacement of Sc^{3+} with other A^{3+} cations, both smaller and larger than scandium, although accompanied by the change of the structure type. The chapter then explores the evolution of the connectivities and coordination within the vanadium sublattice. The related chapter after that – ***Chapter 5*** – discusses doping of the *vanadium* sublattice of t-$Sc_2VO_{5+\delta}$ with cations close in size to V^{3+} and V^{4+}. Also, complementing A_2VO_5 phases in ***Chapter 3***, ***Chapter 5*** revisits Sc_2BO_5 phases which can be thought of products of full replacement of vanadium in t-$Sc_2VO_{5+\delta}$ with B^{x+} cations.

Targeted substitution of V^{5+} in the 2*c* site is an ongoing project that was left out of the thesis. Si^{4+} (r_{IV} = 0.26 Å), P^{5+} (r_{IV} = 0.29 Å), As^{5+} (r_{IV} = 0.335 Å[103]) so far formed competing phases such as $Sc_2Si_2O_7$, $ScPO_4$, ScAs. Arsenic is the most promising candidate for doping due to its size being only within 6% of $r(V^{5+}{}_{IV})$.

Reproducible selective doping of the 2*c* site only or 8*g* site only, or any combination thereof, is a task that concerns the unique vanadium sublattice of t-$Sc_2VO_{5+\delta}$ as well as the related magnetic coupling. As seen in the vanadium sublattice in **Fig. 3.19**, vanadium ions in the 8*g* site (octahedral $V^{3+\ldots4+}$) form corner-shared V_4-clusters, separated by vanadium in the 2*c* site (tetrahedral V^{5+}).

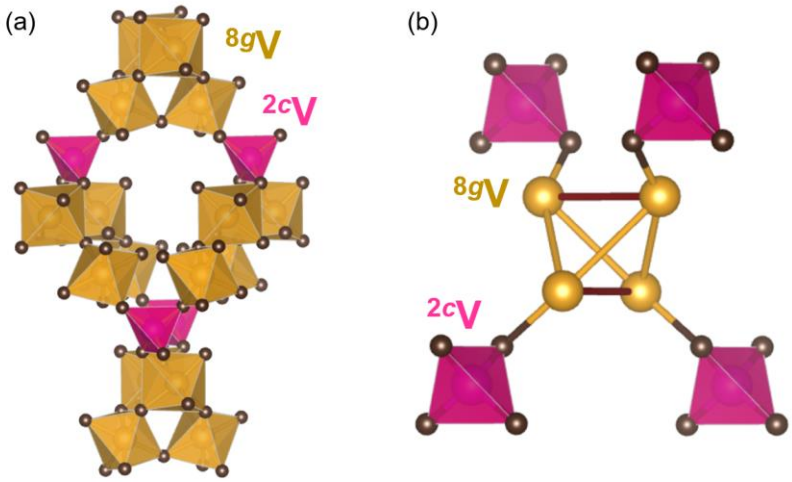

Figure 3.19. Vanadium sublattice of t-$Sc_2VO_{5+\delta}$: (a) – corner-shared tetrahedral 8*g* clusters (yellow octahedra) separated by isolated 2*c* tetrahedra (magenta); (b) – one emphasized V_4-cluster (oxygen around the 8g sites are omitted for clarityies sake) Two V-V bonds in it (dark-red) are slightly longer than the rest.

The paramagnetic $V^{3+\ldots4+}$ are confined to the 8*g* positions. Consequently, the net antiferromagnetic coupling (θ = -1.6(2) K, **Fig. 3.5b**) is confined to the V_4-clusters formed by the 8*g* site only. Targeted substitution of the 8*g* and 2*c* sites will allow exploring the magnetic coupling in the V_4-clusters and between clusters. For example, replacing just 20% of vanadium with Ti^{4+} (r = 0.605 Å in CN = VI *vs* r = 0.58…0.64 Å for $V^{4+/3+}$) favors net ferromagnetic coupling[127] as opposed to net antiferromagnetic coupling observed in the parent structure.

The highly tunable t-$Sc_2VO_{5+\delta}$ structure is promising for further investigations of fundamental magnetism. This lends additional importance to a detailed understanding of t-$Sc_2VO_{5+\delta}$ and the investigation of doped phases.

CHAPTER 4

$A^{3+}_2VO_5$ and A-doped $Sc_2VO_{5+\delta}$ phases

Tetragonal t-$Sc_2VO_{5+\delta}$ is a member of the site- and/or charge-ordered A_2VO_5 family, where A is a trivalent cation. As seen in **Fig. 1.1** and discussed in the introduction, relatively few A_2VO_5 phases have been reported to-date. Across these phases, t-$Sc_2VO_{5+\delta}$ with at least two charge-ordered vanadium species is an outlier. The current chapter attempts to find structural trends describing the known A_2VO_5 phases and synthesize new phases. In particular, the evolution of connectivities within the V sublattice and A-V site mixing as a function of the A^{3+} size are considered.

4.1. V_3O_5 is V_2VO_5

Considering fully octahedral V_3O_5 (V_2VO_5) with a small A^{3+}=V^{3+} cation, at least two ambient structures are known – *P2/c* (#13)[35] and *P2₁/c* (#14)[76]. Both structures were synthesized in a gas transport experiment with $TeCl_4$ as a transport agent [199]. In the *P2/c* structure (**Fig. 4.1**), full charge ordering was reported, correlated with crystallographic shear. In the structure of V_3O_5, polyhedra

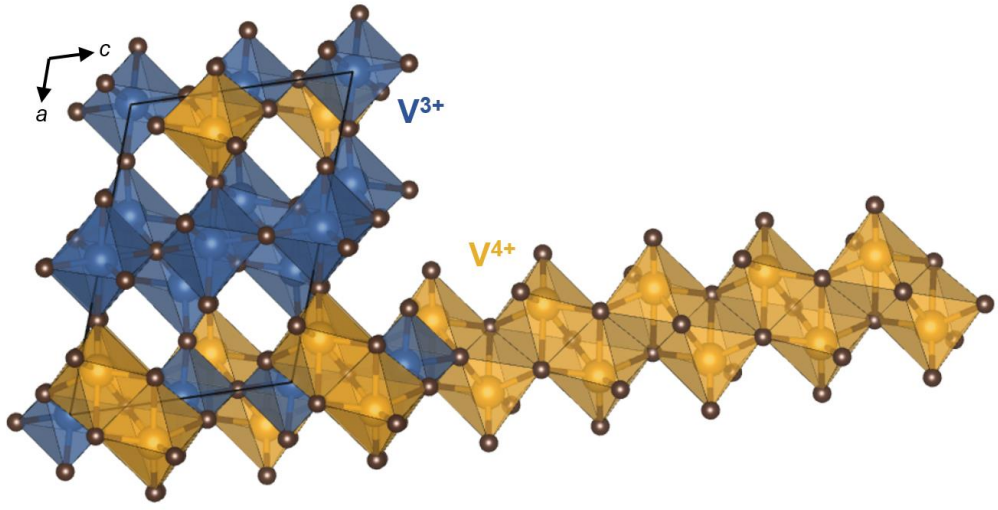

Figure 4.1. Crystal structure of charge-ordered V_3O_5 (*P2/c*). Part of the V-1 sublattice (yellow) is elongated in the *c* direction to show edge- and face-sharing $[V^{4+}O_6]^{8-}$ octahedra.

around The V1 sites (yellow) form 1-dimensional slabs along the *c* axis through edge- and face-sharing. This site is of importance since it accommodates exclusively or predominantly V^{4+} species (r_{VI} = 0.58 Å), while the other three cationic sites (blue) accommodate V^{3+} (r_{VI} = 0.64 Å) in agreement with bond-valence calculations (**Fig 4.2a**). This phase is consistent with the notation A_2BO_5. Bond-valence calculations on the second structure (SG: $P2_1/c$) shown in **Fig 4.2b** are consistent with V^{3+} species only in sites V2 and V3, while site V1 likely has a mixture of V^{3+} and V^{4+} species. Although additional investigations are needed, from BVS only the corresponding structure is rather $V_3O_{4.7}$. There is a large ambiguity in determination of oxygen concentration without a more detailed analysis; for now, this structure is omitted from further considerations.

V_3O_5 seems to be the only V^{3+}-V^{4+} charge-ordered structure among the vanadium oxides and rutile derivatives in particular. It can be contrasted against V_4O_7 with only minor V^{3+}-V^{4+} ordering[200] and fully charge-disordered V_6O_{11}[201] (see supporting BVS plots in **Fig. A.2-1**). With the 10% size difference between the A-cation V^{3+} and the B-cation V^{4+}, V_3O_5 sets the new minimum cation size difference needed for A^{3+}-B^{4+} ordering, as opposed to 28% in idealized $Sc_2V^{4+}O_5$. This ordering is enabled by the structure, wherein the polyhedra that are close to the shear planes are the most distorted (more suitable for Jahn-Teller-active ions like V^{4+}) and compressed (more suitable for smaller ions like V^{4+}).

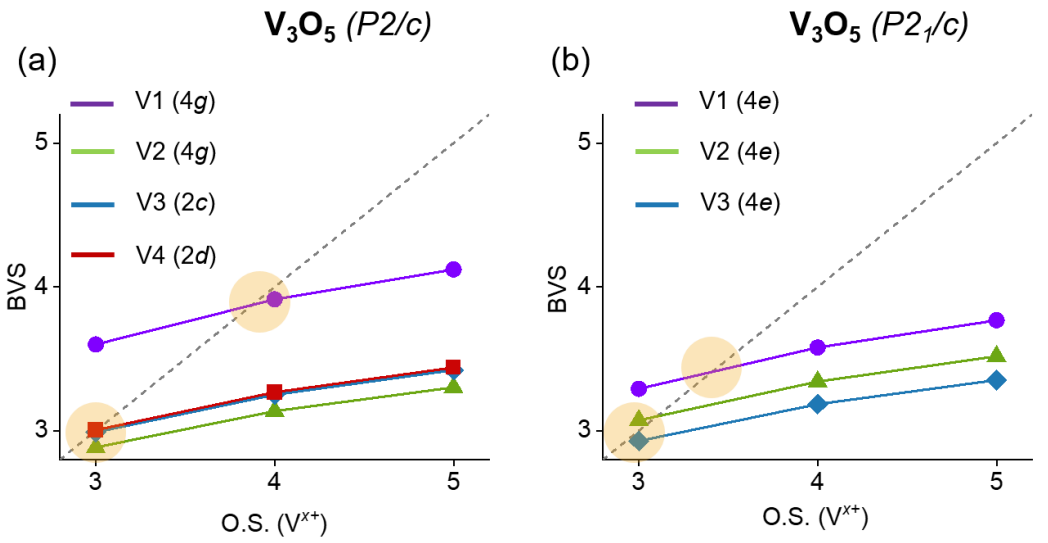

Figure 4.2. Bond-valence sum calculations for vanadium ions in two room-temperature modifications of V_3O_5. Circles mark intercepts of the BVS curves (colored) with the reference line (grey), whose abscissa gives the oxidation state of vanadium.

4.2. Pursuit of $Ti_2VO_{5+\delta}$

Based mostly on ICSD, the ambient phase diagram Ti-V-O is represented by $(Ti,V)_2O_3$ corundums[202], $TiVO_4$ rutile (a small-A counterpart of AVO_4 zircons)[203], all-octahedral berdesinskiite $V^{3+}{}_2Ti^{4+}O_5$[80], and all-octahedral schreyerite $Ti^{2.67+}{}_3V^{5+}{}_2O_9$[204]. Not reported in ICSD, a pseudobrookite Ti_2VO_5 (likely all-octahedral) was also discovered together with a few other Ti-V-O phases[78,79], but no structural data are available.

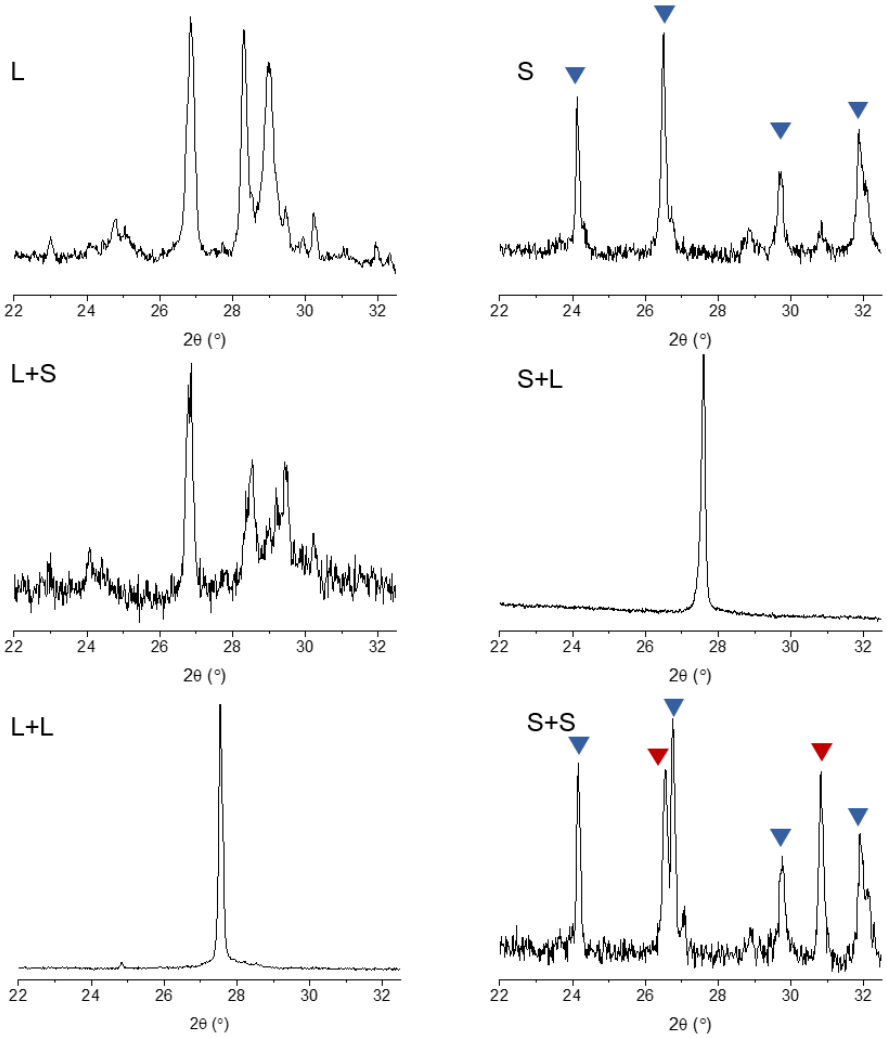

Figure 4.3. XRD patterns of the products of solid-state reactions between Ti_2O_3 and VO_2: L and S refer to static vacuum sustained by locking the sample inside the furnace (with a vacuum tap) or by sealing the sample in quartz. Red and blue markers indicate peaks of Ti_3O_5-type and A_4O_7-type phases, respectively. L+L and S+L conditions ("+" indicates two consecutive heatings) yielded rutiles, while L and L+S yielded mostly A_8O_{15}-type Magnéli phases.

The synthesis of the Ti_2VO_5 phase was attempted multiple times via direct solid-state synthesis reaction Ti_2O_3 (5% imp. Ti_3O_5) + VO_2 at 1100 ºC. In these experiments, it proved important to discriminate between two static vacuum environments – an evacuated quartz tube with a tap (further marked as "L" for "lock", see setup in **Fig. 2.3b**) and a sealed quartz tube ("S", see **Fig. 2.3c**). First, single heatings were done under "S" or "L" conditions, and then successive (second) heatings were done under both conditions, altogether accounting for all four combinations of pairs: S+S, S+L, L+L, and L+S. First heating under "S" condition yielded a Magnéli phase Ti_4O_7[205] ($P\bar{1}$; oxygen-deficient rutile superstructure with the formula A_nO_{2n-1}, $n > 3$[206]) with possibly a minute impurity of corundum ($R\bar{3}c$) and a Ti_3O_5-type phase[74] (*C2/m*). First heating under "L" condition yielded a different Magnéli phase identified as Ti_8O_{15}[207] ($P\bar{1}$). Next, "L+L" and "S+L" reactions yielded a pure-phase rutile ($P4_2/mnm$), "L+S" – a Magnéli phase of the Ti_8O_{15} type, and "S+S" – Magnéli phase of the Ti_4O_7 type with an impurity of the V_3O_5-type[201] phase ($P2_1/c$). Fragments of the XRD patterns of the products are shown in **Fig. 4.3**. In the A_2BO_5 notation, the three prominent phases observed throughout the experiments can be written as $Ti_2VO_{5.25}$ (Ti_4O_7 type), $Ti_2VO_{5.63}$ (Ti_8O_{15} type), and Ti_2VO_6 (TiO_2 type). From it, the oxygen concentration and the associated average oxidation state of the (Ti,V) metal pair increase from the product of the "S" and "S+S" reactions to the product of the "S+L" and "L+L" reactions. Since the target phase is Ti_2VO_5 and the closest to it is $Ti_2VO_{5.25}$, the "S" conditions gave the result that is the closest to the

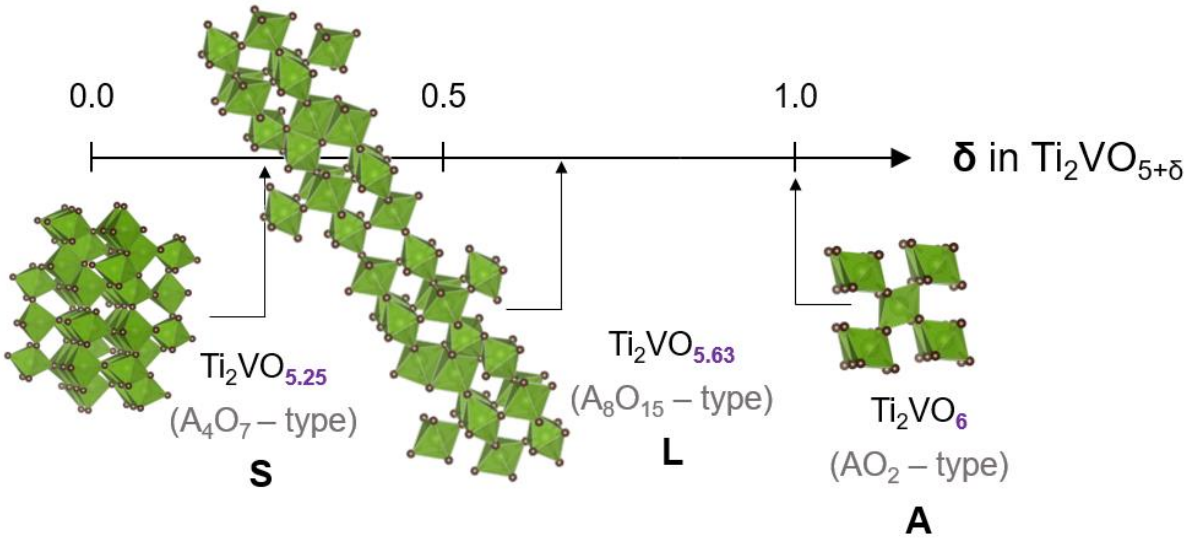

Figure 4.4. $Ti_2VO_{5+\delta}$ structures obtained in vacuum in sealed quartz (S), in an evacuated closed tube (L), and in air (A).

desired composition. Furthermore, similar heating in air ("A") also resulted in the rutile phase, which is consistent with the general understanding of Magnéli phases as oxygen-deficient derivatives of the rutile structure. The three main structure types observed in the described seven reactions ("S", "L", "S+L", …, "A") are organized in ascending order of δ in $Ti_2VO_{5+\delta}$ in **Fig. 4.4**. Simultaneously sufficient and easiest reaction conditions allowing to access these phases are indicated with a corresponding letter ("S", "L", or "A"). Due to the lack of X-ray scattering contrast between neighboring Ti and V, neither site preferences nor oxidation states of metals can be refined from the collected diffraction data, hence the word "type" always accompanied the structures above. However, a tentative assessment of average oxidation states of metals can be done with the BVS analysis, for which the metal-oxygen bonds were obtained from the Rietveld refinement of the XRD data. **Fig. 4.5** is a BVS plot for the rutile sample obtained under "S+L" conditions. The only available cation site of the rutile structure was split into three parts to represent the 2:1 molar ratio of Ti and V, and various idealized (integer) combinations of oxidation states were assigned to them. In blue are compositions with reduced V or Ti species with respect to the nominal charge composition, accounting for slightly reducing nature of vacuum (L and

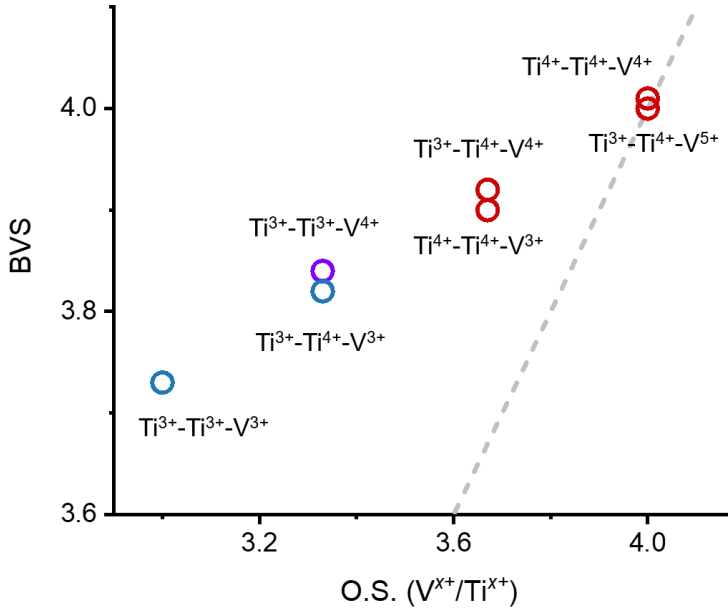

Figure 4.5. BVS plot of a rutile-type phase obtained under "S+L" conditions illustrating the non-triviality of the oxidation state assessment of V and Ti in this oxide. BVS calculations were tried for various distributions of oxidation states: giving a net underoxidized oxide or charge exchange (blue), nominal composition (purple), and overoxidized (red). The best result is consistent with overoxidation of 2/3 of the cations.

especially S) and high temperature. In purple is the nominal composition. In red are compositions where 1/3 or 2/3 of the cations are oxidized, and their proximity to the y = x reference line suggests that the product is partially oxidized despite the precaution taken to evacuate the sample environment ("L") prior to synthesis. Resulting idealized composition then can amount to $Ti_{0.67}V_{0.33}O_3$ in the $AO_{2+\delta}$ notation, or Ti_2VO_6 in the $A_2BO_{5+\delta}$ notation. The closest to $A_2VO_{5+\delta}$-type structure obtained was $Ti_2VO_{5.25}$, or A_4O_7-type Magnéli phase, with projected $\delta = 0.25$. Synthesis showed to be sensitive to the quality of static vacuum. It should be noted that further heating of the A_8O_{15}-type phase ($A_2BO_{5.63}$) under the overall conditions "L+S+S" resulted in a mixture of Magnéli phases, including with lower *n*. Multiple mild reductions under static vacuum might be the right strategy to gradually access the smallest δ, i.e. the A_3O_5 stoichiometry.

In the A_3O_5 family only a few Ti-V-based members are known, occurring naturally as berdesinskiites $V^{3+}{}_2Ti^{4+}{}_{1-x}V^{4+}{}_xO_5$ [80,208,209] as shown in **Fig. 4.6**. They are represented by the title phase V_2TiO_5 ($x = 0$) and V-rich solid solutions between it and V_3O_5, resulting in having a mixture of V^{4+} and Ti^{4+} in the B sublattice[G]. Interestingly, berdesinskiite adopts the same structure as HT modifications of both V_3O_5 [60] and Ti_3O_5 [210], possibly due to having been found in a quartzite rock whose formation requires extreme conditions (high temperature and, less importantly here, pressure). While the attempts to synthesize a Ti_2VO_5 phase from the Ti-rich part of the diagram led to oxygen-nonstoichiometric phases as per **Fig. 4.4**, an attempt to synthesize a composition $V_{2.2}Ti_{0.8}O_{5.1}$ within the range of berdesinskiite solid solutions (marked with a dot in **Fig. 4.6**)

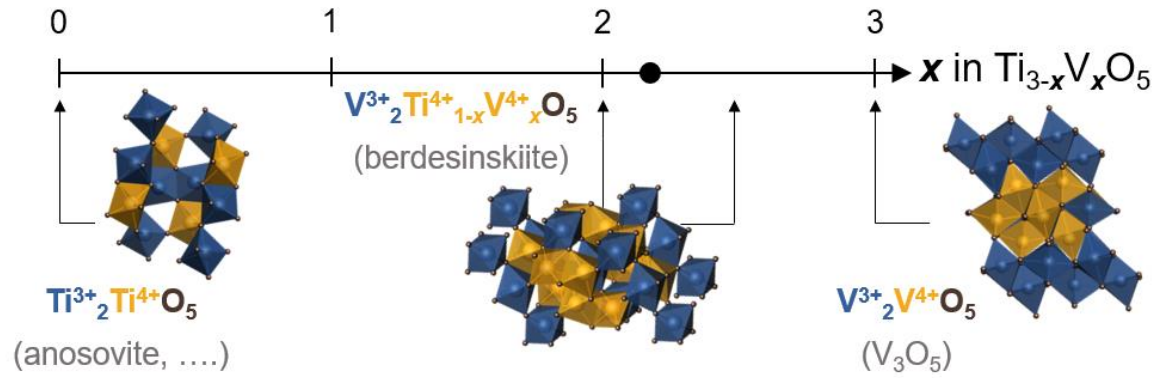

Figure 4.6. Known phases in the $Ti_{3-x}V_xO_5$ series. The dot indicates a composition tried in this work (see ***Appendix 2***).

[G] V-rich berdesinskiites found in nature also contain a 10-20 at. % cationic impurity of Cr^{3+} disordered with V^{3+} ions in the A sublattice.

resulted in a phase isostructural to V_3O_5 (S.G.: *P2/c*). This phase is likely cation- and charge-disordered as suggested by BVS calculations and consists of predominantly V^{3+} and Ti^{4+} from V- and Ti-XANES. Its analysis is presented in **Fig. A-2.2** and **Fig. A-2.3** of ***Appendix 2***. It is then compared with **Fig. A-2.4** illustrating a case with Ti^{3+} instead of Ti^{4+} and the resulting mixture of phases as opposed to a single-phase product in **Fig. A-2.2**. Since Ti and V lack scattering contrast in XRD, **Fig. A-2.5** attempts to estimate the relative content of Ti and V in each of the product phases $V_xTi_yO_z$ by comparing their unit cell volumes with volumes of corresponding (i.e. isostructural) Ti_xO_z and V_xO_z oxides, assuming a linear trend. It should be noted that V-rich titanates are beyond the scope of this thesis and no further investigation was carried out.

4.3. Comment on Al and Ga vanadates

In general, redox inactivity of the A^{3+} cation is a prerequisite for better control over oxide vacancy concentration in A_2VO_5 phases with ordered V_3O_5 being the only exception. Usage of redox-active A^{3+} cations might lead to the reduction of d-metals to lower oxidation states than desirable 3+ and/or formation of competing phases of undesirable stoichiometry (corundums, spinels, various other fluorite superstructures, etc.). The need for redox-inactive cations excludes the majority of d-metals which are otherwise advantageous (e.g. not volatile at solid-state synthesis temperatures used in this work). Among the redox-inactive or less redox-active candidates, only two stable trivalent A^{3+} cations, commensurate with V^{4+}, exist – Al^{3+} and Ga^{3+}. These are relatively small cations known for often preferring tetrahedral environment in $A_xV^{<5+}{}_yO_z$ ternary oxides (note the O.S. of vanadium). For example, in AlV_2O_4 spinel[211] Al^{3+} and $V^{2.5+}$ species prefer tetrahedral (0.39 Å) and octahedral (0.715 Å) environment s, correspondingly, whereas in $AlVO_4$ this preference inverts ($r(Al^{3+}{}_{VI})$ = 0.535 Å; $r(V^{5+}{}_{IV})$ = 0.355 Å). In a hypothetical phase $Al_2V^{4+}O_5$

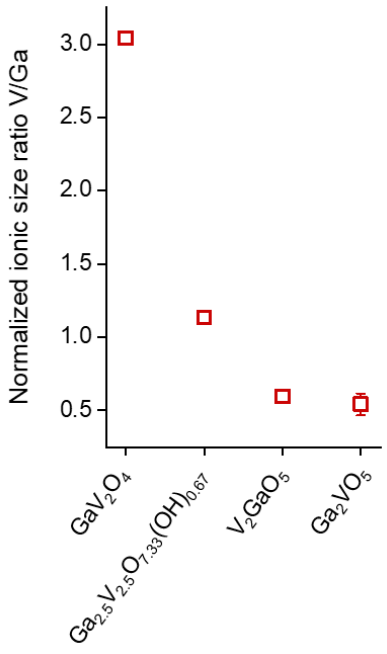

Figure 4.7. Comparative cation radii of Ga and V (adjusted for stoichiometry) of three existing gallium vanadates and one theoretical Ga_2VO_5.

with V^{4+} commensurate with V^{3+}, tetrahedral environment can be expected for Al^{3+}, although not guaranteed. So far, no such phase has been reported. In particular, aluminum proved to be unreactive in solid state in the range of temperatures considered (up to 1500 ºC).

Reported gallium vanadate phases with intermediate oxidation states of vanadium include V_2GaO_5[212], GaV_2O_4[213], $Ga_{2.5}V_{2.5}O_{7.33}(OH)_{0.67}$ (or $Ga_{2.5}V_{2.5}O_8$ when dehydrated[214]), and $V_6Ga_2O_{13}$[215] (with no structural data provided apart from the knowledge of its triclinic crystal system). In V_2GaO_5 and $Ga_{2.5}V_{2.5}O_8$, gallium is found in both octahedral and tetrahedral crystallographic sites, while vanadium sites are exclusively octahedral. In the spinel GaV_2O_4, Ga and V accommodate exclusively tetrahedral and octahedral sites, correspondingly. **Fig. 4.7** illustrates the ratios of average radii of V^{x+} and Ga^{3+} species in $V_xGa_yO_z$ oxides, accounting for their coordination environment and weighted by stoichiometric coefficients: $(x\cdot V)/(y\cdot Ga)$. Also plotted is the hypothetical (desired) $Ga_2V^{4+}O_5$ phase, where error bars show the range between all-tetrahedral and all-octahedral coordination of gallium. The points, plotted in a descending order of the normalized ionic ratio of the two cations, suggest that if the size ratio is the defining factor in phase stabilization, the Ga_2VO_5 phase can be stabilized and the synthetic conditions used to prepare V_2GaO_5 might be a reasonable starting point for the preparation of Ga_2VO_5. However, the direct solid-state synthesis did not provide enough thermal energy to react gallium, while other approaches, considering oxidation of Ga/V^{3+} oxide precursors, were accompanied by evaporation of gallium at the temperature used. Using low-temperature techniques such as sol gel to achieve higher reactivity of Al^{3+} and Ga^{3+} at lower temperature might be key to synthesis of A_2VO_5 phases.

4.4. In_2VO_5

The unique vanadium sublattice of $Sc_2VO_{5+\delta}$ is a 3D network, which is unlike the corrugated vanadium sublattice in the In_2VO_5 phase (**Fig. 4.8a**). Its V^{4+} sublattice consists of one-dimensional edge-sharing ribbons (**Fig. 4.8b**) separated from each other by sheets of In^{3+} in the other two directions. Vanadium polyhedra (**Fig. 4.8c**) are distorted with bond lengths ranging from 1.76 to 2.23 Å. The longer bond, initially not considered as relevant[32], is partially responsible for interesting physics of In_2VO_5, including the switch from the net ferromagnetic to net antiferromagnetic exchange at 120 K[33]. Unlike t-$Sc_2VO_{5+\delta}$, vanadium in In_2VO_5 was shown to be

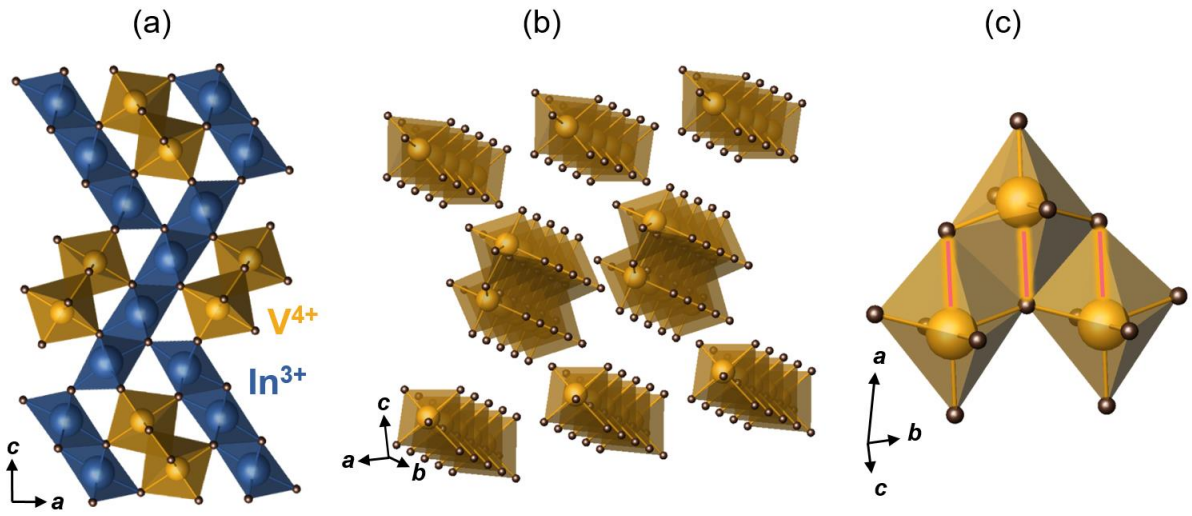

Figure 4.9. In_2VO_5 structure: (a) – polyhedral representation: $[InO_6]^{9-}$ and $[VO_6]^{8-}$ octahedra are shown as blue and yellow; (b) – edge-sharing chains of vanadium-based octahedra; (c) – one fragment of such chain. The longest V-O bonds are highlighted in red.

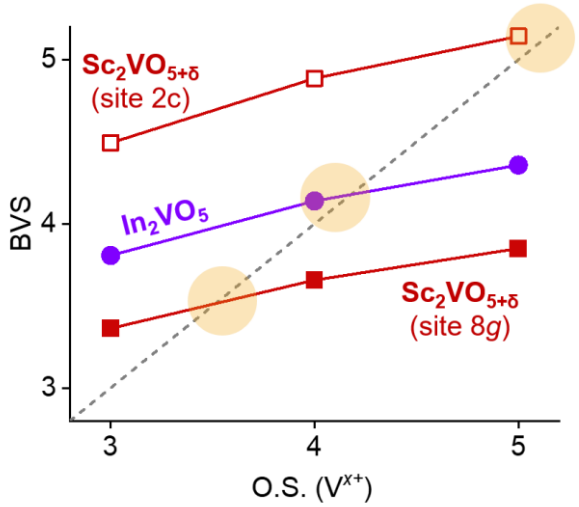

Figure 4.8. BVS plot of In_2VO_5 as compared to t-$Sc_2VO_{5+\delta}$, consistent with tetravalent V^{4+} in In_2VO_5 while mixed V^{3+}-V^{4+} and V^{5+} in sites 8*g* and 2*c* of t-$Sc_2VO_{5+\delta}$.

predominantly tetravalent (d^1) [33,216], which is consistent with BVS from X-ray diffraction data in **Fig. 4.9** (purple line).

4.4.1. $Sc_{2-x}In_xO_5$ solid solutions

In^{3+} cations are situated in two sixfold environments sharing edges with each other and corners with V^{4+}. The octahedral cationic radius of In^{3+} is 0.800 Å, which is only 7% larger than that of octahedral Sc^{3+} and even closer for the 7- and 8-fold coordinated Sc^{3+} in $Sc_2VO_{5+\delta}$. Therefore, from the cation radii alone, a gapless substitutional solid solution $Sc_{2-x}In_xVO_{5+\delta}$ can be anticipated[H]. On the other hand, the two end members of the solid solution are structurally different ($Sc_2VO_{5+\delta}$ being a fluorite superstructure and In_2VO_5 – rather an anti-rutile superstructure with cations and anions swapped), which would not allow a fully miscible solid solution series.

Synthesis of $Sc_{2-x}In_xO_5$ phases with $x = 0.2$ steps was attempted following this equation in static vacuum at 1100 ºC (1 grinding):

$$(1 - {}^{x}/_{2})\, Sc_2O_3 + ({}^{x}/_{2})\, In_2O_3 + VO_2 \rightarrow Sc_{2-x}In_xVO_5. \qquad (4.1)$$

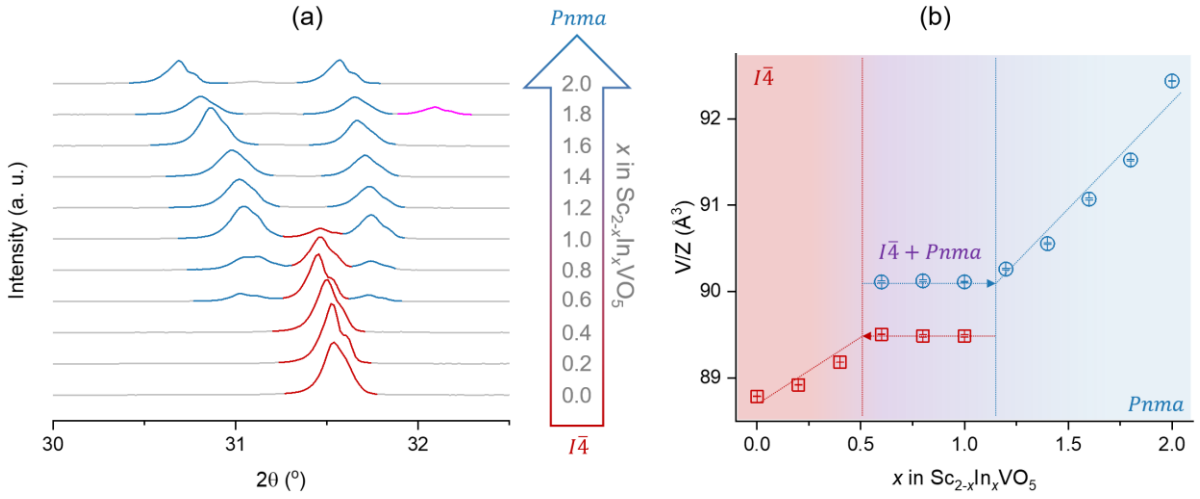

Figure 4.10. The $Sc_{2-x}In_xVO_5$ solid solution: **(**a) – stacked selected fragments of *ex-situ* XRD patterns showing the transition from the Sc_2VO_5-type solid solutions (***I4̄***, red) to In_2VO_5-type solid solutions (***Pnma***, blue) with increasing nominal x (shown on the vertical axis). A two-phase miscibility gap exists in the range from $x = 0.6$ to $x = 1.0$. In pink is the impurity peak; (b) – $Sc_{2-x}In_xVO_5$ phase diagram illustrating the unit formula evolution (from LeBail fitting) with increasing nominal x after ~50 hours of heating with one intermediate grinding. Dotted lines are eye guides. The miscibility gap between two vertical lines is represented by compositions at the borders.

[H] The maximum atomic radii difference of 15% tolerated by solid solutions of substitution is a conventional value adopted from the theory of alloy superstructures[308]

Characteristic fragments of the XRD diffractograms of the products are stacked together in **Fig. 4.10a**. The figure reveals two solid solutions with a miscibility gap:

- From nominal x = 0.0 to x = 0.4, Sc-rich solid solutions of the Sc_2VO_5-type exist. The characteristic (123) peak is highlighted in red.

- From nominal x = 1.2 to x = 2.0, In-rich solid solutions of the In_2VO_5-type exist. The characteristic peaks (203) and (013) are highlighted in blue.

- From x = 0.6 to x = 1.0, both solid solution types are present from co-existence of both red and blue peaks. Another way to illustrate the gap is **Fig. 4.10b** where volume of the unit formula is plotted against the nominal composition. The gap limits are marked with vertical lines, and all

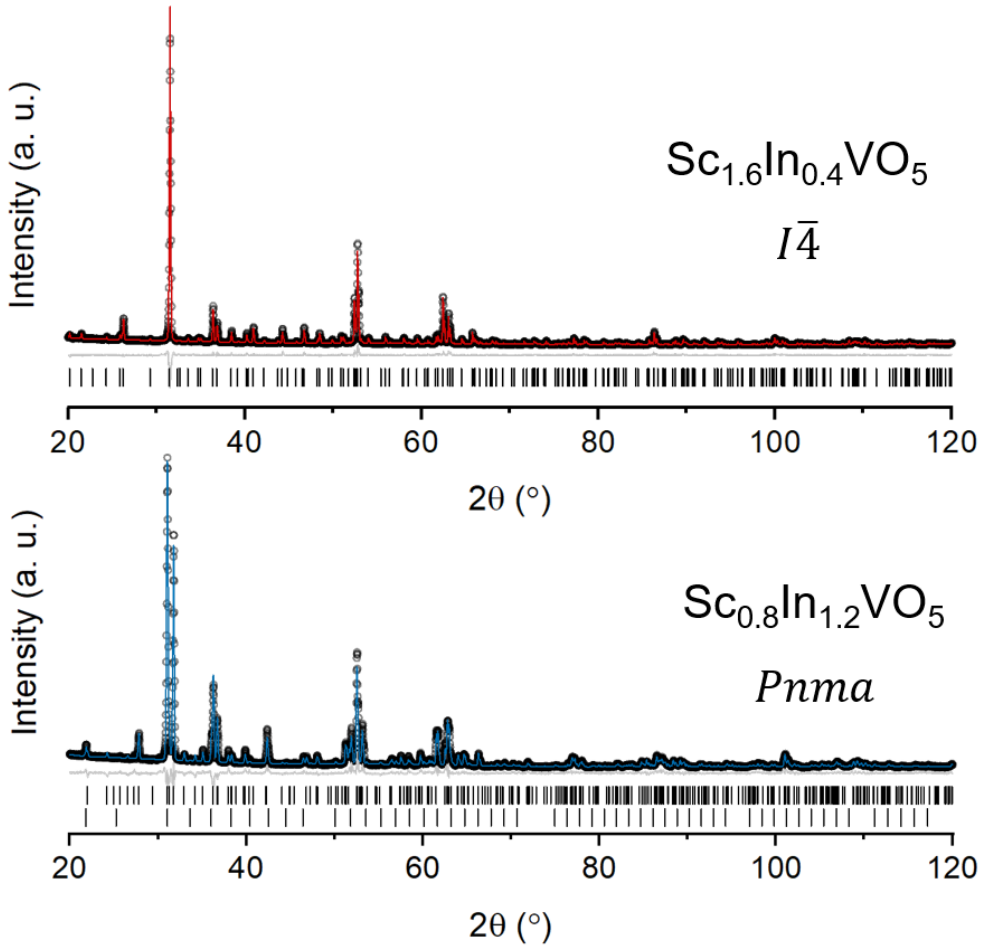

Figure 4.11. Rietveld plots for two solid solutions in the $Sc_{2-x}In_xVO_5$ series: top – with x = 0.4 (t-Sc_2VO_5 type); bottom – with x = 1.2 (In_2VO_5 type; 11 mass % impurity of $InScO_3$ bixbyite). Black – data (Cu-K$\alpha_{1,2}$), red/blue – calculated fit, grey – difference, ticks – Bragg positions.

other lines are guides to the eye. Arrows point at the suggested limits of the solid solutions, as it is expected that the upper (lower) limit of solubility of Sc (In) in the solid solution of the opposite type is reached at the leftmost (rightmost) vertical line. Refined compositions will be published elsewhere, but two preliminary Rietveld refinements against lab XRD data are shown in **Fig. 4.11**. In these refinements, an idealized Sc-V-ordered model was used, and thermal displacement parameters (both cation and anion) as well as oxide occupancies were fixed at values refined for t-$Sc_2VO_{5+\delta}$[31] and In_2VO_5[33]. If enough thermal energy is provided, the A sublattice of t-$Sc_2VO_{5+\delta}$ (top panel) can accommodate 20% of In^{3+}, which translates into an average A site radius of 0.756 Å. Best fit was achieved when In^{3+} occupancy in sites 4*f*, 8*g* #1, and 8*g* #2 was refined to be 9.8(9)%, 22.8(6)%, and 22.4(7)%, respectively. In_2VO_5 structure accommodates up to 30% of Sc^{3+}, i.e. can accommodate an A^{3+} cation with the average radius of 0.784 Å. Assuming a phase-pure sample[I] and no Sc-V mixing in the In_2VO_5-type structure in the bottom panel, the two 4*c* sites of indium contain 58.7(8)% and 21.3(8)% Sc^{3+}. Details of the two fits are given in **Table A-3.1**.

It should be noted that at least in the Sc-rich solid solutions, vanadium is expected to disproportionate akin to the case of pure t-$Sc_2VO_{5+\delta}$. On the other side of the miscibility gap, In-rich solid solutions are expected to have the all-V^{4+} vanadium sublattice. Elucidation of δ in them and its dependence, if any, on the average ionic size of the A^{3+} cation will be done in the future with the help of collected NPD data.

4.5. $Lu_7V_3O_{16}$ as $Lu_{2.1}V_{0.9}O_{4.8}$

The ionic radius of Lu^{3+} (0.861 Å in CN = VI) is larger than that of In^{3+} (0.800 Å) but smaller than that of Yb^{3+} (0.868 Å), both known to form A_2VO_5 phases. The resulting intermediate position of Lu^{3+} raises the question: if the Lu_2VO_5 phase can be obtained, will it crystallize as the In_2VO_5 or Yb_2VO_5 type, or neither? Solid-state synthesis of Lu_2VO_5 was attempted in sealed quartz tubes following this equation:

$$Lu_2O_3 + VO_2 \rightarrow Lu_2VO_5 \qquad (4.2)$$

[I] This is an idealized case. From the refinement and lattice parameter comparison, the sample contained 11 mass % of a bixbyite phase with about 1:1 ratio of Sc:In.

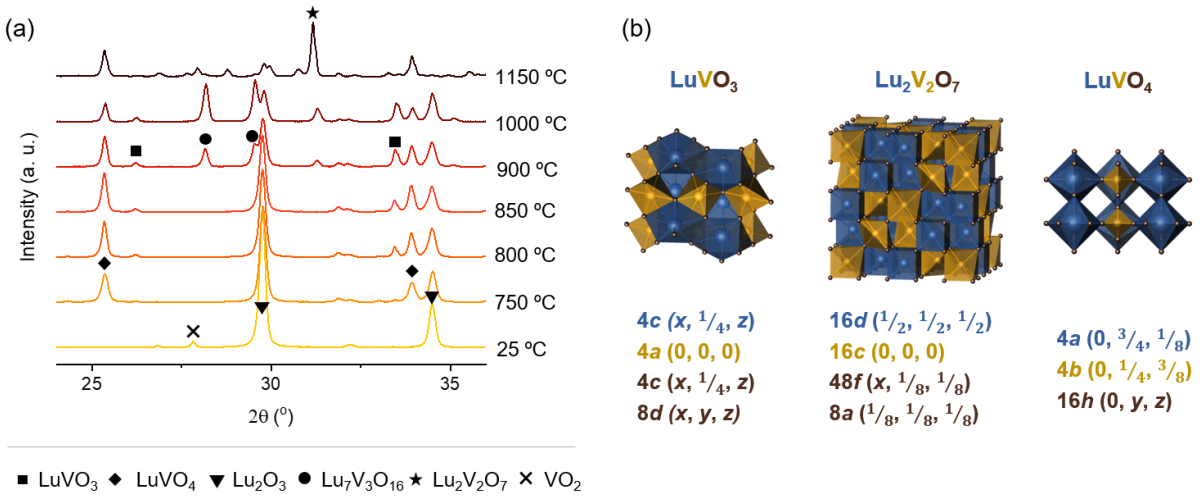

Figure 4.13. Reacting VO_2 and Lu_2O_3 in vacuum: (a) – stack plot of *ex-situ* XRD patterns (Cu-K$\alpha_{1,2}$) tracking the course of the reaction; (b) – structures and atomic site coordinates of well-known stable Lu-bearing phases with V^{3+}, V^{4+}, and V^{5+} encountered in this experiment.

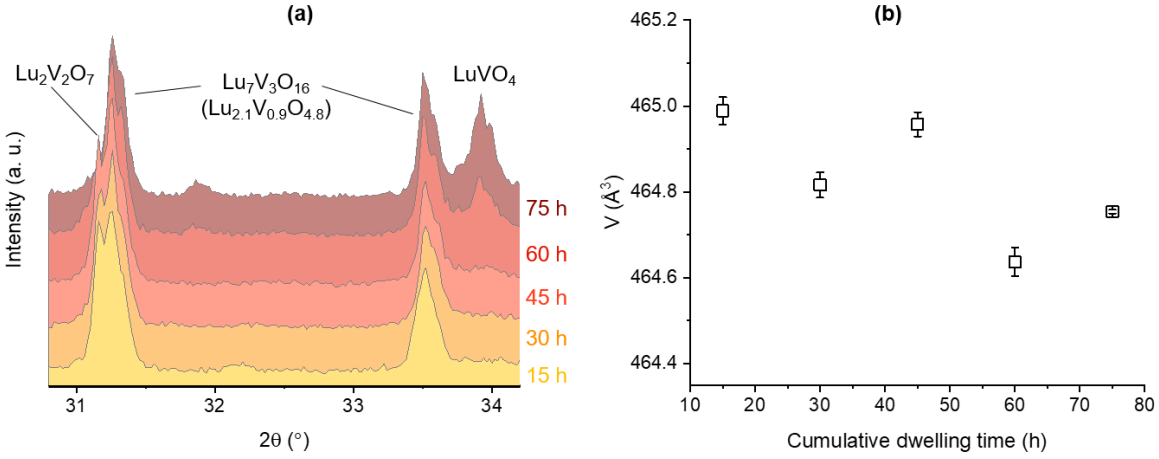

Figure 4.12. Successive heating of the Lu_2O_3+VO_2 mixture at 1200 ºC in static vacuum: (a) – fragment of a stack plot of *ex-situ* XRD patterns (Cu-K$\alpha_{1,2}$) showing major phase $Lu_7V_3O_{16}$ and two impurities – $Lu_2V_2O_7$ disappearing with heating and $LuVO_4$ which took over; (b) – change in the unit cell volume of $Lu_7V_3O_{16}$ with dwelling time.

Products of independent reactions carried out at different temperatures were analyzed with powder XRD, and the resulting patterns are stacked in **Fig. 4.12a**. It is seen that at 750 ºC zircon $LuVO_4$ and perovskite $LuVO_3$ form, marking disproportionation of V^{4+} (VO_2) into V^{5+} and V^{3+}. At higher temperatures, up to 1000 ºC, a phase with mixed 3+/4+ states of vanadium forms, $Lu_7V_3O_{16}$ [217]. This phase was found to co-exist with Lu_2O_3, $Lu_2V_2O_7$, and either $LuVO_3$ or $LuVO_4$

at 1200 ºC[J], but its structure was not solved (it will be, later in the text). At even higher temperature of 1150 ºC, a V^{4+}-containing pyrochlore $Lu_2V_2O_7$ forms instead, which co-exists with $LuVO_4$ and lutetium silicates Lu_2SiO_5, $Lu_2Si_2O_7$ (meaning contamination by the crucible material). At this point $LuVO_3$ was almost absent from the final product, which might be the result of an oxygen leak. Structures of $LuVO_3$ (SG: *Pnma*, #62), $Lu_2V_2O_7$ (SG: $Fd\bar{3}m$, #227), and $LuVO_4$ (SG: $I4_1/amd$, #141) are illustrated in **Fig. 4.12b** together with the list of occupied crystallographic sites defining the structure. Notably pyrochlore is a fluorite superstructure with 12.5% oxide

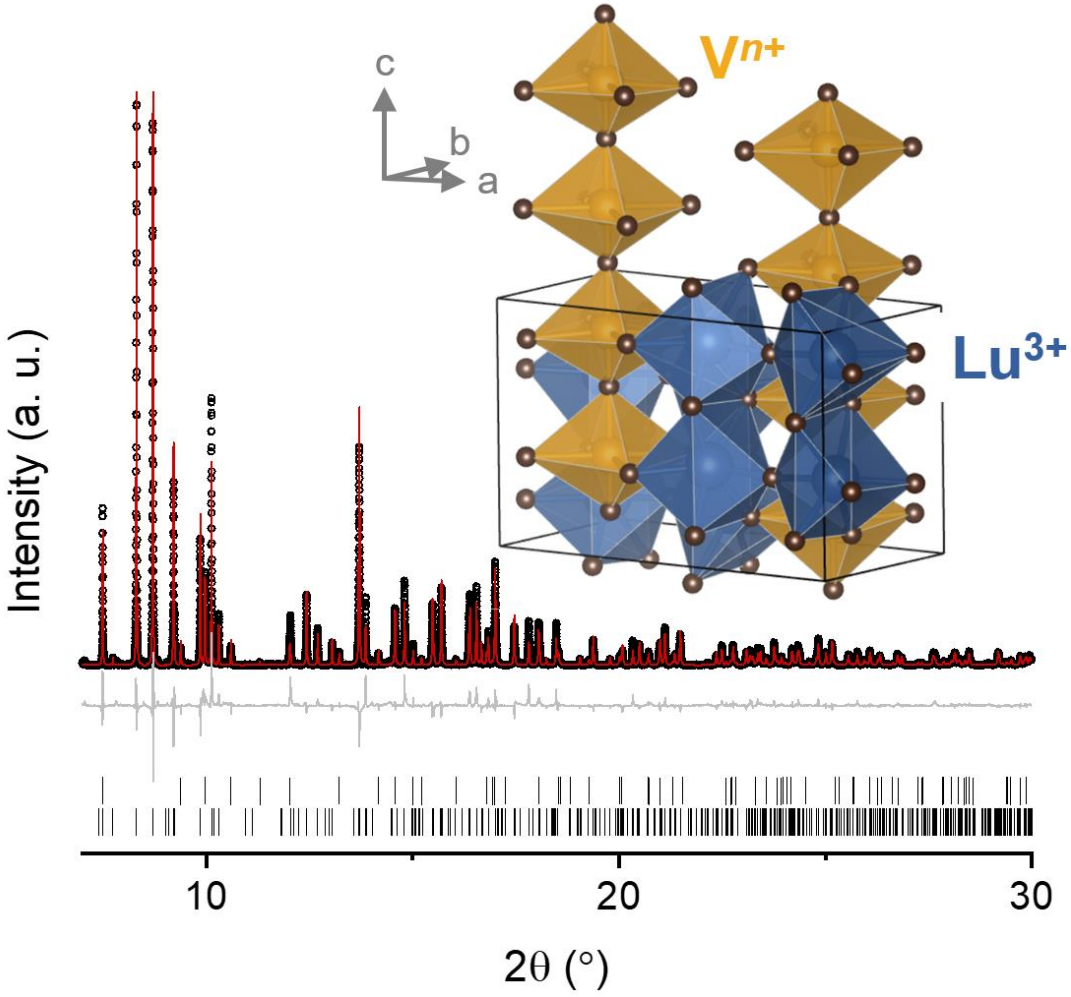

Figure 4.14. Rietveld plot and structure of $Lu_7V_3O_{16}$. Black dots – data (λ = 0.458951 Å), red – calculated fit, grey – difference, ticks – Bragg positions: top – $LuVO_4$ (17 mass %), bottom – $Lu_7V_3O_{16}$, likely non-stoichiometric.

[J] Stoichiometrically and charge-wise it can be represented as a mixture of $LuVO_3$, $Lu_2V_2O_7$, and Lu_2O_3 in the ratio 1:1:2.

vacancies, here competing with an anticipated A_2VO_5 phase with twice the ratio of Sc to V and 16.7% vacancies with respect to the fluorite aristotype.

In a separate experiment, the mixture of Lu_2O_3 and VO_2 was heated for 75 hours at 1200 ºC in a sealed quartz tube with intermediate grindings every 15 hours. As shown in **Fig. 4.13a**, the result was a mixture of $Lu_7V_3O_{16}$-type phase (~80%), $Lu_2V_2O_7$, and minute impurities of Lu_2O_3 (gone on reheating), $LuVO_3$ (same), and $LuVO_4$ (increased on heating). As seen from this emphasized region of the XRD patterns, peaks of $Lu_2V_2O_7$ slowly disappeared with heating, but at the expense of accumulation of a small amount of $LuVO_4$. Rietveld refinement of the product after the 5th heating is presented in **Fig. 4.14** together with the crystal structure of the major phase $Lu_7V_3O_{16}$ (SG: *Pccn*, #56), hitherto unpublished. The refinement model was taken from the structure solution of isostructural $Yb_7V_3O_{16}$ confirmed with a multihistogram XRD+NPD refinement. A comment on this structure solution will be given in ***Section 4.5.1.*** Details of the refinement and structure are given in **Table A-3.2** and include more precise oxide positions and atomic displacement parameters than could be obtained for $Lu_7V_3O_{16}$.

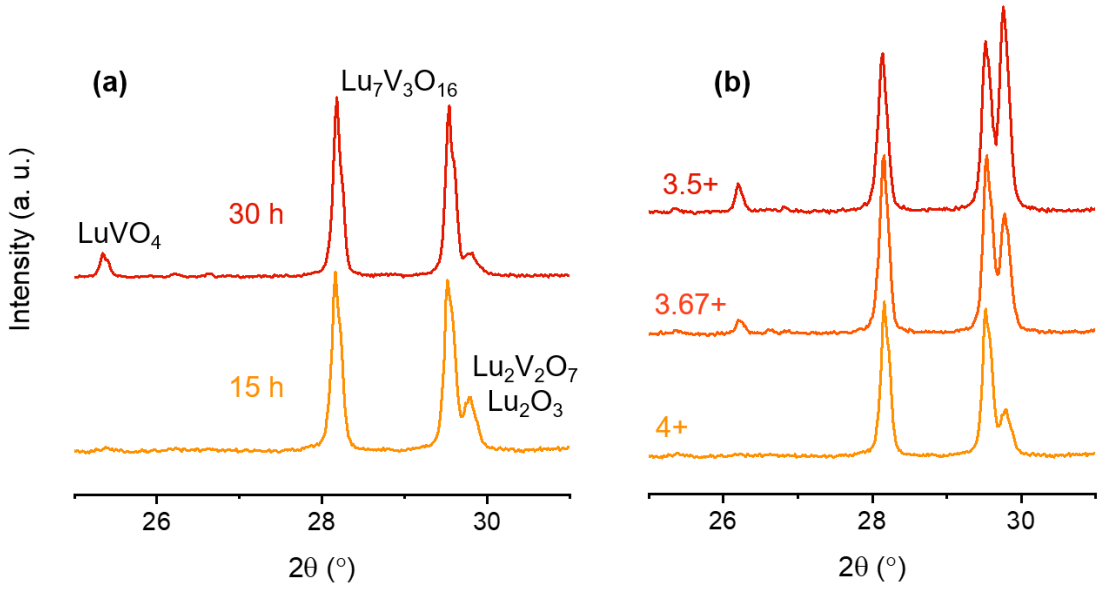

Figure 4.15. Synthesis of $Lu_7V_3O_{16}$: (a) – XRD patterns for two heatings of the mixture 3.5 Lu_2O_3+ 3VO_2; (b) – results of three different heatings of mixtures 3.5 Lu_2O_3 + 3 VO_2 (bottom, same as bottom of panel *a*), 3.5 Lu_2O_3 + 2 VO_2 + 0.5 V_2O_3 (middle), and 3.5 Lu_2O_3 + 1.5 VO_2 + 0.75 V_2O_3 (top). Numbers are nominal oxidation states of vanadium. Radiation – Cu-K$\alpha_{1,2}$.

Interestingly, a range of oxidation states was reported in $Lu_7V_3O_{16}$[217], which suggests the possibility of the topotactic redox in the vanadium site(-s) in order to probe the limits of the oxygen concentration tolerated by the structure. Volume oscillations in **Fig. 4.13b**, superimposed onto the overall unit cell volume decrease, are consistent with this conjecture.

To tune the oxidation state of vanadium in the as-synthesized sample or to observe its threshold, a stoichiometric phase $Lu_7V_3O_{16}$ was attempted from (1) Lu_2O_3 and VO_2 and (2) Lu_2O_3 and a mixture of VO_2 and V_2O_3. The average oxidation states of vanadium in the starting mixtures were 4+ (VO_2), 3.67+ ($2VO_2$: 0.5 V_2O_3), and 3.5+ (VO_2 + 0.5 V_2O_3). The mixture with VO_2 in the starting material yielded ~ 80 mass % of target phase together with 10 mass % of Lu_2O_3 and 7 mass % of $Lu_2V_2O_7$ (**Fig. 4.15a**, orange). Reheating resulted in disappearance of the pyrochlore, depletion of Lu_2O_3, and accumulation of 10 mass % of $LuVO_4$ (red), likely due to slow permeation of air through quartz[218]. More of $LuVO_4$ and Lu_2O_3 and less of $Lu_7V_3O_{16}$ were found in the products when the nominal concentration of V^{3+} in the starting materials mixture was larger (**Fig. 4.15b**). It suggests that reduction of V^{4+} in $Lu_7V_3O_{16}$ to reported $V^{3.67+}$ or even lower might occur via expelling oxygen into the low-oxygen environment of the evacuated tube during synthesis, i.e. there is no need to reduce it from the start via adding V_2O_3. Still, independent reduction as well as oxidation experiments were carried out in flowing 5% H_2 (bal. Ar) and static

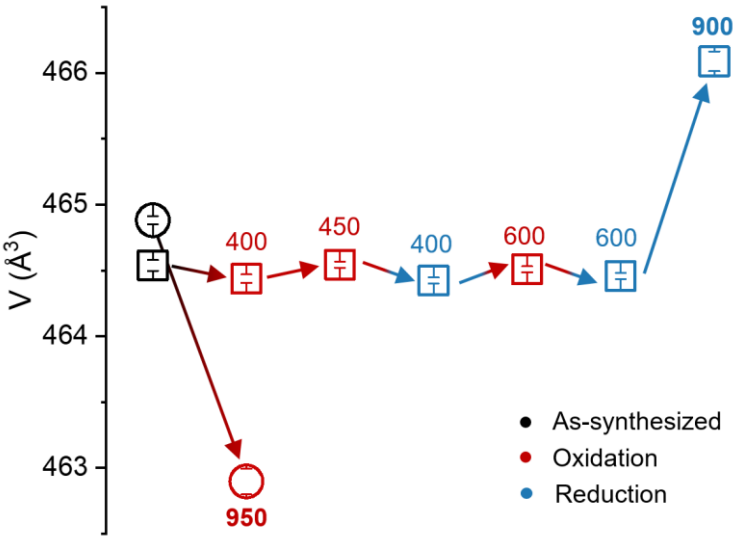

Figure 4.16. Unit cell volume of $Lu_7V_3O_{16}$ during oxidation and reduction at different temperatures (temperature values, ºC, are given above the markers). Squares (□) and circles (○) mark two different experiments. Arrows connect the precursor and the product.

air. **Fig. 4.16** illustrated the change in unit cell volume of two independent samples during several heatings. Composition of the starting materials were: (□) – 80 mass % $Lu_7V_3O_{16}$, 20% $LuVO_4$ (target compound – Lu_2VO_5, four heatings); (○) – 73 % $Lu_7V_3O_{16}$, 14% Lu_2O_3, 6.5% $LuVO_3$ and $Lu_2V_2O_7$ each (target compound – $Lu_7V_3O_{16}$, one heating). In the first experiment (□), volume oscillated around the same value, and visibly increased only at 900 ºC. Further reduction at 1000 ºC led to full reduction of $Lu_7V_3O_{16}$ to $LuVO_3$ (+ some Lu_2O_3). In the second experiment (○), which was only a single heating with oxidation, the volume decreased at 950 ºC. Both the decrease on oxidation and increase on reduction amounted to the relative change in the unit cell volume under 0.5%, which is sufficient to see the change[K] and conclude that topotactic redox is possible around this temperature. A better choice of unit formula is therefore $Lu_7V_3O_{16+\delta}$ or $Lu_{2.1}V_{0.9}O_{4.8+\delta}$ in the A_2BO_5 notation (with a different δ).

This experiment shows that the as-synthesized sample of $Lu_{2.1}V_{0.9}O_{4.8+\delta}$ has an intermediate oxidation state of vanadium, i.e. neither exclusively V^{3+} nor V^{4+}. Further topotactic redox experiments are needed to investigate the threshold of oxidation states (the range of δ), preferably with *in-situ* NPD and XANES.

4.5.1. Structure of $A_7V_3O_{16}$ (A = Lu, Yb, Tm)

Structural details of $Lu_7V_3O_{16+\delta}$ have not been reported in literature, and neither have the two other members of this family – with A = Yb and Tm. Structure of $Lu_7V_3O_{16+\delta}$ was adopted from the results of structure solution of a purer, isostructural sample of $Yb_7V_3O_{16+\delta}$ (to be described in the ensuing section) using synchrotron powder XRD data in Topas software[137]. Several candidates for indexing were found, the best being space groups *I222* (#23) and *Pccn* (#56), both orthorhombic. The best fit was achieved with the *Pccn* space group.

The structure $Yb_7V_3O_{16}$ was solved using synchrotron powder XRD data and then refined against both these XRD data and NPD data from four NOMAD banks, with equal weighting. Rietveld plots are given in **Fig. 4.17** and structural details can be found in **Table A-3.2**. The idealized structure (without cation mixing and oxygen vacancies) is shown in **Fig. 4.18a**. Vanadium sublattice (site

[K] Expansion on reduction suggests that the increase of the ionic radius from V^{4+} to V^{3+} prevails over the compression of the unit cell due to release of oxygen.

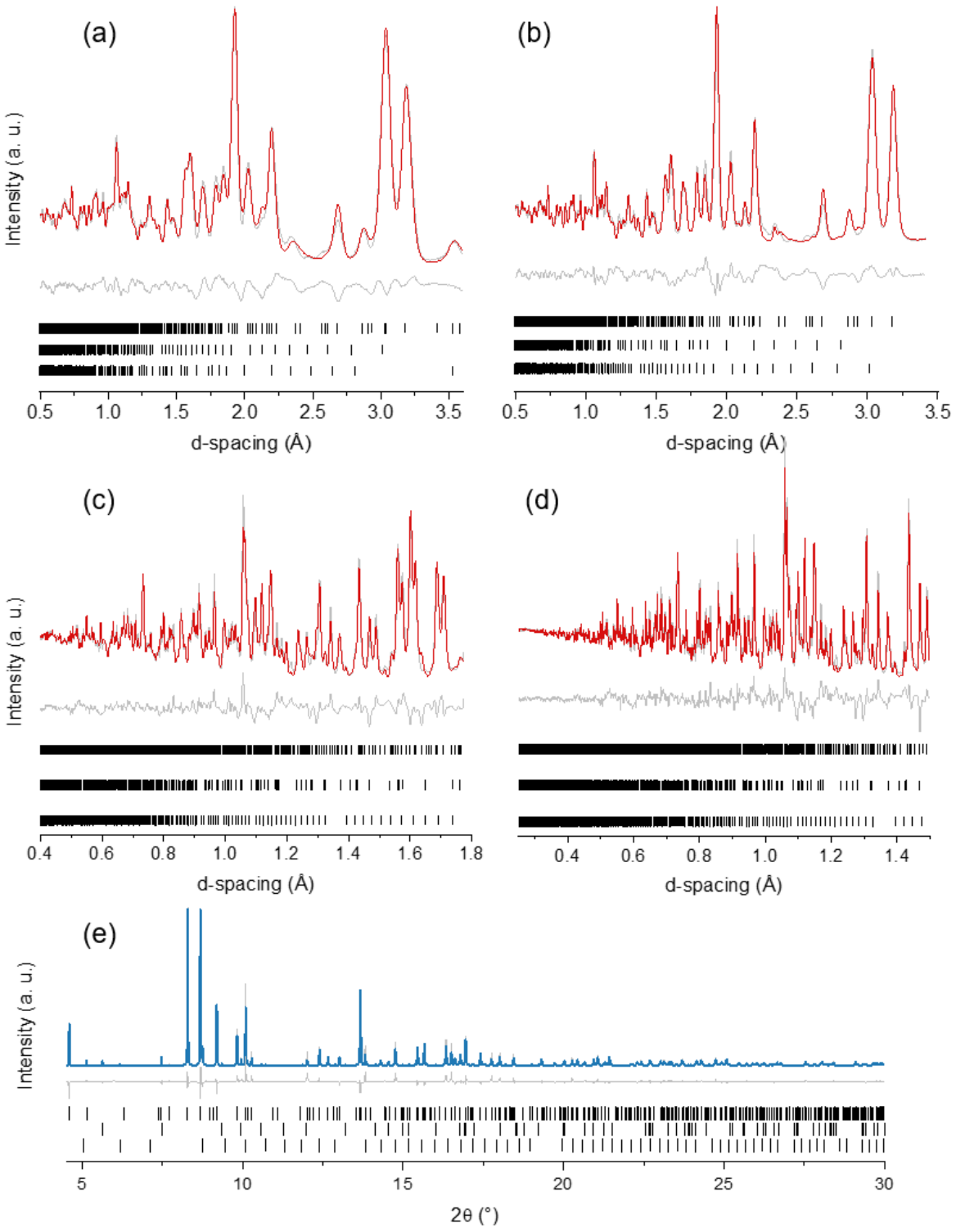

Figure 4.17. Rietveld refinement of $Yb_7V_3O_{16}$ structure against NPD (red, NOMAD) and synchrotron powder XRD (blue, 11-BM, λ = 0.458951 Å) data. Grey – data and difference, red/blue – calculated fits, ticks – Bragg positions: top – $Yb_7V_3O_{16}$ (91 mass %), middle – $YbVO_4$ (2.8 %), bottom – Yb_2O_3 (6.2 %).

4*c*) consists of corner-sharing octahedra stacked along the *c* axis. The sublattice resembles the corrugated -V-O-V- chains in In_2VO_5, but more stretched out. These chains have several peculiarities:

- One apical V-O bond is short at 1.7 Å, i.e. of the length of the V^{5+}-O or V^{4+}-O vanadyl bond[219]. The bond *trans* to it is longer – 1.88 Å, but not as long as equatorial V-O bonds (≥ 2.2 Å);
- The occupancy of the apical oxygen ion positions (brown) is ~73% as denoted in **Fig 4.18b**, where oxides in different crystallographic sites are shown with different colors;
- Atomic displacement of vanadium ≈ 2.2 $Å^2$.

These points suggest that what appears as $[VO_6]^{x+}$ octahedra might be $[VO_5]^{x+}$ polyhedra with lower CN than VI, such as square pyramids. Large atomic displacement of vanadium might be interpreted as a shift of vanadium toward the base of the square pyramid enabled by the absence of one of the O1 oxides. Apical oxides themselves are mobile, with $B_{iso} \approx 1.6$ $Å^2$. However, so are equatorial O4 oxides (purple) with $B_{iso} \approx 1.0$ $Å^2$ and 61% occupancy. It suggests more than one way of local lowering of coordination. On the axis of vanadium CN evolution, it places $A_7V_3O_{16}$ phases between In_2VO_5 with ribbons of $[VO_6]^{8-}$ octahedra and Yb_2VO_5 (Y_2VO_5, Dy_2VO_5) phases with isolated $[VO_4]^{4-}$ tetrahedra.

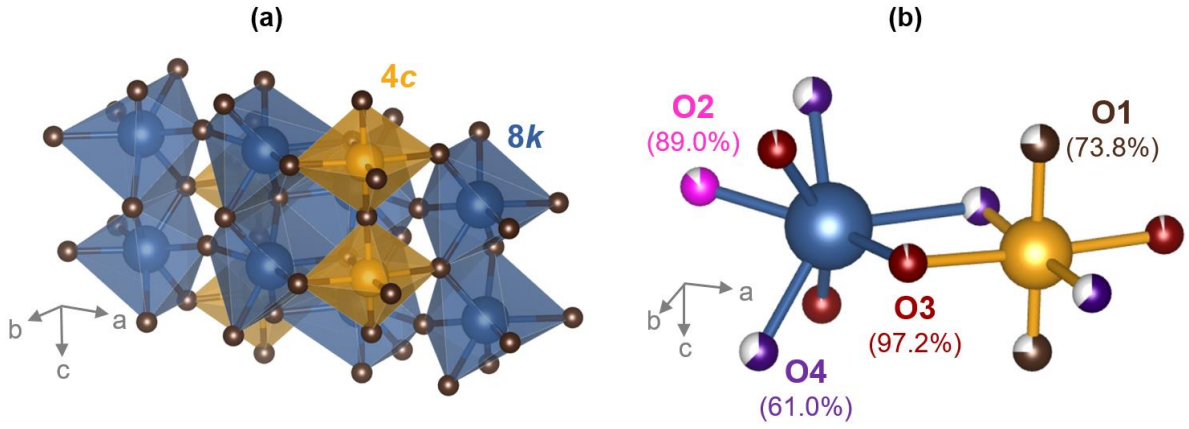

Figure 4.18. Crystal structure of $Yb_7V_3O_{16}$: (a) – polyhedral representation of the unit cell: blue – 8*k* site (89% Yb, 11% V), yellow – 4*c* site (33% Yb, 67% V), brown – anion sites; (b) – ball-and-stick model focusing on the 4 anion sites, shown in different colors. Percentages are oxide occupancies in corresponding anion sites (white = vacant).

Oxygen concentration was found to be 16 per unit formula of as-synthesized $Yb_7V_3O_{16}$ the way it was reported by Kitayama *et al.*[220]. Notably, the presence of oxide vacancies and the intermediate oxidation state of vanadium (3.67+ on average) suggest the possibility of topotactic filling of the vacancies consistent with redox of $Lu_7V_3O_{16}$ in **Fig. 4.15**.

The ytterbium sublattice (site 8*k*) consists of corner- and edge-sharing sevenfold-coordinated capped octahedra which share corners and edges with the vanadium chains. Interestingly, the B site accommodates about 33% Yb to allow for a ~7:3 ratio of A:B cations instead of 8:4. Mixing of a larger cation (Yb, 33%) with the smaller cation (V, 67%) in the B site agrees with the large displacement parameter of the B site (bullet 3).

Interestingly, in light of the redox activity of ytterbium, the oxidation state of vanadium might deviate from the average 3.67+. **Fig. 4.19** shows the BVS plot where the 4*c* site composition is consistent with both 33% Yb^{3+}/67% V^{4+} (red marker) and 33%Yb^{2+}/67% V^{5+} (blue). In the 8*k* site, due to only a small concentration (11%) of vanadium the BVS are predominantly determined by the oxidation state of ytterbium. Purple marker with 1:1 ratio of Yb^{2+}:Yb^{3+} is one way to avoid over- or underbonding in this site. However, it is important to not over-interpret the BVS analysis for this structure, especially since oxygen vacancies are not accounted for. Yb and V XANES data

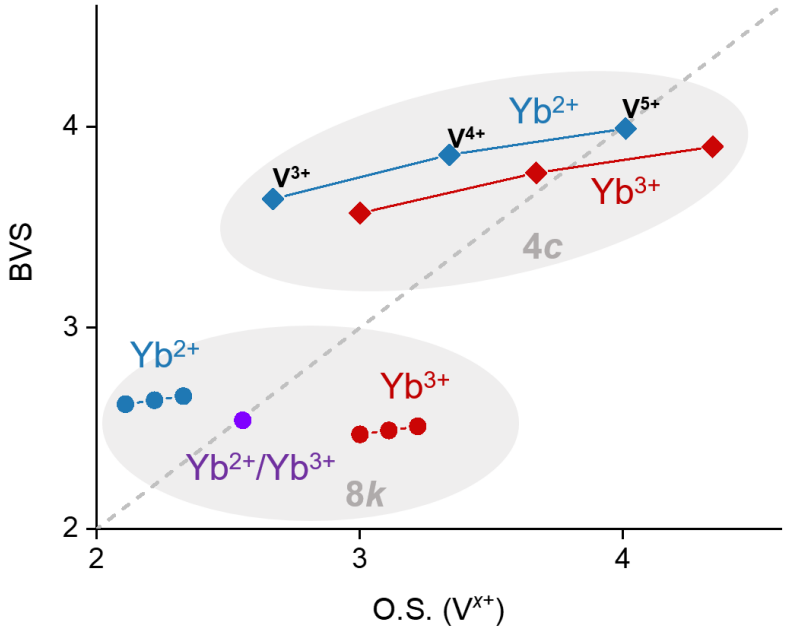

Figure 4.19. BVS plot for Yb/V-O bond distances in $Yb_7V_3O_{16}$, probing many possible oxidation states of both Yb and V: blue – Yb^{2+}, red – Yb^{3+}, purple – mixture of both (with V^{3+}, as an example). ***Note:*** cation mixing is taken into account, but oxide vacancies are not.

would be helpful for a detailed analysis of oxidation states; for now, the phase will be considered as Yb^{3+}-$V^{3.67+}$ phase for simplicity.

4.6. A_2VO_5 phases with A = Y, Yb, Dy

The two structures adopted by the four known hydrothermally obtained A_2VO_5 phases are presented in **Fig. 4.20a** (A = Y, Yb, Dy) and **4.20b** (A = Dy), see Kimani *et al.*[34] The first three phases are isostructural to the triplite (SG: *C2/c*). The lattice consists of 6- and 7-coordinated [AO_n] polyhedra comprising an edge-sharing A sublattice and isolated tetrahedral vanadiums, attached to A^{3+} cations via corners. The second phase is isostructural to the modification of V_3O_5 (SG: *P2₁/c*) that is likely nonstoichiometric from BVS analysis in **Fig. 4.1b**. The lattice of this Dy_2VO_5 polymorph consists of edge-sharing 7- and 8-fold [DyO_n] polyhedra (or 7- and 9-fold, if 2.97 Å bonds are counted) and isolated tetrahedral vanadium, now sharing both corners and edges with dysprosium ions. One interesting feature reported for all four phases is the tetravalent vanadium tetrahedrally coordinated to oxygen ($^{[4]}V^{4+}$). Importantly, the conclusion that tetrahedral vanadium can be tetravalent was substantiated by the existence of two other such cases (Ba_2VO_4[189] and β-Sr_2VO_4[190]) whose structures, however, were refined from limited-quality data. A conjecture can be made that larger distortion of the vanadium polyhedra observed in these phases can accommodate a cation such as V^{4+}, which is larger than V^{5+} usually found in tetrahedra. For

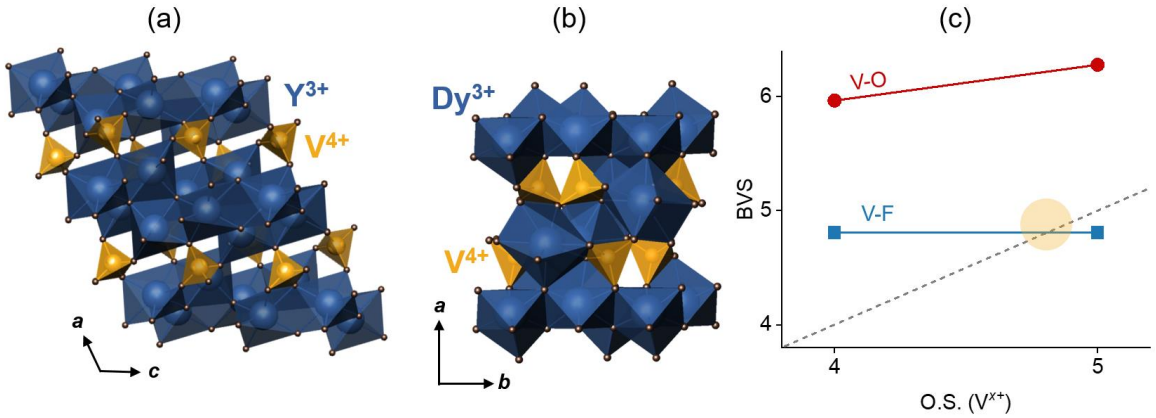

Figure 4.20. Hydrothermal phases A_2VO_5: (a) – structure of Y_2VO_5 (*C2/c*), similar to that of Yb_2VO_5 and Dy_2VO_5-1; (b) – structure of Dy_2VO_5-2 (*P2₁/c*); (c) – BVS plot for V-O and V-F bond distances based on V-O distances in Y_2VO_5 (overlaps with the BVS plot for Dy_2VO_5) to question the oxidation state and/or nearest neighbors of vanadium.

example, bond length (Δ_{BL}) and bond angle distortions (Δ_{BA}) in these phases can be compared against other relevant $A^{3+}{}_2VO_5$ phases: V_3O_5 (*P2/c*), t-$Sc_2VO_{5+\delta}$, and In_2VO_5 (**Fig. 4.21**). It is seen that tetrahedral vanadium in A_2VO_5 phases with A = Y, Yb, and Dy is more distorted than tetrahedral $[V^{5+}O_4]^{3-}$ units in t-$Sc_2VO_{5+\delta}$ (blue markers), so that the Δ_{BA} values are in between Δ_{BA} of $[V^{5+}O_4]^{3-}$ units in t-$Sc_2VO_{5+\delta}$ and distortions of octahedral units in the first three phases $[V^{4+}O_6]^{8-}$ (red markers). However, despite large distortion, the propensity of the tetrahedral site to accommodate a V^{4+} ion, if any, is not immediately obvious. **Fig. 4.20c** is the BVS plot for Y_2VO_5, where the red line illustrates BVS for V^{4+}-O and V^{5+}-O bonds. Despite the fact that BVS is not a precise method, the deviation of the red line from the y=x line (dashed grey line) is remarkable. A better agreement can be achieved if vanadium was pentavalent and/or connected to F^- anions (blue line) originating from the KF mineralizer. However, KF was only used in the synthesis of primitive Dy_2VO_5 ($P2_1c$), while the three *C*-centered phases ($C2/c$) were synthesized with K_2CO_3. A carbonate anion from K_2CO_3 is unlikely to be incorporated in the structure and be unnoticed in single crystal XRD data analysis. Even an extra $0.5 \cdot O^{2-}$ per formula, that would convert $Y_2V^{4+}O_5$ into $Y_2V^{5+}O_{5.5}$ and minimize the V-O overbonding, would be visible and thus is unlikely to be present. Overall, reported rare tetrahedral coordination of V^{4+} ions in these phases requires additional corroboration.

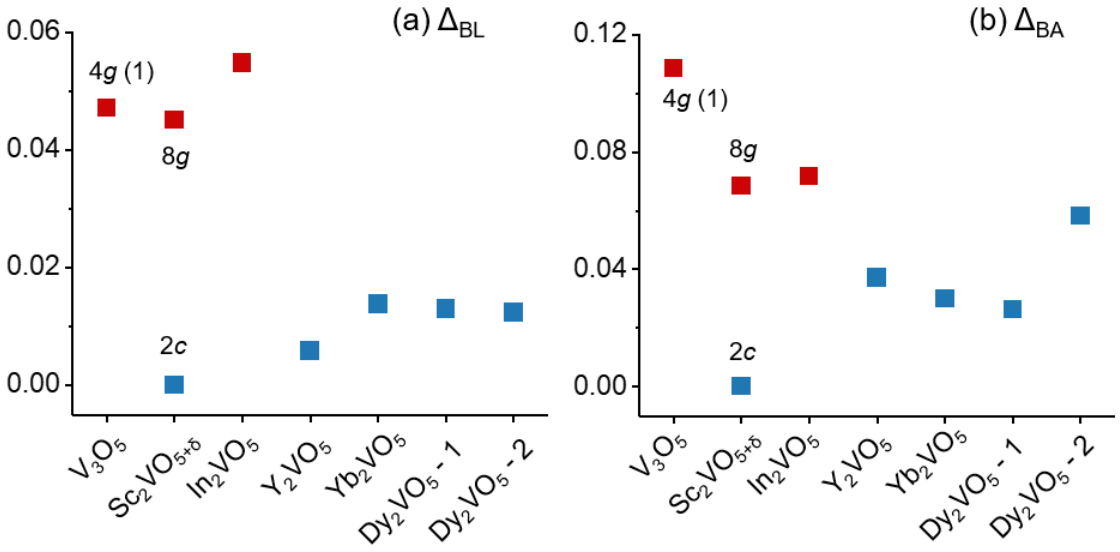

Figure 4.21. Relative distortions of V-O bond lengths (a) and O-V-O bond angles (b) in reported ordered A_2VO_5 phases. Red and blue markers are distortions within vanadium-based octahedra and tetrahedra, respectively.

Our own attempts to synthesize Y_2VO_5 and Yb_2VO_5 by a solid state route resulted in formation of stable zircons and perovskites, as well as more exotic $Yb_7V^{3.67+}{}_3O_{16}$[220] (addressed in ***Section 4.5.1***) or $Y_8V^{5+}{}_2O_{17}$[221] phases. The synthesis was conducted in a sealed evacuated quartz tube at 1200 ºC for 45 h with two intermittent grindings.

For A = Yb^{3+}, the final product was a mixture of $Yb_7V_3O_{16}$, $YbVO_4$, $Yb_2V_2O_7$, and Yb_2O_3 (yellow pattern in **Fig. 4.22a**). Similar to the case with A = Lu, the pyrochlore phase (and Yb_2O_3 which might be an unreacted starting material) disappeared over the course of three heatings, while concentrations of $Yb_7V_3O_{16}$ and $YbVO_4$ increased. Interestingly, during heating the concentration of zircon YVO_4 increased faster than that of $LuVO_4$ in the respective case. Although the difference in the dynamics must be affected by the quality of sample grinding and the used sample mass, the radius of the A^{3+} cations might be a contributor. For A = Y, the product of the first heating (yellow pattern in **Fig. 4.22b**) was identified as a mixture of YVO_3 (perovskite), YVO_4 (zircon), and "low-T" $Y_8V^{(5+)}{}_2O_{17}$ [221] – a triclinic phase[222] not reported in ICSD. The pyrochlore phase was not found – its synthesis requires geological pressure[223]. This case (A = Y) favored much faster disproportionation of vanadium into $YV^{3+}O_3$ and $Y_8V^{5+}{}_2O_{17}$ than in the ytterbium case which produced the intermediate $Yb_7V^{3.67+}{}_3O_{16}$, stable $Yb_2V^{4+}{}_2O_7$, and virtually no $YbVO_3$: $r(Y^{3+})_{VI}$ =

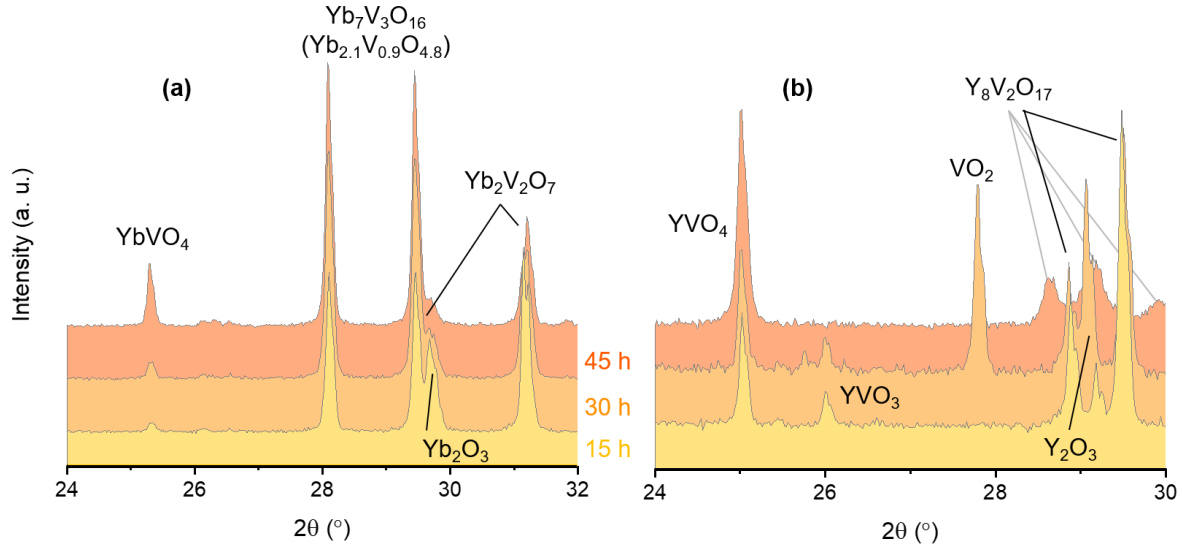

Figure 4.22. Fragments of stack-plots of *ex-situ* XRD patterns: (a) – following three successive heatings of the mixture Yb_2O_3 + VO_2 resulting in the major phase $Yb_7V_3O_{16}$; (b) – same for Y_2O_3 + VO_2, resulting in major phase $Y_8V_2O_{17}$ which decomposes into starting materials and then forms another polymorph upon further heating.

0.900 Å *vs* $r(Yb^{3+})_{VI}$ = 0.868 Å. Moreover, the zircon phase YVO_4 became one of the major phases in this reaction already after the first heating, as opposed to the case of Lu and Yb where several successive heatings were required. In other words, the V^{5+} product accumulated faster when a larger A^{3+} cation (Y^{3+}) was introduced. It might point at the propensity of larger A^{3+} cations to co-exist with the smaller V^{x+} cation such as V^{5+} (also see the case of A = Ho[224]), and not only in orthovanadate YVO_4 but also as a part of $Y_8V^{5+}{}_2O_{17}$. The light-orange pattern corresponds to the reheated mixture of the three Y vanadates. As seen from the figure, the $Y_8V_2O_{17}$ phase partially decomposed into Y_2O_3 and VO_2 with no intermediate products, unlike the ytterbium mixture. The structure of the $Y_8V_2O_{17}$ phase has not been solved and is of lower priority in this work, since it is not based on V^{4+} and has a 4:1 stoichiometric ratio of cations. Further heating (dark-orange) resulted in the accumulation of even more YVO_4 and a minor phase of the "high-T" modification of $Y_8V_2O_{17}$[221]. Interestingly, no Y_2O_3 or VO_2 were found after 45 h.

Looking just at Lu, Yb, and Y vanadates above, it cannot be concluded that a larger cation radius (Y > Yb, Lu) alone requires a larger A:V stoichiometric ratio. For instance, recently reported $La_7V^{(5+)}{}_3O_{18}$[225] with r(La) > r(Y) and pentavalent vanadium has a 7:3 ratio of cations, which contradicts this assumption. Dependence of stoichiometry on temperature alone is similarly inconclusive, since high temperature favors the 8:2 ratio over 7:3 across the Yb vanadates[222] while 8:2 over 10:2 in the Er and Gd vanadates[226]. Several parameters might be in play. However, it can be said that V^{5+} species seem to comfortably coexist with larger rare earths (Er, Y, Gd, La) in this series at this temperature, while lower oxidation states can be stabilized around slightly smaller A^{3+} cations (Lu), and both were found for Yb and Tm[227,228]. See **Fig. A-3.1** and **Table A-3.4** for details of $Tm_7V_3O_{16}$.

4.7. Sb_2VO_5 and Bi_2VO_5

A separate group of A_2VO_5-type phases, with A being lone pair bearing cations, includes Sb_2VO_5 and Bi_2VO_5, predominantly reported with ordered cation sublattices. Bismuth has almost the same octahedral radius (1.030 Å) as lanthanum (1.032 Å), but its vanadates form different structures. At least three Bi_2VO_5 modifications exist (α, β, γ)[54,69,70] which can be seen as reduced (and occasionally Bi-deficient[229]) variants of the corresponding BIMEVOX ceramics $Bi_2VO_{5.5}$, including an orthorhombic Aurivillius-type $Bi_4V_2O_{10}$[71], and a cubic defect fluorite[83] which,

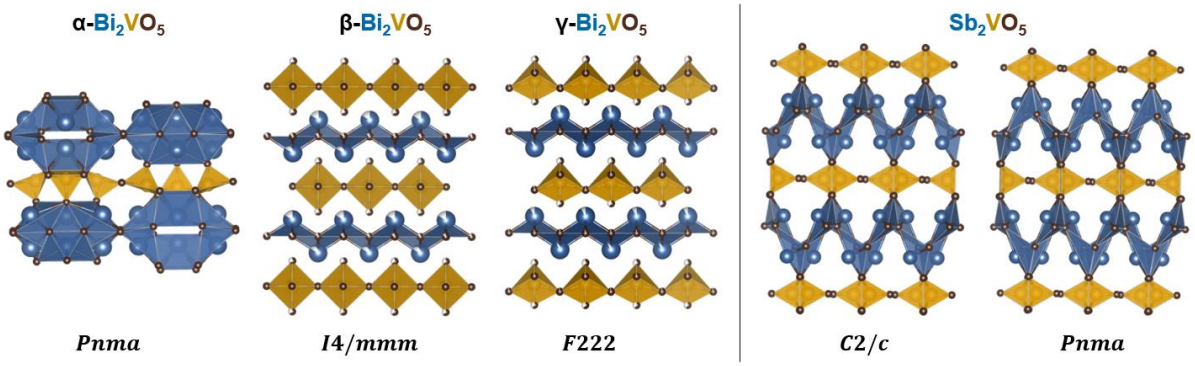

Figure 4.23. Polyhedral representation of reported ordered bismuth (a) and antimony (b) vanadate structures belonging to the A_2VO_5 family.

however, lacks crystallographic description. **Fig. 4.23** (left) shows three polymorphs of Bi_2VO_5, from lower-T alpha phase to higher-T gamma phase, all of which are layered and/or have a network of tunnels accommodating the lone pair of bismuth. Oxidized bismuth vanadates mostly group into two families with $BiVO_4$[230,231,232]and $Bi_4V_2O_{11}$[233,234,234] ($Bi_2VO_{5.5}$) stoichiometry. The reduced analogue – $BiVO_3$[235] exists only at high pressure, unlike any other AVO_3 phase mentioned so far. The lone electron pair of bismuth is a variable that hampers its direct comparison to other A_2VO_5 structures. However, the same tunnel structure makes its vanadates promising for fast ion conduction[236]. The octahedral radius of antimony (0.76 Å) is in between those of scandium (0.745 Å) and indium (0.800 Å). Despite this proximity of cationic radii, Sb_2VO_5 was found to form structures different from those of t-$Sc_2VO_{5+\delta}$ and In_2VO_5, driven by the necessity to accommodate the lone pair associated with Sb^{3+}. Sb_2VO_5 has two modifications[55,56], both ordered (see view down the *c* axis for both in **Fig. 4.23**, right). Similar to Bi_2VO_5, both Sb_2VO_5 phases consist of well separated A and B layers which form a network of tunnels to accommodate the lone pair of antimony. Also, as in the case of bismuth, antimony vanadates with V^{5+} exist under ambient conditions (e.g. see Aurivillius-derived triclinic $Sb_4V_2O_{11}$ [237] and a rutile $SbVO_4$ [203]), but vanadates with V^{3+} have not been found.

As said above, due to the stereochemically active lone pair on the A^{3+} cations, cation-ordered Bi_2VO_5 and Sb_2VO_5 phases cannot be directly compared against other A_2VO_5 phases with more spherical A^{3+} cations. In fact, their whole phase diagrams Bi-V-O and Sb-V-O differ from the rest of the A-V-O systems, obscuring any predictions and trends.

4.8. Conclusion

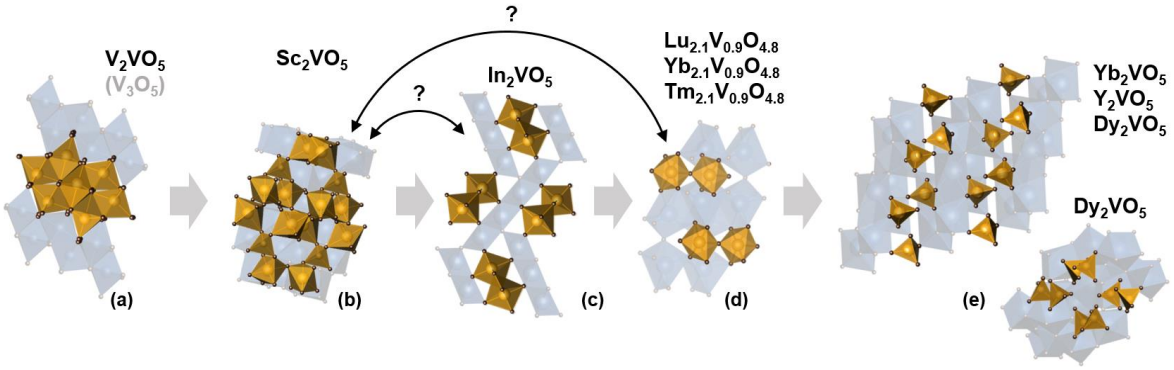

Figure 4.24. Ordered A_2VO_5 phases arranged in ascending order of the A^{3+} radius in the same coordination with oxygen. Emphasized are vanadium sublattices. Arrow suggests swapping some structures to achieve a more sensible arrangement (see next figure) where the phases are listed in the ascending order of the *real* A^{3+} radius.

Table 4.1. Characteristics of the ***vanadium*** sublattice of the A_2VO_5 phases with various A^{3+} cations.

A^{3+} cation	V	Sc	In	Lu/Yb/Tm	Yb/Y/Dy
Connectivity	Face, edge	Corner	Corner, edge	Corner	Isolated
Dimensionality	1D	3D	1D	1D	0D
CN	VI	IV, VI	VI (V + I)	V or VI	IV

The diagram in **Fig. 4.24** arranges the reported A_2VO_5 structures in ascending order of the ionic radius of A^{3+} in the same coordination (e.g. octahedral), excluding structures with lone-pair-bearing cations. As is seen in the figure, the vanadium sublattice evolves. **Table 4.1** lists several features of the vanadium sublattice, such as coordination number (the count of nearest oxide neighbors), connectivity (related to the number of shared oxides between neighboring polyhedra), and dimensionality (in how many directions the vanadium sublattice is spreading, if any). In this table only the connectivity can be rationalized: as the size of the A^{3+} increases, vanadium ions in the B sublattice move away, while dimensionality and coordination number do not seem to change monotonously with the increase of A^{3+} size. What further complicates the analysis is that the four hydrothermal phases might be of different stoichiometry and/or composition. It is then suggested

that the structures should be arranged in ascending order of ***real*** radii of A^{3+}, the way it is now proposed in **Fig. 4.21**, rather than in the ascending order of the ***octahedral*** radii of A^{3+}, so that:

- In_2VO_5 comes before $Sc_2VO_{5+\delta}$, since $r_{VI}(In^{3+}) < r_{VII\text{-}VIII}(Sc^{3+})$;
- $Sc_2VO_{5+\delta}$ splits between B = $V^{3+\ldots4+}$ (octahedral site 8*g*, below) and B = V^{5+} (tetrahedral site 2*c*, above);
- Hydrothermally obtained oxo-vanadates A_2VO_5 (A = Y, Yb, Dy) follow the 2*c* tetrahedral V^{5+} of $Sc_2VO_{5+\delta}$, while phases with A = Lu, Yb, Tm belong after the 8*g* octahedral site of $Sc_2VO_{5+\delta}$.
- It is suggested to introduce an additional axis of V coordination number. In this light, oxygen-deficient phases $A_7V_3O_{16}$ ($A_{2.1}V_{0.9}O_{4.8}$) take an intermediate place between octahedral units of t-$Sc_2VO_{5+\delta}$ and tetrahedral units of t-$Sc_2VO_{5+\delta}$ and A_2VO_5 (A = Yb, Y, Dy) phases.

This approach makes all three trends in the table monotonic. Like before, the change from face- and edge-sharing to isolated vanadium polyhedra is a consequence of moving vanadium ions apart in the presence of larger A^{3+} cations. The decrease in CN of vanadium with increasing A^{3+} size might be a consequence of more efficient packing, whereby larger A^{3+} cations coexist with smaller

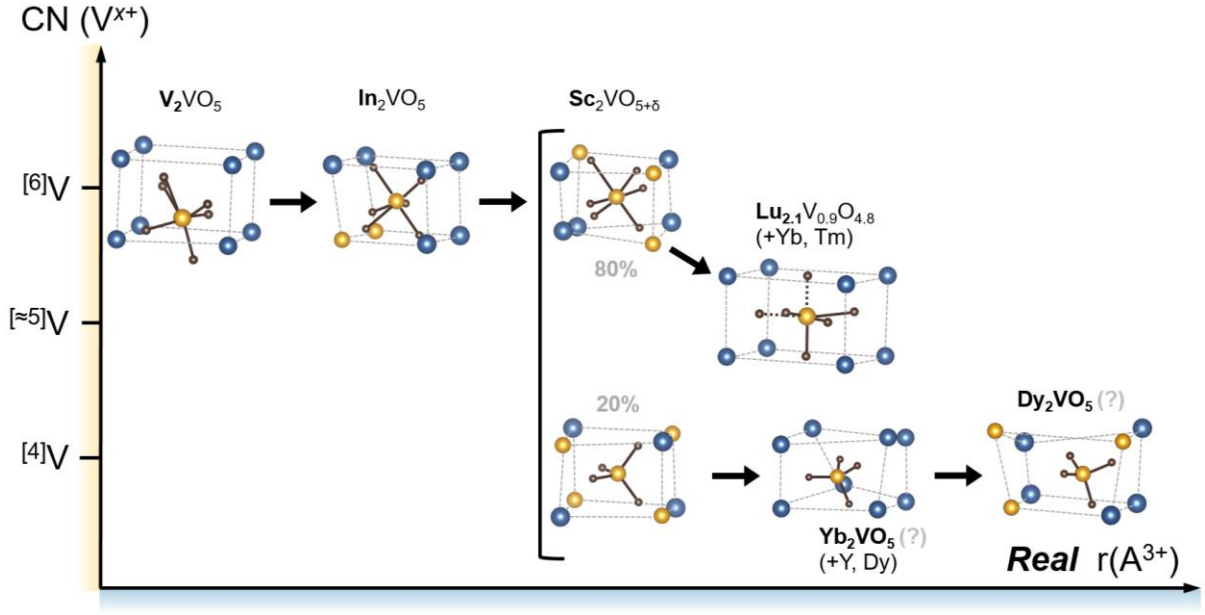

Figure 4.25. Fragments of A_2VO_5 structures arranged in ascending order of the real A^{3+} radius (along the x axis) with an additional axis (y) reflecting the coordination number of vanadium. Atomic cages shown are built around the vanadium center (yellow V^{x+}) surrounded by blue A^{3+} and brown O^{2-} and have the same number of next-nearest neighbors for the ease of visual comparison. Question marks refer to the remaining uncertainty on whether hydrothermal phases have the reported oxygen concentration.

B cations (especially in 2:1 ratio), especially tetrahedral. In other words, at a certain point the A^{3+} cation adopts a larger than CN = 6 coordination number, which then requires the V^{4+} cation to adopt a smaller than CN = 6 coordination number. As for dimensionality: (1) A_2VO_5 phases start off with 1D ribbons of vanadium; (2) $Sc_2VO_{5+\delta}$ with slightly larger Sc^{3+} is a tipping point where strong repulsion between highly charged V^{5+} species drives a new lattice which happens to be three-dimensional; (3a) finally, even larger A^{3+} cations (series with Y, Yb, Dy) disconnect individual vanadium ions within this 3D lattice, more so the smaller tetrahedral vanadium, while (3b) vanadium chains in phases with A = Lu, Yb, and Tm stretch out more than in In_2VO_5.

While all of these trends can be rationalized (*a posteriori*), they cannot be predicted (*a priori*) by looking at the periodic table, which is the main shortcoming of **Fig. 4.24**. It is an interesting feature of the A_2VO_5 family. To have a better grip on predictions:

- Other structure-affecting factors should be considered, beyond the radius of the A^{3+} cation and related geometric parameters, such as electronegativities[238].
- More A_2VO_5 phases need to be discovered.

To confirm the place of hydrothermal phases (A = Yb, Y, Dy ×2) with tetrahedral vanadium among other A_2VO_5 phases, analysis of the oxidation state of vanadium is necessary. Single crystal XRD analysis used by Kimani at al.[34] is unlikely to miss extra oxide ions or any alternative anions consistent with commonly tetrahedral V^{5+} (aside from a fluoride which was present in the synthesis of Dy_2VO_5). Moreover, hydrothermal conditions might enable stabilization of rare species such as $^{[4]}V^{4+}$. However, as it was mentioned in ***Section 4.6***, the rare instances of tetrahedral coordination of V^{4+} ions in oxides have been reported in the two first-of-a-kind vanadates[189,190] analyzed with diffraction data of limited resolution. The other few examples are minute impurities in the tetrahedral sublattice of silicon[194,239] or aluminum[193]. It is further exacerbated by (1) the absence of tetrahedral V^{4+} from reviews of bonding in vanadate minerals[219] and hydrothermally obtained VO_n oxides[240], (2) shorter V-O bond distances (A = Y, Dy) than in $ScVO_4$ and even reference phases Ba_2VO_4/β-Sr_2VO_5[34], and related (3) severe overbonding of vanadium from BVS calculations (**Fig. 4.20c**). It was decided to exclude the four hydrothermal phases from the discussion of other A_2BO_5-type phases in ***Chapter 7***.

CHAPTER 5

$Sc_2B^{4+}O_5$ and B-doped $Sc_2VO_{5+\delta}$ phases

5.1. Connectivities in the B sublattice of Sc_2BO_5 phases

A_2VO_5 phases considered in the previous chapter can be seen as derivatives of t-$Sc_2VO_{5+\delta}$ in which Sc^{3+} cations were substituted with alternative A^{3+} cations. With this in mind, connectivity trends in the B-metal sublattice and the degree of A-B cation-ordering were shown as dependent on the ionic radius of the A^{3+} cation. The current chapter continues the same logic but instead considers replacing V^{x+} in in the vanadium sublattice, while still focusing on the same connectivities and the A-B ordering. The chapter further considers partial doping of the B-sublattice and discusses the role of dopants' radii, redox-activity, and charges on phase stability, cation ordering, and oxygen concentration.

Fig. 5.1 shows a series of Sc_2BO_5-type phases sorted in ascending order of the B^{4+} cation radii, from 0.26 Å for tetrahedral Si^{4+} to 0.69 Å for octahedral Sn^{4+}. The phases shown are Sc_2SiO_5 ($C2/c$, #15)[47], Sc_2GeO_5 ($C2/c$, #15)[22], $Sc_2VO_{5+\delta}$ (discussed above and shown as stoichiometric, for convenience), Sc_2TiO_5 ($Cmcm$, #63)[12], and Sc_2SnO_5 ($P4_2/mnm$)[241].

Sc_2SiO_5[47] was reported as a monoclinic structure obtained by a sol-gel method. In the structure, Si occupies isolated distorted tetrahedra, while scandium is located in corner- and edge-sharing

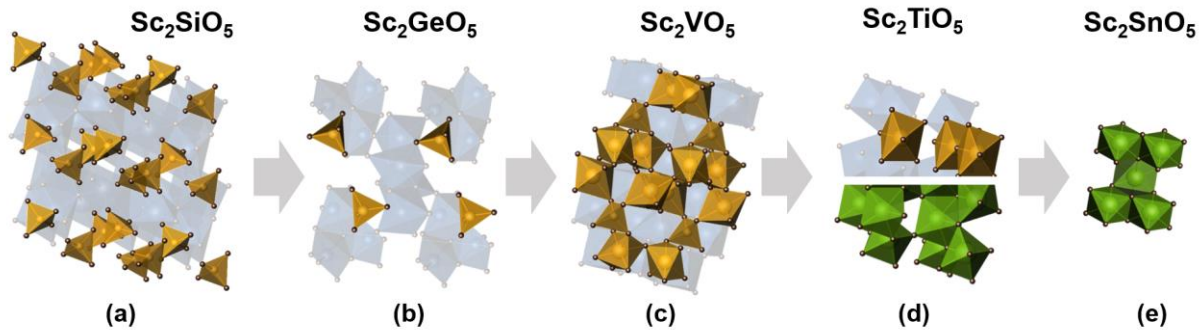

Figure 5.1. Reported A_2BO_5 structures arranged in ascending order of the B^{4+} radius. Emphasized are B sublattices (yellow). In vastly cation-disordered Sc_2TiO_5 and fully cation-disordered Sc_2SnO_5, disorder of Sc^{3+} (blue, faded) and B^{4+} cations is shown in green.

octahedra. BVS calculations with R_0 = 1.624 Å[179] for silicon produced a value of +4.1 which is very close to the expected valence sum of +4. Monoclinic Sc_2GeO_5 was obtained hydrothermally at 500 ºC[22] and was observed in our experiments at 1100 ºC in static vacuum as a competing phase during preparation of Ge-doped $Sc_2VO_{5+\delta}$. In the structure, Ge^{4+} occupies two isolated tetrahedral sites, while larger Sc^{3+} occupies corner-sharing and edge-sharing octahedra, similar to Sc_2SiO_5. In $Sc_2VO_{5+\delta}$, which is also a member of this series, the V^{x+} cations reside in corner-sharing octahedra and tetrahedra in reduced (octahedral) or oxidized (in tetrahedra) state. About 10% of vanadium is mixed with scandium, meaning that the structure is predominantly cation-ordered[31]. In orthorhombic Sc_2TiO_5[12], both cationic sites accommodate both A and B cation, with the A site (in the A_2BO_5 notation) almost fully disordered and the B site mostly populated with A cations, to be discussed below. Similar to Sc_2GeO_5, this structure was found as a competing phase when preparing Ti-doped $Sc_2VO_{5+\delta}$. Finally, hydrothermally obtained tetragonal Sc_2SnO_5[241] (not attempted in this work) has only one cation site which forms an edge-sharing octahedral network. Cation sites are shown in green in **Fig. 5.1**, implying a mixture of the blue A-sublattice and the yellow B-sublattice. This phase was not found as an impurity in the corresponding solid-state synthesis of Sn-doped $Sc_2VO_{5+\delta}$; instead, its competitor $Sc_4Sn_3O_{12}$ was identified.

The extent of site mixing increases from Sc_2SiO_5 to Sc_2SnO_5 in the Sc_2BO_5 series and can be explained with the increasing radius of the B^{4+} cation from 0.26 Å for Si^{4+}_{IV} (or 0.40 Å in CN = VI to compare the octahedral radii) to 0.69 Å for Sn^{4+}_{VI}, i.e. toward the size of scandium (0.745 Å). Notably, the size of the B cation can explain the change of polyhedral connectivity of the B sublattice from isolated in the silicate and the germanate to corner sharing in the vanadate, but cannot explain the isolated octahedral chains in the B sublattice of the titanate.

In this light, remarks are needed on Sc_2GeO_5 and Sc_2TiO_5. If longer Ge-O bonds (up to 2.9 Å) in the germanate are counted, Ge-centered polyhedra in Sc_2GeO_5 adopt fivefold and sixfold coordination instead of fourfold, now sharing corners and edges to form one-dimensional slabs rather than being isolated. **Fig. 5.2** compares BVS for tetrahedral Ge^{4+} in both sites (solid squares) with expanded coordination (solid pentagon and hexagon). For the site 4*e* (blue), the BVS agreement improves only marginally, as both markers are very close to the dotted reference line, slightly more so for the sixfold site. Similarly, site 8*f* (red) is not improved much, but in this case both markers are far from the reference line. A much better agreement may be achieved if 30% of Sc is mixed into the 8*f* site (open pentagon), but only if the size difference between Sc^{3+} and Ge^{4+}

(CN = V) of 33% can be tolerated (radii were extrapolated for Sc_V and interpolated for Ge_V from other known radii reported by Shannon *et al.*[103]). For comparison, a similar radii difference between V and Sc in the octahedral 8*g* site of $Sc_2VO_{5+\delta}$ is ~18% (smaller than Sc-Ge) which results in only ~9% of overall Sc-V cation mixing (larger than Sc-Ge). This lack of mixing in $Sc_2VO_{5+\delta}$ despite the closer proximity of cation radii can probably be explained with the existence of pentavalent vanadium in the tetrahedral 2*c* site, which favors cation ordering. Even if 30% site mixing is ambitious, *some* degree of mixing can be expected in Sc_2GeO_5, which not only leads to more reasonable BVS but also makes this phase a bridge connecting Sc_2SiO_5 with isolated tetrahedra and phases with larger B^{4+} cations and a more connected B sublattice.

Fig. 5.3 is a BVS plot for Sc_2TiO_5. It shows cases of having Ti^{3+}, Ti^{4+}, and mixed Ti^{4+}-Sc^{3+} composition of both 8*f* (green and purple) and 4*c* (red and blue) cation sites. Encircled are reported values of $3Sc^{3+}$:$2Ti^{4+}$ (8*f*) and $4Sc^{3+}$:Ti^{4+} (4*c*), found similarly through BVS calculations. This is important in understanding why the 8*f* site highlighted in **Fig. 5.1** – the richest in Ti^{4+} and thus treated as the B-sublattice – seemingly breaks the trend of increasing connectivities throughout the Sc_2BO_5 series. It is because a sizable degree of site mixing exists in Sc_2TiO_5, rendering each of

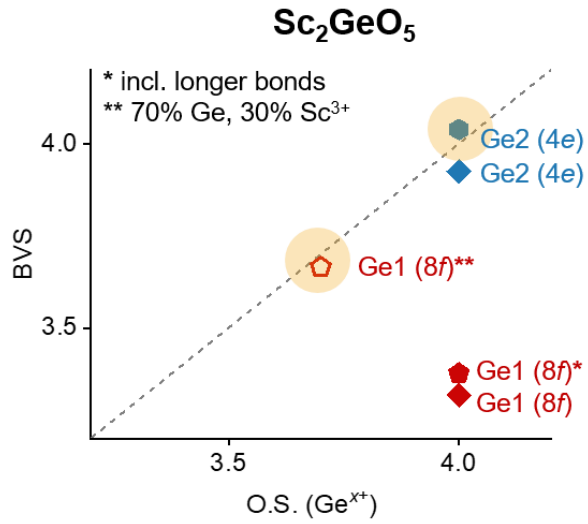

Figure 5.2. BVS plot of Sc_2GeO_5 suggesting that site Ge-1 (8*f*) is mixed with 30% Sc^{3+}. To satisfy cation size requirements, longer Ge-O distances should be accounted for. Doing it in both Ge sites improves BVS.

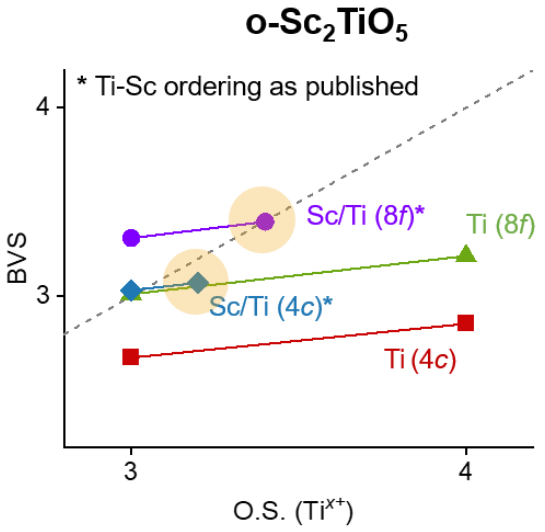

Figure 5.3. BVS plot for Sc_2TiO_5: green and red lines correspond to the two cation sites if populated only with Ti, purple and blue lines correspond to the same sites if Ti and Sc are mixed. Circles show the reported degree of site mixing.

the cation sites partly a B-site and thus making the B-sublattice corner- and edge-shared rather than 2D ribbons, this now continues the trend of connectivities.

Revised connectivities in Sc_2TiO_5 and Sc_2GeO_5 and flexibility of sizes and coordinations of vanadium in $Sc_2VO_{5+\delta}$ complete the gradual trends in the Sc_2BO_5 series. In particular:

(1) tetrahedral coordination of the B sublattice expands to octahedral, through an intermediate double coordination in the vanadate;

(2) isolated B atoms grow into an edge-sharing network in the stannate trough intermediate corner-sharing in the vanadate;

(3) the degree of the A-B site ordering decreases from full order in the silicate to full disorder in the stannate;

(4) the symmetry of the crystal system increases from monoclinic to orthorhombic and tetragonal. All of these are expected when the ionic radius of the B cation increases and approaches that of the A cation. The evolution of the B sublattice in this series thus resembles **Fig. 4.25**, where mostly similar trends were observed upon the decrease of the A^{3+} cation size. Interestingly, in both cases, $Sc_2VO_{5+\delta}$ was an outlier with its two types of B coordination and three oxidation states of B present at once, which renders this structure exotic.

5.2. Typical phases competing with $A_2B^{4+}O_5$: $A_2B_2O_7$ and $A_4B_3O_{12}$

Trivalent Sc and tetravalent B cations are known to form not only ordered or partially ordered oxides from the family A_2BO_5, but also $A_2B_2O_7$ and $A_4B_3O_{12}$ among some others. This becomes important when preparing B-doped $Sc_2VO_{5+\delta}$ phases (next section). An exhaustive A-B-O phase diagram based on ICSD and SciFinder entries is given in **Fig. A-5.1**, while a few relevant phases are selected for **Fig. 5.4**. It illustrates the temperature ranges used to synthesize ordered (top 3 rows) and disordered (bottom 3 rows) phases of all three compositions (A_2BO_5, $A_2B_2O_7$, $A_4B_3O_{12}$) with B cations ranging from small Si (small blue spheres) to larger Zr (large red spheres). The overlap of the temperature ranges is significant, but it can be said that A_2BO_5 phases of various symmetries[12, 22, 82,47,241] were obtained at slightly lower temperatures overall. Also, they contain smaller B cations on average and sometimes require hydrothermal conditions to be stabilized (B = Ge, Sn). At higher temperatures they compete with rhombohedral allendeites $Sc_4B_3O_{12}$ ($R\bar{3}$, #148)[241,242,243,244,245,246,247] or $Sc_2B_2O_7$ phases such as thortveitites ($C2/m$, #12) with smaller B

cations[128,248] and allendeite-related phases or pyrochlores ($Fd\bar{3}m$, #227) with larger B cations[249,250,251,252,253]. Allendeite $Sc_4B_3O_{12}$ phases are partially cation-ordered and fully anion-vacancy-ordered. Cation ordering in $Sc_2B_2O_7$ phases depends on the ratio of ionic radii of the A and B cations, while the anion sublattice is always ordered. Of particular interest is ubiquitous titanium for which, unlike other Sc-B-O phases[L], all three stoichiometries above can be stabilized as fully disordered Sc-Ti-O phases[81,127,254,249]. In contrast, the ambient Sc-V-O diagram with the average oxidation state of vanadium about 4+ is represented only by the polymorphs of $Sc_2VO_{5+\delta}$. **Fig. A-5.2** shows the global instability index (GII) calculated for reported and predicted Sc_2BO_5, $Sc_2B_2O_7$, and $Sc_4B_3O_{12}$ ordered phases with B = V and Ti. In the GII plot, all phases but high-pressure $Sc_2V_2O_7$ are correctly expected to be stable at ambient conditions, interestingly including the yet unknown allendeite $Sc_4V_3O_{12}$. This structure can be expected to form; however, so far only the overoxidized $ScV^{5+}O_4$ or over-reduced $Sc_2V^{3+}O_{4.5}$ phases were found. It illustrates why in the reactions described in the ensuing sections, no other vanadium phases will compete with the target tetragonal defect fluorite superstructure.

It should be noted that observing the formation of the ordered $A_4B_3O_{12}/A_2B_2O_7$ phases at higher temperature than the formation of A_2BO_5 phases is not the same as to claim that higher temperature

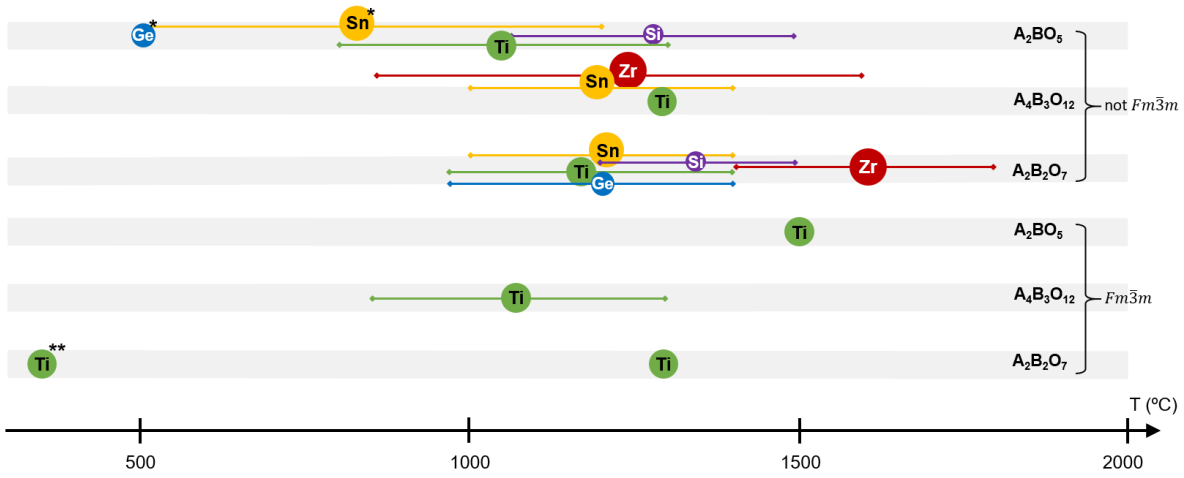

Figure 5.4. Temperatures or temperature ranges within which the reported Sc_2BO_5, $Sc_2B_2O_7$, and $Sc_4B_3O_{12}$ phases were synthesized. Elements are B^{4+} cations. Asterisks denote hydrothermal synthesis (*) as opposed to solid-state (default) and metastability of the product (**).

[L] Disordered cubic $Sc_4Zr_3O_{12}$ can be obtained by irradiation of its ordered variant with Ne^+ particles[246].

favors formation or is required for the formation of $A_4B_3O_{12}/A_2B_2O_7$ phases. Diffusion of material across the grain boundary (affected by grinding of starting materials) is very likely and perhaps the differences in ionic radii of cations affect phase formation more directly. However, it can be speculated that in case of comparable thermodynamic stability and grain sizes of all three families of phases, the ordering temperature of a fully disordered fluorite would be higher (lower) for the structure with the lowest (highest) concentration of ordered vacancies, such as the $A_2B_2O_7$ (A_2BO_5) stoichiometry.

5.3. Looking at phase competition with finer steps: doped series $Sc_2V_{1-x}B_xO_{5+\delta}$

Substitution of vanadium in the $Sc_2VO_{5+\delta}$ template serves several interconnected reasons, including:

- Investigation of the range of concentrations of the dopant (hence cation size and charge) tolerated by the structure. It can answer the questions: (a) what drives cation preferences for certain coordination during phase formation? (b) what is the relation between the nature (size, charge, etc.) of the dopant and its proclivity for forming a pure phase of the desired symmetry?
- Probing the threshold of the oxygen concentration introduced into or removed from the structure on doping.

When doping an ionic oxide, matching the size and charge of the dopant and the host is a good starting point. In the case of t-$Sc_2VO_{5+\delta}$, several cations were chosen to match the size and the charge of V^{4+} (or V^{3+}) in the 8*g* site. They were also compared with V^{5+} populating the 2*c* site under the approximation that a cation closer to $V^{4+}{}_{VI}$ than to $V^{5+}{}_{IV}$ in size and charge would rather replace the former. Building an analogy with functional groups in organic chemistry, preferred coordination or coordination of cations in starting materials might be yet another factor in solid-state reactions. However, coordination heavily overlaps with the charge and size, i.e. with the two factors that are already considered.

5.3.1. $Sc_2V_{1-x}B_xO_{5+\delta}$ phases with redox-inactive or stable B^{4+} cations

Red markers in **Fig. 5.5** denote ionic radii of the selected doping candidates for the 8*g* site: (top to bottom) Zr^{4+}, Sn^{4+}, Ti^{4+}, Ge^{4+} in octahedral coordination[103]. Ionic radii of V^{3+} and V^{4+} in the

parent phase t-$Sc_2VO_{5+\delta}$ are shown in grey for reference. It can be seen that the selected dopants are commensurate with $V^{3+\ldots4+}$ rather than with V^{5+}, save for germanium, and all have the charge +4. As for preferred coordination, related both to size and charge of the cation, octahedral coordination can be found for all four cations: Ge^{4+} [255], Ti^{4+} [254], Sn^{4+} [241], Zr^{4+} [256], while tetrahedral for at least three: Ge^{4+} [22], Ti^{4+} [257], Sn^{4+} [258], and much rarer Zr^{4+} [259] due to its large cation radius with respect to the radius of oxygen. Several members of the $Sc_2V_{1-x}B_xO_{5+\delta}$ series were attempted following eq. 5.1 in static vacuum at 1100 °C:

$$Sc_2O_3 + (1-x)\,VO_2 + x\,BO_2 \rightarrow Sc_2V_{1-x}B_xO_{5+\delta} \qquad (5.1)$$

with x = 0.8 (aiming at the octahedral site), 0.2 (equivalent to the content of the tetrahedral site, for contrast), and occasionally 0.5±0.1 (equivalent to 50±10% of the vanadium sublattice). Products were studied with powder XRD, and fragments of the resulting patterns are stacked in **Fig. 5.6**. Ground by hand, Ti-bearing products crystallized as major $I\bar{4}$ phase, in case of $x \geq 0.4$ with impurities of unreacted starting materials and the competing pseudobrookite Sc_2TiO_5. Ball-mill grinding would give purer final products even with x=0.8 as was shown recently [127], but was not attempted for this reaction in the current work.

Similarly, for the Ge system, a single phase product of the Sc_2VO_5 type was found at x=0.2, while competing phases Sc_2GeO_5 and $Sc_2Ge_2O_7$ were observed at higher x and accounted for 50 mass % of the product at x= 0.8. In case of Sn, the composition with x = 0.2 similarly yielded a pure phase of the Sc_2VO_5 type, while the other compositions were dominated by the rhombohedral $Sc_4Sn_3O_{12}$ phase, as expected from **Fig. 5.4**, and left-overs of the bixbyite Sc_2O_3. In contrast, the two Zr-bearing products (green) contain competing phases like $Sc_4Zr_3O_{12}$ (or $Sc_2Zr_5O_{13}$ of the same symmetry) and the bixbyite impurity regardless of the composition. V-rich product (x = 0.2) has only

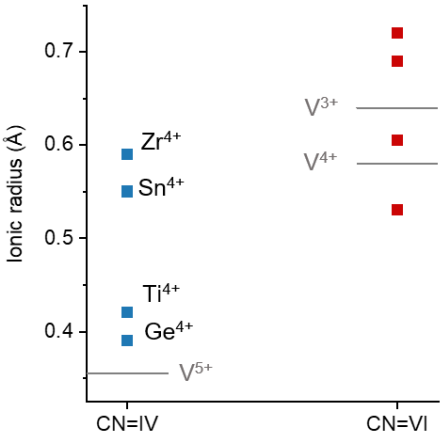

Figure 5.5. Tetrahedral (blue) and octahedral (red) Shannon ionic radii of suggested dopants into the V sublattice of t-$Sc_2VO_{5+\delta}$. Grey lines are references – tetrahedral V^{5+} and octahedral V^{3+}/V^{4+} in t-$Sc_2VO_{5+\delta}$ itself.

60 mass % of the tetragonal phase, while Zr-rich product (x = 0.8) contains ZrO_2 and no tetragonal phase.

It is seen that whenever a larger doping cation (B) is introduced, more of the competing phases (competing with the Sc_2VO_5 type) are found in the product. Aside from B = Zr, B-doped compositions with x = 0.2 can be obtained as a single phase. It other words, the vanadium sublattice of $Sc_2VO_{5+\delta}$ can accommodate at least 20% of a dopant. In the case of Zr, its octahedral radius

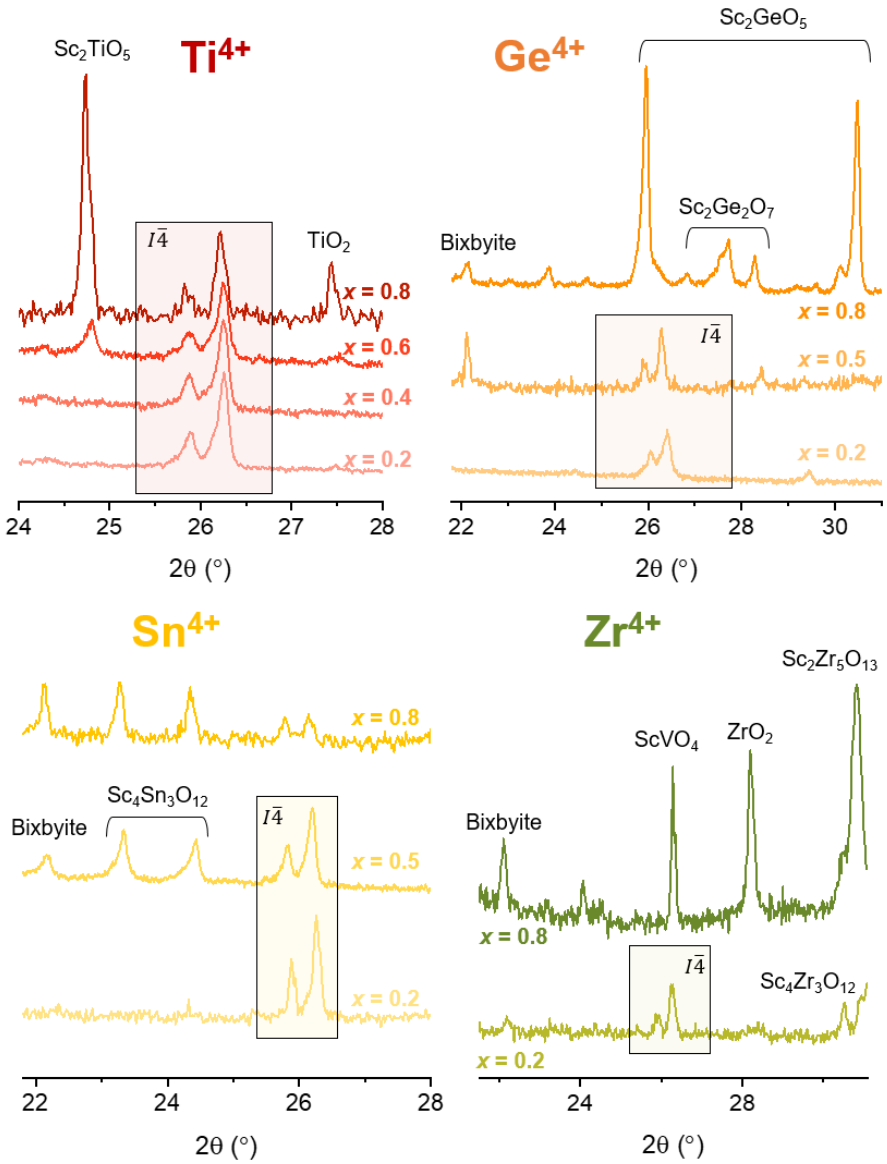

Figure 5.6. Fragments of stack plots of *ex-situ* XRD patterns following the attempts to synthesize $Sc_2V_{1-x}B_xO_{5+\delta}$ phases. Main products and impurities are indicated. Characteristic peaks (123) of the target phase ($Sc_2VO_{5+\delta}$-type) are enclosed in boxes.

approaches that of Sc, but due to either lack of thermal energy to react Zr or due to the charge difference between it and Sc^{3+}, even the smallest *x* failed to yield a single-phase product.

5.3.2. $Sc_2V_{1-x}B_xO_{5+\delta}$ phases with redox-active B^{x+} cations

Many redox-active transition metals in the oxidation state +4 adopt an ionic radius in the range discussed above. However, at the temperatures required to react those with scandium, 3d metals later than vanadium in the periodic table favor oxidation states between +1 and +3. Consequently, competing phases such as $ScBO_2$ and $ScBO_3$ can be found in the Sc-B-O diagram. Apart from the surplus of starting materials during the synthesis of the target series $Sc_2V_{1-x}B_xO_{5+\delta}$, these phases are expected to compete with the desired A_2BO_5 stoichiometry. **Fig. 5.7** provides ionic radii of four metals of choice in tetrahedral (CN=IV) and octahedral (CN = VI) coordination. Bars indicate ranges of ionic radii expected under the synthetic conditions, related to the expected oxidation states for tetrahedral $Cr^{4+\ldots5+}$, $Mn^{4+\ldots5+}$, $Fe^{2+\ldots3+}$, and Co^{2+}; octahedral $Cr^{3+\ldots5+}$, $Mn^{3+\ldots4+}$, $Fe^{2+\ldots3+}$, $Co^{2+\ldots3+}$. It is seen that all four (especially Cr, Mn, Co) are potential dopants for the 8*g* site, while two (Cr and Mn) are simultaneously well suited to dope the 2*c* site.

The series $Sc_2V_{1-x}B_xO_{5+\delta}$ was synthesized similar to eq. 5.1 with the dopant sources being B_2O_3 (B = Fe^{3+}) or B_3O_4 (B = $Co^{2.67+}$), or BO_2 (Mn^{4+} and Cr^{4+}). For iron, already at *x* = 0.2 a major bixbyite phase was found, and even more so at larger *x* (**Fig. 5.8**). The phase with *x* = 0.8 is almost a pure bixbyite. For manganese, the sample with *x* = 0.2 has a 10% bixbyite impurity while the one with *x* = 0.8 is mostly a bixbyite with minor unidentified impurities. Formation of bixbyite requires three prerequisites – (1) high enough temperature to randomize cations; (2) close ionic radii of the cations and, correlated, (3) reduced net cation charge with respect to that of the corresponding fluorite or fluorite superstructure. While (1) is taken care of at

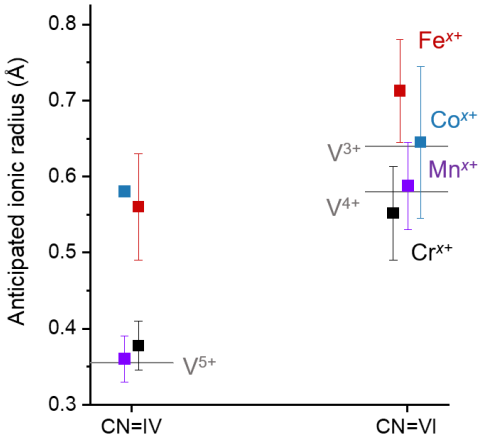

Figure 5.7. Tetrahedral (left) and octahedral (right) Shannon ionic radii of suggested redox-active dopants into the V sublattice of t-$Sc_2VO_{5+\delta}$. The vertical bars show ranges of expected sizes (expected oxidation states). Grey lines are references – tetrahedral V^{5+} and octahedral V^{3+}/V^{4+} in t-$Sc_2VO_{5+\delta}$ itself.

1100 ºC for the given cations, (2) and (3) are fulfilled both for Fe^{3+}, which cannot oxidize further, and Mn^{4+} which undergoes reduction as will be shown in the upcoming ***Section 5.4.2*** for the sample with x = 0.2. Chromium and cobalt undergo reduction too. For example, the cobalt-bearing phase with x = 0.3 contains ~15% of bixbyite, which for x = 0.7 is present as a major phase and for x = 1.1 coexists with another major phase – rock salt $Co^{2+}O$, which suggests further reduction. Moreover, in all cobalt reactions, sample crucibles acquired a deep blue colour where the samples

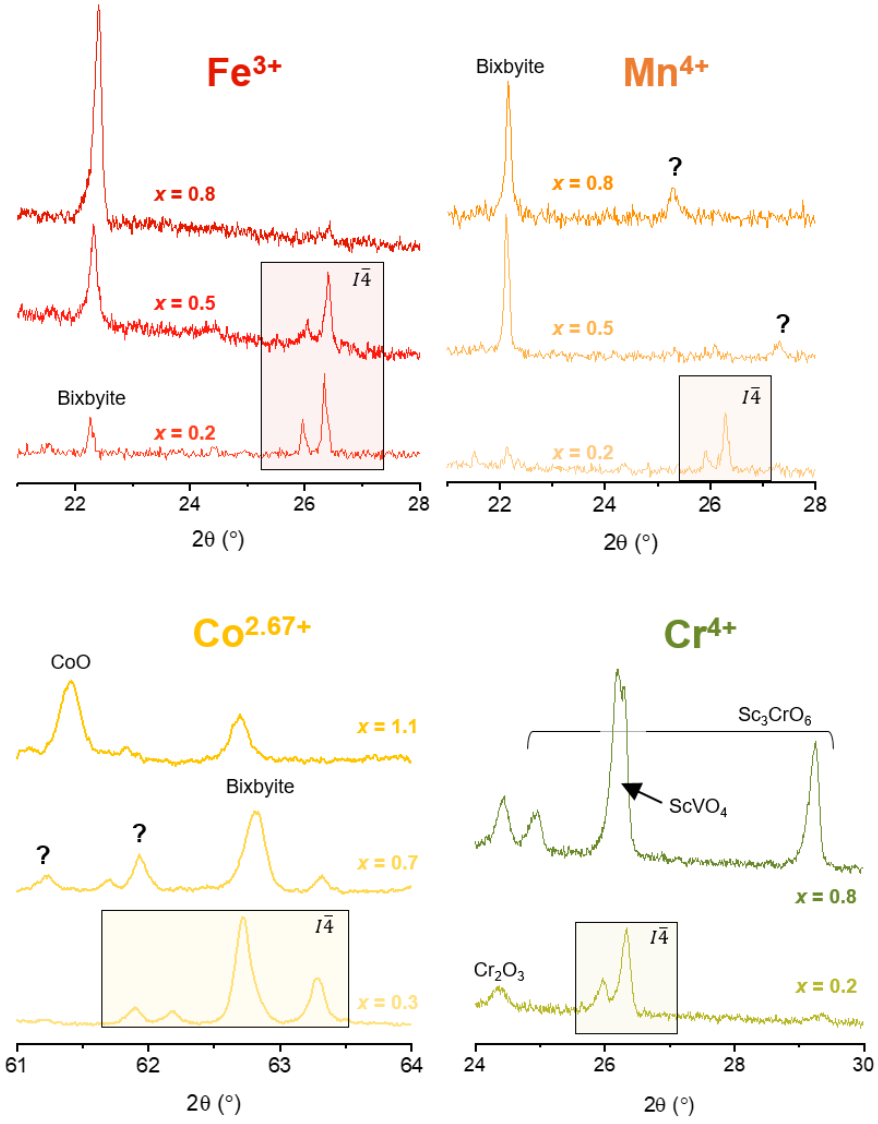

Figure 5.8. Fragments of stack plots of *ex-situ* XRD patterns following the attempts to synthesize $Sc_2V_{1-x}B_xO_{5+\delta}$ phases with redox-active B cations. Main products and impurities are indicated. Characteristic peaks of the target phase ($Sc_2VO_{5+\delta}$-type) are enclosed in boxes. Chromium data were borrowed from Richtik, 2021.

were in direct contact with them, likely due to the formation of "cobalt blue" $Co^{2+}Al_2O_4$ – a spinel with reduced cobalt.

5.3.3. Diffraction studies on phases with x = 0.2. The ordering coefficient

A series $Sc_2V_{1-x}B_xO_{5+\delta}$ with x = 0.2 (0.3) and B = Ti, Sn, Ge, Cr, Co, Fe, and Mn was chosen for further analysis, including NPD/XRD and XANES. From diffraction, information regarding oxygen concentration and site mixing was obtained. Notably, (1) a purer sample with cobalt (x = 0.3) was synthesized, although with no success of further reproduction; and (2) phases with Fe and Mn were not studied with diffraction methods due to large bixbyite impurities (reaching 30 mol. %) which would at the very least affect the quantification of site mixing. However, both were still studied with XANES, where tetrahedral coordination (absent in the bixbyite) was of interest.

The XRD and NPD patterns are presented in **Fig. A.4-1** of the Appendix, also listing minor impurities which were too minute to seriously affect calculations, and structural details are summarized in **Table A.4-1**. Refinements were carried out against NPD (TOF) data and lab-based

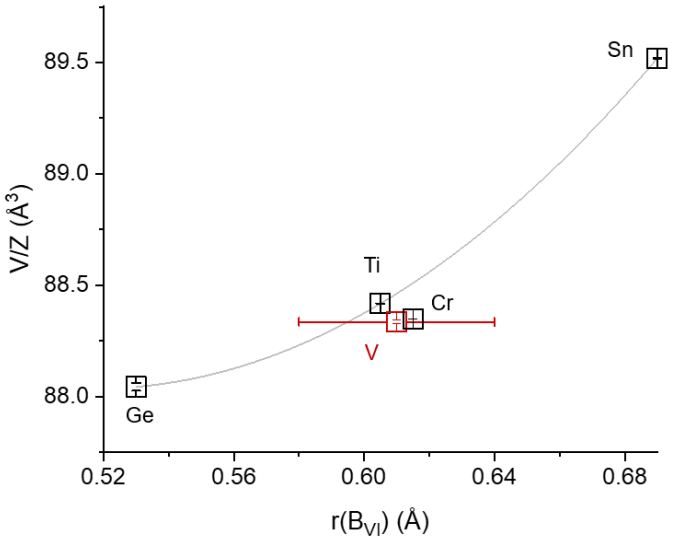

Figure 5.9. Evolution of the unit cell volume in the single-phase series $Sc_2V_{0.8}B_{0.2}O_{5+\delta}$ (B = Ge, Cr, Ti, Sn, and reference V). Grey line is a polynomial through Ge, Ti, and Sn – redox-inactive 4+ cations: $y = A + Bx + Cx^2$ with A = 101.4, B = -51.5, C = 49.8.

XRD[M]. **Fig. 5.9** provides a plot of refined unit formula volumes of the five phases $Sc_2V_{0.8}B_{0.2}O_{5+\delta}$ with B = Ge, V, Cr, Ti, Sn as a function of their octahedral (CN = VI) ionic radii. The error bar along the *x* axis indicates a range of expectations for the ionic radius of vanadium depending on its charge. Overall, the volumes increase with the increasing radius of the B dopant, but not linearly: the best attempt to describe it was a second-order polynomial passing through only three points; all three are stable tetravalent cations: Ge, Ti, Sn. With more points this dependence can be used as a calibration curve for other potential dopants within the range of ionic radii considered, given (1) the sample is mostly a pure phase and (2) the dopant can be stabilized as a 4+ species in an octahedral environment. The latter excludes chromium, which is mostly present in its Cr^{3+} state as will be shown below.

5.3.3.1. Oxygen concentration

Oxygen concentration per unit formula, calculated as a weighted sum over refined occupancies of the oxygen sites, is plotted in **Fig. 5.10a**. The oxide stoichiometry increases with increasing octahedral radius of the tetravalent dopant, and a reasonable fit was achieved with a second-order polynomial for the stable tetravalent cations Ge, Ti, and Sn. Chromium was left aside due to being trivalent, and vanadium – due to its mixed oxidation state, although inclusion of at least the latter would not affect the quality of the fit. A comment should be made on how the oxygen site occupancies were refined. Panel **b** shows a fragment of the correlation matrix among all occupancies (all cations and anions) and displacement parameters in an example refinement of $Sc_2V_{0.8}Sn_{0.2}O_{5+\delta}$ where all (as opposed to some) mentioned parameters were refined. In the color scheme, the strongest correlation between pairs of parameters is shown with more vibrant red (+) or blue (-); for legend – see **Table A.4-2**. In particular, a series of matrix cells parallel to the diagonal of the matrix are vibrant, meaning reasonably strongly correlating (60-80%) pairs of refineable parameters. In general, strong correlation hampers the meaningfulness of the refined values and belies the need to refine each of them in the first place. Consequently, only one of the correlated parameters in each pair (such as oxygen O-1 occupancy – oxygen O-1 displacement

[M] Refinements were done against NPD and lab-based XRD data with non-equal weights. Ideally, for better resolution and wider angular range lab-based XRD data should be replaced with synchrotron XRD data – and then using a better histogram weighting scheme would be more reasonable.

B_{iso}) was refined, while the other was assigned a reasonable value and fixed. In particular, isotropic atomic displacement parameters of oxygen were fixed to the values refined for pure t-$Sc_2VO_{5+\delta}$[31] used here as a reference, and it is exactly this result that was plotted in panel **a**. The same plot but after refining the B_{iso} values for all oxygens resulted in panel **c**, which is a much more scattered plot. In this panel, the concentration of oxygen in Ti and Sn compounds almost reaches 5 per unit formula ($\delta = 0$) but never exceeds it. However, the parent structure of t-$Sc_2VO_{5+\delta}$ still has the

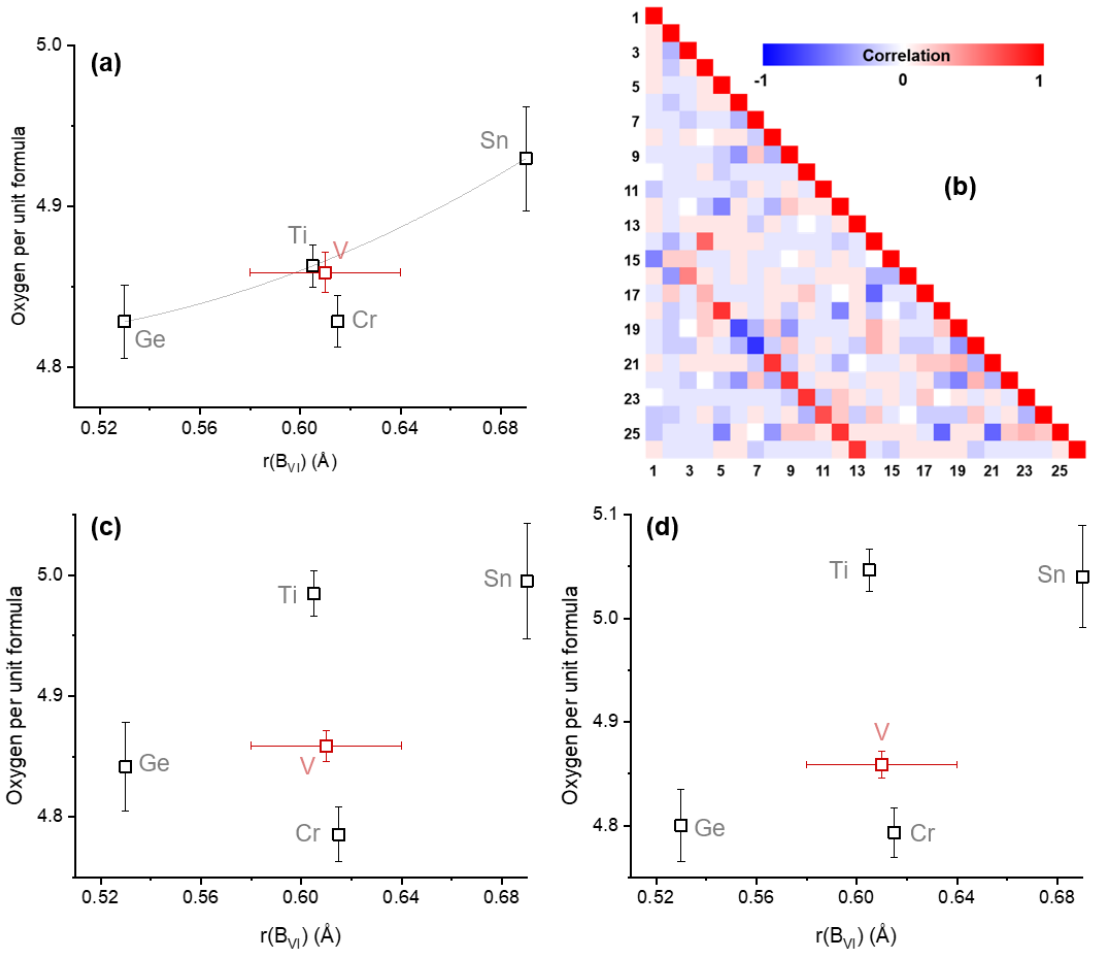

Figure 5.10. To the refinement of oxygen concentration in $Sc_2V_{0.8}B_{0.2}O_{5+\delta}$ (B = Ti, Ge, Cr, Sn): (a) – oxygen per unit formula when all B_{iso} (O^{2-}) were fixed at the values refined for B = V (red, reference). Grey line is a polynomial through Ge, Ti, and Sn – redox-inactive 4+ cations: $y = A+Bx+Cx^2$ with A = 5.22, B = -1.82, C = 2.01; (b) – example of a correlation matrix (a fragment) including thermal displacement parameters and occupancies of anions and cations after the refinement of $Sc_2V_{0.8}Sn_{0.2}O_{5+\delta}$. The paler the colour – the weaker the correlation. For parameters, see legend in **Table A.4-2**; (c) – oxygen per unit formula when all B_{iso} (O^{2-}) were freely refined; (d) – oxygen per unit formula when all B_{iso} (O^{2-}) were freely refined and an additional oxygen site (#9) was included.

capacity to accommodate the excess oxygen if the default eight sites are not enough to accommodate all of it (if $\delta > 0$). It happens at the expense of two vacant sites, one of which is a general site 8*g* (*x*, *y*, *z*) and one is a special site 2*b* (0, 0, ½). The additional general oxygen positions are situated around the diamagnetic vanadium, while the special positions are in the centers of the paramagnetic V_4-clusters. These sites are expected to participate in the oxygen-driven phase transition from the tetragonal to the cubic polymorph and will be discussed in ***Chapter 6***; for now, both were included in the next iteration of the Rietveld refinement, yielding panel **d**. In it, the additional site 8*g* accepted some oxygen – up to 1 atom per unit cell (with ~50 anions) for Sn and half an atom for Ti.

Out of the three refinements, results in panel **a** are the most meaningful since they circumvent the issue of correlation; however: (1) lab-based X-ray diffraction has limited resolution and angular range (hence synchrotron X-ray data are needed); (2) not enough compositions were studied to prove the suggested trend. This implies that the presented values of δ might be not final.

Regardless, the endeavor of probing the maximum allowed concentration of oxygen and locating the excess, if any, is still relevant. From previous reports[127], Ti^{4+} can be incorporated in the $Sc_2V_{1-x}B_xO_{5+\delta}$ series up to $x = 0.8$, which yields a single phase $Sc_2Ti^{4+}_{0.8}V^{5+}_{0.2}O_{5.1}$[N]. One interesting direction of future work on this sample is Fourier mapping based on neutron diffraction data. The goal is to observe the scattering intensity from the additional $0.1 \cdot O^{2-}$ which would be an indirect signature of all-Ti^{4+} in the 8*g* site.

5.3.3.2. Site preferences

Cation site mixing among Sc, V, and B was refined as follows. Cation exchange between Sc and V in $Sc_2VO_{5+\delta}$ was taken as a reference and fixed, amounting to 0.087 Sc in the 8*g* site of V, 0.122, 0.010, and 0.016 of V in the 4*f* and two 8*g* sites of Sc, and no Sc in the 2*c* site of V[31]. The B cation was mixed at a refineable concentration into the remaining V or Sc sites. All occupancies of B cations in five sites were constrained to add up to 20% of the B sublattice, or $x = 0.2$ in the formula $Sc_2V_{0.8}B_{0.2}O_{5+\delta}$. The results are plotted in **Fig. 5.11**, where five cation sites are shown on the X

[N] In the reactions above, the competing pseudobrookite Sc_2TiO_5 can be removed if the starting materials are ball-milled, which was not viable for any samples with $x > 0.2$ used in this chapter due to their small amount, and in some cases with $x = 0.2$ full reduction of vanadium in the starting materials was observed, e.g. in $Sc_2V_{0.8}Sn_{0.2}O_{5+\delta}$. All samples with $x = 0.2$ for which neutron data are available were reground by hand to prevent reduction in the ball mill.

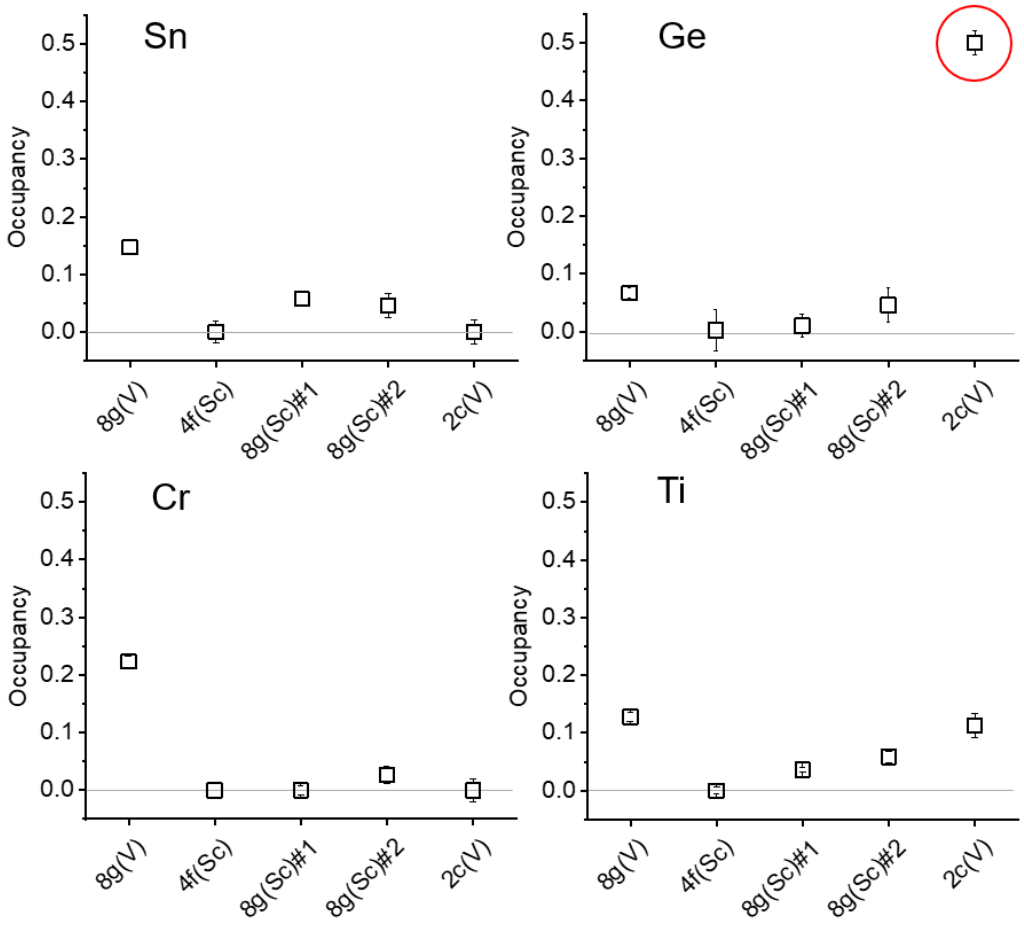

Figure 5.11. Occupancies of the five cationic sites of $Sc_2V_{0.8}B_{0.2}O_{5+\delta}$ phases (B = Ge, Cr, Ti, Sn) with regard to B cations, refined from NPD/XRD data. Encircled is the concentration of Ge^{4+} in the tetrahedral site (50%) which stands out.

axis and the fractional site occupancy of each cation is along the Y axis (note: to get the final concentration, Y values are to be multiplied by the site multiplicity – 2, 4, or 8 – and added up). It is seen that all four dopants partially or predominantly prefer the octahedral (8*g*) site of vanadium, with tin and titanium also preferring other general sites (scandium sites of sevenfold geometry), titanium – partially and germanium – predominantly preferring the tetrahedral site of vanadium (2*c*). These results are sensible in light of **Fig. 5.5** (for Sn, Ti, Ge) and **Fig. 5.7** (for Cr) – the smaller the size of the B dopant, the larger its preference for the tetrahedral site over the octahedral

site. As a measure of net site mixing, it is further proposed to use an *ad hoc* ordering coefficient which can take the following form[O]:

$$Cation\ ordering = \sum_j^P \frac{\sum_i^N \left(\left| O_{ij} - \frac{x_j}{\sum x_j} \right| \cdot M_i \right)}{\sum_i^N M_i}, \qquad (5.2)$$

where ***P*** is the number of species considered, ***N*** is the number of distinct cationic sites considered, O_i is the site occupancy (concentration of the cation ***j*** in the site ***i***), M_i is the multiplicity of the site ***i***, and x_j is the stoichiometric coefficient of the j^{th} cation in the unit formula. Thus, the formula quantifies the deviation of the current occupancies from the cation-disordered state. For example, in case of full cation disorder in $Sc_2V_{0.8}Ge_{0.2}O_{5+\delta}$ each cation site out of five is expected to consist of 66.7% Sc (=2/3), 26.7% V (=0.8/3), and 6.6% Ge (=0.2/3), where 3 in the denominator is the total count of cations per unit formula. However, in reality scandium prefers three sites (4*f* and two 8*g*), while V prefers two sites (8*g* and 2*c*) and Ge replaces some of Sc and V in three sites, as per **Fig. 5.11**. Expected occupancies upon hypothetical disordering are thus the term $x_j / \sum x_j$, while refined occupancies are O_{ij}. Ordering coefficients were then calculated for the four B dopants above based on **Fig. 5.11** and are plotted in **Fig. 5.12** (black markers[P]) against the reference –

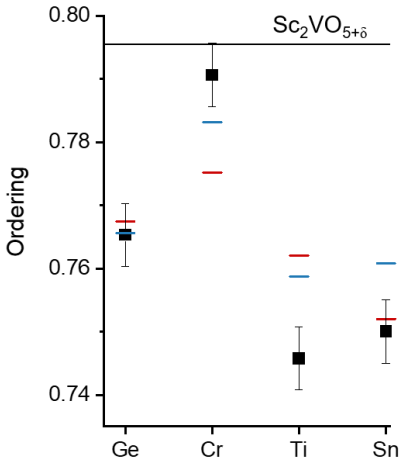

Figure 5.12. Cation ordering in the $Sc_2V_{0.8}B_{0.2}O_{5+\delta}$ series (B = Ge, Cr, Ti, Sn). Black, blue, and red markers correspond to the refinement conditions for panels (a), (c), and (d) of **Fig. 5.10**. The reference line is B = V. Note the scale of the Y axis.

[O] The coefficient resembles the numerator of the Bragg-Williams equation[309], but (1) using site multiplicities instead of atomic pair swapping probabilities and (2) expressing the average ordering instead of the local ordering. The used form of the equation seems sufficient if the same structures are compared. Otherwise, the differences between the fully ordered and the fully disordered site compositions, similarly summed over all sites and weighted by the multiplicities, should be added as the denominator.

[P] Black markers in **Fig. 5.12** were produced by the same refinement as **Fig. 5.10a**. Over-refinement (refining the B_{iso} of oxygen – blue markers in **Fig. 5.12**, related to **Fig. 5.10c**) brings ordering values close to each other, while further introduction of an additional oxygen site 8g (red markers in **Fig. 5.12**, related to **Fig. 5.10d**) arranges tetravalent Ge, Ti, and Sn such that their ordering coefficients decrease with increasing ionic radii. However, as said above, results of over-refining are less reliable due to strong correlation between occupancies (hence ordering) and B_{iso}.

t-$Sc_2VO_{5+\delta}$. In spite of the same order of magnitude, it can be noted that V (reference) and Cr produced a marginally larger ordering coefficient. It can be related to their redox-activity, whereby tiny V^{5+} (product of disproportionation of initial V^{4+}, along with V^{3+}) strongly prefers tetrahedral sites, while Cr^{3+} (product of reduction of initial Cr^{4+}; described further in the text) perfectly matches the mean octahedral radius of the two vanadium species in the 8*g* site and hence prefers it the most (see **Fig. 5.11**). The behavior of Ge, Ti, and Sn with respect to each other is less obvious: the ordering trend is non-monotonous among the three, although the trend goes down with the increased radius if errors are concerned.

With the help of many more doped phases crystallizing in the same structure type, this formula can be further developed into a useful mathematical tool for assessing the extent of site ordering. Furthermore, divorcing it from the structure type and observing its change throughout phase transitions and phase decomposition may be helpful in quantifying and predicting the latter due to their relation to lattice energy and the relation of the ordering coefficient to entropy. For the same purpose, unit cell volumes (**Fig. 5.9**) are helpful in approximating the lattice enthalpy[260] insofar as thermodynamic products of reconstructive reactions (rather than kinetic products of topotactic reactions) are concerned.

5.4. XANES on characteristic samples of $Sc_2V_{1-x}B_xO_{5+\delta}$ series

X-ray absorption near-edge structure spectroscopy (XANES) was performed on the tetragonal phases above, with the nominal 20% of the B sublattice doped with Ge, Sn, Ti, Mn, Cr, Fe, and 30% Co. The most conclusive analysis was done on the V edge, for which linear combination fitting (LCF) with standards was performed. Due to being extremely diluted, the B-dopant edge was not possible to study with LCF; instead only qualitative (comparison of the spectra) and semi-quantitative (pre-edge to edge intensity ratio) descriptions are given below. The tin edge was not studied due to the setup being more demanding at the time.

A comment should be made on the bixbyite impurity found in the samples with B = Mn, Fe, and Co and for this reason not studied extensively with diffraction methods: from smaller lattice parameter than that of Sc_2O_3 (a = 9.84 Å), the bixbyite impurity in the said phases is not pure Sc_2O_3. This impurity can contain any B-dopant as well as vanadium and any ratio thereof. For convenience, the approximation was adopted that the bixbyite contains only Sc and V. This did

not affect the qualitative interpretation of XANES, since only the tetrahedral environment (absent in the bixbyite) was of interest. Then, from the unit volume calibration curve for $Sc_{2-x}V_xO_{3+\delta}$ solid solutions[99] the bixbyite composition in the case of B = Mn (14% bixbyite impurity) was estimated to be $Sc_{1.8}V_{0.2}O_3$, rendering the composition of the tetragonal phase $Sc_{1.92}V_{0.87}Mn_{0.21}O_{5+\delta}$. For B = Fe, ~19% of the bixbyite impurity was found, similarly estimated to be $Sc_{1.6}V_{0.4}O_3$, which makes the composition of the tetragonal phase $Sc_{1.95}V_{0.83}Fe_{0.22}O_{5+\delta}$. The single-phase product obtained with B = Co was estimated to have a composition $Sc_{1.94}V_{0.77}Co_{0.29}O_{5+\delta}$. The overall formula of the series is then $Sc_{1.96\pm0.04}V_{0.82\pm0.05}B_{0.255\pm0.035}O_{5+\delta}$.

5.4.1. K-edge of vanadium

Fig. 5.13 shows the results of linear combination fitting of the vanadium K-pre-edge feature. The following standards were available: V_2O_3 (V^{3+}, octahedral), $ScVO_3$ (V^{3+}, two octahedral environments), VO_2 (V^{4+}, octahedral), $ScVO_4$ (V^{5+}, tetrahedral), and V_2O_5 (V^{5+}, square pyramidal, or distorted octahedral with one elongated apical bond). The weight of each standard in LCF directly translates in the atomic composition. Thus, the concentration of V^{5+} species was found to be between 12.3(1.9)% for B = Ge^{4+} and 37.0(1.6)% for B=Mn^{4+} (nominal), as compared to 27.0(1.0)% for B = V^{4+} (pure $Sc_2VO_{5+\delta}$)[31]. Lower oxidation states of vanadium in higher coordination and marginally distorted centrosymmetric polyhedra produce low intensity (transmission, μt); however, the software used[172] was able to discriminate between V^{4+} and V^{3+} species. Nevertheless, quantification of the V^{3+} and V^{4+} content should be taken with a grain of salt, since (1) even the slightest contribution of V^{5+} (the sharpest feature) vastly overrides the intensity of other species; (2) the level of the signal-to-noise ratio (SNR) is often insufficient and comparable with the intensities of lower-valence contributions; (3) only a limited number of standards were used.

Concentration of V^{5+} was plotted in **Fig. 5.14** against the expected Shannon ionic radii[103] of the dopants B^{x+} in octahedra (such as site 8*g*, panel **a**) and tetrahedra (such as site 2*c*, panel **b**). The term "expected" refers to the most stable species known; if several species are known to be stable, an average radius value was taken and the horizontal lines centering on the symbol indicate the ionic radii of these species. Data points with no horizontal range represent redox inactivity under the given conditions. In panel **a**, an almost linear relation was found between oxidized V^{5+} and

octahedral radius of the dopant. The dotted line marks the concentration of the tetrahedral 2*c* sites in the structure (20%), and the markers above this line point at the surplus of tetrahedral V^{5+} ions for all dopants but Ge^{4+}. These excessive tetrahedral V^{5+} ions must be located in the 8*g* site of the respective $Sc_2V_{1-x}B_xO_{5+\delta}$ structures and likely retain tetrahedral coordination or at least a few very short (~ 1.7 Å) bond distances, which XANES is particularly sensitive to. This can be realized if two corners of the 8*g* octahedra are absent owing to overall oxygen deficiency of the phase ($\delta<0$). In such a case these two vacant oxygen ions should be arbitrary, or statistically disordered with the remaining oxygens, since the average polyhedron description from XRD is still sixfold. An alternative rationale behind the sharp pre-edge feature, consistent with having short V-O bonds, is extreme distortion of the polyhedron and/or off-center position of the central cation.

From **Fig. 5.14a**, the bigger the dopant's radius the larger its preference for octahedral environments. Notably, it is the sixfold radius of the dopant (panel **a**) and not the tetrahedral radius (panel **b**) and or the ratio of the radii (not shown) that drives the site preference. Reaction conditions – high temperature (1100 ºC) and static vacuum – may be another contributor, since they both favor reduced species over oxidized ones, and more reduced ions have larger radii than the more oxidized ions of the same nature, and the larger radii prefer larger coordination polyhedra.

5.4.2. K-edges of B-site dopants

5.4.2.1. Titanium

As mentioned above, owing to low concentration of B in the sample, only qualitative (comparison of the appearance of spectra) or semi-quantitative (plotting normalized intensities of the pre-edge features) evaluation of the concentration of dopants can be made. Consequently, the pre-edge feature of the Ti spectra is only qualitatively compared against a few other Ti-containing oxide phases in **Fig. 5.15a**. The standards include Ti_3O_5[19] (mixed $Ti^{3+/4+}$ in multiple octahedral environments; contains impurities of Magnéli phases Ti_nO_{2n-1}), TiO_2 ($Ti^{4+}{}_{VI}$), $Bi_{12}TiO_{20}$ ($Ti^{4+}{}_{IV}$)[130], and orthorhombic o-Sc_2TiO_5 ($Ti^{4+}{}_{VI+VI}$)[12], as well as the cubic c-Sc_2TiO_5 polymorph[81,127] with expected cubic (CN = VIII) and/or near-cubic (VII) coordination of Ti^{4+}. Generally, Ti XANES is complex as it may produce of up to 9 features[261]. Furthermore, comparison with known data is complicated due to pre-edge energies in the present experiment positively shifted with respect to

some reported values[262] (possibly due to different calibration) and juxtaposition of multiple factors such as different oxidation states, coordination numbers, and bond lengths. To rationalize the peaks in the present data, intensities of the observed pre-edge features were divided by the edge intensities and plotted as a function of energy, as is illustrated in the scatter plot in **Fig. 5.15b**. The error bars originate from the broad or plateau character of the peaks, as well as unresolved peak shoulders of similar intensity. For simplicity, only the area that is not faded out is considered – it focusses on the most intense components of the standards (colored bubbles) and the analyte $Sc_2V_{0.8}Ti_{0.2}O_{5+\delta}$ (squares) lying not on the edge jump portion of the spectrum. Apart from the low-intensity feature in the center of the emphasized area, tetrahedral Ti^{4+} (purple), as expected, has the highest intensity[167,263] and is shifted to smaller E values with respect to the analyte, likely indicating no tetrahedral Ti^{4+} in the analyte or only a minute concentration thereof. Octahedral Ti^{4+} in TiO_2 (green) and o-Sc_2TiO_5 (yellow, likely associated with site 8*f*) are close in absolute and relative intensities of their peaks, but o-Sc_2TiO_5 has more features, likely associated with more crystallographic sites in the latter (for example, site 4*c* is less populated by titanium and likely less intense in XANES as a result). Intensity of Ti in octahedral TiO_2 is higher than in the analyte, likely due to the slightly shorter Ti-O bonds[168] on average or, rather, more short bonds in TiO_2 (**Fig. 5.15c**). This leads to higher overlap between the d-character (parity-forbidden) and the p-character (allowed) of the receiving molecular orbital, claimed by some authors to result from hybridization of $3d_{Ti}$ (t_{2g}) and $2p_O$[261] or $3d_{Ti}$ and $4p_{Ti}$[263] atomic orbitals. Bond lengths and not necessarily the distortion of the coordination polyhedron are considered to affect this overlap the most, and for TiO_2 both bond length and angle distortions are indeed smaller on average than in other octahedral Ti^{4+}-bearing phases rich in Ti^{4+}: Ti_3O_5 (site Ti-1) and Sc_2TiO_5 (**Fig. A-4.2a**). In the mixed-valence titanium oxide Ti_3O_5 (**Fig.5.15**, blue), the tallest feature is marginally lower and more blue-shifted than the most pronounced feature of o-Sc_2TiO_5, likely due to the lower average oxidation state of Ti in Ti_3O_5. Bond lengths and their distortions are similar in magnitude between the two, consistent with similar height of the pre-edge features (**Fig. 5.15b** and **Fig. 5.15c**). Features of the cubic Sc_2TiO_5 phase (red) resemble those of what is likely the 4*c* site of the orthorhombic polymorph (faded) in intensity but shifted closer to what is likely the 8*f* site in energy. The oxidation states are expected to be the same in this range of energies, hence lower intensity points at longer Ti-O bonds (**Fig. 5.15c**). The markers of the $Sc_2V_{0.8}Ti_{0.2}O_{5+\delta}$ phase are between those of the two Sc_2TiO_5 polymorphs, but the appearance of the strongest peak

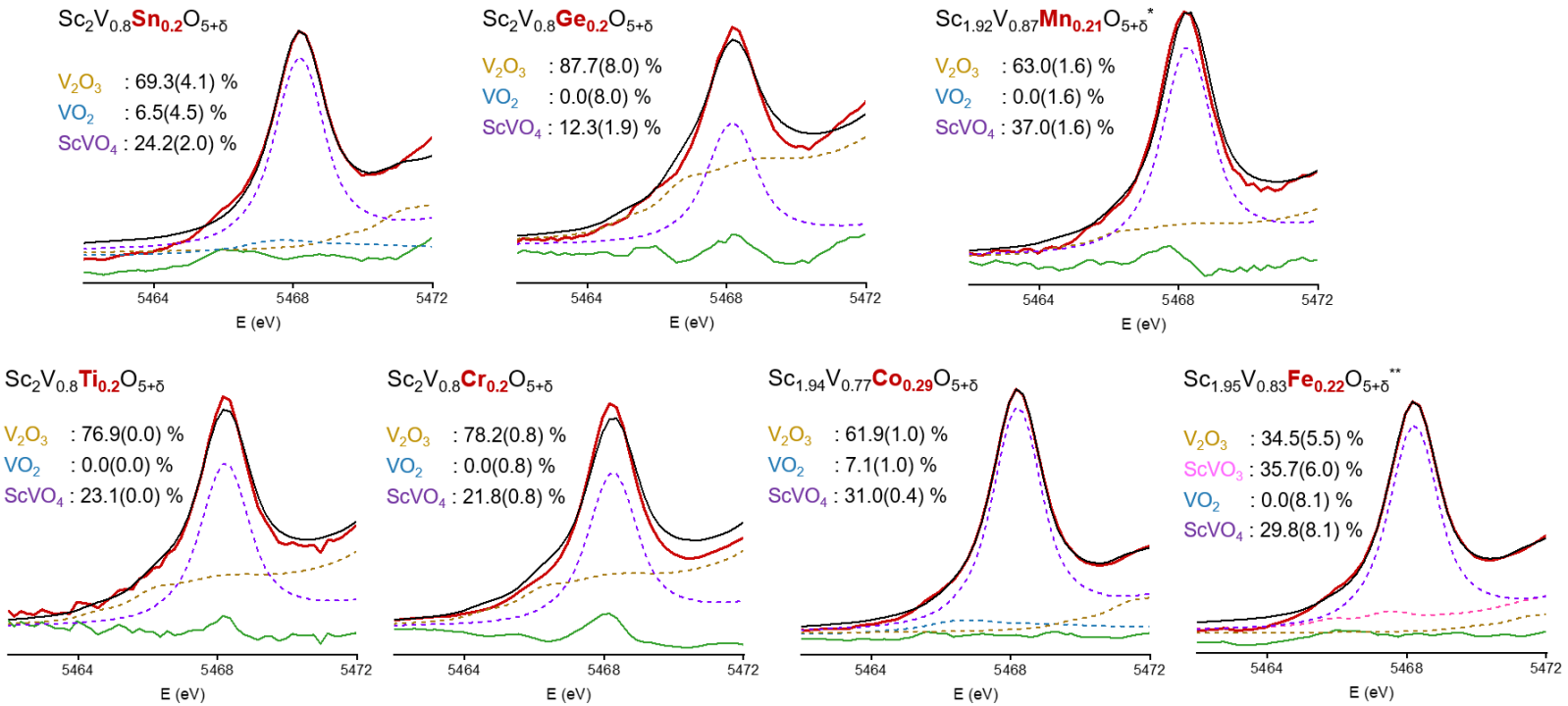

Figure 5.13. Linear combination fits of the K-pre-edge feature (XANES) of doped $Sc_2VO_{5+\delta}$-type phases (incl. those with impurities). Black curve is experimental data, red – total fit, green – difference. Used standards are V_2O_3 (V^{3+}_{VI}, yellow), $ScVO_3$ (V^{3+}_{VI+IV}, pink), VO_2 (V^{4+}_{VI}, blue), $ScVO_4$ (V^{4+}_{IV}, purple).

(~4969 eV) resembles that of the orthorhombic polymorph more. Fitting (not shown) of relatively noisy data on $Sc_2V_{0.8}Ti_{0.2}O_{5+\delta}$ (too little Ti for a reliable signal, as said before) worked better with o-Sc_2TiO_5 as the only fit component, suggesting the titanium environment in this polymorph is the closest to that of the analyte. The bond-length distortion in the 8*g* site of the analyte is commensurate with those of Ti_3O_5 and o-Sc_2TiO_5 (**Fig. A-4.2**), while the average bond length approaches that of TiO_2 (the shortest among octahedral standards) but with a large error bar. At the same time, there seems to be no or not much titanium in the 2*c* site, which otherwise would drastically increase the pre-edge intensity owing to the short Ti-O bond distances. Comparing the bond distances in the 2*c* site of $Sc_2V_{0.8}Ti_{0.2}O_{5+\delta}$ and in $Bi_{12}TiO_2$ in the same figure, if the 2*c* site was populated with Ti^{4+} the pre-edge absorption of the analyte would be much higher. As per **Fig. 5.11**, Rietveld refinement suggests Ti is mostly split between the 2*c* and 8*g* site populating them by 16(2)% and 14(1)%, correspondingly, which translates into ~1:5 ratio of tetrahedral and octahedral titanium. From XANES, this ratio is lower, and this disagreement might stem from the constrains adopted in the refinement (fixed mixing of Sc and V). Overall, virtually none or very little tetrahedral titanium was found in $Sc_2V_{0.8}Ti_{0.2}O_{5+\delta}$.

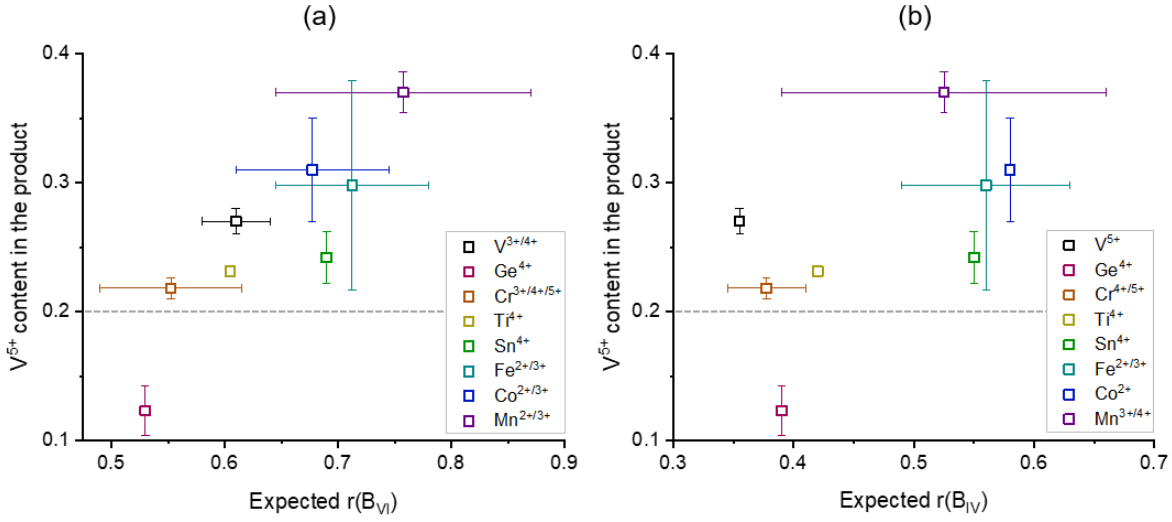

Figure 5.14. Complementary to XANES fitting, concentration of tetrahedral V^{5+} in the $Sc_2VO_{5+\delta}$-type phases (incl. those with impurities) changing with the expected octahedral (a) and tetrahedral (b) radii of the dopants. Grey line at 0.2 shows that only 20% of all V^{5+} in the structure can reside in the 2*c* sites. *Note: the cases of Fe, Co, and Mn should be adjusted for impurities. Note-2: due to the limited set of standards for XANES, tetrahedral V^{5+} is the best description of the pre-edge feature at hand but not necessarily the best overall (hence values above 0.2).*

5.4.2.2. Other 3d metals

The middle panels in **Fig. 5.16** show a series of scatter plots locating the apexes of the pre-edge features of $Sc_{1.96\pm0.04}V_{0.82\pm0.05}B_{0.255\pm0.035}O_{5+\delta}$ (squares) among the pre-edge features of references (circles). Panel (a) compares $Sc_2V_{0.8}Cr_{0.2}O_{5+\delta}$ (negligible impurities of Sc_2O_3 and $ScVO_4$) with CrO_2 ($Cr^{4+}{}_{VI}$, red) and Cr_2O_3 ($Cr^{3+}{}_{VI}$, blue). The wavy segment of $Sc_2V_{0.8}Cr_{0.2}O_{5+\delta}$ between 5992 and 5995 eV was not plotted as a single peak in the scatter plot and was neglected, but it might contain multiple peaks of lower intensity relative to the edge intensity. The only well-resolved peak at 5991 eV is closer in absorbance to that of the Cr^{3+} standard than to Cr^{4+}, but Cr^{4+} cannot be ruled out entirely on these grounds, since Cr^{4+} in CrO_2 is characterized by the closest bond length and angle distortion values to the 8*g* site of the tetragonal phase and would perfectly fit there on this ground (**Fig. A-4.2**). The edge jump in **Fig. 5.16i** tells more about the oxidation state. According to Kunzl[264], the absorption energy typically scales with the oxidation state. Applying Kunzl's law to the edge jump energies in particular, the analyte (black) mostly contains Cr^{3+}, as

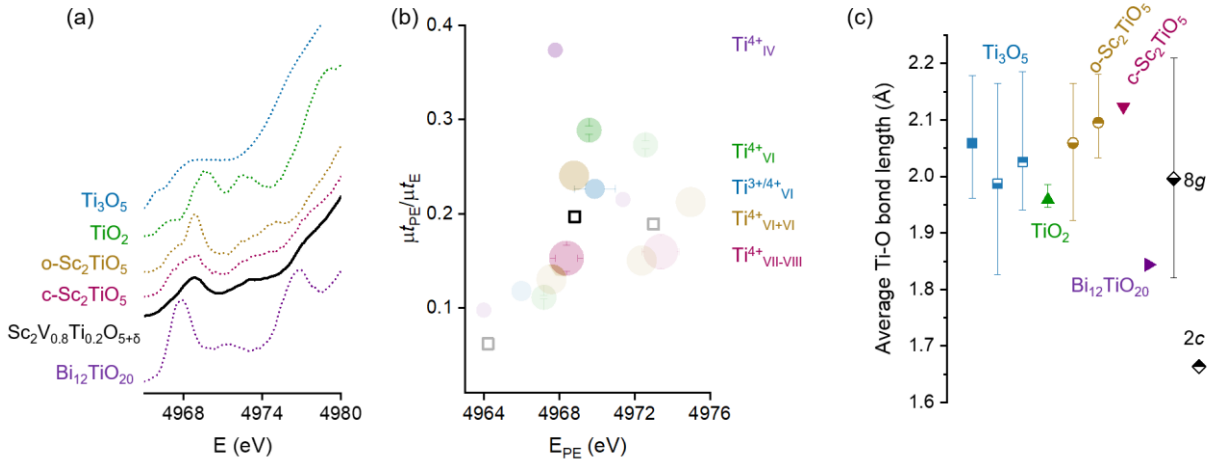

Figure 5.15. Analysis of XANES data on the K-edge of titanium (E = 4966 eV): (a) stack plot of pre-edge features of Ti-bearing standards (colorful) and the analyte (black), Y axis being absorption intensity (a. u.). The colour scheme is the same throughout all panels; (b) scatter plot of pre-edge intensities normalized to the respective edge intensities. Error bars are used when the peak is broadened (not resolved enough). Faded are features of insufficient intensity and features on the edge jump, to leave out only the apparent "clean" transitions; (c) average Ti-O bond lengths around distinct sites, known to affect both intensity and energy in XANES. The sites content is: Ti^{3+}, Ti^{4+}, $2Ti^{3+}$:$3Ti^{4+}$ (Ti_3O_5, octahedral); Ti^{4+} (TiO_2, octahedral); $2Ti^{4+}$:$3Sc^{3+}$, $2Ti^{4+}$:$4Sc^{3+}$ (o-Sc_2TIO_5, octahedral); Ti^{4+}:$2Sc^{3+}$ (c-Sc_2TiO_5, cubic); tetrahedral Ti^{4+} in $Bi_{12}TiO_{20}$; octahedral site 8*g* and tetrahedral 2*c* (for comparison) of the analyte. Error bars cover the range of Ti-O distances in a respective polyhedron.

the energies of the edge jump (E_0) are similar for $Sc_2V_{0.8}Cr_{0.2}O_{5+\delta}$ and Cr_2O_3 (blue). Although the dependence does not always hold true due to factors like backscattering of electrons[265] affecting E_0, shape of the jump, its slope, and the order of magnitude of the edge jump, the energy of Cr_2O_3

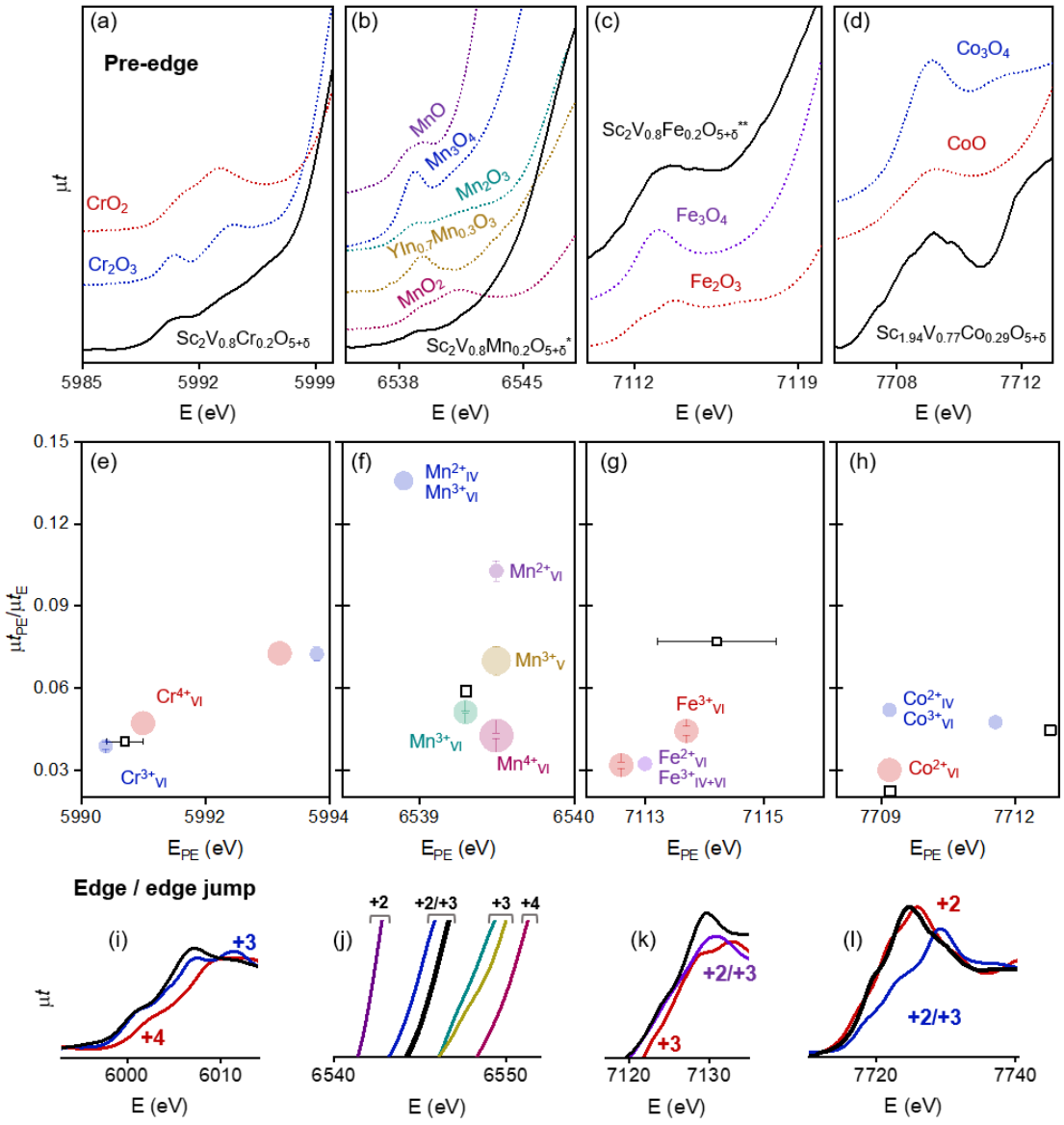

Figure 5.16. XANES absorption edge features of the B cation in four $Sc_2V_{1-x}B_xO_{5+\delta}$ phases with nominal $x = 0.2$ for B = Cr (a, e, i), Mn (b, f, j), and Fe (c, g, k) and $x = 0.3$ for B = Co (d, h, l): (a)-(d) – pre-edge features in transmission mode; (e)-(h) – normalized intensities of the pre-edge; markers are transmission maxima or their average values if the pre-edge had a plateau character rather than a defined peak (error bars indicate the range of the plateau-ness); (i)-(l) – edge or edge jump portions of the spectra; numbers are oxidation states of B cations. Analyte is black, standards are colorful.

and the analyte match, which suggests trivalent chromium in the analyte. The reduction of chromium at high temperature is not unexpected[266].

Panel **b** compares $Sc_{1.92}V_{0.87}Mn_{0.21}O_{5+\delta}$ ("$Sc_2V_{0.8}Fe_{0.2}O_{5+\delta}$" with a 20-25% impurity of supposedly $Sc_{1.85}V_{0.15}O_3$ and 3% Mn_3O_4) with MnO ($Mn^{2+}{}_{VI}$, purple), Mn_2O_3 ($Mn^{3+}{}_{VI}$, green), MnO_2 ($Mn^{4+}{}_{VI}$, red), Mn_3O_4 ($Mn^{2+}{}_{IV}$ + $Mn^{3+}{}_{VI}$, blue), and $YIn_{0.7}Mn_{0.3}O_3$[129] ($Mn^{3+}{}_{V}$, yellow). The peak of the analyte aligns well with the peak of Mn_2O_3 (green) in absorbance and energy, likely indicating trivalent octahedral manganese in the $Sc_{1.80}V_{0.95}Mn_{0.25}O_{5+\delta}$ phase. Only marginally higher intensity of the analyte's pre-edge peak points at an admixture of reduced and/or lower-coordinated manganese. Notably, no strong distortion was found from the NPD/XRD data despite high Jahn-Teller activity of Mn^{3+} (d^4), suggesting either different oxidations states in the analyte or irrelevance of the Jahn-Teller mechanism to the formation of this phase. From examining the edge jump[267] (panel **j**), grouping of the mid-jump fragments of the spectra into distinct Mn^{2+}, $Mn^{2+/3+}$, Mn^{3+}, and Mn^{4+} bundles perfectly following Kutzl's dependence and the fact that Mn_3O_4 (blue) is the closest to the analyte (black) suggest that Mn species in the analyte are stabilized as a mixture of Mn^{2+} (d^0) and Mn^{3+} (d^4). The latter agrees with slightly higher pre-edge intensity in the analyte *vis-à-vis* pure Mn_2O_3. Reduction of manganese at high temperature is not unexpected[268].

Panel **c** compares $Sc_{1.92}V_{0.83}Fe_{0.25}O_{5+\delta}$ ("$Sc_2V_{0.8}Fe_{0.2}O_{5+\delta}$" with a 30% impurity of supposedly $Sc_{1.55}V_{0.45}O_3$) with Fe_2O_3 ($Fe^{3+}{}_{VI}$, red) and Fe_3O_4 ($Fe^{2+}{}_{VI}$ + $Fe^{3+}{}_{IV+VI}$, purple). No clear conclusion can be drawn from Fe XANES, since all signatures are vastly different. However, as the 2*c* site of $Sc_{1.92}V_{0.83}Fe_{0.25}O_{5+\delta}$ is likely occupied by V^{5+} (see **Fig. 5.13** and **5.14**), Fe must be in a higher-coordinated site. From the proximity of the 2+/3+ standard (Fe_3O_4, purple, see panel **k**) and the analyte (black), a mixture of divalent and trivalent iron is expected in $Sc_{1.92}V_{0.83}Fe_{0.25}O_{5+\delta}$. As the pre-edge to edge ratio of the analyte lies above the Fe_3O_4 standard (panel **c**), iron in the analyte is likely in a more distorted octahedron or off-center. It agrees with slightly higher bond-length distortions in the 8*g* site of the analyte in **Fig. A-4.2** yet disagrees with the bond-angle distortions. To reconcile, it is suggested that Fe occupies Sc sites, especially in light of the gigantic ionic radius of octahedral Fe^{2+} (0.780 Å) which is close to that of Sc^{3+} (0.745 Å).

Panel **d** compares $Sc_{1.78}V_{0.89}Co_{0.33}O_{5+\delta}$ (with a 20% impurity of Sc_2O_3) with CoO ($Co^{2+}{}_{VI}$, red) and Co_3O_4 ($Co^{2+}{}_{IV}$ + $Co^{3+}{}_{VI}$, blue). There was no pure $Co^{3+}{}_{VI}$ standard available for the XANES experiment for comparison. As expected, tetrahedral Co^{2+} (blue) has higher absorbance than octahedral Co^{2+} (red), which is higher than the pre-edge of $Sc_{1.94}V_{0.77}Co_{0.29}O_{5+\delta}$. Consistent with

Fig. 5.13, this points at higher coordinated cobalt. From examining the absorption edge itself (panel **l**), the edge jump for the Co^{3+} reference lags behind that of Co^{3+} and that of the analyte by about 3 eV, suggesting that the oxidation state of Co in $Sc_{1.78}V_{0.89}Co_{0.33}O_{5+\delta}$ is much closer to +2 than +3, consistent with the bright-blue tinting of the alumina crucible underneath the sample (likely from $Co^{2+}Al_2O_4$). NPD data were only available for a sample of the composition $Sc_{1.86}V_{0.90}Co_{0.24}O_{5+\delta}$ (with a 25% of supposedly $Sc_{1.8}V_{0.2}O_3$), and distortions from a joint XRD/NPD refinements are plotted in **Fig. A-4.2**. Only Co^{3+} in the octahedral site of the standard spinel is distorted enough to justify its contribution, if any, to bond angle distortions in the octahedral site of the analyte (black line), but not the bond length distortion. Worth noting, only octahedral Co^{3+} matches vanadium in size (0.61 Å vs 0.58…0.64 Å), while octahedral Co^{2+} exactly matches scandium (0.745 Å). This and the presence of only divalent cobalt suggest that cobalt is only present in the Sc sites rather than in any vanadium sites.

5.4.2.3. Germanium

For d-metals with a partially or fully unoccupied d-shell, no XANES pre-edge features are expected in a regular centrosymmetrical environment; consequently, any violation of centrosymmetry, such as distortion and lowering of the coordination number, would result in a non-zero pre-edge intensity due to relaxation of the parity rule. However, for Ge^{4+} (a p-element) as well as d-species with full d-shells [269], no transitions are expected in the pre-edge region at all and hence only the edge is left for analysis. Similarly, octahedral Ge^{3+} complexes do not have pre-edge features[270], but various noncentrosymmetric Ge^{2+} complexes do[271], save GeS (a mixture of threefold and linear geometries)[272]. The absence of pre-edge features in **Fig. 5.17** (arrow) hints that neither $Sc_2V_{0.8}Ge_{0.2}O_{5+\delta}$ (black) nor standards (colored) contain noncentrosymmetric Ge^{2+} (nor do they have Ge^{3+}, but also due to its unprecedented scarcity). It leaves out Ge^{4+}, in consistence with absent pre-edge features in its other oxide phases with tetrahedral[272], octahedral coordination[273], and mixed eightfold centrosymmetric and fourfold noncentrosymmetric coordination[274]. To solve for the particular coordination environment of Ge^{4+} from spectroscopic data, EXAFS data should be collected and analyzed, which is beyond the scope of this work. However, from **Fig. 5.13** and **Fig. 5.14** it indirectly follows that germanium can populate both octahedral 8*g* and tetrahedral 2*c* sites, consistent with its suitable ionic radius in respective

geometries (**Fig. 5.5**) and most importantly the Rietveld refinement against NPD and XRD data (**Fig. 5.11**).

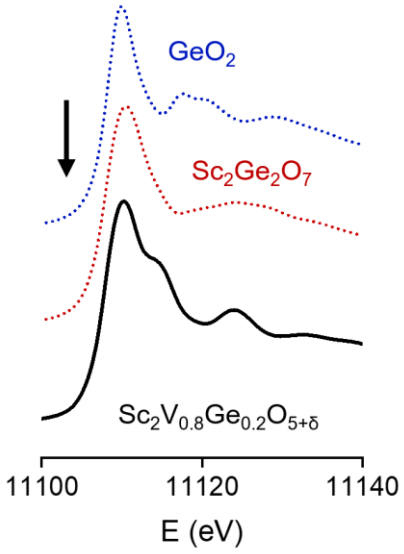

Figure 5.17. A stack plot of K-absorption edges (XANES) of GeO_2 with octahedral Ge^{4+} (blue), $Sc_2Ge_2O_7$ with tetrahedral Ge^{4+} (red), and analyte $Sc_2V_{0.8}Ge_{0.2}O_{5+\delta}$ (black). Pre-edge features are absent as emphasized with a black arrow.

5.5. Conclusion and further considerations

5.5.1. On the $Sc_{1.96\pm0.04}V_{0.82\pm0.05}B_{0.255\pm0.035}O_{5+\delta}$ series

Fig. 5.18 is a plot of the revised concentration of V^{5+} in the $Sc_{1.96\pm0.04}V_{0.82\pm0.05}B_{0.255\pm0.035}O_{5+\delta}$ series as a function of the ionic radius of the B cation from XANES. The plots are very noisy, since data were collected on only a few phases with different charges of the dopants: B^{2+} (Co), $B^{2+\ldots3+}$ (Fe, Mn), B^{3+} (Cr), $B^{3+\ldots4+}$ (V), and B^{4+} (Ge, Ti, Sn). All eight points can still fit into the 95% confidence band of a second-order polynomial (**a**) or a straight line (**b**), the most extreme outlier being the pure vanadate t-$Sc_2VO_{5+\delta}$ which lies in the 95% prediction band of both. A better trend is expected if different oxidation states are separated, for which more data points (phases) are needed. Moreover, lack of phase purity in the samples with Fe, Mn, and Co could have affected the appearance of the data and hence the predictive power of the trend.

5.5.2. Oxygen concentration threshold across the $Sc_2V_{0.8}B_{0.2}O_{5+\delta}$ series

The main goal of doping the t-$Sc_2VO_{5+\delta}$ structure with cations commensurate with vanadium was to observe the capacity of the V sublattice to accommodate ions of various sizes and comment on size-dependent site preferences. Thus, in the virtually single-phase series $Sc_2V_{0.8}B_{0.2}O_{5+\delta}$ with B = Ti, Ge, Sn, and Cr, site preferences of the dopant do depend on its ionic radius (**Fig. 5.11**), especially octahedral (**Fig. 5.14a**), and to a lesser extent – on its redox-activity. The latter was indirectly shown with the *ad hoc* calculator of cation ordering (**Fig. 5.12**) which revealed slightly stronger site preferences for redox-active Cr and V than for the other, redox-inactive cations. However, this too speaks to the role of the cation radius in site ordering, since a redox-active cation changes its radius during a redox reaction.

However, in view of various final (as opposed to nominal) charges of the dopants as quantified with XANES and summarized in **Fig. 5.18** above, doping also invites the opportunity to discuss its effect on the concentration of oxygen in the host structure via non-topotactic means (as opposed to topotactic, like in **Fig. 3.18**). This discussion is provided herein.

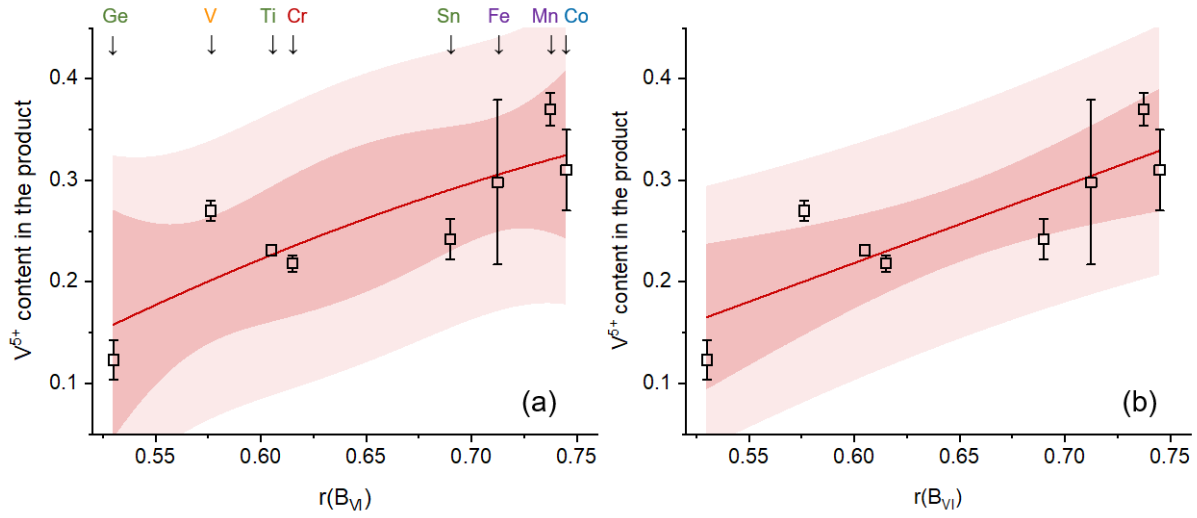

Figure 5.18. Content of V^{5+} (inferred from LCF) plotted as a function of real (from XANES) octahedral radius of B cations in $Sc_{1.96\pm0.04}V_{0.82\pm0.05}B_{0.255\pm0.035}O_{5+\delta}$ phases. Data were generously fitted with a: (a) – polynomial $y = A + Bx + Cx^2$, where A = -0.65(1.66), B = 2.05(5.21), C = -1.00(4.04), R^2 = 0.581; (b) – a straight line $y = A + Bx$, where A = -0.24(13), B = 0.76(21), R^2 = 0.646. Darker and paler bands are 95% confidence and 95% prediction bands, respectively. Doping elements are colored to discriminate among oxidation states: blue 2+, purple 2.5+ (formally), red 3+, yellow 3.7+, green 4+.

The introduction of the lower-charged dopant (lower than the average cation charge on all vanadium in the B sublattice) must meet the cation size requirements of the host structure. It also challenges the lower threshold of oxygen concentration and in the extreme creates too many oxide vacancies for the structure to form. In the t-$Sc_2VO_{5+\delta}$ structure this lower threshold is expected to be met at $\delta = -0.3$, which comes from the fully reduced 8*g* site: $Sc_2V^{3+}_{0.8}V^{5+}_{0.2}O_{4.7}$. From XANES data (**Fig. 5.16**), in $Sc_2V_{0.8}B_{0.2}O_{5+\delta}$ samples with B = Mn, Fe, and Co (impure) lower than nominal oxidation states of the dopants were stabilized at 1100 ºC (**Fig. 5.16**). The smallest δ (around -0.2) occurred in $Sc_2V_{0.8}Cr_{0.2}O_{5+\delta}$ (**Fig 5.10**). In it, chromium mostly replaces vanadium, judging by the refined site occupancies. However, from XANES data (**Fig 5.16i**), nominal Cr^{4+} species undergo reduction to Cr^{3+}, which marginally lowers δ with respect to the all-vanadium t-$Sc_2VO_{5+\delta}$ reference. **Fig. 5.19** illustrates this and other ensuing cases with a diagram, where the height of

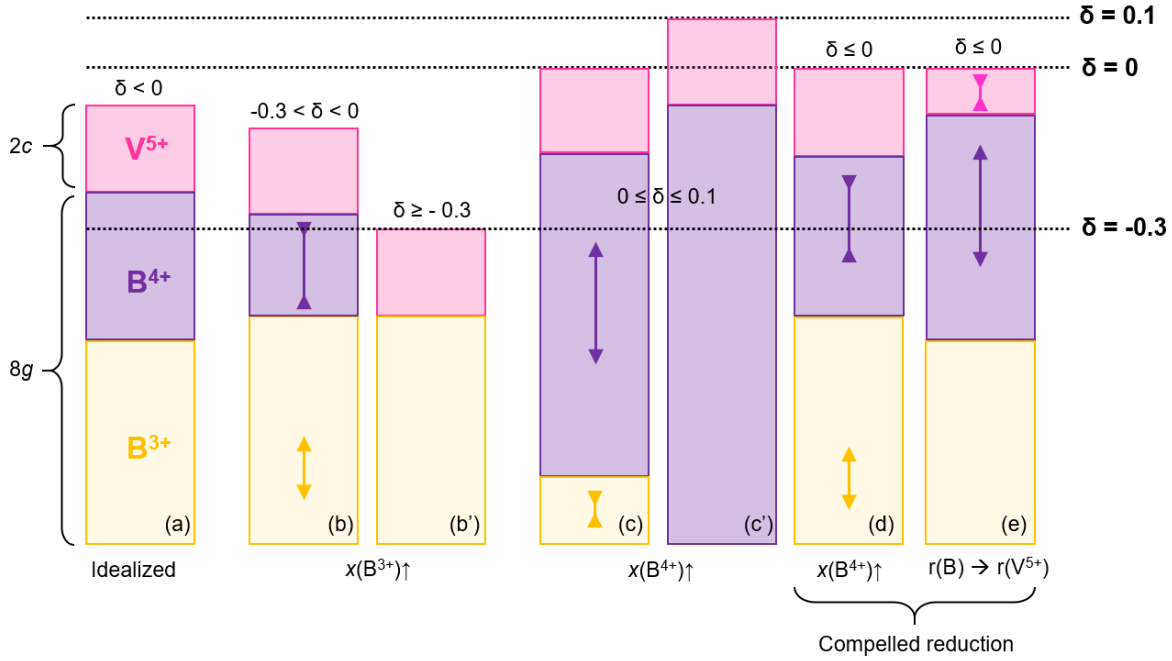

Figure 5.19. Schematic illustration of ways to manipulate δ in $Sc_2V_{1-x}B_xO_{5+\delta}$ by doping the B sublattice and some potential trade-offs: (a) – t-$Sc_2VO_{5+\delta}$ with V^{5+} in the tetrahedral site (magenta) and mixed V^{3+} and V^{4+} in the octahedral site (yellow and purple); (b) – decreasing δ by introducing more of B^{3+}, incl. until there are no more tetravalent cations in the octahedral site (b'); (c) – increasing δ by introducing more of B^{4+} dopant, until the bar "δ=0" (main oxygen sites filled) or "δ=0.1" (c') is reached corresponding to having fully tetravalent 8*g* sublattice if allowed; (d) – an alternative case: if oxygen concentration is limited by $\delta = 0$, introduction of B^{4+} might drive reduction of the redox-active dopant; (e) – case of Ge: if B^{4+} is small enough to fit in the site 2*c*, δ will increase to accommodate B^{4+} but decrease at the same time via relocating V^{5+} from 2*c* to 8*g*, accompanied by its (vanadium) reduction.

yellow, purple, and magenta blocks represents the relative contributions of trivalent, tetravalent, and pentavalent species to the overall charge of the B-sublattice in t-$Sc_2VO_{5+\delta}$-based structures. Three thresholds are shown with black lines:

- $\delta = -0.3$ is the said minimum theoretical threshold of oxygen concentration tolerated by the structure. It corresponds to all-trivalent 8*g* site of the B sublattice. It is close to $\delta = -0.5$, which for the Sc-V-O system means a cubic bixbyite;
- $\delta = 0$ is a threshold nearly reached in this work, corresponding to fully occupied eight known sites of oxygen;
- $\delta = 0.1$ is a theoretical threshold corresponding to only tetrahedral species in the 8*g* site. Somewhere past this point the tetragonal structure oxidatively transitions to the fluorite and then decomposes into a zircon and Sc_2O_3.

The case of Cr is shown in panel **b** where the population of trivalent species in the 8*g* site grows at the expense of the tetravalent species in the same site, resulting in a lower value of δ with respect to its value in as-prepared $Sc_2VO_{5+\delta}$ used as a reference (panel **a**). It is not the same as the theoretical case in panel **d**, where the dopant is forced to reduce when the net oxidation state of the 8*g* site is limited, say, by $\delta = 0$: Cr likely reduces because of its lower chemical potential at high temperature and not because the $Sc_2VO_{5+\delta}$-type structure dictates it.

Further decrease of δ would be possible via increasing the value of *x* in $Sc_2V_{1-x}B^{3+}_xO_{5+\delta}$ (down to the lower limit in panel **b'**) or choosing a dopant with lower final oxidation state (e.g. Co^{2+}), but competing phases such as Sc_3CrO_6, CoO, and various bixbyites started interfering with the formation of a pure product already at $x = 0.2$ (**Fig. 5.8**) and thus complicated the assessment of δ in the major product. Interestingly, since Co^{2+} and Sc^{3+} are equal in size (0.745 Å in CN = VI), cobalt is capable of replacing scandium rather than vanadium, which would lower δ further if a single-phase product (subject to unambiguous analysis of oxygen concentration) had formed.

On the other hand, incorporation of a larger concentration of the 4+ cation into the mixed 3+…4+ sublattice of t-$Sc_2VO_{5+\delta}$ challenges the upper threshold of the allowed oxygen concentration. The largest δ corresponds to exclusively tetravalent vanadium in the 8*g* site: $Sc_2V^{4+}_{0.8}V^{5+}_{0.2}O_{5.1}$. The largest value of δ achieved in the $Sc_2V_{0.8}B_{0.2}O_{5+\delta}$ series was about -0.07 for B = Sn, as per NPD/XRD refinements (**Fig. 5.10**). However, overcoming this limit via increasing the Sn concentration further was again overridden by the formation of competing phases (e.g. $Sc_4Sn_3O_{12}$, **Fig. 5.6**), similar to the case of dopants with lower oxidation states. If $\delta = 0$ is a real upper threshold

(**Fig. 5.19c**), introduction of more B^{4+} will be possible at the expense of decreasing concentration of V^{3+} in the 8*g* site rather than the increase of δ. Alternatively, if δ = 0.1 is the upper threshold, it will be achieved with a tetravalent-only 8*g* site (panel **c'**). DC susceptibility measurements on the recently reported phase $Sc_2V_{0.2}Ti_{0.8}O_{5.1}$[127] are consistent with δ = 0.1 rather than δ = 0 as the upper threshold. It means that panel **c'** rather than **c** is correct.

Notably, from **Fig. 5.10a**, the incorporation of $0.2{\cdot}Ge^{4+}$ or $0.2{\cdot}Ti^{4+}$ did not result in the same value of δ as incorporation of the same amount of Sn^{4+}. It is due to different size-dependent site preferences of the cations: smaller Ge^{4+} partially occupies the 2*c* site as per **Fig. 5.11**, replacing highly charged V^{5+}. Thus, half of V^{5+} species naturally preferring the 2*c* site is forced into the 8*g* site, likely requiring reduction of vanadium, as schematically illustrated in **Fig. 5.19e**. It means that control over the concentration of vacancies depends not only on the charge of the dopant species, but also on its ionic radius.

Thus the strategy of manipulating δ by doping (non-topotactically) in an ideal single-phase $Sc_2V_{1-x}B_xO_{5+\delta}$ phase can be summarized as follows (see **Fig. 5.19**):

- Introduction of a stable tetravalent cation commensurate with octahedral vanadium (Ti, Sn) increases δ: larger *x* increases δ beyond zero;
- Introduction of a trivalent cation (Cr, even if nominal tetravalent) decreases δ;
- Introduction of a tetravalent cation commensurate with vanadium in the site 2*c* (Ge) decreases δ;
- Another extreme case is the introduction of a large cation commensurate with Sc^{3+}. Successful doping corresponding to this case was not achieved because of the competing phases, but by extension of the same logic a lower-charged cation (Co^{2+}) will decrease δ, while a higher-charged one (Zr^{4+} or better larger) will increase it.

5.5.3. Phases competing with the A_2BO_5 stoichiometry

Regarding the competing phases encountered in **Fig. 5.6** and **Fig. 5.8**, they are thermodynamic products of alternative reaction paths available for the same cations (as in $Sc_2V_{1-x}B_xO_{5+\delta}$) under the same synthetic conditions. As it was seen in **Fig. 5.4** and was observed elsewhere[275] no straightforward and rigorous difference in temperature regimes exist between ordered $A_2B_2O_7$ ($Fd\bar{3}m$ or $C2/m$) and $A_4B_3O_{12}$ ($R\bar{3}$) oxides that share the same A and B cations. Formation of any

of these two alongside the desired A_2BO_5-type phases might owe to poor grinding of the starting material, so that the local ratio of AO_x and BO_y grains is not 2:1 but rather 1:1 (2:2) or 4:3. In this case, better grinding of the starting material can overcome this problem. However, ball milling seems to drive reduction of vanadium (contradicting previous observations[83], unless the reduced species was tin). It was also proposed that a competition of factors such as time, temperature, crystalline domain size, defect energy, and sometimes pressure takes place, which defines whether the kinetic or the thermodynamic product of these stoichiometries will form[7,275]. **Fig. A-5.1** illustrates some phases from four competing families in question: A_2BO_5, $A_2B_2O_7$, $A_4B_3O_{12}$, and $AO_{2-\delta}$, where A = Al, Ga, V, Ti, Fe, Sc, In, Y, Ln and B = Si, Ti, V, Mn, Ge, Sn, Zr, Ru. The Y axis of the plot is the volume of the unit cell (V/Z), while the X axis represents the ratio of the average radius of the net cation to the radius of oxygen (1.38 Å everywhere, for simplicity). The clear separation of the four families is likely due to the different number of atoms per unit formula – eight for A_2BO_5, 11 for $A_2B_2O_7$, 19 for $A_4B_3O_{12}$, and three for $AO_{2-\delta}$ (although all fluorites considered were reported in one of the three other stoichiometries. Along the X axis the real radii were plotted, i.e. stoichiometry and coordination numbers taken into account, as opposed to considering radii in the same coordination environment. This makes **Fig. A-5.1** a post-factum description of the structural families rather than a tool for predictions, unlike some other diagrams – the r(B)-r(A) space[275] or the ρ_c-ρ_a space[7] (where ρ_c is the ratio of the cation size to the average cation size in the formula and ρ_a is the cation-to-anion size ratio, see ***Chapter 7***). A similar assessment, including in various phase spaces, should be done with as many similar parameters (those which can distinguish among competing phases) as possible in order to be able to predict formation of competing phases[Q]. Recent success with improving predictions of the perovskites formation via a machine learning (ML) algorithm[276] suggests ML can be promising in this endeavor as well.

[Q] As a first guess, all three presented stoichiometries can be imagined as oxygen-deficient with respect to the fully oxidized fluorite aristotype AO_2, and the concentration of oxygen vacancies (□) in each family can be such a distinguishing factor: 1/6 in A_2BO_5□, 1/7 in $A_4B_3O_{12}$□$_2$, and 1/8 in $A_2B_2O_7$□.

CHAPTER 6

Pseudocubic c-$Sc_2VO_{5+\delta}$

$Sc_2VO_{5+\delta}$ exists in two modifications. The ordered t-$Sc_2VO_{5+\delta}$ phase can form oxidatively from $Sc_2VO_{4.5}$ at 800 ºC as was mentioned in ***Chapter 3***. The disordered alternative c-$Sc_2VO_{5+\delta}$ forms oxidatively at ~350 ºC from the same precursor. In both $Sc_2VO_{5+\delta}$ structures, much larger Sc^{3+} ions coexist with much smaller V^{5+} ions, but both cations occupy the same crystallographic site in the fluorite, as follows from the average structure analysis. The current chapter reconciles this disorder and the intuition that the oxygen environment around these two cations should differ locally as a result of cation size and charge differences.

6.1. Average structure of c-$Sc_2VO_{5+\delta}$

In **Fig. 3.13b**, c-$Sc_2VO_{5+\delta}$ was shown as a part of the redox scheme. If only the oxidative paths are concerned and only the vanadium coordination is emphasized, the same figure can be redrawn as **Fig. 6.1**. Here, the oxidation of $Sc_2VO_{4.5}$ (CN=VI) to c-$Sc_2VO_{5+\delta}$ (CN ≤ VIII) and finally to $ScVO_4$ (CN = IV) passes through a maximum in CN dictated by the fluorite structure – oxidative route "1". The Rietveld plot for this structure against synchrotron X-ray and neutron powder diffraction data is shown in **Fig. 6.2**, while relevant crystallographic data are summarized in **Table A-6.1**. Another oxidative route is possible – route "2", which is the oxidation of t-$Sc_2VO_{5+\delta}$ (CN = IV and VI) to c-$Sc_2VO_{5+\delta}$ and to $ScVO_4$; it also passes through a similar maximum. In this maximum, the ionic radii of Sc^{3+} and V^{4+} (the only published cubic Shannon radius for vanadium[103]) are 0.87 and 0.72 Å, respectively, which produces a 21% size difference. While this ratio is not much larger than the 15% used as a tentative threshold for site mixing in substitutional solid solutions, it is expected to increase for smaller V^{5+} which is moreover known to favor much smaller coordination (CN = IV or V) than that of a fluorite (CN = VIII from average structure description or CN = VII locally, if oxygen vacancies are accounted for). It can be noticed:

(1) The existence of this maximum does not agree well with the anticipated gradual shrinkage of vanadium from its trivalent to its pentavalent state. In other words, vanadium changes its

coordination environment from larger octahedral to smaller tetrahedral through an intermediate seven- or eightfold coordination, the largest.

(2) In terms of cationic ordering, both oxidation routes seem to pass through the fully disordered fluorite regardless of cation ordering in its immediate precursor – cation disordered bixbyite in the first route or the cation-ordered superstructure in the second route – in **Fig. 6.1a** yellow and green polyhedra represent ordered and disordered cation sites, respectively.

Both points (1) and (2) are addressed separately in the upcoming sections.

6.2. Local cation ordering

6.2.1. Vanadium XANES

The two oxidation routes in **Fig. 6.1** were also followed with *in-situ* X-ray absorption near-edge structure spectroscopy (XANES), and the results are plotted in **Fig. 6.3**. In the absorption pre-edge energy range for a centrosymmetric cationic environment, such as CN = VI (bixbyite) and VIII

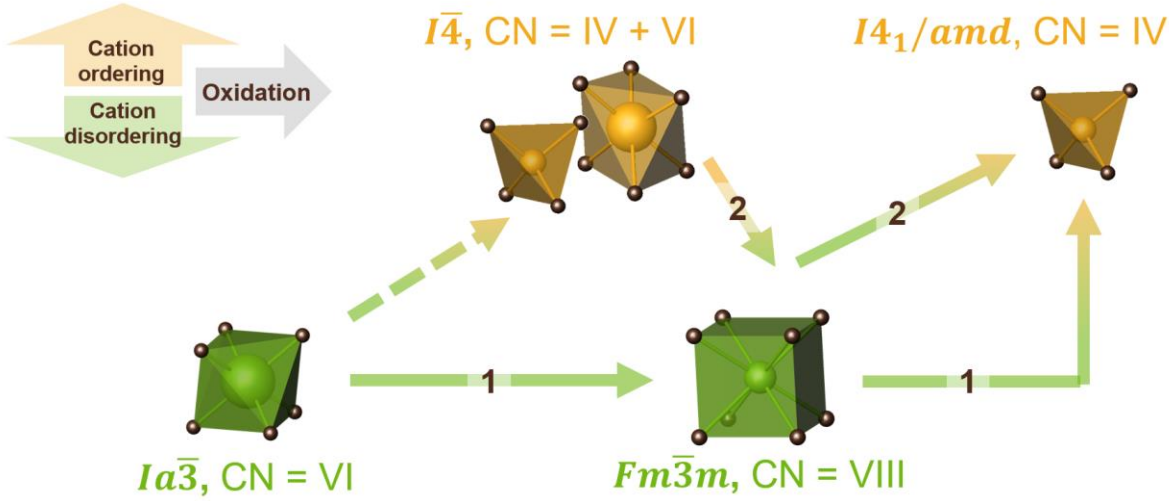

Figure 6.1. Coordination geometry around vanadium in the oxidation route 1, $Sc_2VO_{4.5}$ ($\boldsymbol{Ia\bar{3}}$) → c-$Sc_2VO_{5+\delta}$ ($\boldsymbol{Fm\bar{3}m}$) → $ScVO_4$ ($\boldsymbol{I4_1/amd}$) and oxidation route 2, t-$Sc_2VO_{5+\delta}$ ($\boldsymbol{I\bar{4}}$, can be obtained from $Sc_2VO_{4.5}$) → c-$Sc_2VO_{5+\delta}$ → $ScVO_4$ as expected from the average structure derived from powder XRD. Cation order and disorder are shown as yellow and green vanadium polyhedra, respectively, and oxygen is in brown.

(fully oxidized fluorite[R]), no strong pre-edge features are to be expected. This is due to the symmetry-forbidden transitions from the *s* character core level to the unoccupied *d* character states of the accepting molecular orbital, responsible for absorption features in this energy range. By contrast, lack of centrosymmetry within the coordination polyhedron, such as in tetrahedral environments (e.g. zircon $ScVO_4$) or any strongly distorted environments, introduces the *p* character to the receiving molecular orbital(s). In the figure, bixbyite $Sc_2VO_{4.5}$ with two types of $[VO_6]^{9-}$ units has a weak pre-edge feature (panel **a**, yellow) owing to only mild distortion; in contrast, zircon $ScVO_4$ (black) shows a strong pre-edge peak associated with short bonds in CN = IV. Similarly, tetragonal $Sc_2VO_{5+\delta}$ (panel **b**, green) has a fairly strong pre-edge feature caused by tetrahedral V^{5+} species comprising at least 20 % of the vanadium sublattice (**Fig. 3.5 c,d**), which is still weaker than the pre-edge of $ScVO_4$ where all vanadium adopts CN=IV. Unexpectedly for the fluorite with its large centrosymmetric coordination, the corresponding absorption feature is huge. This indicates that the coordination environment around vanadium in c-$Sc_2VO_{5+\delta}$ is either very strongly distorted or non-centrosymmetric, or both. The strong intensity is unlikely to only

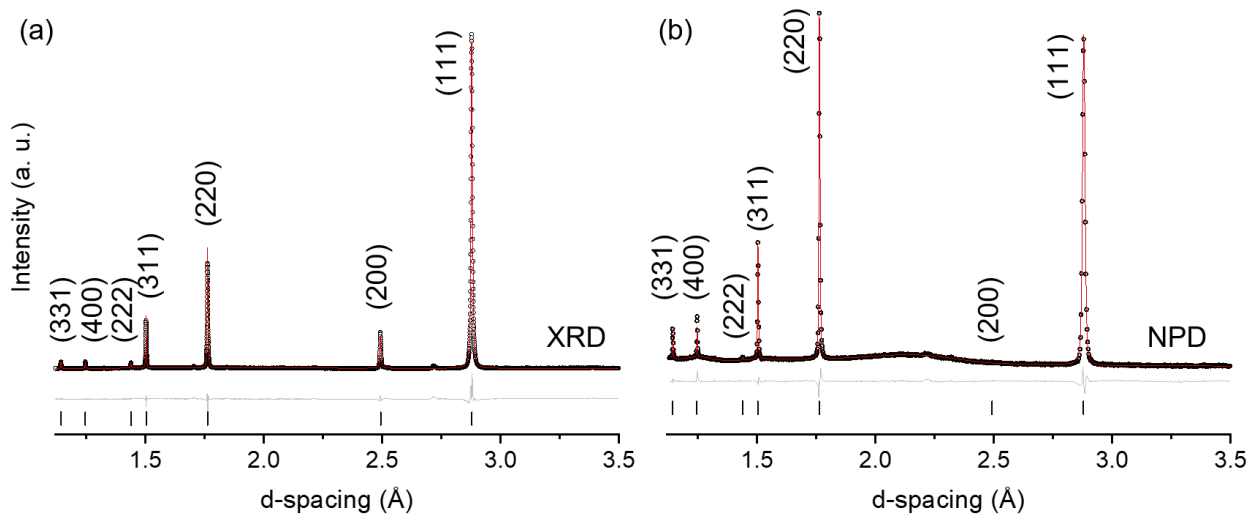

Figure 6.2. Rietveld plots of c-$Sc_2VO_{5+\delta}$ (oxidation product of $Sc_2VO_{4.5}$) refined against synchrotron X-ray (λ = 0.412839 Å, panel *a*) and neutron (*b*) powder diffraction data: black circles – experimental data, red line – calculated pattern, grey line – difference, vertical ticks – Bragg peak positions. For crystallographic details and constraints – see ***Appendix 6***. From the good agreement between data and model, the average cubic fluorite description of this phase is very reasonable.

[R] Notably, fully oxidized Sc-V-O fluorite is $Sc_2VO_{5.5}$, i.e. the maximum anion:cation ratio is 1.8:1, not 2:1. It implies that eightfold coordination of cations might not be reached, as is mentioned further in the chapter.

stem from CN=VII (incomplete cube) also expected in a defect fluorite or from a sufficiently distorted cube, since a high intensity pre-edge peak is expected for short metal-ligand bonds rather than lack of centrosymmetry *per se* [168].

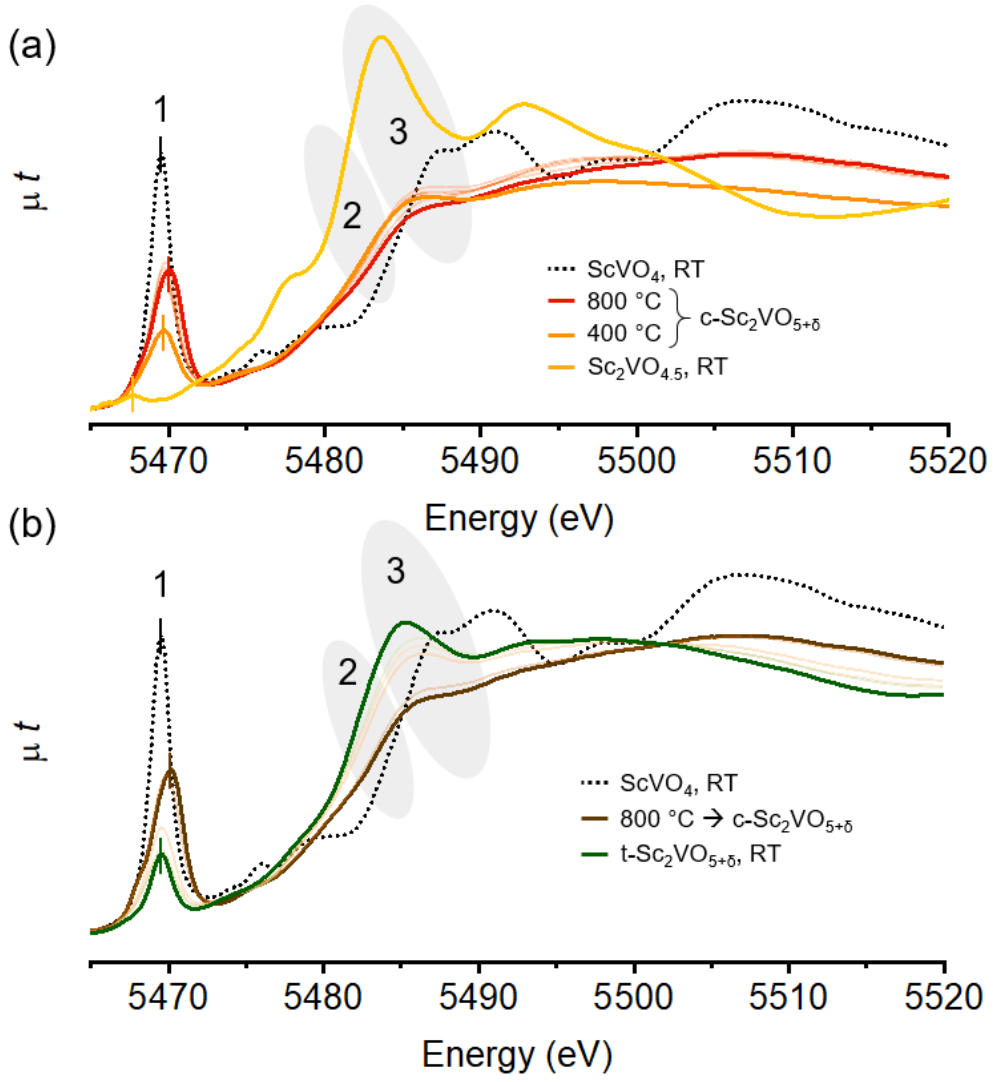

Figure 6.3. *In-situ* oxidation of $Sc_2VO_{4.5}$ (a, yellow) and t-$Sc_2VO_{5+\delta}$ (b, green) in O_2/He flow followed with XANES on the K absorption edge of vanadium (5465 eV). Superimposed are RT data on $ScVO_4$ from an independent measurement, for peak position and shape reference (dotted black). Numbers are regions of interest: 1 – pre-edge, 2 – edge jump, 3 – edge. Faded lines are spectra collected between: (a) – 600 ºC and 750 ºC; (b) – 600 ºC to 800 ºC.

6.2.2. X-ray and neutron PDF

Total scattering experiments were performed on both c-$Sc_2VO_{5+\delta}$ samples – obtained from $Sc_2VO_{4.5}$ (**Fig. 6.4a**) and from t-$Sc_2VO_{5+\delta}$ (**Fig. 6.4b**). Blue and red curves are, correspondingly, X-ray and neutron G(r)-PDF data. In both inserts, bond distances pertaining to the first two coordination spheres of c-$Sc_2VO_{5+\delta}$ are emphasized. Present in both blue traces are two large peaks corresponding to metal-oxygen distances of 1.7 Å and 2.1 Å. The longer metal-oxygen bond distance (2.1 Å) is close to the expected metal-oxygen bond in the fluorite[S] and very typical of vanadium species V^{3+} and V^{4+} in coordination environments larger than tetrahedral as well as for

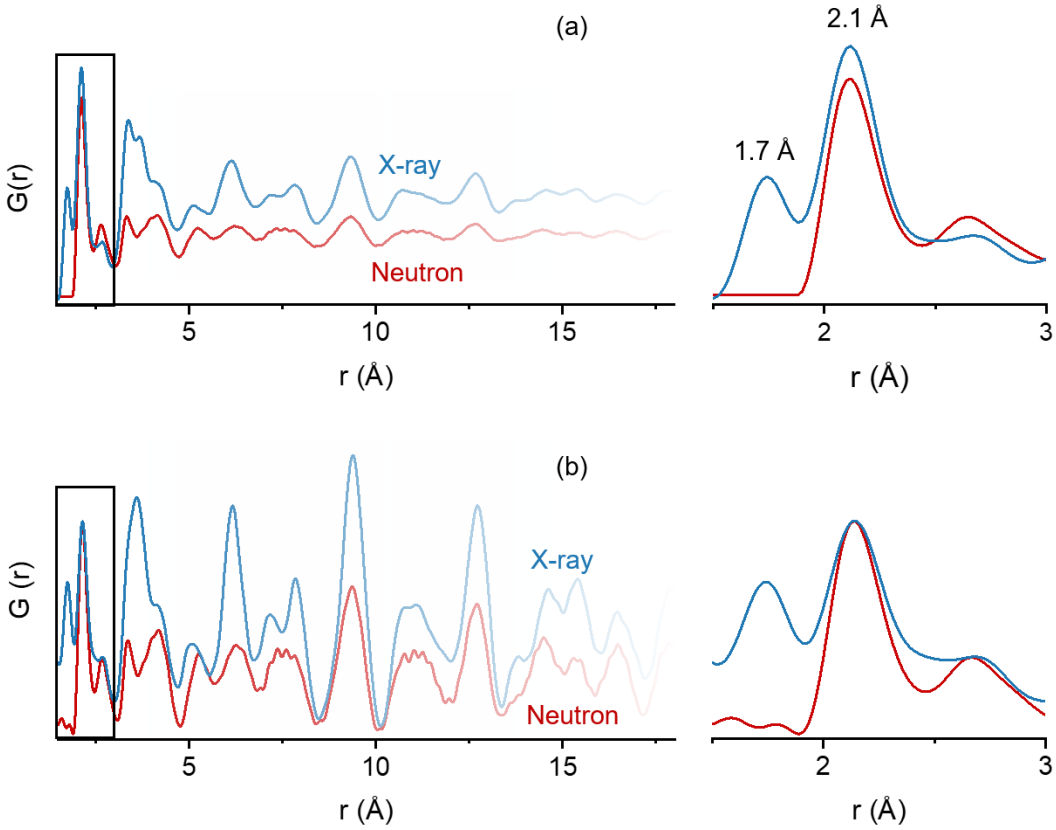

Figure 6.4. X-ray (blue) and neutron (red) pair distribution function data on two c-$Sc_2VO_{5+\delta}$ samples: (a) – obtained from $Sc_2VO_{4.5}$; (b) – obtained from t-$Sc_2VO_{5+\delta}$ (contains small impurities of Sc_2O_3 and $ScVO_4$). Left panels show a larger range of data, while the right panels zoom into the framed region to reveal the peaks pertinent to the first and second coordination spheres. Shorter and longer metal-oxygen bond lengths are indicated.

[S] Metal-oxygen bond lengths ($\overline{A-O}$) in the cubic fluorite with the edge length *a* are equal to one quarter of the body diagonal of the unit cell: a ≈ 5 Å => $\overline{A-O} \approx 5 \cdot \sqrt{3}/4 = 2.1$ Å.

scandium. The shorter distance, is characteristic for tetrahedral V^{5+}_{IV}-O bonds, such as in t-$Sc_2VO_{5+\delta}$, $ScVO_4$, etc. Since vanadium is the only neutron-transparent species in the system, the absence of this peak (1.7 Å) in both red curves (neutron PDF) is evidence that this bond is only formed between vanadium and oxygen, not scandium and oxygen. Hence this is the bond distance responsible for high intensity of the vanadium pre-edge feature in XANES (both panels of **Fig. 6.3**).

Bond distances and the overall structure were obtained from a multihistogram PDF refinement of the local structure of c-$Sc_2VO_{5+\delta}$ obtained from $Sc_2VO_{4.5}$. The refinement was done on an 8×8×8 supercell which initially contained disordered cations (1366 Sc atoms and 682 V atoms) and disordered anions (3584 O atoms and 512 oxide vacancies). At least three independent refinements were done with the number of moves ranging from 1 to 12 million and *r* value limited to 3, 5, 10, and 20 Å. The lower *r* limit was considered to better fit the peaks below 3 Å. However, the difference in the fit quality is marginal between the best fits (r = 3 and 5 Å) and the second best fits (r = 10 and 20 Å). In the discussion below, the refinement with r_{max} = 20 Å was used. 50 independent refinements were done for this *r* range. Fits for one of them are presented in **Fig. 6.5**[T]. The stoichiometry used in the PDF refinement was $Sc_2VO_{5.25}$ (δ = 0.25) as obtained from a preliminary NPD Rietveld refinement of the average structure. The composition reported in **Table A-6.1** is $Sc_2VO_{5.17(1)}$ as obtained from a joint synchrotron XRD + NPD refinement. Given the ~90% correlation between δ and B_{iso}, the two compositions are in reasonable agreement, especially for the purpose of comparison of V and Sc coordination and overall distribution of ions in the structure.

The refined structure is shown in polyhedral representation in **Fig. 6.6a**. Notably, orientation of polyhedra, CN, and Sc-V mixing pattern differ after every run, since polyhedra and cation positions are disordered. A more reproducible pattern thereof is the folded RMC structure in **Fig. 6.6b** which is a jusxtaposition of 512 fluorite-like individual cells onto one. This view shows clusters of ions around their expected special positions: oxygen around (¼ ¼ ¼) and mixed Sc/V around (0 0 0). The spreadout clusters in place of ions in special positions are in agreement with large B_{iso} values of 4.45(1) Å^2 for cations and 8.93(6) Å^2 for anions from the average structure refinement. It is suggested that oxygen shifts toward vanadium to form shorter V-O bond distances

[T] Together with pair distribution function G(r), two related functions were fitted simultaneously for better reliability: total-scattering factor F(q) and differential correlation function D(r). For relation between them – see Keen, 2001[158].

(1.73 Å, in X-ray PDF data), but from this image alone it is not immediately apparent whether vanadium shifts too. However, it is seen that on the scale of 512 unit cells there is no anisotropic shift of any cluster in any direction. Thus, the "average local" structure is consistent with the average structure in that c-$Sc_2VO_{5+\delta}$ is a disordered fluorite. Closer examination of the folded RMC structure led to the discussion of conductivity and bonding, presented in the ensuing sections.

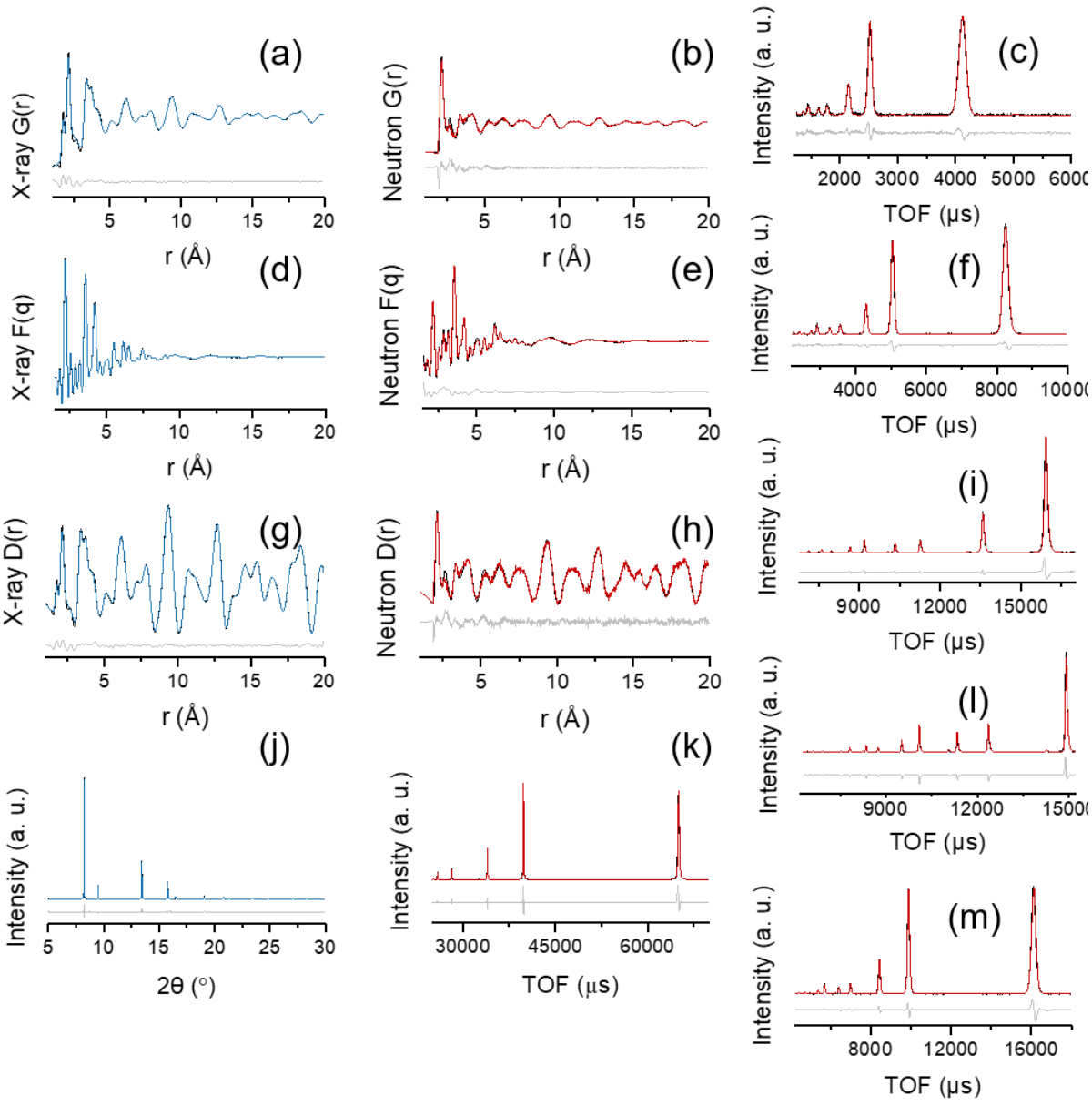

Figure 6.5. Results of fitting the c-$Sc_2VO_{5+\delta}$ structure in RMCProfile against: (a) and (b) – G(r) data; (d) and (e) – F(q) data; (g) and (h) – D(r) data; (j) – synchrotron powder XRD data; (c), (f), (i), (l), and (m) – NOMAD NPD data; (k) – POWGEN NPD data. Black – measured, red – neutron fit, blue – X-ray fit, grey – difference.

6.2.2.1. RMC structure as the foundation of the future conductivity work

Similar diffuse oxide clusters[277] and related broad distributions of oxygen bond lengths[278,279,280] have been reported in RMC cells of some oxide ion conductors[U]. It suggests that displacement of oxide ions in the PDF data, including data measured at room temperature, might be connected to its mobility in an ion conducting material. Fluorite-type structures are known to be prone to oxide ion conduction[3,281], and although measureing oxide ion conductivity in c-$Sc_2VO_{5+\delta}$ was beyond the scope of the thesis, several related observations can be made. In a fluorite structure, O^{2-} conduction is realized either (1) directly from occupied oxygen site to unoccupied oxygen site or (2) through an intermediate octahedral void, empty in fluorites[282,283]. This is illustrated in **Fig. 6.7a, b** on a fragment of a fluorite unit cell with relevant metal ions (blue), oxides (red), oxide vacancies (red-yellow), and octahedral voids (black). The first mechanism is associated with an oxide ion passing through a line connecting two metal ions (let's call it a dyad, panel *a*), while in the second mechanism it passes through two triades of metal ions to temporarily occupy an

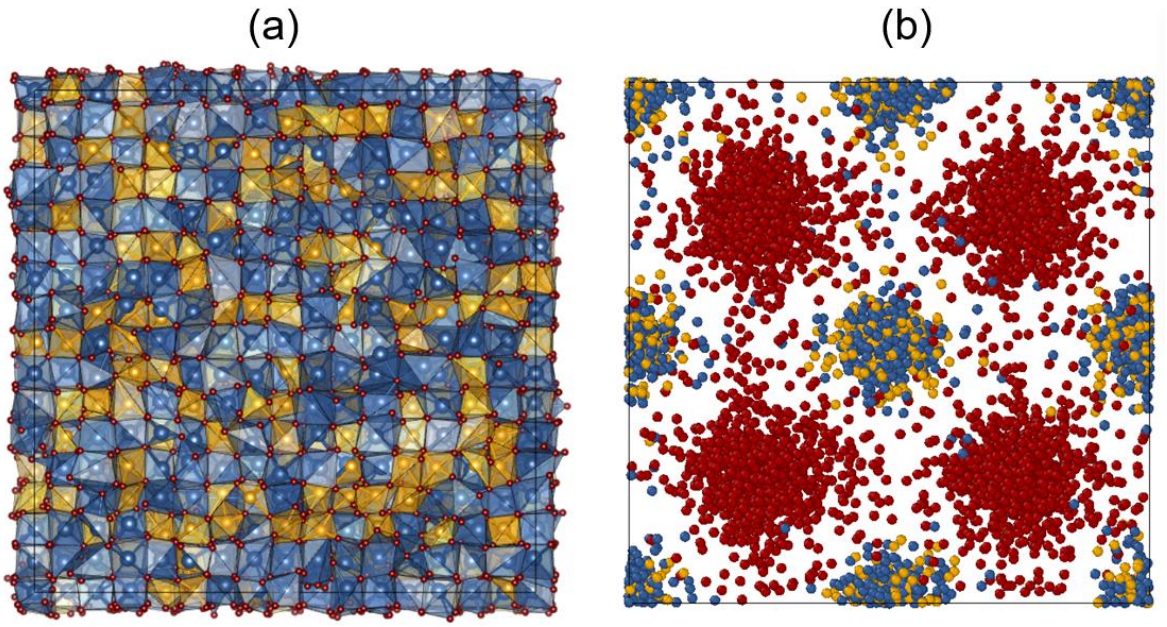

Figure 6.6. Refined supercell of c-$Sc_2VO_{5.25}$, viewed along the *X* axis: (a) – polyhedral representation; (b) – juxtaposition of 512 cells onto one unit cell, illustrating diffuse clusters of Sc (blue), V (yellow), and O (red) ions expected from their large B_{iso} values.

[U] Diffuse O^{2-} clusters were shown in ion-conducting phases, including but not limited to the fluorite type. Some fluorite structures do not have this property[310].

octahedral void (panel *b*). It is suggested that displacement of oxides toward dyads or triads of metal ions can be a prerequisite for oxide ion conduction via one of these two mechanisms. Panels **c** and **d** of **Fig. 6.7** are representative slices of the folded RMC structure along (020) and (111) planes that pass through some of the metal dyads (see green line) and triads (see blue triangle). Displaced oxides are much more anticipated in the (111) plane than in the (020) plane but are

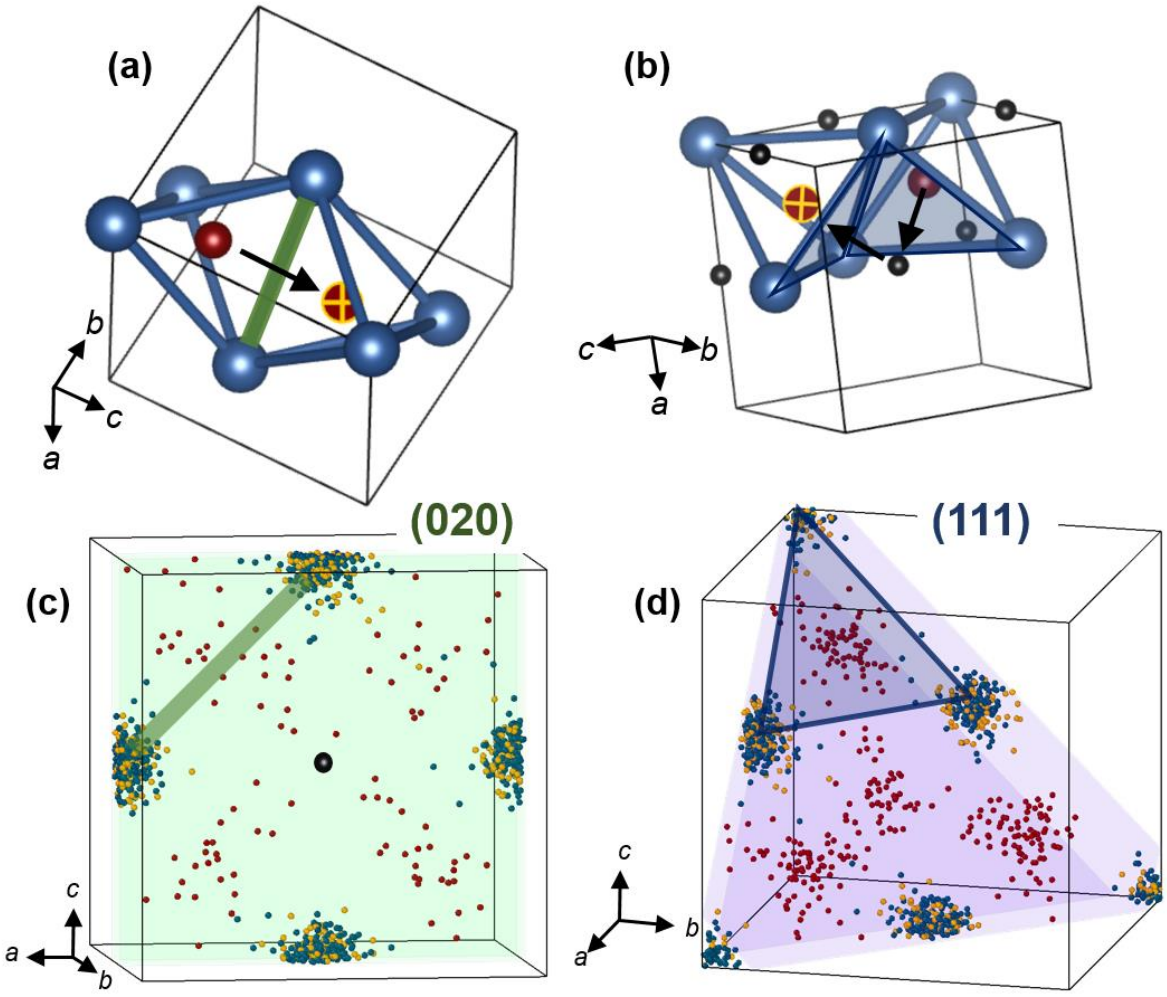

Figure 6.7. Oxide ion displacement in the fluorite structure: (a) – schematic illustration of one possible displacement path lying between oxygen sites during conduction, i.e. crossing a metal-metal dyad (line); (b) – another possible mechanism – through an intermediate octahedral void, crossing two metal triads (triangles); (c) – (020) plane of the folded RMC structure of c-$Sc_2VO_{5+\delta}$ showing displaced oxides in the plane of dyads like the one highlighted; (d) – (111) plane showing displaced oxides in the planes of triads like the one highlighted. Each plane is a 0.75 Å-thick slab. Blue – centers of metal ions (a,b) or only Sc (c,d), yellow – V (c,d), red – oxides (a-d), red/yellow – vacancies (a,b), black – octahedral voids (b,c).

present in both[v]. Planes (110) and (400) are presented in **Fig. 6.8**. Plane (110) cuts through metals, oxides, and some octahedral voids. Plane (400) cuts exclusively through oxygen sites. Displaced oxides between oxygen sites would favor the first mechanism, whereas oxides in octahedral holes would favor the second mechanism. Both planes (110) and (400) suggest oxides are scattered between oxygen sites, especially the closest ones, but not so much around the octahedral voids. If

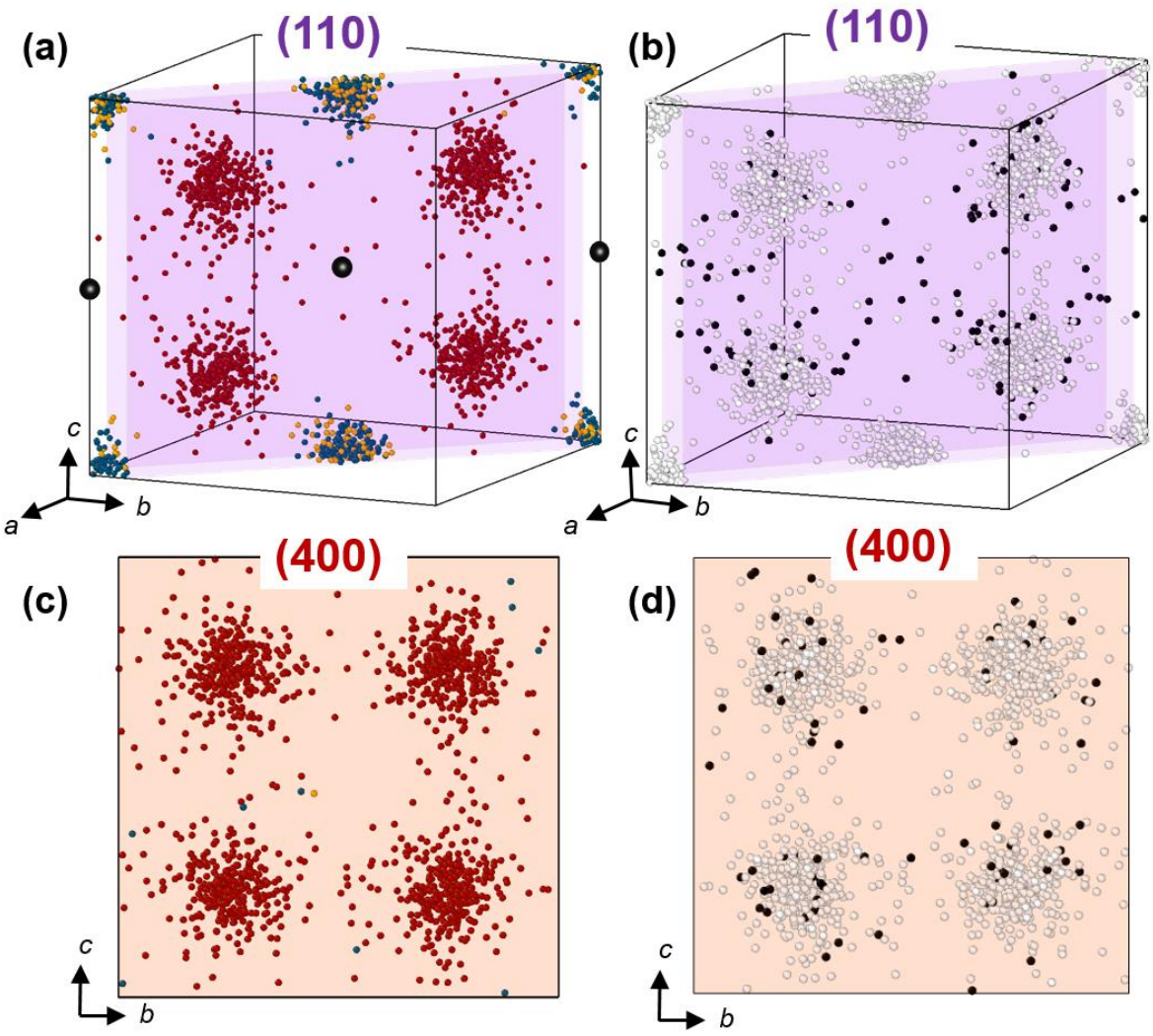

Figure 6.8. (110) and (400) planes in the folded RMC structure of c-$Sc_2VO_{5+\delta}$, passing through: (a) – oxygen sites (red), Sc/V sites (blue/yellow), octahedral voids (black); (b) – same, but with oxygen vacancies shown (black) and the rest – hidden or faded; (c) – only oxygen sites; (d) – same but with oxygen vacancies shown (black). Each plane is a 0.75 Å-thick slab.

[v] There are more oxides in the (111) plane than in (020), but this is a consequence of geometry: any oxygen in the center of a metal tetrahedron is closer to the face of the tetrahedron (metal triad) than to its edge (metal dyad).

oxide displacement in the static RMC structure is indeed telling of oxide ion conduction, the mechanism of hopping from occupied oxygen site to vacant oxygen site is more readily available in c-$Sc_2VO_{5+\delta}$. It should be noted that displacement of oxides is not tantamount to oxide migration: oxide ions migrate via vacancy hopping. Oxide ion vacancies are emphasized in panels **b** and **d** separately. In the (110) plane they are scattered between oxygen sites similar to displaced oxides, perhaps slightly closer to the octahedral holes. while in the (400) plane they are concentrated around the oxygen sites. Thus the arrangement of oxide ion vacancies in this RMC structure does not contradict the assumption that oxide ions would prefer to migrate through the metal dyads, given the right potential and temperature are applied. To check this prediction, high-temperature

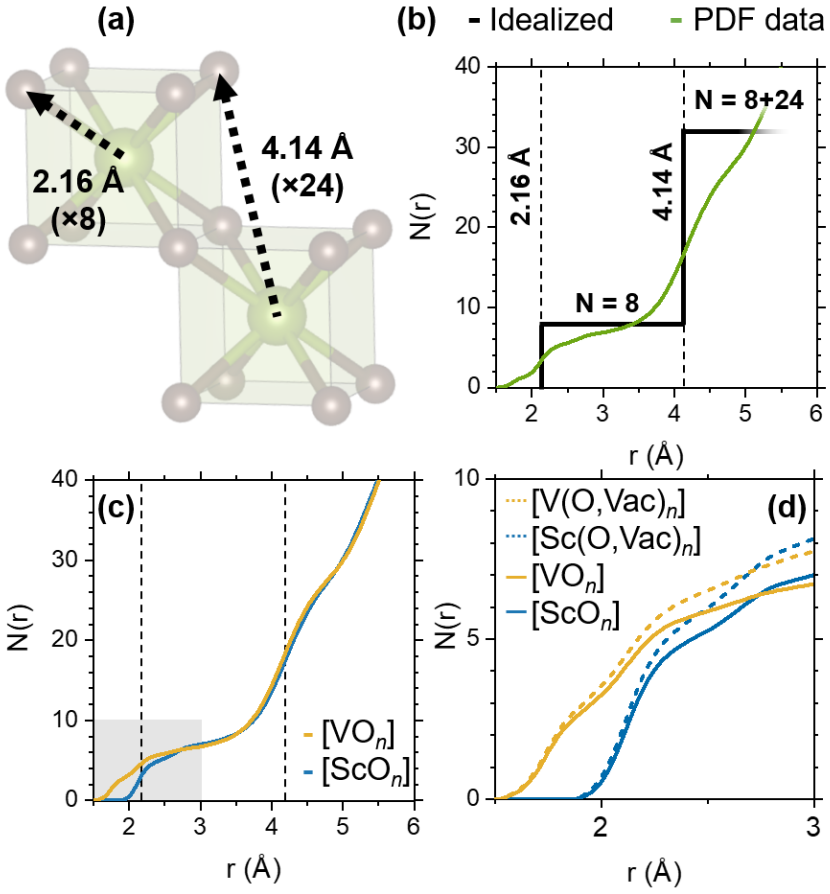

Figure 6.9. V-O and Sc-O bond distances in c-$Sc_2VO_{5+\delta}$: (a) – idealized metal-oxygen cubes as expected from the average structure with the two shortest bonds indicated; (b) – expected idealized (black), i.e. in the absence of atomic vibrations, and real (green) N(r) profiles for the (Sc/V)-O bonds; (c) – experimental N(r) plot for V-O (yellow) and Sc-O (blue) correlations with average metal-oxygen bond lengths plotted as references; (d) – enlarged shaded area from panel *c* with two new lines (dotted) accounting for O^{2-} vacancies.

PDF data (350 ºC ≤ T < 700 ºC) would be required. However, already at this stage it should be appreciated that a static RMC structure stimulates the inquiry into dynamic processes.

6.2.2.2. V-O, Sc-O, O-O, Sc-Sc, V-V coordination

Metal-oxygen coordination. **Fig. 6.9a** is a fragment of the average structure of disordered c-$Sc_2VO_{5+\delta}$. The two shortest (Sc/V)-O bonds are indicated, comprising the first coordination shell with 8 oxygen neighbors and the third coordination shell with 24 oxygen neighbors (the second shell consists of the shortest metal-metal bonds). Local-scale information on bond lengths *r* and the number of neighbors *N* at a distance *r* from each other was obtained from the RMC refinement in the form of a correlation number plot *N(r)*. A typical *N(r)* plot is a step function whose "steps" correspond to single *N* values per range of *r*[162,284]. A correlation number plot expected for the structure in panel *a* (but idealized – no atomic displacement) is given in black in **Fig. 6.9b**, with average (Sc/V)-O bonds shown as dotted lines for reference. The real *N(r)* plot is superimposed in green; it was obtained as an average of Sc-O and V-O correlations. Due to the disorder of both cations and anions, the distribution of bond distances was broadened, which resulted in less defined steps. Sc-O and V-O correlations are plotted separately in **Fig. 6.9c**. The plots overlap after ~3.5 Å, as expected for disordered cations, but show a stark difference at small *r*, enlarged in **Fig. 6.9d**. The difference is the additional feature in the V-O correlation plot, stemming from the PDF peak at 1.73 Å in the raw X-ray PDF data (**Fig. 6.4a**). It can be seen that below 3 Å: (1) at any fixed *r*, V^{x+} ions have more oxygen neighbors than Sc^{3+} ions do, while (2) at any fixed *N*, Sc-O bond distances are longer than V-O distances. This means that despite the overall cation disorder, there are local differences in V and Sc environment. It is reasonable to expect shorter V-O bonds to mostly form around V^{5+} rather than around V^{4+}-, since V^{5+} is smaller than V^{4+} in any coordination environment. From literature, the average V^{5+}-O bond distance is 1.717(56) Å[285] in its most widely occurring CN = 4, which agrees with the identified distance of ~1.73 Å. All other bond distances are expected to mostly contribute to the peak at 2.12 Å as shown in **Fig. A.6-1** where the most frequently occurring V-O and Sc-O bond lengths are superimposed on the first two peaks of the X-ray PDF data.

Fig. 6.9d also shows net correlation numbers around V (dashed, yellow) and Sc (dashed, blue). Net *N* accounts for both oxide ions (corresponds to solid lines) and vacancies (not shown

separately); it reaches the expected value CN = VIII in the shown range of *r*. From N(r) plots, vacancies can be found at larger distances from the metal; e.g. at *r* = 1.73 Å there are only O^{2-} anions around V^{x+} (V^{5+}) cations.

Fig. 6.9 shows the distribution of neighboring ions at particular distances from the central ion but does not imply that ions at shorter (longer) distances form their own polyhedra with smaller (larger) CN. Complementary to **Fig. 6.9** is **Fig. 6.10** which shows actual coordination numbers of [VO_n] and [ScO_n] polyhedra limited by a reasonable value or r_{max} = 3.0 Å. From this histogram, more than half of the [VO_n] polyhedra found in the 8×8×8 supercell are [VO_7] (33%) and [VO_6] (27%), correspondingly. These numbers are followed by [VO_8] (20%), [VO_5] (12%), etc. All these polyhedra were distorted, and many are non-centrosymmetric by definition (*n* = 4, 5, 7). As a result, the intense pre-edge feature in XANES should likely be explained by several factors: short V-O distances, non-centrosymmetric [VO_n] polyhedra, and polyhedral distortion, rather than one particular common type of polyhedron. Notably, these shorter V-O bonds coexist with longer V-O bonds within the same polyhedra, and not a single [VO_n] polyhedron based on exclusively short bonds was found in the RMC structure that was used to prepare **Fig. 6.5**.

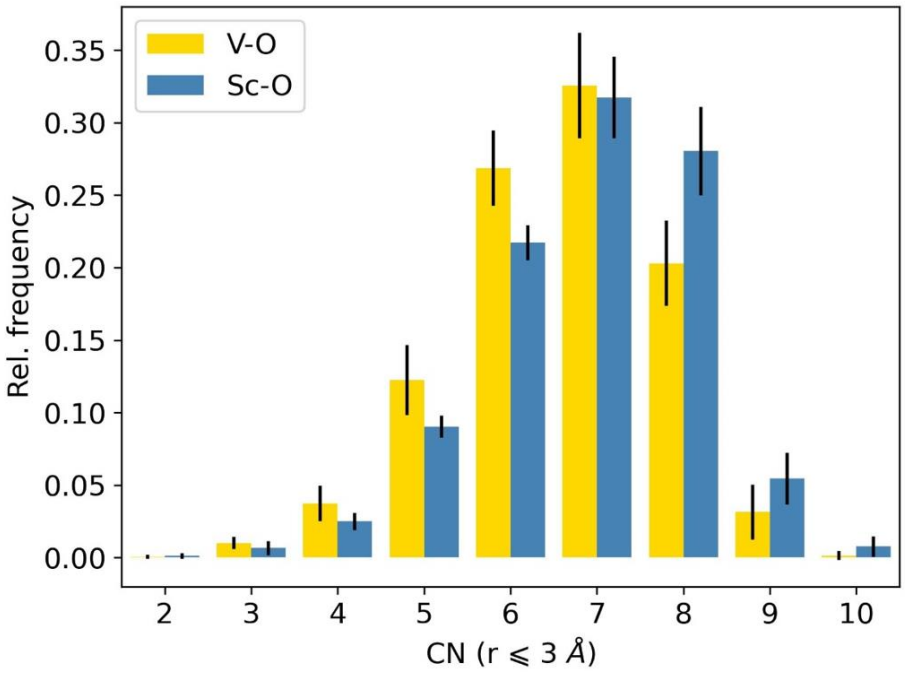

Figure 6.10. Coordination numbers of [VO_n] (yellow) and [ScO_n] (blue) polyhedra in c-$Sc_2VO_{5+\delta}$ from its local structure refinement. Bond lengths are limited by r_{min} = 1.6 Å and r_{max} = 3.0 Å. Averaged over 10 independent refinements.

Overall, vanadium shows preference toward shorter bonding with oxygen than scandium does, despite cation disorder. [ScO_n] polyhedra have a preference for n = 7, 8, and 6 (in this order) while [VO_n] polyhedra have a preference for n = 7, 6, and 8, as well as a minor preference for n = 5. This is a direct consequence of the larger ionic radius of Sc^{3+}. On the larger scale (at larger r) these differences disappear from the correlation plot, and in the average structure probes c-$Sc_2VO_{5+\delta}$ looks fully disordered, including site- and charge-disorder.

Oxygen-oxygen coordination. **Fig. 6.11a** shows a cube of oxygens around a mixed Sc/V center with expected O-O bond distances for the average structure – 2.49 Å along the edge of the cube, 3.53 Å along the face diagonal, 4.32 Å along the body diagonal. The same distances are shown as dashed reference lines in the N(r) plot for O-O correlations, **Fig. 6.11b**. The plot is completely bereft of any plateaus, in agreement with considerable displacement of oxide ions – recall diffuse oxygen clusters in the RMC structure. The absence of plateaus implies a broad distribution of O-O bond lengths. As suggested in ***Section 6.2.2***, ion displacements invite the discussion of oxide ion mobility.

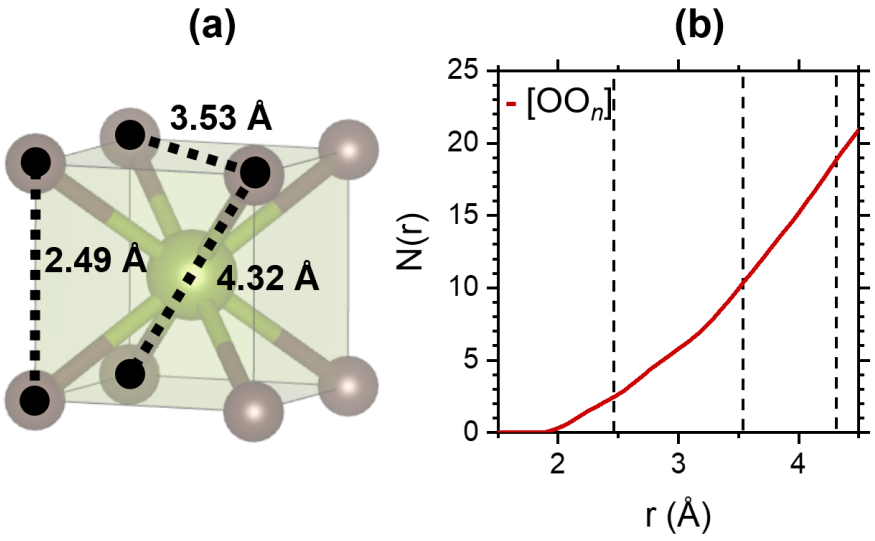

Figure 6.11. O-O bond distances in c-$Sc_2VO_{5+\delta}$: (a) – in idealized metal-oxygen cubes comprising the average structure; (b) – correlation number plot. Dashed lines are the three shortest O-O distances from the average structure, for reference.

Metal-metal coordination.

Fig. 6.12a shows the two shortest metal-metal distances from the Rietveld refinement. These are V-V, Sc-V, and Sc-Sc distances altogether, since V and Sc are disordered. **Fig. 6.12b** shows separately the *N(r)* plots for V-V and V-Sc pairs, and **Fig. 6.12c** shows *N(r)* plots for Sc-V and Sc-Sc pairs. If plateaus at 4…4.5 Å are taken as a reference (average distance of 3.53 Å with 12 neighbors in the coordination shell), each V^{x+} ion has 3 V^{x+} and 9 Sc^{3+} neighbors, while each Sc^{3+} ion has 4 V^{x+} and 8 Sc^{3+} neighbors. The number of cation neighbors adds up to 12 in each case, and the ratios are reasonably close to the 2:1 stoichiometric ratio of Sc^{3+} and V^{x+} in the formula. Both plots entirely agree with the expectations from the average structure, including washing out of the stepwise profile due to large cationic displacement. The benefit of the RMC refinement is the ability to separate Sc and V contributions owing to their stark neutron contrast. Sc-O, V-O, O-O, Sc-V, Sc-Sc, and V-V pairs are shown separately in **Fig. A-6.2** as partial PDFs.

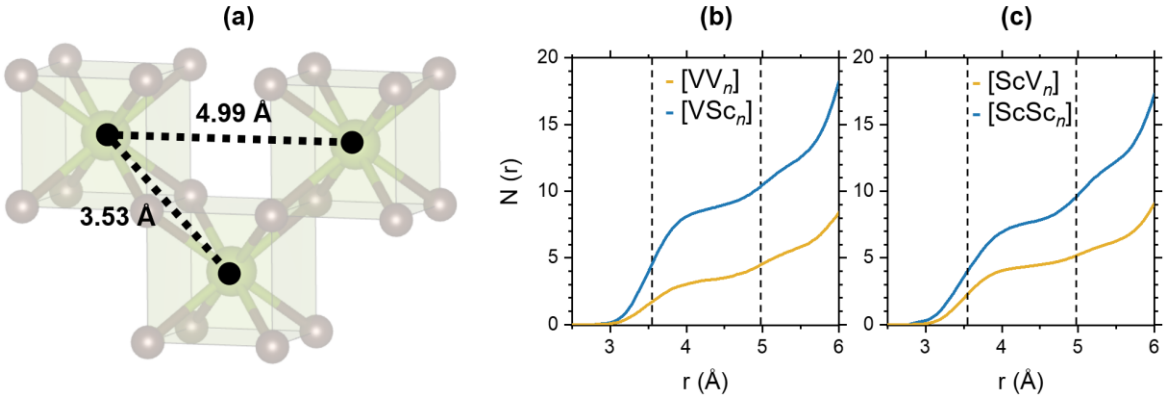

Figure 6.12. Metal-metal bond distances in c-$Sc_2VO_{5+\delta}$: (a) –two shortest distances in the average fluorite structure; (b) – correlation number plots for V-V (yellow) and V-Sc (blue) pairs; (c) – same for Sc-V (yellow) and Sc-Sc (blue) pairs. Dotted lines are two shortest metal-metal distances from the average structure, for reference.

6.2.2.3. Additional notes

The cubic polymorph c-Sc_2VO_5 is not the only example of a mismatch between the average and local structure description, previously observed in fully disordered[153,286], occasionally disordered[287], as well as mostly ordered[152,288] structures. Several scenarios of local distortion of

the metal-oxygen polyhedra on the local scale can be found in the literature. In the Mn-doped BaF_2 fluorite[289], it is proposed that four out of eight corner fluoride ions around the central Mn^{2+} cation shift toward it, forming two interpenetrating tetrahedra. This is a case of dynamic orientational disorder observed at low temperatures (below 50 K)[W]. In contrast, an impurity of Cr^{2+} in the same host material leads to an off-centering of the cation rather than the anions: chromium shifts toward the four in-plane fluoride ions in an attempt to adopt a near-square-planar configuration[290]. Another case is the fluorite $Bi^{3+}{}_{11}V^{5+}O_{19}$[291] with an even starker size contrast between bismuth (r_{VIII} = 1.17 Å) and vanadium than in c-$Sc_2VO_{5+\delta}$. The particular type of local disorder was not identified, although a comment was made on atypical BVS around vanadium. In all these cases the structure was still treated as fully disordered on average. The difference between any of these scenarios and the case of c-$Sc_2VO_{5+\delta}$ is the lack of a discernable universal mechanism of formation of the short V-O bonds in the latter. Local structure probes used for c-$Sc_2VO_{5+\delta}$ discovered shorter V-O bonds which are averaged out at the expense of more abundant longer Sc-O bonds. This bond length ordering is also buried under the site disorder and large atomic displacement of cations and anions in the average structure data. From the larger displacement of oxygen, shortening of V-O bonds likely involves the pulling of oxide ions toward highly charged vanadium. This step seems important during the formation of zircon-type $ScVO_4$ – a fully ordered lattice of eightfold Sc^{3+} and tetrahedral V^{5+} – and concomitant separation of Sc_2O_3, upon further heating. Interestingly, the fluorite-type c-$Sc_2VO_{5+\delta}$ can be contrasted against the bixbyite-type $YPrO_{3+\alpha}$, also obtained topotactically[198]. For the composition $\alpha = 0.43$, the disordered cation (Y/Pr) is displaced along the body diagonal of the unit cell passing through the partially occupied (α) vacant oxide sites. It is reasonable to expect that tuning the size of the cation pair between the radii of Sc_2/V (fluorite-type) and Y/Pr (bixbyite-type) would make the metal-to-oxygen shift as probable as oxygen-to-metal. Additionally, it would be interesting to study the local structure of $ScVO_{3.7}$[93] – a fluorite-type phase with 1:1 ratio of Sc^{3+} and $V^{4.4+}$, or any other topotactically obtained fluorite or fluorite superstructure.

The next section considers c-$Sc_2VO_{5+\delta}$ obtained from tetragonal t-$Sc_2VO_{5+\delta}$. From X-ray and neutron PDF data, both c-$Sc_2VO_{5+\delta}$ phases have peaks at 1.73 Å (**Fig. 6.4**), unaccounted for by the

[W] This kind of dynamic orientational disorder implies that any four of the eight equidistant (from each other) anions create a tetrahedron around the cation. Another type of the dynamic orientational disorder can be created by anions which travel through the structure and form and break labile bonds with the nearest metal centers, creating the illusion of rotation of the coordination polyhedron[311].

average description. However, the RMC structure of the post-tetragonal phase was not solved due to the lack of an unambiguous average structure model, to be discussed further. Instead, another structural peculiarity was found, this time with NPD, absent in c-$Sc_2VO_{5+\delta}$ obtained from $Sc_2VO_{4.5}$.

6.3. Residual cation ordering. Two fluorites

Two c-$Sc_2VO_{5+\delta}$ phases prepared from $Sc_2VO_{4.5}$ (400 ºC) and t-$Sc_2VO_{5+\delta}$ (650 ºC) at ambient conditions were scanned with *ex situ* NPD. Interestingly, the two look vastly different, as shown in the large-*d* portion of the powder neutron diffractograms in **Fig. 6.13**. The (011) peak assigned in the tetragonal setting ($I\bar{4}$, similar to t-$Sc_2VO_{5+\delta}$) is present in the product of oxidation of t-$Sc_2VO_{5+\delta}$ but absent in the product of oxidation of $Sc_2VO_{4.5}$. Although the former is mildly overoxidized and contains impurities of Sc_2O_3 and $ScVO_4$, the peak at 7 Å is not due to any of these impurities. Together with a few other smaller superstructure peaks, this peak thus belongs to the c-$Sc_2VO_{5+\delta}$ phase obtained from the tetragonal polymorph. Superstructure peaks invisible with

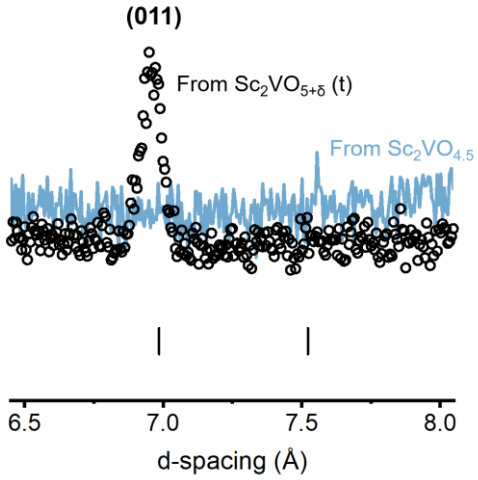

Figure 6.13. Large-d fragments of NPD diffractograms of c-$Sc_2VO_{5+\delta}$ obtained from $Sc_2VO_{4.5}$ (blue) and t-$Sc_2VO_{5+\delta}$ (black). In the black dataset a string superstructure peak is present resembling that in t-$Sc_2VO_{5+\delta}$ and indexed in its space group despite the absence of t-$Sc_2VO_{5+\delta}$ itself. Central wavelength 2.665 Å.

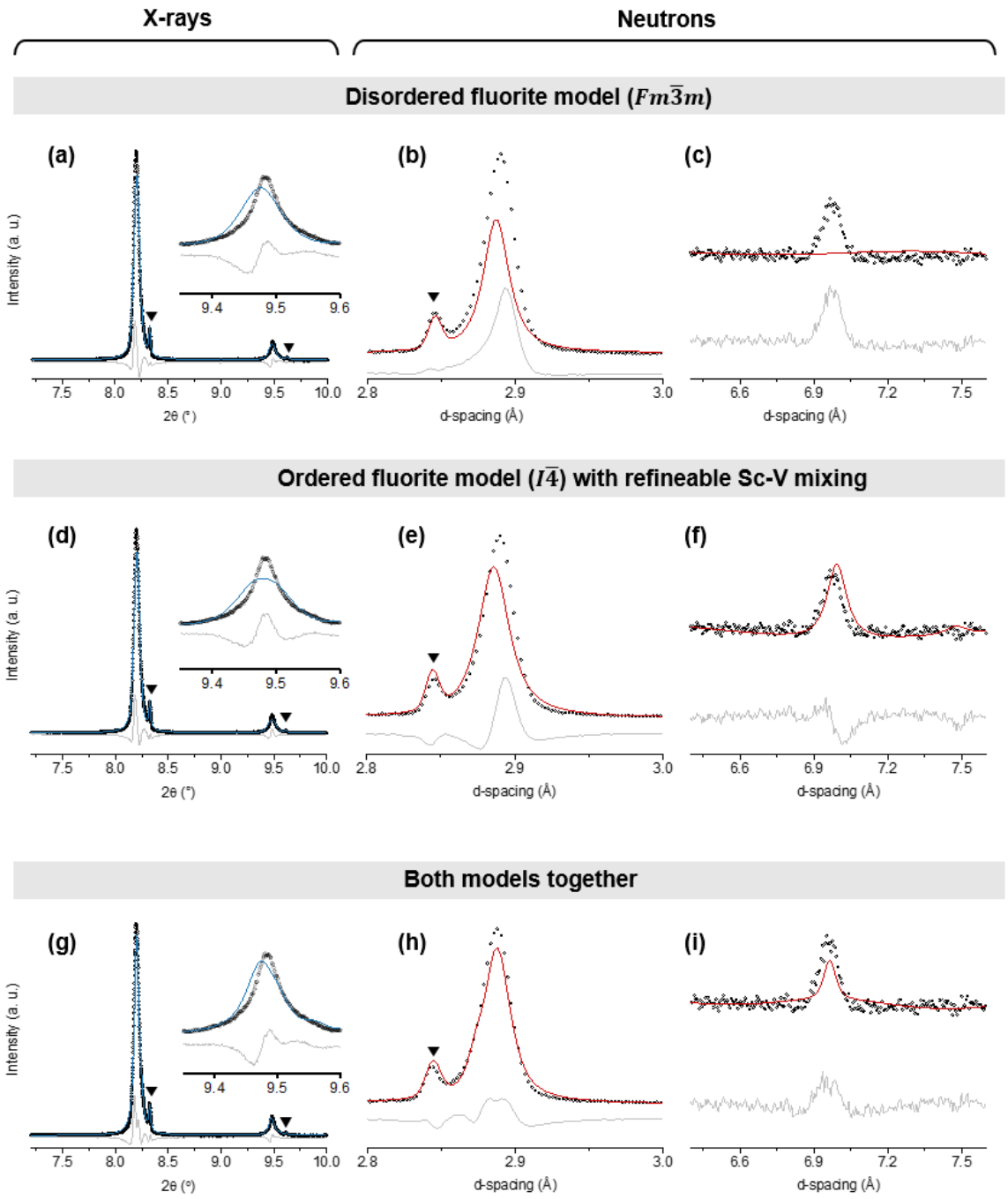

Figure 6.14. Fragments of Rietveld plots of c-$Sc_2VO_{5+\delta}$ (oxidation product of t-$Sc_2VO_{5+\delta}$) against synchrotron X-ray and neutron powder diffraction data: black circles are experimental data, red line is calculated data, grey line is the difference, black triangles are impurity peaks (Sc_2O_3). First column is XRD data, middle and right columns are neutron data. Upper row: fully disordered fluorite model was used (R_{wp} = 9.15 %); middle row: predominantly ordered t-$Sc_2VO_{5+\delta}$ was used with freely refined cation ordered and 10 anion sites offered (R_{wp} = 11.3 %); bottom row: both models were used, converged with the 3:1 mass ratio of cubic and tetragonal phases in the mixture (R_{wp} = 10.4 %).

XRD but visible with NPD are a signature of V-Sc cation ordering, since Sc and V are indistinguishable in X-rays while having a stark scattering contrast in neutrons. This residual ordering is long-range. In contrast, c-$Sc_2VO_{5+\delta}$ as obtained from $Sc_2VO_{4.5}$ remains fully cation-disordered on average, since it is a product of topotactic oxygen insertion into a cation-disordered cationic framework formed at high enough temperature to ensure such disorder (1500 ºC).

6.3.1. Notes on the Rietveld refinement

The cubic oxidation product of the t-$Sc_2VO_{5+\delta}$ sample has too few XRD and NPD peaks to allow determining the detailed structure such as cation positions and occupancies. Efforts to refine this phase against synchrotron powder XRD and NPD data were still made, as illustrated in **Fig. 6.14**. The top row shows fits with a fully disordered fluorite model ($Fm\bar{3}m$, red) which was used earlier to fit the polymorph of c-$Sc_2VO_{5+\delta}$ obtained oxidatively from $Sc_2VO_{4.5}$. While all peaks in the X-ray pattern are described, such as the emphasized peaks (111) and (200) in panel **a**, and the main structure peaks in the NPD pattern like (111) in panel **b**, the said characteristic superstructure peak in panel **c** is not addressed, rendering the fluorite model incorrect. Furthermore, the insert in panel **a** and panel **b** suggest that (1) the peak positions are off, and hence so are the lattice dimensions, (2) peak shapes are not matched, which is partially the consequence of strain. Another model tried is an ordered fluorite based on t-$Sc_2VO_{5+\delta}$ ($I\bar{4}$, middle row), where cation exchange was allowed and refined and two vacant oxygen sites were also used (note: actual t-$Sc_2VO_{5+\delta}$ was not found). This model is marginally better than the fluorite in that it addresses the superstructure peak around 7 Å in the neutron data in panel **f**, but it still has most of the same shortcomings as the fully disordered model. The bottom row is an improved fit with both the cubic (fully disordered) and the tetragonal (mostly ordered but with refineable disorder) models used simultaneously, in the mass ratio of 3:1 in the best refinement achieved so far. The superstructure peak $(011)_t$ in panel **i** is addressed, and only lacks intensity, while the fit of the main structure peaks in panels **g** and especially **h** are improved. The remaining mismatch of the peak positions is especially well seen in the inset to panel **g** where the overlapped peaks $(200)_c$ and $(310)_t$ are shown. This might suggest several alternative scenarios, most likely that this product is a mixture of phases with different (1) oxygen content or (2) degree of strain. As mentioned above, too few peaks are present in the data, particularly in the neutron data, to solve the structure reliably and refine the exact ordering scheme.

The local structure of this polymorph was not refined either, due to lack of a reliable average structure refinement. However, similar to the fully disordered polymorph c-$Sc_2VO_{5+\delta}$, its small-*r* X-ray and neutron PDF data also revealed the shorter V-O bond distances (**Fig. 6.4b**). These shorter V-O bonds relate to high absorption in XANES data (**Fig. 6.3b**). The neutron diffraction peak at about 7 Å (**Fig. 6.13**) that suggests residual cation ordering inherited from the tetragonal precursor also suggests the possible origin of the short V-O bonds – former bonds between the 2*c* vanadium and surrounding oxides.

6.3.2. Vacant anion sites

A comment should be made on the presumed mechanism of the oxidative transition from t-$Sc_2VO_{5+\delta}$ to the fluorite-looking superstructure c-$Sc_2VO_{5+\delta}$. Since t-$Sc_2VO_{5+\delta}$ was published as having 8 oxygen sites for 50 oxide ions per unit cell while the as-synthesized sample had 48.5 (i.e. $Sc_2VO_{4.85}$), oxidation is expected to start with topotactic insertion of $1.5 \cdot O^{2-}$. Associated oxidation of V^{3+} to V^{4+} in the octahedral 8*g* site indeed starts off topotactically, as was observed in **Fig. 3.18a**. Importantly, oxidation of all V^{3+} ($Sc_2VO_{4.7}$) to all V^{4+} ($Sc_2VO_{5.1}$) in the 8*g* site corresponds to $\delta = 0.1$. In other words, it requires an additional oxygen site (if the structure allows) beyond the eight identified oxygen sites to accommodate extra $0.1 \cdot O^{2-}$. Two vacant sites were found in the structure after visual inspection, keeping in mind the structural relation to fluorite, i.e. expecting each metal cation to be coordinated to eight oxide ions and oxide vacancies in total. However, Fourier mapping of NPD data on samples with tetravalent dopants in the 8*g* site was not sensitive enough to resolve additional oxygen in the expected sites, whereas oxidized samples of t-$Sc_2VO_{5+\delta}$ were likely not oxidized far enough. Nevertheless, some evidence of occupied additional sites was still offered by DC susceptibility measurements[127] (see ***Section 5.5.2***) and NPD/XRD Rietveld refinement (see **Table 4.2)**.

The second oxidation stage is non-topotactic, or at least predominantly so, from the observation of retained cation ordering. Since the ideal fluorite structure has eightfold-coordinated cations and fourfold coordinated-anions, the following should happen in t-$Sc_2VO_{5+\delta}$ upon its oxidation (**Fig. 6.15**):

- Site 4*f* of scandium is a distorted cube if longer Sc-O bond distances (2.81 Å *vs* 2.07…2.33 Å) are counted as was already suggested in **Fig. 3.3** [31] and is illustrated in detail in **Fig. 6.15a**.

Additionally, it completes the fourfold coordination of the two distant O^{2-} ions, hitherto the only threefold-coordinated oxygens;

- A vacant oxygen site exists in the center of the paramagnetic $[VO_6]_4^{x-}$ cluster, which is a special position 2*b* (0, 0, ½). In **Fig. 6.15b**, an oxygen ion (magenta) fills this void, accomplishing a sevenfold coordination around the hitherto octahedral vanadium in the 8*g* site. To the reported

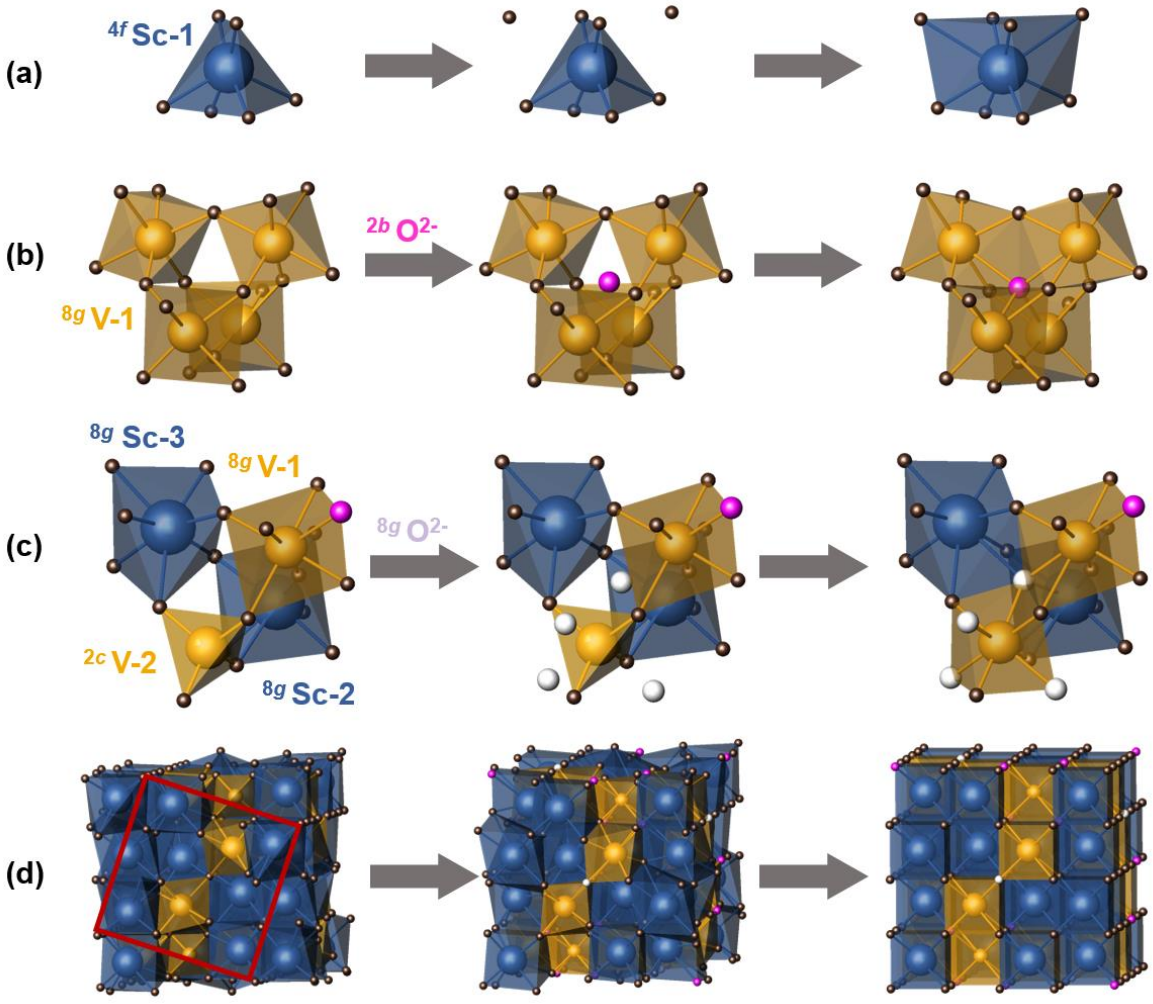

Figure 6.15. Schematic illustration of oxidation of t-$Sc_2VO_{5+\delta}$ to idealized ordered c-$Sc_2VO_{5+\delta}$: (a) – inclusion of longer Sc-O bonds around Sc-1 (4*f*) to make it eightfold; (b) – additional oxygen site 2*b* (pink) in the center of the paramagnetic vanadium cluster; (c) – additional oxygen sites 8*g* (white) around hitherto tetrahedral vanadium (2*c*); (d) – unit cell of t-$Sc_2VO_{5+\delta}$ without additional oxygen sites (left) and with additional sites shown (middle), and the geometrically regular fluorite lattice after filling the vacant sites with oxygen, cation order retained (right). Blue – Sc, yellow – V, brown – O in eight main anion sites; red box – *ab* plane of the unit cell.

maximum of 50 oxygen ions in the unit cell (or $Sc_2VO_{5.0}$) accommodated by the eight known anion sites, it adds two atoms per unit cells or 0.2 per unit formula ($Sc_2VO_{5.2}$);

- Another type of oxygen vacancies is in the 8*g* site, approximately at (0.24, 0.45, 0.30). Four such vacancies are situated around each tetrahedral vanadium site 2*c*. **Fig. 6.15c** illustrates how filling these sites with oxygen (white) accomplishes an eightfold coordination around this vanadium, as well as around the three 8*g* cation sites, which includes the paramagnetic vanadium site and two hitherto sevenfold scandium sites. If filled entirely, these sites add eight oxygen ions to the 50 oxygen ions per unit cell of t-Sc_2VO_5 or 0.8 to the unit formula, making it $Sc_2VO_{5.8}$, or Sc_2VO_6 (or $3{\cdot}AO_2$ in the fluorite notation) if the 2*b* site is filled as well. Which vacant site of the two is the first to accept oxygen (2*b* or not 2*b*) is yet to be determined; however, the refinement of $Sc_2V_{0.8}Sn_{0.2}O_{5+\delta}$ against neutron and lab X-ray powder diffraction data (see **Fig. 5.10** and **Table A-5.2**) offers some evidence that the general site 8*g* accepts oxygen (up to 15% if over-refined) already during synthesis, while the special site 2*b* does not. Importantly, disorder in the resulting fluorite can only be achieved if all vacant oxygen sites accept oxygen.

The summarized process of vacancy filling is schematically shown in **Fig. 6.15d**, where a distorted tetragonal superstructure t-$Sc_2VO_{5+\delta}$ oxidizes to a geometrically regular fluorite superstructure (idealized ordered c-$Sc_2VO_{5+\delta}$) when the abovementioned vacant sites are filled with O^{2-} ions. This simplified scheme is consistent with the partially topotactic nature of the oxidation of t-$Sc_2VO_{5+\delta}$ to c-$Sc_2VO_{5+\delta}$.

6.3.3. Oxidative formation of partially ordered c-$Sc_2VO_{5+\delta}$

Oxidation of t-$Sc_2VO_{5+\delta}$ to c-$Sc_2VO_{5+\delta}$ was followed closer with *ex*-situ XRD in air at 630 ºC, below the $ScVO_4$ formation temperature. The sample was heated for a total of ~500 hours with multiple re-grindings. As illustrated in **Fig. 6.16a**, at 630 ºC the phase conversion plateaus at ~90% between 200 and 400 hours of heating. During this time, the disappearing tetragonal phase grew in unit cell volume by 5-6% as determined from the only remaining superstructure peaks at about $2\theta = 26.5º$, while the pseudocubic (fitted in the $Fm\bar{3}m$ space group for ease) phase volume grew by 2% as shown in **Fig. 6.16c**. The likely explanation of this difference concerns different lattice densities of the two phases, wherein oxides populate pre-existing and readily available vacancies in the fluorite lattice while vacancies in the fully ordered tetragonal supercell are less available and

the cell will have to expand to let O^{2-} ions in. It should be noted that uncertainties are less reliable beyond 100 h of heating where the superstructure peaks of t-$Sc_2VO_{5+\delta}$ become weaker (**Fig. 6.16b**). Simultaneously, the main fluorite peaks of t-$Sc_2VO_{5+\delta}$ are buried under the peaks of c-$Sc_2VO_{5+\delta}$ and obscured by large FWHM values, peaking at the same heating time (**Fig. 6.16d**). At this point, both main phases are present (t and c), rendering the fluorite peaks unresolved doublets, in addition to the breadth of the individual peaks. This individual peak broadening begins already

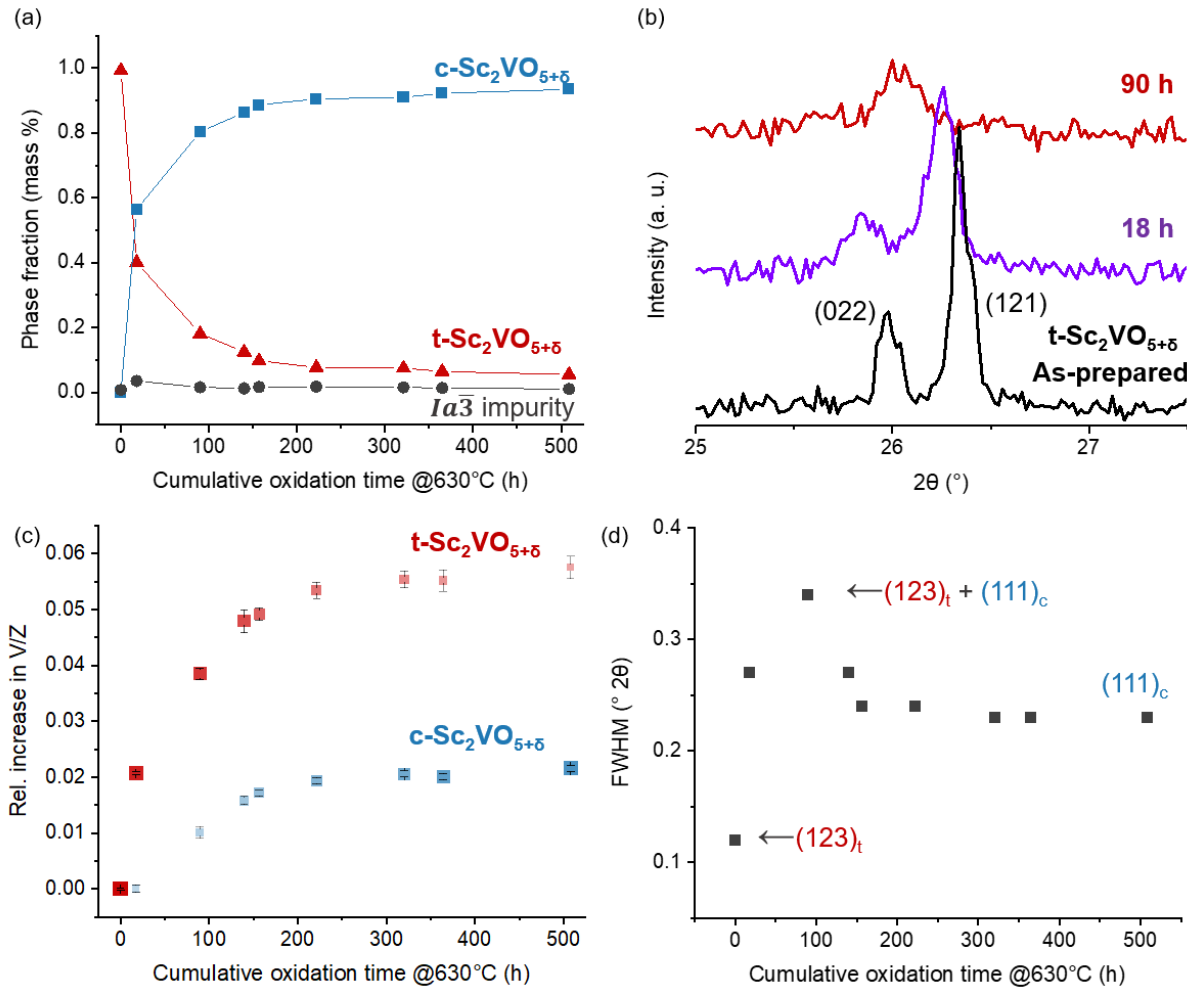

Figure 6.16. Oxidation of t-$Sc_2VO_{5+\delta}$ at 630 ºC: (a) – evolution of phase content: t-$Sc_2VO_{5+\delta}$ – red, c-$Sc_2VO_{5+\delta}$ – blue, Sc_2O_3 – grey; (b) – broadening and disappearance of the characteristic superstructure peaks of t-$Sc_2VO_{5+\delta}$ during the first 90 h of heating; (c) – relative increase in unit formula volume of the two $Sc_2VO_{5+\delta}$ phases (t – red, c – blue). Declining (growing) phase content is shown with decreasing (increasing) size and increasing transparency (opacity) of the markers; (d) – evolution of FWHM of the $(123)_t/(111)_c$ peak at $2\theta \approx 31^o$; the oxidation product was indexed in the $\boldsymbol{Fm\bar{3}m}$ space group for convenience.

in the tetragonal phase, suggesting the break-down of crystalline domains of t-$Sc_2VO_{5+\delta}$, likely from forcing oxide ions through the structure while not providing sufficient thermal energy to accommodate the cations accordingly. This stage corresponds to the ascending part of the trend peaking when both phases are present, while the decaying part of the trend corresponds to the disappearance of the tetragonal precursor and equilibration of the c-$Sc_2VO_{5+\delta}$ phase. Equilibration at even higher temperature is expected to narrow down the peaks of c-$Sc_2VO_{5+\delta}$ if the products of its over-oxidation ($ScVO_4$ + ½ Sc_2O_3) did not form instead.

This section illustrates that pure-phase c-$Sc_2VO_{5+\delta}$ can be obtained from t-$Sc_2VO_{5+\delta}$ only under the right conditions. In contrast, fully disordered c-$Sc_2VO_{5+\delta}$ can be easily obtained from $Sc_2VO_{4.5}$ with the only limiting factor being the availability of the oxidant. Extent of ordering is a factor controlling the mobility of oxide ions coming in to populate oxide vacancies. In both polymorphs, the extent of ordering is partially or predominantly inherited from their respective precursors.

6.3.4. Topotactic reduction of partially ordered c-$Sc_2VO_{5+\delta}$

The sample used for the XRD, NPD, and PDF studies above was also reduced in pure hydrogen at 400 ºC for 45 h. The product is a mixture of phases (**Fig. 6.17a**), including the starting fluorite (denoted as having SG $Fm\bar{3}m$ basing only on XRD data for simplicity), t-$Sc_2VO_{5+\delta}$ ($I\bar{4}$), a mixture of two bixbyite phases ($Ia\bar{3}$), zircon $ScVO_4$ ($I4_1/amd$), and an unidentified impurity modelled as another bixbyite. None of the two identified bixbyites is pure Sc_2O_3 present in the starting material, but rather a mixed Sc-V oxide. Using the calibration graph for the $Sc_{2-x}V_xO_3$ systems[99], the composition of the two bixbyites was estimated to be $Sc_{1.82}V_{0.18}O_3$ (close to Sc_2O_3) and $Sc_{1.32}V_{0.68}O_3$ (≈$Sc_2VO_{4.5}$) after 15 h of reduction. In **Fig. 6.17b**, the relative decrease of the unit formula (V/Z) is shown for the main phases, wherein the x = 0.18 phase (green) and x = 0.68 phase (grey) barely change in volume and oscillate around 1% loss, respectfully. This pattern suggests that the x = 0.68 phase is a product of reduction of both the initial fluorite and tetragonal $Sc_2VO_{5+\delta}$, while the latter is a parallel product of reduction of the fluorite. The topotactic nature of the process necessitates the preservation of the cation-ordering scheme throughout the process, i.e. partial cation ordering in the $Sc_{1.32}V_{0.68}O_3$ bixbyite similar to its two precursors. This sample will be investigated with neutron powder diffraction.

Comparing the rates of topotactic reduction and oxidation (**Fig. 6.16c** and **Fig. 6.17b**), volume increase of c-$Sc_2VO_{5+\delta}$ is smaller than that of its precursor t-$Sc_2VO_{5+\delta}$ upon oxidation but larger upon reduction. For example, volume increase reaches 1% after 100 h at 630 ºC but 1% decrease is achieved already after 15 h at 400 ºC.

(1) This can be explained if c-$Sc_2VO_{5+\delta}$ starts off more oxidized relative to t-$Sc_2VO_{5+\delta}$ (**Fig. 6.16c**) and hence has little room left for oxidation.

(2) Another possible explanation connects this figure to the third refinement model in **Fig. 6.14** where two fluorite-related phases (fully disordered and partially ordered) were used to fit the diffraction data. Since the t-$Sc_2VO_{5+\delta}$ superstructure peaks disappear shortly after 90 h of heating (**Fig. 6.16b**), the red markers in **Fig. 6.16c** might actually correspond to the partially ordered fluorite indexed in the space group of t-$Sc_2VO_{5+\delta}$. This fluorite would be harder to oxidize, hence argument (1) also applies.

In conclusion, the c-$Sc_2VO_{5+\delta}$ phase exists as two products. A fully *disordered* fluorite-type phase can be obtained topotactically from a bixbyite $Sc_2VO_{4.5}$ at 400 ºC. Its cation and anion

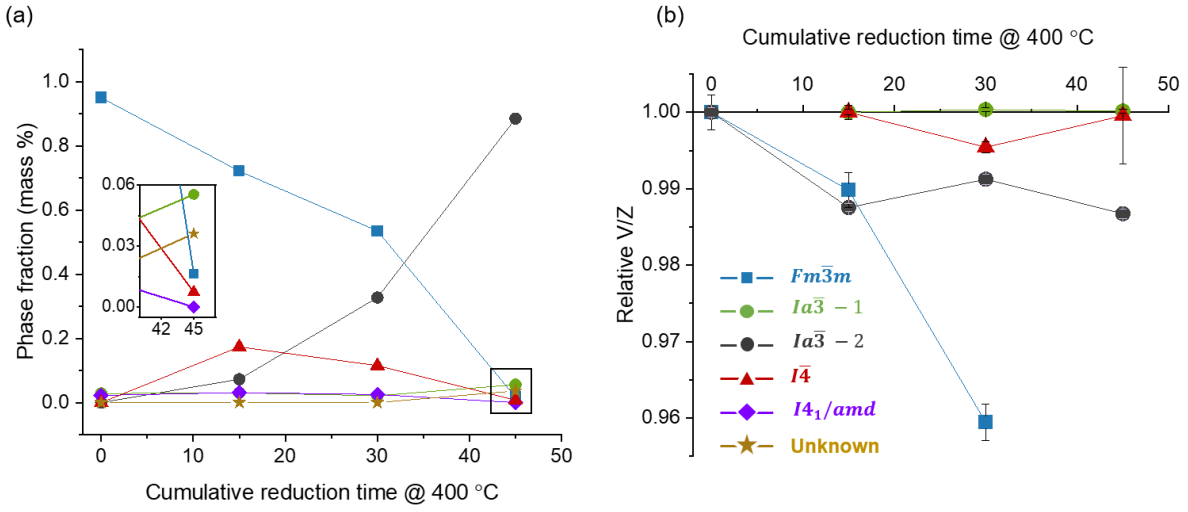

Figure 6.17. Topotactic reduction of the partially ordered fluorite c-$Sc_2VO_{5+\delta}$ at 400 ºC in pure hydrogen flow: (a) – phase content (squared area is enlarged in the insert), where blue is c-$Sc_2VO_{5+\delta}$, grey is its immediate bixbyite reduction product, green is some other bixbyite (see text), red is t-$Sc_2VO_{5+\delta}$, purple is $ScVO_4$, and yellow is an unknown phase modelled as a cubic bixbyite ($\boldsymbol{Ia\bar{3}}$); (b) – evolution of the unit formula volume V/Z of the reduction products, relative to their pre-reduction values of V/Z, where Z = 4 for $\boldsymbol{Fm\bar{3}m}$ implying fluorite notation $Sc_{1-x}V_xO_{2-\delta}$, 10 for $\boldsymbol{I\bar{4}}$, and 16 for $\boldsymbol{Ia\bar{3}}$.

disorder is long-range, but local preferences of V and Sc ions toward different coordination polyhedra still exist and manifest themselves on the scale of the 8×8×8 supercell. A partially *ordered* pseudo-cubic phase can be obtained from t-$Sc_2VO_{5+\delta}$ at 650 ºC. From at least partial retention of long-range cation ordering (NPD data), the oxidative route is at least partially topotactic. Despite the topotactic formation, oxidation of t-$Sc_2VO_{5+\delta}$ to c-$Sc_2VO_{5+\delta}$ requires higher temperature than oxidation of $Sc_2VO_{4.5}$ to disordered c-$Sc_2VO_{5+\delta}$. This can be associated with the cation-ordered lattice of t-$Sc_2VO_{5+\delta}$ which traps oxide anions more effectively as opposed to the cation-disordered bixbyite with more available oxide vacancies.

6.4. Indium analogue of cubic $Sc_2VO_{5+\delta}$ or reduced In_2VO_5?

The search for the indium-bearing analogue of the Sc_2VO_5 fluorite was inspired by the proximity of ionic radii of Sc^{3+} and In^{3+} (7.4 % difference for CN = VI[103]), which also offered the possibility to partially include In^{3+} into the t-Sc_2VO_5 structure and vice versa, as discussed in ***Section 4.4***. Finding a fluorite with In^{3+} and $V^{4+\ldots5+}$ would have been possible considering high tolerance of the fluorite-type structure of a wide range of cation sizes and charges[292,293], especially when approaching topotactically. Considering other A:B ratios than 2:1, not many indium vanadates are known, possibly owing to easy over-reduction of In^{3+} to In^0 and its evaporation when working at high temperature and/or at even mildly reducing conditions. The latter excludes high-temperature synthesis, inviting to attempt a kinetic pathway. A bixbyite $In_2VO_{4.5}$ was hence attempted at 450 ºC in CO/CO_2 flow, similar to the synthesis of $InVO_3$ from $InVO_4$ [294]:

$$In_2VO_5 + \frac{1}{4}CO \rightarrow In_2VO_{4.5} + \frac{1}{4}CO_2 \qquad (6.1)$$

The reaction yielded an impure product co-existing with the starting In_2VO_5 phase, and higher purity was not achieved after (1) adjusting the $CO:CO_2$ ratio or (2) increasing the dwelling time or (3) temperature in the used range of parameters 1-3. Rietveld refinement was first done with the expected bixbyite $In_2VO_{4.5}$ as the major phase. As seen in **Fig. 6.18(a)**, small peaks at lower 2θ were not addressed by the bixbyite model and were initially considered unidentified impurities. The model gave the expected lattice dimension and readily refines to full In-V

disorder. A much better model, however, is a reduced $In_2VO_{5+\delta}$ phase. Refinement is shown in panel (b) and, as seen, the low-angle peaks are now accounted for by the structure. The phase is cation-ordered as expected after low-T reduction of the ordered precursor. From lab XRD, δ was refined to -0.19(5). Higher-resolution XRD data as well as NPD data are needed for more accurate oxygen stoichiometry and positions. For this reason, preliminary structural data are not provided here. It should be noted that the reduced ordered $In_2VO_{5-\delta}$ model is favored over the $In_2VO_{4.5}$ bixbyite model from observing its gradual oxidation in oxygen flow (not shown): above 400 ºC, In_2VO_5 forms again. This suggests a topotactic relation between In_2VO_5 and its identified reduction product, which poses two questions: (1) is the ordered reduction product $In_2VO_{5+\delta}$ ($\delta<0$) similar to the analogue of the ordered bixbyite-looking phase seen on reduction of both t-$Sc_2VO_{5+\delta}$ and c-$Sc_2VO_{5+\delta}$? (2) can the disordered fluorite be obtained at all? The first question would benefit from neutron diffraction on larger and purer samples and will be the subject of future work. Regarding the disordered fluorite, its topotactic synthesis from a bixbyite requires a cation-disordered bixbyite. For comparison, synthesis of the Sc analogue $Sc_2VO_{4.5}$ needs 1500

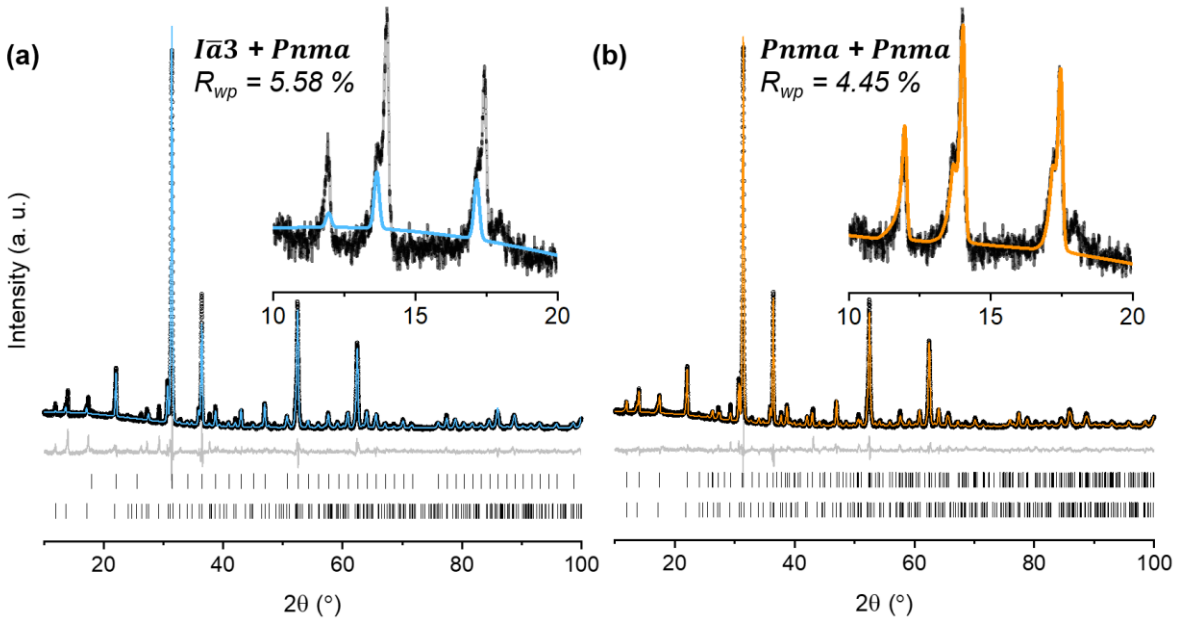

Figure 6.18. Rietveld refinements of lab XRD data (Cu-Kα$_1$) on the products of In_2VO_5 reduction: (a) – modelled with a bixbyite $In_2VO_{4.5}$ (30 mass % impurity of starting In_2VO_5); (b) – modelled with oxygen-deficient $In_2VO_{5-\delta}$ (16 % of In_2VO_5). Black – experimental data, colored – calculated profile, grey – difference, vertical ticks – Bragg peak positions of the major reduction product (top) and remaining In_2VO_5 (bottom). Insets show low-angle peaks which were mostly addressed only with the second refinement model (save for the small peak at 2θ = 18°).

ºC. This temperature is well beyond the In^{3+} to In^0 reduction point and metal indium evaporation point, which likely means that successful synthesis of $In_2VO_{4.5}$ is improbable.

Despite the absence of the disordered variant of In_2VO_5, the In-V-O diagram is now enriched by its cation-ordered topotactic product. Interestingly, the X-ray pattern of this product almost entirely resembles a pattern of the bixbyite. This observation inspires a future structural investigation of how the anionic lattice of structurally different In_2VO_5 adapts to the topotactic oxygen loss.

6.5. Conclusion

Two c-$Sc_2VO_{5+\delta}$ phases – oxidation products of $Sc_2VO_{4.5}$ and t-$Sc_2VO_{5+\delta}$ – retain the cation ordering scheme of their precursors. The oxidation product of the bixbyite is thus fully cation-disordered, while the oxidation product of the tetragonal superstructure is at least partially ordered. Estimates of the exact extent of ordering are hindered by too few main structure peaks and their broadness (likely caused by strain), but the superstructure peak at 7 Å (NPD) is a strong indication of cation ordering. Similar to t-$Sc_2VO_{5+\delta}$, both c-$Sc_2VO_{5+\delta}$ phases have shorter V-O bond lengths (≈1.7 Å) in X-ray PDF data responsible for strong pre-edge absorption in vanadium XANES.

Pseudocubic c-$Sc_2VO_{5+\delta}$ obtained from t-$Sc_2VO_{5+\delta}$ likely inherited these shorter bonds from the $[VO_4]^{3-}$ tetrahedra around the 2*c* sites of t-$Sc_2VO_{5+\delta}$. The idealized oxidation scheme of t-$Sc_2VO_{5+\delta}$ offered in **Fig. 6.15** requires capping of these tetrahedra when filling oxide vacancies yet does not contradict the pertinence of shorter V-O bonds.

Owing to its high crystallinity and higher purity, it was possible to refine both average and local structures of c-$Sc_2VO_{5+\delta}$ obtained from $Sc_2VO_{4.5}$. From its RMC refinement against total scattering data, shorter V-O bonds co-exist with longer V-O bonds in a number of polyhedra, more abundant being (in descendant order) $[VO_7]^{n-}$, $[VO_6]^{n-}$, $[VO_8]^{n-}$, and $[VO_5]^{n-}$. These shorter bonds are likely created by mobile oxygen (B_{iso} = 8.93(6) $Å^2$) shifting towards vanadium, and this shift appears isotropic (with no preferred direction) on the scale of the 8×8×8 supercell. This phase is a case of V/Sc cation disorder with significant V-O/Sc-O bond length ordering. Similar RMC refinements of c-$Sc_2VO_{5+\delta}$ obtained from t-$Sc_2VO_{5+\delta}$ requires a well-understood average structure and, ideally, a single-phase sample. As was illustrated with the three Rietveld models, strained peaks, and a 100 hour-long synthesis of almost pure-phase material, local structure refinement at this stage is

impossible. Instead, long-range residual ordering was found in NPD data. This ordering takes the form of the residual superstructure of t-$Sc_2VO_{5+\delta}$ (**Fig. 6.13**) and speaks to at least partially topotactic nature of the oxidation route t-$Sc_2VO_{5+\delta}$ → c-$Sc_2VO_{5+\delta}$.

Unlike the $Sc_2VO_{5+\delta}$ system, In_2VO_5 so far was identified exclusively as a fully ordered phase. As the product of topotactic oxidation, the disordered fluorite requires an already cation-disordered bixbyite. However, such bixbyite cannot be obtained due to reduction and evaporation of indium, while a lower temperature in the range from 450 to 550 ºC is not sufficient to disorder cations when reducing In_2VO_5. A product of topotactic reduction, preliminarily refined to $In_2VO_{4.81(5)}$, was found instead. Recalling low-T reduction of both t-$Sc_2VO_{5+\delta}$ and c-$Sc_2VO_{5+\delta}$, a phase whose XRD pattern looks identical to that of a bixbyite was also identified, but with suspected retention of cation ordering. The pair "In_2VO_5 – topotactic reduction product" and "t/c-Sc_2VO_5 – topotactic reduction product" open up a series of kinetic pathways that might provide insights into the relation between solid-state structure and solid-state reactivity.

CHAPTER 7

Order – disorder competition in $A_2VO_{5\pm0.5}$ and $AVO_{3.5\pm0.5}$ phases

The range of A^{3+} cation sizes and V^{x+} oxidation states generates the diversity of crystal structures formed by A^{3+}-V^{x+}-O phases described or mentioned in the previous chapters. In the current chapter, these phases are grouped by stoichiometry, and the structure trends within the resulting phase families are discussed, with a particular emphasis on the ionic radii.

7.1. $A_2VO_{5\pm0.5}$ and $AVO_{3.5\pm0.5}$ phase diagrams

The structures of $A_2VO_{5\pm0.5}$ and $AVO_{3\pm0.5}$ phases are summarized in **Fig. 7.1**[X]. The Y axis of the figure is the nominal oxidation state of vanadium, which also can be thought of as a B cation size axis covering the range of ionic radii from 0.355 Å for $V^{5+}{}_{IV}$ (top) to 0.640 Å for $V^{3+}{}_{VI}$ (bottom). The X axis lists nominal A^{3+} cations in ascending order of the cation radius in the same coordination, from V^{3+} to La^{3+}. Yellow (V^{x+}) and blue (Sc^{3+}) colors of polyhedra indicate predominantly cation-ordered or charge-ordered structures, while green polyhedra indicate cation- and charge-disordered structures. Green circles in the $A_2VO_{5\pm0.5}$ diagram mark absent phases. Attempts to synthesize those phases resulted in phases with 1:1 A:V stoichiometric ratio (i.e. $AVO_{3\pm0.5}$ phases) and a surplus of A_2O_3. The following observations and comments can be made.

- Ti^{3+} exists in corundums only with V^{3+} ($Ti_2VO_{4.5}$, $TiVO_3$), while in V^{4+} and V^{5+} phases it undergoes charge exchange with vanadium, leading to Ti^{4+}. As a result, the Magnéli phase $Ti_2VO_{5+\delta}$ and structurally-related rutile $Ti_2VO_{5.5+\delta}$ (as well as $TiVO_{4+\delta}$) are oxygen-nonstoichiometric, where δ strongly depends on the amount of oxygen available during synthesis. Depending on the nominal oxidation state of vanadium in the starting mixture, either a Magnéli phase (V^{4+}, **Fig. 4.4**) or a rutile phase (V^{5+}) can be expected. The rutile phase $TiVO_{4+\delta}$ with a 1:1

[X] In **Fig. 7.1**:
* unclear oxidation state of vanadium and related oxygen stoichiometry; also, requires hydrothermal pressure;
** A:V ratio deviates from 2:1.

ratio of cations is a project on its own: it was reported as an oxygen-stoichiometric phase with Ti^{3+} and V^{5+} coexisting in the only crystallographic site[203]. XANES analysis of coordination and oxidation states of Ti and V in it is shown in **Fig. A-7.1**, ***Appendix 7***. The formula is closer to

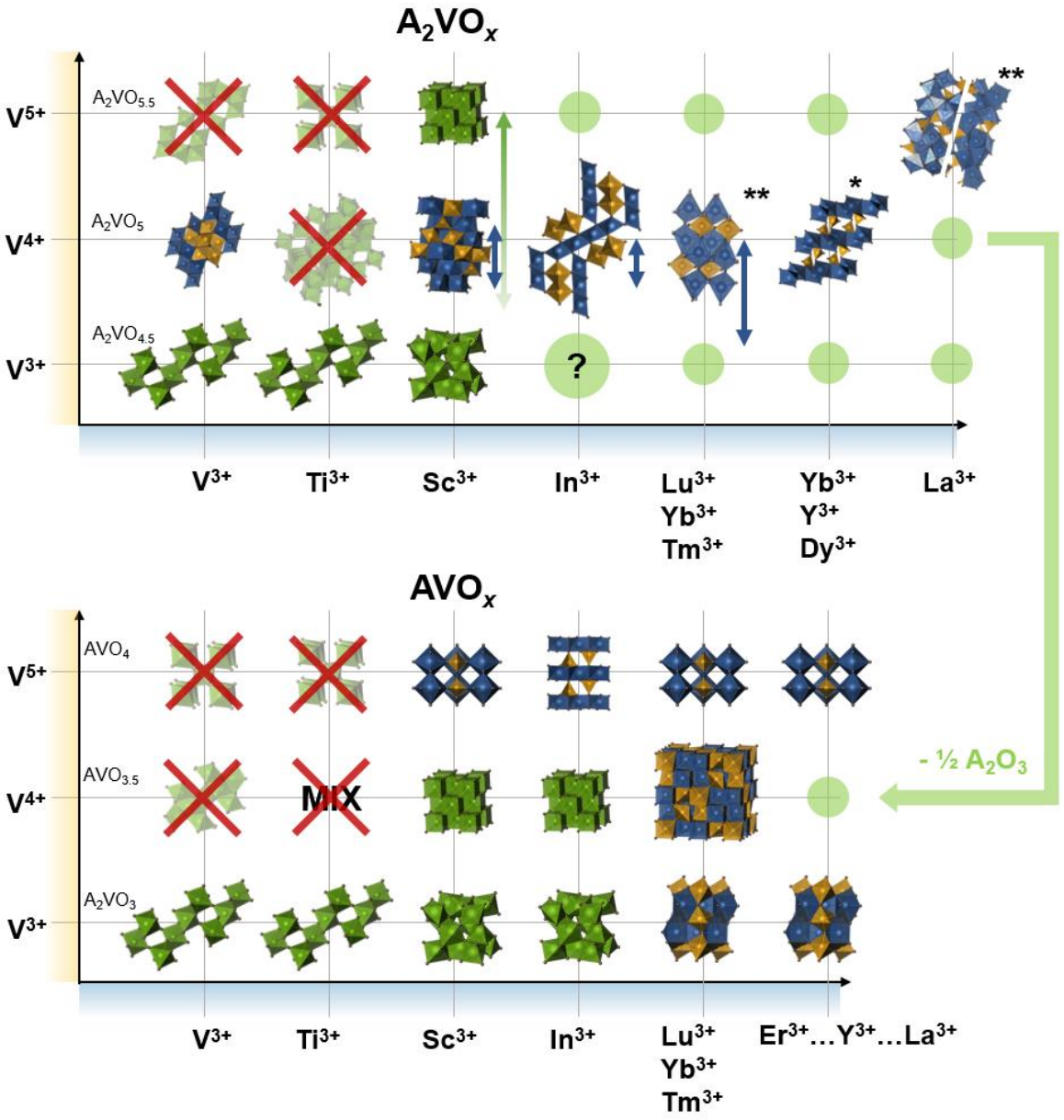

Figure 7.1. A_2VO_x (x = 5±0.5) and AVO_x (x = 3.5±0.5) phase diagrams. Axes are radii of A^{3+} (X, blue) and V^{x+} cations (Y, yellow). Blue/yellow and green polyhedra mean order or disorder, including charge (dis)order. Green circles are absent phases thermodynamically outcompeted by the phases in the corresponding nods of the other diagram, with a bixbyite side product (A_2O_3). Double arrows indicate a range of oxidation states in a defect fluorite (green) or an ordered phase next to the arrow (blue). "Mix" refers to a mixture of corundum and Magnéli phases.

$Ti^{4+}{}_{VI}V^{5+}{}_{VI}O_{4.5}$. The $Ti_2VO_{5+\delta}$ phase of the Ti_4O_7 type differs from other A_2VO_5 phases in having Ti^{4+} instead of Ti^{3+}. In the diagram, all phases with nominal Ti^{3+} but experimental Ti^{4+} in the A site(s) are crossed out. In contrast, V_3O_5 (=V_2VO_5) rightfully belongs to the A_2VO_5 phases, since its A^{3+} and B^{4+} cations strongly prefer different crystallographic sites. Although it is impossible to comment on site mixing in V_3O_5, since both sites are occupied by the same chemical species, charge ordering meets the requirement for A_2VO_5 phases, which is in contrast to the titanium-bearing analogue. A prediction can be made that it takes an A^{3+} cation smaller than V^{3+} to yield a cation disordered phase for A_2VO_5 stoichiometry. One exception is c-$Sc_2VO_{5+\delta}$ (product of topotactic oxidation of $Sc_2VO_{4.5}$) with V^{4+} and V^{5+} species in the B sublattice. If oxidized to all-V^{5+} or to as much of the V^{5+} concentration as the structure can tolerate before collapsing into $ScVO_4$ and ½ Sc_2O_3, the structure of c-$Sc_2VO_{5+\delta}$ can be imagined to be c-$Sc_2VO_{5.5}$, i.e. it belongs to the top row, the way it is drawn in the diagram.

- Similar to the titanium vanadates, V^{3+}-bearing phases with intermediate A^{3+} cations (Sc, In) appear cation-disordered. In V^{3+} phases (bottom rows of both diagrams) with cations from Ti^{3+} to In^{3+}, the disorder primarily owes to the proximity of A and B radii. In Ti^{3+}-V^{4+} and Ti^{3+}-V^{5+} phases the cation radii are even closer owing to the oxidation of titanium, which makes titanium cations smaller.
- In the cation-ordered phases, the ionic size of A^{3+} is much larger than that of vanadium. This holds true for A_2VO_5 phases and a plethora of $AVO_{3\pm0.5}$ phases, while the missing $A_2VO_{5\pm0.5}$ phases decompose into the corresponding $AVO_{3\pm0.5}$ phases and a surplus of A_2O_3 to compensate for the change in the A:V ratio. This indicates that the threshold of structural stability lies between 1:1 and 2:1 ratio of A:V. In this regard, $A_{2.1}V_{0.9}O_{4.8+\delta}$ phases (A = Lu, Yb, Tm) seem to be borderline cases. They were found to be more preferred than competing pyrochlores $A_2V_2O_7$ at 1200 ºC.
- Cation ordering in $AVO_{3\pm0.5}$ phases considered is governed by the A:B size ratio. Zircons AVO_4 (A = Sc, Y, Ln) are cation-ordered as opposed to rutiles $AVO_{2+\delta}$ (A = V, Ti), while perovskites AVO_3 (A = Lu, Y, Ln) are ordered as opposed to corundums (A = V, Ti) and bixbyites (A = Sc, In). While formation of perovskites and non-perovskites can be moderately well predicted from the radii of individual ions[295], the former is complicated due to (1) A = Ti^{4+} rather than Ti^{3+} in the rutile and (2) the uniqueness of In^{3+} preferring the $CrVO_4$-type structure[296] instead of zircons expected for this A^{3+} radius value. The zircon phase in particular also appears to be instrumental

in synthesis of t-$Sc_2VO_{5+\delta}$ and its derivatives. Direct synthesis of t-$Sc_2VO_{5+\delta}$ from $ScVO_4$, $ScVO_3$, and Sc_2O_3 can be considered a reconstructive reaction of two structural motifs – that of a bixbyite (the higher-coordinated network of t-$Sc_2VO_{5+\delta}$) and that of a zircon (tetrahedrally coordinated vanadium species separated by higher coordinated cations of lower charge), both based on the *fcc* lattice. During the reductive formation of t-$Sc_2VO_{5+\delta}$, zircon (starting material) can react with $ScVO_3$ or $Sc_2VO_{4.5}$ (products of over-reduction) to give the desired phase via the same mechanism. Interestingly, even for the direct synthesis of Ti- and Co-doped derivatives of t-$Sc_2VO_{5+\delta}$, zircon $ScVO_4$ was found as an intermediate at 800 ºC and then disappeared above 1000 ºC.

- As was discussed in ***Section 4.5.3***, there is a possibility that the hydrothermally obtained series A_2VO_5 with A = Y, Yb, Dy**[34]** has a different formula and/or stoichiometry. Tetravalency of vanadium in these phases was established on the basis of two precedents**[189,190]** which themselves were derived from neutron data of limited quality. In the temperature regimes covered in this work and elsewhere**[217]**, corresponding products of the solid-state syntheses deviated from the 2:1 ratio of A:V cations, producing 2.1:0.9 for A = Lu, Yb, and Tm (with reported $V^{3.67+}$) and 4:1 for A = Yb, Y, etc. (with reported V^{5+}); the latter are not shown in the scheme. Competing products were pyrochlores $A_2V_2O_7$ (for cations smaller then Y, and in general smaller than Er) and disproportionated mixtures of perovskites AVO_3 and zircons AVO_4. Interestingly, $La_7V_3O_{18}$ with pentavalent vanadium was recently reported**[225]**. Phases with >2:1 ratio of A:V cations (closest to 2:1) so far were of the two varieties: (1) $A_8V_2O_{17}$ with V^{5+} and larger A^{3+} cations and (2) $A_7V_3O_{16}$ with $V^{3.67+}$ and smaller A^{3+} cations. The new lanthanum phase suggests that there is no explicit relation between the size of the lanthanide ion and the particular stoichiometry of the phase. It also exists in two modifications, both shown in the figure, and is a competitor of the zircon phase. Similar to Y and lanthanides after Tm, lanthanum is not represented by its pyrochlore phase $A_2V_2O_7$ in the ambient-pressure phase diagram $AVO_{3\pm0.5}$**[297]**. From this, the largest ratio of A:V radii, larger than in all vanadates considered so far, seems to shift the thermodynamic minimum from $AVO_{3.5}$-type phase (1:1) to $A_2VO_{5.5}$-type phase (~2:1). More research should be done on lanthanide vanadates to confirm this, including establishing the related oxidation state of vanadium with spectroscopic methods.
- Finally, cation-disordered cubic fluorite phases with nominal V^{4+} exist for A = Sc and In in the ratio 1:1, while in the ratio 2:1 only c-$Sc_2VO_{5+\delta}$ can be found. For larger A^{3+} cations, the fluorite is outcompeted by fully ordered In_2VO_5 (A = In, 2:1) or pyrochlore $A_2V_2O_7$ (A < Er, 1:1).

As mentioned above, for cations of the size of yttrium and even already for Yb a kinetic product $A_8V_3O_{18}$ can be found which is then quickly taken over by its thermodynamic competitor AVO_4, both with pentavalent vanadium. Y-based pyrochlore can be accessed via the high-pressure paths only, adding an additional dimension to the diagram, which is beyond the scope of the thesis. The mechanism of the order-disorder transition in the most well studied fluorite-pyrochlore pair is not yet entirely understood. Both accumulation of point defects in the anion sublattice leading to its disordering and planar defects (antiphase domains) in the cation sublattice were proposed[298].

7.2. Stability fields. Prediction versus description

If some parameters describing individual ions in ionic solids, such as sizes and charges, can be used to quantify and consequently predict cation-/charge disordering/ordering and stability/decomposition, it would be a powerful tool for the rational design of functional materials.

The best attempt to evaluate cation ordering in the thesis was done with a quick *post-factum* formula based on the refined mixing parameter. It is relevant when working within the same structure type, as was suggested in eq. 5.2. Although occupancies included in the formula showed to be related to the cation radius, the formula itself does not include radii and cannot work as a tolerance factor.

Quantification of ordering *across* the structure types, moreover allowing predictions, is a much more complicated venture. In the first approximation it can be replaced with predicting the structure type *per se*, since often either predominant (or full) order or predominant (or full) disorder is allowed by the same structure type. Such quantification might be done with a tolerance factor or a stability field. Tolerance factors (1) are coefficients typically calculated from the ratios of ionic radii of the cations or cation-anion bond distances, or cation to anion radii; (2) usually rely on geometry; (3) group around different values for different structures or groups of structures. An example of a tolerance factor is the Goldschmidt factor[295] frequently used to predict formation of a perovskite *vs* a non-perovskite (bixbyite, linobate, corundum, …), and its derivatives[276] and analogues for other stoichiometries[7]. More pertinent to the current work, several factors delineating pyrochlores and fluorites were reported (see Fuentes *et al*.[299] and references therein). The simple factor $t = r(A^{3+}{}_{VIII})/r(B^{4+}{}_{VI})$[300] with $t < 1.457$ favoring fluorites was shown to predict structures better than the more complex factors accounting for cation polyhedral distortions and

the anion radius[301]. This is due to the fact that pyrochlores can still allow a degree of disorder which is hard to predict. One solution to this problem would be a separate coefficient predicting the degree of ordering, to be then incorporated into the tolerance factor; finding a solution to this problem is one of the immediate future prospects. The tolerance factor above was later expanded to include $A_4B_3O_{12}$ and A_2BO_5 phases[275], limited to B≠V due to the notorious lack of vanadate phases in these families.

Where quantification is difficult or ambiguous, it is possible to at least have an expectation of a particular stoichiometry or even symmetry under some favored conditions. It was proposed recently[275] that A_2BO_5, $A_2B_2O_7$, $A_4B_3O_{12}$, cubic fluorites ($AO_{2-\delta}$), and some other phases can be distinguished based on the cation to anion stoichiometric ratio, which increases in the direction $AO_{2-\delta}$ → $A_2B_2O_7$ (incl. disordered) → $A_4B_3O_{12}$ → A_2BO_5. At the same time, if not a function of temperature, anion- or full disordering depends on the ratio of A to B cation radii and on the absolute values thereof. For example, in the series $A_2B_2O_7$ as plotted in the r(B)-r(A) space for CN = VI, fluorites form with large B^{4+} cations and smaller A^{3+} cations, layered perovskites form with smaller B^{4+} cations and larger A^{3+} cations, and pyrochlores form everywhere in between. In the A_2BO_5 series, smaller A^{3+} and B^{4+} cations favor ordered lower-symmetry phases, while larger cations favor disordered high-symmetry phases. The fluorite-pyrochlore pair $ABO_{3.5+\delta}$-$A_2B_2O_7$ with B≠V is the most extensively studied order-disorder competition. On the one hand, disordering of a pyrochlore into a fluorite owes to the size proximity of A^{3+} and B^{4+} cations. Thus, Sickafus *et al.*[302] investigated the propensity toward antisite defect formation (site mixing of single ions on the level of defects) and found that fluorites can form in the system with $r(B_{VI}) \geq 0.72$ Å (Zr) and $0.9 \text{ Å} \leq r(A)_{VI} \leq 1.03$ Å (Y – La). On the other hand, disordering can be imagined as an extreme case of antisite defect creation which for thermodynamic reaction products is driven by entropy and hence persists with an increased temperature. The latter is also true for the pair o-Sc_2TiO_5 – c-Sc_2TiO_5, wherein a high-temperature phase transition occurs from a partially disordered pseudobrookite to a disordered fluorite. One limitation of such prediction for vanadates, however, is the redox activity of vanadium. Its wide range of available oxidation states and related ionic radii is a rose with thorns. An example of the "rose" is the opportunity to topotactically access metastable phases e.g. $ScVO_{3.5}$ and $InVO_{3.5}$, while "thorns" are uncontrollable disproportionation of V^{4+} in t-$Sc_2VO_{5+\delta}$ yet stability in V_3O_5 and In_2VO_5. As was discussed in ***Section 4.8***, its disproportionation might be due to the need for larger Sc^{3+} (in larger coordination than In!) to

coexist with smaller vanadium V^{5+}, but (1) it cannot be predicted as of yet from comparing the cation radii in the same coordination ($r(Sc^{3+})_{VI} < r(In^{3+})_{VI}$) and (2) while it addresses the stabilization of tetrahedral vanadium in hydrothermal phases, it does not address $A_7V_3O_{16}$ phases. An attempt to systematize several families of vanadates is presented below.

7.2.1. Structure stability fields

Recently, O'Quinn *et al.*[7] suggested a structural stability field model wherein the concentration of oxide vacancies is taken into account. In other words, all plotted phases have a common denominator – for example, they can be considered as oxygen-defect with respect to one structure type such as fluorite. This field is a plot in the system of axes (ρ_C, ρ_A), where ρ_C is the largest cation ratio of the two:

$$\rho_C = max\left\{\frac{<r_C>}{r_A}, \frac{r_A}{<r_C>}\right\}, \qquad (7.1)$$

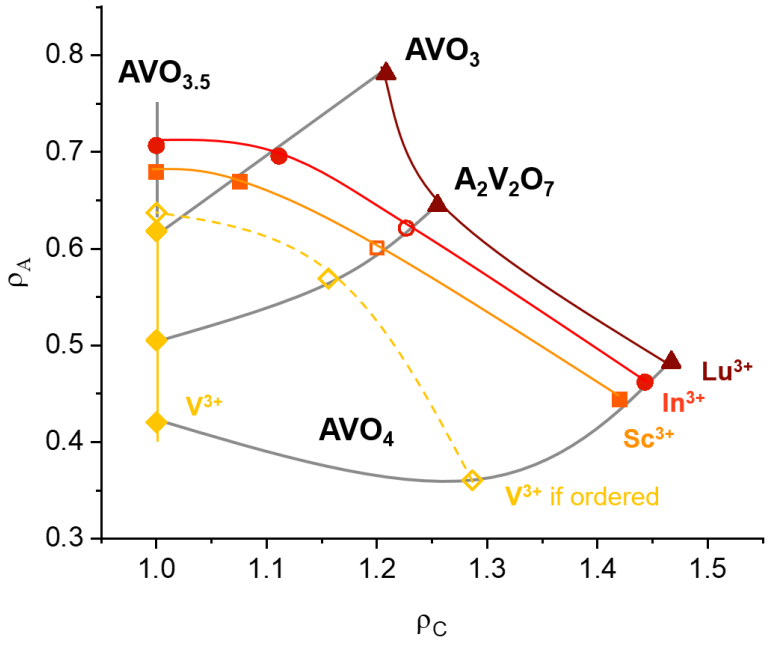

Figure 7.2. Stability field for $A_2V_2O_7$, AVO_3, $AVO_{3.5}$, and AVO_4 phases with cation ratio 1:1. The first three phases were treated as oxygen-deficient with respect to AVO_4. Close markers are reported phases, empty markers are hypothetical phases. Grey lines connect similar stoichiometric families, colorful lines combine phases with the same A^{3+} cation.

with $\langle r_C \rangle$ – the average cation radius, r_A – radius of the A cation, and

$$\rho_A = \frac{\langle r_C \rangle}{r_O \cdot \left(x_O / (x_O + x_V) \right)}, \qquad (7.2)$$

where r_O – radius of the oxide anion (taken as 1.38 Å[103]), and x_O and x_V – number of oxide anions and oxide vacancies per unit formula. For example, for In_2VO_5 with octahedral In^{3+} and V^{4+}: (1) r_A = 0.80 Å, r_V = 0.58 Å, hence $\langle r_C \rangle$ = (2*0.80+0.58)/3 = 0.73 Å; (2) ρ_C = 0.80/0.73 = **1.10**; (3) r_O = 1.38 Å, x_O = 5, x_V = 1, hence ρ_A = 0.727/(1.38*5/6) = **0.63**. Notably, while the authors used the cation radii in the same environment to discriminate between, say, fluorites and pyrochlores just on the grounds of the ionic size ratios (within the same stoichiometry), below the real radii were taken in order to comment on the effect of cation ordering on the appearance of the stability field (moreover, across different stoichiometries). The stability field in **Fig. 7.2** illustrates several V^{3+}-vanadates $AV^{3+}O_3$, pyrovanadates $A_2V^{4+}{}_2O_7$ ($AV^{4+}O_{3.5}$), and orthovanadates $AV^{5+}O_4$ with the cation ratio A:V = 1:1, where A = Lu (dark-red), In (red), Sc (orange), and V (yellow). All phases are plotted on the same scale, and to do so they were normalized to the ratio of cations to anions 1:2, i.e. to the stoichiometry of a fluorite or a zircon, producing $x_O/(x_O+x_V)$ = 3/4, 7/8 (3.5/4), and 4/4, respectively. Solid markers are known phases, while open markers are theoretically plausible phases (i.e. $Sc_2V_2O_7$, $In_2V_2O_7$) or speculative phases (i.e. VO_2 if it were a zircon or V_4O_7 if it were

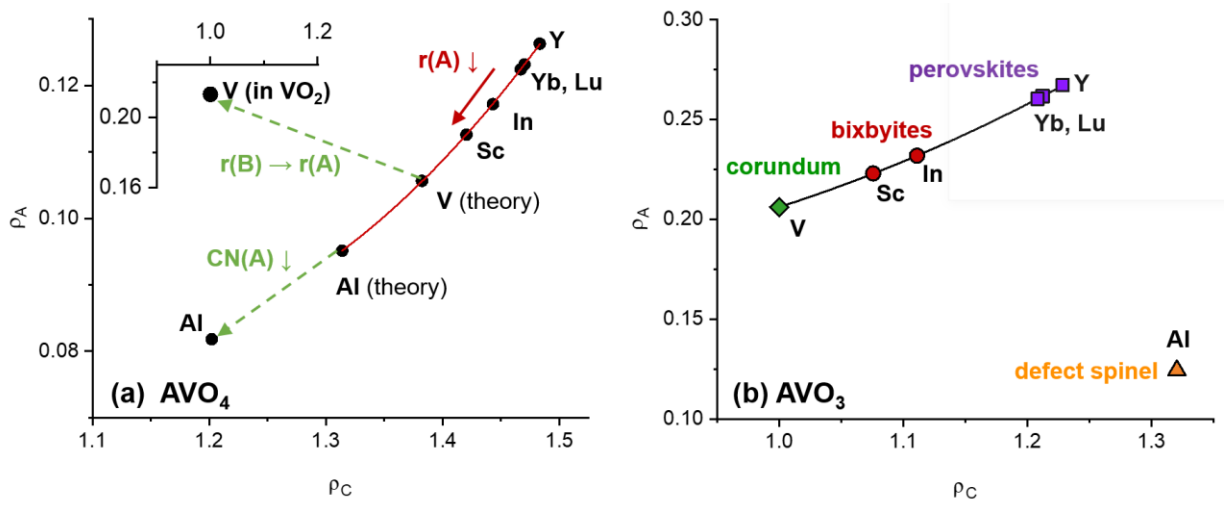

Figure 7.3. Stability fields for AVO_4 (a) and AVO_3 (b) phases with different A^{3+} cations. In panel (a), the red line is a polynomial $\rho_A = 0.46(2) - 0.68(3)\rho_C + 0.31(1)\rho_C^2$, R^2 = 0.99996; in panel (b), the black line is a polynomial $\rho_A = 0.30(1) - 0.39(2)\rho_C + 0.29(1)\rho_C^2$, R^2 = 0.99998.

a pyrochlore). Grey lines are guides to the eye passing through the stoichiometric families of phases. These guides are well-apart and become more horizontal the larger the A:B size ratio, while the line cutting through the disordered fluorite phases ($AVO_{3.5}$) is vertical. So is the yellow line connecting charge-disordered vanadium phases: V_2O_3 (=$V^{3+}V^{3+}O_3$); VO_2 (=$V^{4+}V^{4+}O_4$), and V_4O_7 (= $V^{3.5+}{}_2V^{3.5+}{}_2O_7$). This is in contrast with the speculative case of full charge ordering in these oxides – $V^{3+}V^{5+}O_5$ "zircon" (bottom left) and $V^{3+}{}_2V^{4+}{}_2O_7$ "pyrochlore" – center, which together with unchangeable V_2O_3 lie on the curved line (dashed yellow) akin to cation- and charge-ordered phases with A = Lu, In, Sc. Thus, this diagram draws a clear distinction between cation- (or charge-) ordered and disordered phases: fully disordered phases line up along the Y axis (necessarily passing through $\rho_C = 1$), while fully ordered and non-defect phases mostly line up along the X axis, with ordered oxygen-defect phases in between. And since O'Quinn's parameters ρ_C and ρ_A are related to the cation size ratio and cation to anion size ratio, correspondingly, the diagram is an illustration of which ionic radii (cationic and anionic) can exist in which stoichiometries. **Fig. 7.3** and **Fig. 7.4** give a closer look at these phases, with a few other A^{3+} cations taken into consideration. Zircons AVO_4 are presented in **Fig. 7.3a**, where both observed and theoretical (A = V, Al) phases are plotted in the same space. The trend line connecting genuine zircons (Y to Sc) is almost linear, but adding projected V and Al zircons (a hypothetical case of V and Al forming zircon phases) turns it into a second-order polynomial. Real $AlVO_4$[211] (triclinic) does not deviate much from this trend (it is connected with a dotted green line, which is an extension of the red polynomial). Since A^{3+} cations in this phase are ordered with tetrahedral vanadium, the trend line indicates the decrease in the A cation size and its coordination number, as emphasized by a large leap from zircon-$AlVO_4$ with CN(Al) = VIII to real $AlVO_4$ with CN(Al) = VI. This is not the case for real VO_2 (monoclinically distorted rutile, cation- and charge-disordered by definition) – see inset, especially axis labels. **Fig. 7.3b** presents the AVO_3 phase space for the same A^{3+} cations. The diagram is much more structurally diverse, and all phases but Al-deficient spinel[303] end up on the same line. The structural diversity is likely due to fewer O^{2-} anions per unit formula than in AVO_4, which gives more control over the structure type to the radii of the A and B cations, which are in closer proximity in the AVO_3 phases than in AVO_4. From Y to V, the structure of the thermodynamic product changes several times from perovskite (purple) to bixbyite (red), to corundum (green). Thus, the trend vividly illustrates the Goldschmidt tolerance factor in two dimensions as well as the decrease of unit cell density. Driving the change in this

series is mostly the size of the A^{3+} cation, since the B-cation is always V^{3+}. In the spinel, the B site is split between Al^{3+} and V^{3+} in 1:2 ratio (cation disorder in one site), which might be the reason for its separation from the rest of the phases of the same stoichiometry.

Similar trends were plotted for V^{4+}-bearing phases $A_2V_2O_7$ (including $AVO_{3.5}$) and ordered A_2BO_5-type phases, including A_2VO_5 and Sc_2BO_5 phases, in **Fig. 7.4**. For pyrochlores (red line in panel **a**), a high-pressure phase with A = Y, ambient phases with A = Yb and Lu, and hypothetical phases ("theory") with A = In, Sc, and V are presented. Hypothetical phases include a yet

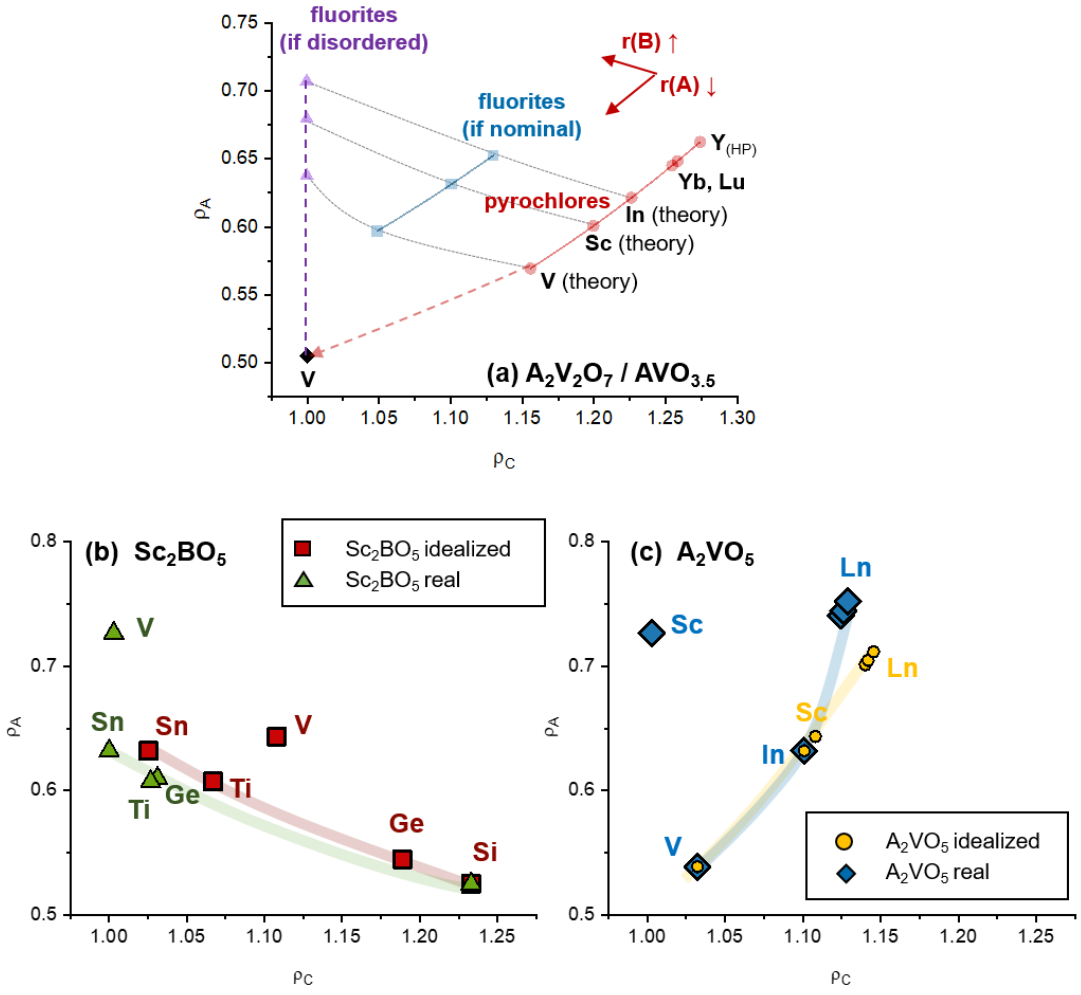

Figure 7.4. Stability fields for ordered and disordered $A_2V_2O_7$ (a), Sc_2BO_5 (b), and A_2VO_5 (c) phases. In panel (a), pyrochlore phases (red) and idealized ordered fluorites (blue) can be described by polynomials $\rho_A = 1.14(3) - 1.65(5)\rho_C + 1.00(2)\rho_C^2$ with $R^2 = 1$ and $\rho_A = 0.78 - 0.98\rho_C + 0.76\rho_C^2$ with $R^2 = 1$, while the purple line passing through actual disordered fluorites is a straight line $\rho_C = 1$. In panels (b) and (c), "idealized" phases are cation-ordered and fully stoichiometric – A_2BO_5, and lines are guides to the eye.

unreported structure for A = In, unreported as a pure phase but anticipated or reported without crystallographic details pyrochlore with A = Sc[188,304], and V_4O_7 (or $V_2V_2O_7$, A = V) if it were a cation- and charge-ordered pyrochlore rather than a mostly disordered Magnéli phase. The trend line connecting these points can be described with a second-order polynomial. It is visibly shifted from the blue trend line passing though the defect fluorite structures $A_2V_2O_7$ (or $AVO_{3.5}$), represented by metastable $InVO_{3.5}$, $ScVO_{3.5}$[93], and V_4O_7 if it were a fluorite. The difference between the blue and purple lines, both representing the same structures, is in whether the cation disorder was taken into account, which makes the purple line the true defect fluorite trend line, while making the blue line the line that allows a sensible comparison with pyrochlores from the standpoint of cation size (or rather the coordination number, which is related to size). From red to blue, the radius of the B cation (vanadium) increases from 0.58 Å to 0.65…0.72Å, together with an increase in coordination number from VI to VII…VIII. From blue to purple, the ionic radii of A and B cations are replaced with just one average radius due to full cation disorder between A and B cations, which is the main distinction from O'Quinn's approach. Notably, the real V_4O_7 phase (black symbol) lies on the extrapolated disordered fluorite trend due to A-B cation mixing, like in any average fluorite. **Fig. 7.4b** is a similar plot of A_2BO_5-type phases considered in ***Chapters 4*** and ***5***. Markers of different colors represent different phase families: red – idealized (fully-ordered) Sc_2BO_5 phases from B = Si to B = Sn; green – actual Sc_2BO_5 phases (with partial cation disorder and non-integer stoichiometry); yellow – idealized A_2VO_5 phases (ordered, stoichiometric, all-V^{4+}); blue – actual A_2VO_5 phases. Most phases in both idealized and real (experimental) series align well in a straight or curved line – see guides to the eye. Minor deviations from the main trends or between idealized and real phases are due to cation disorder (Sc-Ge, Sc-Ti in panel *b*) and violation of stoichiometry in $A_7V_3O_{16}$ phases (panel *c*). Major deviations are associated with t-$Sc_2VO_{5+\delta}$ present in both panels *b* and *c*. They are related to the oxygen deficiency ($\delta = -0.15$) affecting ρ_A and be the presence of smaller V^{5+} cations and 9% Sc-V cation disorder affecting ρ_C.

7.3. Conclusion

The A-V-O phase diagram with A ranging from V^{3+} to Ti^{3+} (which turned out to be mostly Ti^{4+}, smaller than V^{3+}) is structurally diverse. The radius of the A^{3+} cation increases toward the right

part of the phase diagram, i.e. away from the radius of the average V^{4+}, and A-V cation ordering follows this increase. No structures were found so far with the largest A^{3+} cation coexisting with V^{4+} in the 2:1 stoichiometric ratio: most frequently, disproportionated phases AVO_3 and AVO_4 can be found instead, both with 1:1 stoichiometric ratio of A and V cations. Where octahedral V^{3+} and V^{4+} exist, topotactic chemical redox process can carefully tune V^{3+} to V^{4+} and vice versa (done for A = Sc, expected for A = Lu, Yb, Tm).

A few stoichiometric families were plotted simultaneously and then individually in the O'Quinn's structure stability field based on real radii of the cations (as opposed to radii in the same coordination). Such a representation clearly separates these families of phases and allows locating other isostructural phases with different A^{3+} cations in the same space and hypothetically – vanadates with intermediate oxidation states of vanadium. Furthermore, it contrasts cation-ordered and disordered phases, even those having the same stoichiometry (such as fluorites and pyrochlores). While the considered AVO_3, $A_2V_2O_7$, and AVO_4 phases with real radii of the cations involved almost exclusively ended up on the same respective second-order polynomials, A_2VO_5 and Sc_2BO_5 stability fields were less predictable, mostly due to t-$Sc_2VO_{5+\delta}$ with its minor cation ordering and vanadium disproportionation. The appearances of the plots are also affected by non-integer cation stoichiometry and small variations of oxide vacancy concentration. All these parameters are tightly related and some are dependent upon synthetic conditions.

CHAPTER 8

Conclusion and future work

This work covers the solid-state synthesis, the characterization, and control of oxide defects in oxygen-deficient solids with different extents of cation and anion ordering. Using the $Sc_2VO_{5+\delta}$ system, it was shown that crystal structures can be looked at as *static* snapshots of *dynamic* structure evolution processes during reconstructive and especially topotactic synthesis and redox reactions. These processes were followed with *ex-situ* and *in-situ* X-ray and neutron scattering experiments and spectroscopic techniques. Complementary average and local structure probes were shown to be an effective toolkit for studying ion ordering, charge ordering, cation-oxygen coordination, and charge speciation as well as local coordination preferences for reconciling average structures. For example, if only average structure probes had been used, vanadium disproportionation in t-$Sc_2VO_{5+\delta}$ (***Chapter 3***) and the different coordination preferences of V^{5+} and Sc^{3+} in c-$Sc_2VO_{5+\delta}$ (***Chapter 6***) would have been overlooked.

One of the main foci of this work is the defect fluorite system $Sc_2VO_{5+\delta}$ forming as low-T cubic or high-T tetragonal phase. This system is a versatile template to study cation order-disorder interplay, charge ordering, structure stability, control of oxide vacancy concentration, radii-determined site preferences, crystal structure relationship through topotactic chemistry, passivation (poor conduction) hindering redox reactions, and fundamental magnetism. The tetragonal defect fluorite superstructure t-$Sc_2VO_{5+\delta}$ was recently revisited and extensively studied with XRD, NPD, XANES, and DC magnetometry[31]. It was shown to be predominantly cation-ordered, non-stoichiometric (δ=-0.15 for an as-prepared sample), and the only A_2VO_5-type phase where vanadium exists in three oxidation states preferring two different coordination environments – CN=IV for V^{5+} and CN=VI for $V^{3+\ldots4+}$. Topotactic oxygen uptake and removal around the octahedral vanadium site is possible between 300 ºC and 500 ºC. The range of oxygen concentrations studied is narrower than the predicted possible range tolerated by the structure (defined by all-V^{3+} and all-V^{4+} composition of the octahedral site), and further experiments with prolonged heating are needed to probe the limits of the O^{2-} concentration. The discussed four synthetic routes showed how t-$ScVO_{5+\delta}$ is related to other vanadates, namely: (1) to the zircon

$ScVO_4$ – through non-topotactic oxidation, (2) to the bixbyite $Sc_2VO_{4.5}$ – through non-topotactic reduction, (3) to the pseudo-cubic fluorite c-$Sc_2VO_{5+\delta}$ (with partially retained cation ordering) – through topotactic oxidation, and (4) to a bixbyite phase (with expected retained ordering) – through topotactic reduction. Notably, during oxidative and reductive formation of t-$Sc_2VO_{5+\delta}$, the product was formed as a passivating layer on the interface between the starting bixbyite or zircon that constantly needed to be broken up. This indirectly points at the poor oxide ion conducting properties of t-$Sc_2VO_{5+\delta}$ expected from its ordered anion sublattice. Another synthetic route – *in vacuo* from three components – used both bixbyite (with V^{3+}) and zircon (with V^{5+}) precursors in varying ratios. The aim was to directly seed the two vanadium sites (octahedral and tetrahedral), otherwise found upon disproportionation of a V^{4+}-bearing starting material. This synthesis exploited the general strategy of an organic chemical experiment, where coordination polyhedra around vanadium were meant to mimic functional groups. Future work on t-$Sc_2VO_{5+\delta}$ should include but are not limited to (1) targeted doping of the 2*c* vanadium site for rational design of magnetic phases, (2) oxide ion conducting work, to shed more light on the nature of passivation of high-T redox reactions, (3) energy calculations to address possible reductive formation of metastable c-$Sc_2VO_{5+\delta}$ from $ScVO_4$, (4) further probing of the limits of oxygen concentration, and (5) studying cation-ordering and the local structure in products of topotactic reduction and oxidation reactions of t-$Sc_2VO_{5+\delta}$.

The ordered t-$Sc_2VO_{5+\delta}$ system belongs to a family of ordered A_2VO_5 phases, and ***Chapter 4*** focusses on these phases. This family so far included charge-ordered V_3O_5 and ordered In_2VO_5. Four reported hydrothermally obtained phases with A = Y, Yb, and Dy (×2) were included in this family as well; however, in this work they were treated with caution due to the rare and not sufficiently explained coordination number of V^{4+}. Three new members with slightly different cation stoichiometry were suggested – $A_{2.1}V_{0.9}O_{4.8+\delta}$ with A = Lu, Yb, and Tm previously reported as $A_7V_3O_{16}$[217,220,228]. These are mixed-valence vanadates thermodynamically outcompeting their respective pyrochlores $A_2V_2O_7$ at 1200 ºC. Phases with A = Lu, Yb, and Tm are isostructural; structure solution was done on the most phase-pure A = Yb sample against synchrotron powder XRD and NPD data. The phase was indexed in space group *Pccn* with sixfold Yb^{3+} and sevenfold $V^{3.67+}$ coordination. The vanadium sublattice is formed by corner-sharing chains, similar to the corrugated V^{4+} chains in In_2VO_5 but more stretched out. The 2.1:0.9 ratio of cations and 2:1 ratio

of corresponding cation sites were reconciled with a 33% admixture of Yb^{3+} in the $V^{3.67+}$ site. Two out of four oxygen sites are >25% deficient, which might locally translate into a lower cation coordination (such as CN = V). Oxygen stoichiometry in the as-synthesized sample was refined to O_{16} per $Yb_7V_3O_{16}$ unit formula, which corresponds to the net oxidation state of vanadium of 3.67+. Due to size proximity of V^{3+} and V^{4+} in CN = VI and from the oscillation of the unit cell volume throughout multiple heatings of $Lu_{2.1}V_{0.9}O_{4.8+\delta}$, vanadium in all three phases (A = Yb, Lu, Tm) is expected to be prone to topotactic redox reactions – above 900 ºC from separate experiments. One of the future goals is to follow the oxidation with an *in-situ* NPD experiment to establish whether its unit cell volume increases (like in $Sc_2VO_{5+\delta}$ with smaller cations) or decreases (like in $YPrO_{3+\delta}$ with larger cations).

Throughout the A_2VO_5-type series, with increasing radius of A^{3+}, connectivities and dimensionality of the vanadium sublattice change from corrugated chains of edge- and face-sharing octahedra to spread-out isolated tetrahedra, if hydrothermal phases[**34**] are taken into consideration. When A_2VO_5-type phases are plotted in ascending order of A^{3+} radii as opposed to nominal, t-$Sc_2VO_{5+\delta}$ (with $r(Sc^{3+})_{VII...VIII} > r(In^{3+})_{VI}$) serves as a bifurcation point: its octahedral vanadium character is akin to the only vanadium environment in $A_{2.1}V_{0.9}O_{4.8+\delta}$ phases (from the preliminary structure solution), while its tetrahedral vanadium motif is akin to the only vanadium environment in phases with A = Y, Yb, and Dy. Similar propensity toward the isolated tetrahedral environment was observed in the Sc_2BO_5 phases (B = Si, Ge, V, Ti, Sn) the smaller the B^{4+} cation became.

In ***Chapter 5***, the octahedral site of the t-$Sc_2VO_{5+\delta}$ structure was doped with several cations commensurate with V^{3+} and V^{4+}. The goal of the chapter was to demonstrate targeted manipulation of oxide vacancy concentration and to probe the dependence of cation ordering as a function of the size and charge of the dopant via non-topotactic means. Virtually single phase samples in the $Sc_2V_{1-x}B_xO_{5+\delta}$ system were obtained with x = 0.2 and nominal B = Ge^{4+}, Ti^{4+}, Sn^{4+}, Cr^{4+}. When doping above this concentration (in ~0.2 steps), as well as when doping with Zr^{4+}, Mn^{4+}, Fe^{3+}, or $Co^{2.67+}$, competing phases started to form, most often belonging to Sc_2BO_5, $Sc_2B_2O_7$, and $Sc_4B_3O_{12}$ types as well as common binary oxides with the general formula B_xO_y. For the single-phase solid solutions with x=0.2, the octahedral ionic radius of the B cation showed to be a good predictor of site preferences of the dopant. For instance, ~50% of the tetrahedral site of the $Sc_2V_{0.8}Ge_{0.2}O_{5+\delta}$

accommodates smaller Ge^{4+} from neutron diffraction data, while larger cations populate the octahedral site of vanadium and occasionally the scandium sites. Site preferences were then quantified with an *ad hoc* ordering coefficient which also revealed that phases with redox-active dopants such as Cr and V are slightly more cation-ordered. XANES showed that chromium in $Sc_2V_{0.8}Cr_{0.2}O_{5+\delta}$ exists as Cr^{3+} as opposed to nominal Cr^{4+}, while Ge and Ti most probably stay in their 4+ state (no data for Sn^{4+} were available). Purely trivalent ions (Cr) or tetravalent ions (Ge, Ti, and Sn) are useful in probing the lower and upper threshold of oxygen concentration in the tetragonal polymorph. $Sc_2V_{0.8}Sn_{0.2}O_{5+\delta}$ has the highest oxygen concentration among the single phase solid solutions considered, but less than $\delta = 0$ which is not enough to entirely fill the eight initially reported anion sites. The $Sc_2V_{1-x}Ti_xO_{5+\delta}$ system is the most promising due to commensurability of Ti^{4+} and $V^{3+\ldots4+}$ – a single phase can be obtained with larger x if ground for longer prior to heating (shown elsewhere[127]). Neutron data with Fourier mapping will be a way to establish (*i*) whether oxygen uptake for the largest x (=0.8) happens beyond the known eight oxygen sites or (*ii*) whether the vacant anion sites are invoked. In general, t-$Sc_2VO_{5+\delta}$ is an excellent template for (1) probing the tolerance of the structure toward 8*g* site dopants of various ionic radii and charges; (2) controlling the concentration of oxide ion vacancies with topotactic chemistry or tuning it by doping. One particular goal is to confirm that oxide ion concentration can be tuned by all-4+ cation(-s) in the 8*g* site ($\delta = 0.1$) and is not limited by the capacity of 8 known oxygen sites ($\delta=0$).

Another goal is to verify the two oxide vacancy sites in the anion sublattice by populating them and using scattering density maps to observe them. Two vacant sites were indeed found by exploring the structure; they are expected to partake in the oxygen-driven phase transition from t-$Sc_2VO_{5+\delta}$ to c-$Sc_2VO_{5+\delta}$. One site is general (x, y, z) with $x \approx 0.24$, $y \approx 0.45$, and $z \approx 0.31$; it is situated around the tetrahedral vanadium site of t-$Sc_2VO_{5+\delta}$. The other site is special (0, 0, ½), situated inside the V_4-clusters formed by the octahedral vanadium site. When these sites are fully filled with oxygen (with maximum occupancy 91.7% from charge neutrality!), the average coordination of cations is brought to CN = VIII, which establishes a regular fluorite lattice. However, such a fluorite exists only in a narrow window of temperatures and quickly (and non-oxidatively) decomposes into $ScVO_4$ and Sc_2O_3 (2:1 ratio) already above ~650-700 ºC. Interestingly, the neutron diffraction data show a strong superstructure peak (7 Å) resembling the

characteristic peak of t-$Sc_2VO_{5+\delta}$. In the absence of t-$Sc_2VO_{5+\delta}$ in the product, this peak belongs to c-$Sc_2VO_{5+\delta}$ and is a manifestation of retained long-range cation ordering in the otherwise cubic phase. Efforts to obtain reliable structural details of this phase are complicated by having too few diffraction peaks, in addition to being strained, per the number of parameters needed to be refined. Three Rietveld refinement models were suggested, the best being a mixture of a fully disordered fluorite ($Fm\bar{3}m$) and partially ordered fluorite - based on t-$Sc_2VO_{5+\delta}$ ($I\bar{4}$) but with refineable Sc-V mixing. A purer sample was attempted at a slightly lower temperature of 630 ºC – and at any recorded point of its heating profile, accompanied by oxidation, the refinement is still better when a two-phase model is used. Topotactic reduction of this oxidized sample at 400 ºC resulted in a bixbyite phase. The topotactic nature of the reduction suggests retention of cation mixing in the bixbyite. It is further suggested that this bixbyite is similar to the bixbyite that was observed on reduction of t-$Sc_2VO_{5+\delta}$ above 460 ºC during the topotactic reduction experiment targeting the 8*g* site. The extent of suspected cation ordering in the bixbyite-looking product will be further obtained from a joint XRD/NPD experiment when a large and pure enough bulk sample is obtained.

In both (pseudo-)cubic phases c-$Sc_2VO_{5+\delta}$ obtained from t-$Sc_2VO_{5+\delta}$ and $Sc_2VO_{4.5}$ in ***Chapter 6***, the average structure from XRD is indeed consistent with a cubic fluorite, whereas both vanadium XANES and PDF show signatures of shorter V-O bonds (shorter than Sc-O), which suggests V-Sc ordering on the local scale. Refinement of PDF data on c-$Sc_2VO_{5+\delta}$ obtained from t-$Sc_2VO_{5+\delta}$ will only be possible after the average structure is refined with a single-phase model or a single-phase sample is finally obtained. PDF refinement of c-$Sc_2VO_{5+\delta}$ obtained from $Sc_2VO_{4.5}$ was performed with a large-box RMC method on an 8×8×8 supercell (512 unit cells). In this c-$Sc_2VO_{5+\delta}$, V-O, Sc-O, and especially O-O bond distances form a broad distribution, in agreement with large atomic displacements of all three species. Short V-O bonds, responsible for high absorption pre-edge feature in vanadium XANES, do not form polyhedra of their own – they are diluted by longer V-O bonds in a wide range of coordination geometries. On average, Sc^{3+} ions have a slight preference for CN = VIII (distorted cubes), while V^{x+} ions have a slight preference for the most abundant CN = VII (O^{2-}-deficient cubes). Folding of all 512 unit cells onto one cell to show the displacement of ions away from their average positions invites a discussion of oxide ion conduction. If c-$Sc_2VO_{5+\delta}$ enables conduction, displacement of oxide ions and oxide ion vacancies in the folded RMC structure might be telling of the preferred O^{2-} ion migration path. In

particular, the majority of displaced O^{2-} ions were found between nearest special positions of oxides (or tetrahedral voids) as shown with the (400) plane, while nearly no O^{2-} ions were found around the octahedral holes as shown in the (110) plane. In the same plane views, oxide ion vacancies were found either around special positions of oxygen or between them and marginally closer to octahedral voids than oxide ions themselves. Future work will investigate the predictions of oxide ion mobility stemming from the static picture of their displacement. Impedance spectroscopy and high-T neutron PDF analyses will be necessary to confirm oxide ion conduction and to locate the displaced oxides at conducting temperatures, correspondingly.

Additionally and unlike c-$Sc_2VO_{5+\delta}$, no disordered indium analogue was found in the In-V-O system. This synthesis started with obtaining a new phase that deemed a cubic bixbyite $In_2VO_{4.5}$ based on laboratory X-rays, which then was carefully oxidized. From examination of the low-angle superstructure peaks and the wide main structure peak, as well as from the topotactic nature of this reduction, the phase was established to be a reduced form of In_2VO_5, refined as $In_2VO_{4.81(5)}$. No high-resolution XRD or NPD data were available to reliably refine oxygen positions. Future work will (1) investigate the evolution of the vanadium sublattice during topotactic reduction of In_2VO_5 and (2) liken it to the case of t-$Sc_2VO_{5+\delta}$ whose reduction at 400 ºC also yielded a bixbyite-looking phase with suspected retention of long-range cation ordering. The observed window of vanadium oxidation states for t-$Sc_2VO_{5+\delta}$ and $In_2VO_{5+\delta}$ opens up an opportunity to manipulate the concentration of oxide ion vacancies to drive structural changes. Further, the resemblance of XRD patterns of their topotactic (hence likely ordered) redox products with bixbyite patterns inspire to further probe the limits of structural stability of parent phases in terms of O^{2-} concentration beyond which the structure transitions or decomposes. Topotactic redox reactions unlock the opportunity to look at redox-related structures as milestones of structure evolution – a dynamic process that can clarify solid-state reaction mechanisms. For the fluorite structure in particular, remarkable stability toward a range of cationic sizes and charges was shown. Such stability greatly owes to the topotactic nature of the synthesis.

In ***Chapter 7***, ordered and disordered phases mentioned throughout this thesis were sorted by ionic radius of A^{3+} and $V^{3+\ldots5+}$ cations to be presented in two phase diagrams – A_2VO_x (x = 4.5, 5.0, 5.5) and AVO_x (x = 3.0, 3.5, 4.0). Cation ordering is observed in phases with larger A^{3+} cations and larger r_A/r_B ratio. It is especially pronounced in the AVO_x diagram where more phases have

been experimentally obtained than in the A_2BO_x diagram. The lack of large-A^{3+} phases in the latter is associated with their decomposition into respective AVO_x phases and a surplus of ½ A_2O_3 observed in particular during solid-state redox reactions with A = Sc, In, Lu, Yb, Y.

To rationalize the effect of relative ionic sizes of the two cations and oxygen in A_2VO_5/Sc_2BO_5, AVO_3, AVO_4, $A_2B_2O_7$ (especially B = V^{4+}), and $A_4B_3O_{12}$ phases on structure and/or stoichiometry, structure stability fields were plotted. They are a convenient tool visualizing ion-size-dependent cation- and charge-ordering, starting and final states of redox processes, potentially application of pressure (fluorite→ pyrochlore, bixbyite→ perovskite, etc.), and, from their name, stability regions of stoichiometric families. Ordered zircons AVO_4 and pyrochlores $A_2V_2O_7$ group together, while phases with smaller A^{3+} cations stick out. For the AVO_3 stoichiometry, a handful of considered phases mostly group together regardless of cation ordering and structure type in the range from A = V^{3+} and A = Ln^{3+}. In contrast, A_2VO_5 and Sc_2BO_5 phases are more diverse: oxygen and metal non-stoichiometry and especially the aliovalent vanadium sublattice of t-$Sc_2VO_{5+\delta}$ make the plots more diffuse. This speaks to the lower predictive power of A_2VO_5 stability fields, but so does the scarcity of A_2VO_5 phases. Notwithstanding the abundancy of A^{3+} species in the *d* and *p* blocks of the Periodic Table, there are not enough stable A^{3+} cations that could stabilize an A_2VO_5 phase in a solid-state reaction. A more realistic classification-prediction project could instead focus on preferred stoichiometry of competing phases in the general A^{3+}-B^{4+}-O^{2-} system discussed in this work (A_2BO_5, $A_2B_2O_7$, $A_4B_3O_{12}$), not necessarily limited to the case of B = V^{4+}.

Results of this work are expected to contribute to the study of cation ordering, tuneable oxide vacancies, and other topics related to features of metal oxide structures and their manipulation. Successful implementation of average and local structure techniques to redox-active vanadate systems endorses the usage of more common average structure probes always in tandem with complementary local probes even for the most well-studied structure types.

References

1 F. J. DiSalvo, *Science (80-.).*, 1990, **247**, 649–655.

2 J. Mizusaki, in *New research trends of fluorite-based oxide materials*, eds. A. Nakamura and J. Mizusaki, Nova Science Publishers, Inc., New York, 2015, pp. 1–28.

3 J. B. Goodenough, *Nature*, 2000, **404**, 821–823.

4 M. H. Park and C. S. Hwang, *Reports Prog. Phys.*, 2019, **82**, 124502.

5 Q. Xu, W. Pan, J. Wang, C. Wan, L. Qi, H. Miao, K. Mori and T. Torigoe, *J. Am. Ceram. Soc.*, 2006, **89**, 340–342.

6 S. R. G. Christopoulos, A. Kordatos, M. W. D. Cooper, M. E. Fitzpatrick and A. Chroneos, *Mater. Res. Express*, 2016, **3**, 105504.

7 E. C. O'Quinn, D. L. Drey and M. K. Lang, *Front. Chem.*, 2021, **9**, 1–9.

8 J. A. Kilner, *Solid State Ionics*, 2000, **129**, 13–23.

9 G. S. Zhdanov and A. A. Rusakov, *Dokl. Akad. Nauk SSSR*, 1952, **82**, 901–904.

10 V. D. Risovany, E. E. Varlashova and D. N. Suslov, *J. Nucl. Mater.*, 2000, **281**, 84–89.

11 M. Shiojiri, S. Sekimoto, T. Maeda, Y. Ikeda and K. Iwauchi, *Phys. Status Solidi*, 1984, **A**, 55–64.

12 U. Kolitsch, *Acta Crystallogr.*, 2003, **E59**, 36–39.

13 T. Gaewdang, J. P. Chaminade, P. Gravereau, A. Garcia, C. Fouassier, P. Hagenmuller and R. Mahious, *Mater. Res. Bull.*, 1993, **28**, 1051–1060.

14 R. D. Aughterson, G. R. Lumpkin, G. J. Thorogood, Z. Zhang, B. Gault and J. M. Cairney, *J. Solid State Chem.*, 2015, **227**, 60–67.

15 V. P. Tiedemann and H. Müller-Buschbaum, *Z. anorg. allg. Chem.*, 1982, **494**, 98–102.

16 M. Drofenik, L. Golič, D. Hanžel, V. Kraševec, A. Prodan, M. Bakker and D. Kolar, *J. Solid State Chem.*, 1981, **40**, 47–51.

17 A. E. Austin and C. M. Schwartz, *Acta Crystallogr.*, 1953, **6**, 812–813.

18 A.-M. Lejus, D. Goldberg and A. Revcolevschi, *Comptes Rendus des Séances l'Académie des Sci.*, 1966, **C**, 1223–1226.

19 S. Asbrink and A. Magneli, *Acta Crystallogr.*, 1959, **12**, 575–581.

20 A. A. Rusakov and G. S. Zhdanov, *Dokl. Akad. Nauk SSSR*, 1951, **77**, 411–414.

21 M. Onoda, 1998, **73**, 67–73.

22 Y. A. Gorbunov, B. A. Maksimov, Kharitonov Yu. A. and N. V. Belov, *Crystallography*,

1974, **19**, 1081–1083.

23 P. Berastegui, S. Hull, F. J. García García and J. Grins, *J. Solid State Chem.*, 2002, **168**, 294–305.

24 D. Voll, C. Lengauer, A. Beran and H. Schneider, *Eur. J. Mineral.*, 2001, **13**, 591–604.

25 E. M. Rivera-Munoz and L. Bucio, *Acta Crystallogr. Sect. E Struct. Reports Online*, 2009, **65**, i60.

26 L. Brixner, J. Calabrese and H. Y. Chen, *J. Less-Common Met.*, 1985, **110**, 397–410.

27 S. Ďurovič and P. Fejdi, *Silikáty (Prague)*, 1976, **2**, 97–110.

28 Y. Y. Mikhailov, B. I. Pokrovskii and L. N. Komissarova, *Dokl. Chem.*, 1971, **193**, 403–404.

29 H. Cong, H. Zhang, B. Yao, W. Yu, X. Zhao, J. Wang and G. Zhang, *Cryst. Growth Des.*, 2010, **10**, 4389–4400.

30 G. Samandari, University of Manitoba, 2017.

31 D. Vrublevskiy, J. A. Lussier, J. R. Panchuk, C. Mauws, J. C. Beam, C. R. Wiebe, A. P. Grosvenor and M. Bieringer, *Inorg. Chem.*, 2021, **60**, 872–882.

32 P. J. Senegas, J.-P. Manaud and J. Galy, *Acta Cryst.*, 1975, **B31**, 1614–1618.

33 A. Möller, T. Taetz, N. Hollmann, J. A. Mydosh, V. Kataev, M. Yehia, E. Vavilova and B. Büchner, *Phys. Rev. B*, 2007, **76**, 134411.

34 M. M. Kimani, C. D. McMillen and J. W. Kolis, *Inorg. Chem.*, 2012, **51**, 3588–3596.

35 S. Asbrink, *Acta Cryst.*, 1980, **B36**, 1332–1339.

36 H. Horiuchi, N. Morimoto and M. Tokonami, *J. Solid State Chem.*, 1976, **17**, 407–424.

37 P. Boullay, D. Mercurio, A. Bencan, A. Meden, G. Drazic and M. Kosec, *J. Solid State Chem.*, 2003, **170**, 294–302.

38 G. Cao, S. McCall, Z. X. Zhou, C. S. Alexander, J. E. Crow, R. P. Guertin and C. H. Mielke, *Phys. Rev. B - Condens. Matter Mater. Phys.*, 2001, **63**, 1–10.

39 W. H. McCarroll, C. Darling and G. Jakubicki, *J. Solid State Chem.*, 1983, **48**, 189–195.

40 H. Kerner-Szeskleba and G. Tourné, *Bull. Soc. Chim. Fr.*, 1976, **5**–**6**, 729–735.

41 D. M. Colabello, F. E. Camino, A. Huq, M. Hybertsen and P. G. Khalifah, *J. Am. Chem. Soc.*, 2015, **137**, 1245–1257.

42 L. L. Kochergina, O. I. Kondratov, Y. S. Shorikov, V. V. Fomichev and P. K.I., *Russ. J. Inorg. Chem.*, 1982, **27**, 638–640.

43 A. D. Savel'eva, M. B. Varfolomeev, V. V. Fomichev and K. I. Petrov, *Russ. J. Inorg. Chem.*, 1977, **22**, 1628–1630.

44 K. Waltersson, *Acta Crystallogr. Sect. B*, 1976, **32**, 1485–1489.

45 W. Jeitschko, D. H. Heumannskämper, M. S. Schriewer-Pöttgen and U. C. Rodewald, *J. Solid State Chem.*, 1999, **147**, 218–228.

46 O. Muller and R. Roy, *Mater. Res. Bull.*, 1969, **4**, 349–360.

47 M. D. Alba, P. Chain and T. González-Carrascosa, *J. Am. Ceram. Soc.*, 2009, **92**, 487–490.

48 K. Fukuda, T. Iwata and E. Champion, *Powder Diffr.*, 2006, **21**, 300–303.

49 G. D. Gatta, N. Rotiroti and M. Zucali, *Mineral. Mag.*, 2009, **73**, 359–371.

50 C. L. Melcher, R. A. Manente, C. A. Peterson and J. S. Schweitzer, *J. Cryst. Growth*, 1993, **128**, 1001–1005.

51 O. Hirsch, K. O. Kvashnina, L. Luo, M. J. Süess, P. Glatzel and D. Koziej, *Proc. Natl. Acad. Sci. U. S. A.*, 2015, **112**, 15803–15808.

52 A. Olafsen, A. K. Larsson, H. Fjellvåg and B. C. Hauback, *J. Solid State Chem.*, 2001, **158**, 14–24.

53 C. Artini, F. Locardi, M. Pani, I. Nelli, F. Caglieris, R. Masini, J. R. Plaisier and G. A. Costa, *J. Phys. Chem. Solids*, 2017, **103**, 59–66.

54 S. Sorokina, R. Enjalbert, P. Baules, A. Castro and J. Galy, *J. Solid State Chem.*, 1996, **125**, 54–62.

55 J. T. Szymanski, *Can. Mineral.*, 1980, **18**, 333–337.

56 S. Merlino, P. Orlandi, N. Perchiazzi, R. Basso and A. Palenzona, *Can. Mineral.*, 1989, **27**, 625–632.

57 A. Y. Shashkov, V. A. Efremov, B. A.A., N. V. Rannev, Y. N. Venevtsev and V. K. Trunov, *Zhurnal Neorg. Khimii (Russian J. Inorg. Chem.)*, 1986, **31**, 1391–1396.

58 B. Aurivillius, C.-I. Lindblom, P. Sténson and H. M. Seip, *Acta Chem. Scand.*, 1964, **18**, 1555–1557.

59 C. Sussieck-Fornfeld, Ruprecht-Karls-Universität Heidelberg, 1988.

60 S.-H. Hong and S. Asbrink, *Acta Cryst.*, 1982, **B38**, 713–719.

61 F. X. Zhang, J. W. Wang, M. Lang, J. M. Zhang and R. C. Ewing, *J. Solid State Chem.*, 2010, **183**, 2636–2643.

62 J. S. Knyrim and H. Huppertz, *J. Solid State Chem.*, 2007, **180**, 742–748.

63 J. S. Knyrim and H. Huppertz, *Zeitschrift fur Naturforsch. - Sect. B J. Chem. Sci.*, 2008, **63**, 707–712.

64 M. A. Petrova and R. G. Grebenshchikov, *Glas. Phys. Chem.*, 2008, **34**, 603–607.

65 L. D. Iskhakova, A. B. Ilyukhin, S. A. Kutovoi, V. I. Vlasov, Y. D. Zavartsev, V. F. Tarasov and R. M. Eremina, *Acta Crystallogr. Sect. C Struct. Chem.*, 2019, **75**, 1202–1207.

66 C. Cascales, J. A. Campa, E. Gutiérrez Puebla, M. A. Monge, C. Ruíz Valero and I. Rasines, *J. Mater. Chem.*, 2002, **12**, 3626–3630.

67 O. Joubert, M. Ganne, R. N. Vannier and G. Mairesse, *Solid State Ionics*, 1996, **83**, 199–207.

68 E. V Isaeva and B. I. Pokrovskii, *Acta Cryst.*, 1978, **B34**, 1051–1059.

69 P. Millán, J. M. Rojo and A. Castro, *Mater. Res. Bull.*, 2000, **35**, 835–845.

70 C. Satto, P. Millet, P. Sciau, C. Roucan and J. Galy, *Mater. Reseacrh Bull.*, 1999, **34**, 655–664.

71 J. Galy, R. Enjalbert, P. Millan and A. Castro, *C. R. Acad. Sci. Paris, Ser. II*, 1993, **317**, 43–48.

72 S. Kaiman, D. C. Harrisi, J. E. Dutrizac and B. Street, *Can. Mineral.*, 1980, **18**, 329–332.

73 G. Andersson, *Acta Chem. Scand.*, 1954, **8**, 1599–1606.

74 S. Asbrink, S. Friberg, A. Magneli and A. Andersson, *Acta Chem. Scand.*, 1959, **13**, 603.

75 T. Takahashi, H. Iwahara and T. Esaka, *J. Electrochem. Soc.*, 1977, **124**, 1563.

76 H. Horiuchi, M. Tokonami, N. Morimoto, K. Nagasawa, Y. Bando and T. Takada, *Mater. Res. Bull.*, 1971, **6**, 833–844.

77 Z. C. Wang, S. Yin and E. R. Bernstein, *J. Phys. Chem. Lett.*, 2012, **3**, 2415–2419.

78 A. R. Landa-Cánovas and L. C. Otero-Díaz, *Solid state Sci.*, 2003, **5**, 225–233.

79 S. Halpegamage, Z. Wen, X. Gong and M. Batzill, *J. Phys. Chem.*, 2016, **C**, 14782–14794.

80 H.-J. Bernhardt, K. Schmetzer and O. Medenbach, *Neues Jahrb. fuer Mineral.*, 1983, 110–118.

81 B. I. Pokrovskii, Y. Y. Mikhailov and L. N. Komissarova, *Dokl. Akad. Nauk SSSR*, 1970, **190**, 1117–1120.

82 J. Ito, *Am. Mineral.*, 1971, **56**, 1105–1108.

83 A. Castro, P. Milla, J. Ricote and L. Pardo, *J. Mater. Chem.*, 2000, **10**, 767–771.

84 A. R. West, *Basic Solid State Chemistry*, John Wiley & Sons, Ltd., Chichester, 2nd edn., 1999.

85 F. K. Lotgering, *J. Inorg. Nucl. Chem.*, 1959, **9**, 113–123.

86 R. D. Shannon and R. C. Rossi, *Nature*, 1964, **202**, 1000–1001.

87 H. R. Oswald and J. R. Günter, in *Current Topics in Materials Science. Vol. 2. Crystal Growth and Materials.*, eds. E. Kaldis and H. J. Scheel, North-Holland Publishing Company, Amsterdam, 1976, pp. 415–433.

88 J. R. Günter and H.-R. Oswald, *Bull. Inst. Chem. Res.*, 1975, **53**, 249–255.

89 C. A. Bridges, G. R. Darling, M. A. Hayward and M. J. Rosseinsky, *J. Am. Chem. Soc.*, 2005, **127**, 5996–6011.

90 K. G. Sanjaya Ranmohotti, E. Josepha, J. Choi, J. Zhang and J. B. Wiley, *Adv. Mater.*, 2011, **23**, 442–460.

91 R. E. Schaak and T. E. Mallouk, *Chem. Mater.*, 2002, **14**, 1455–1471.

92 S. Flynn, S. Sanghvi, M. L. Nisbet, K. J. Griffith, W. Zhang, P. S. Halasyamani, S. M. Haile and K. R. Poeppelmeier, *Chem. Mater.*, 2020, **32**, 4785–4794.

93 S. P. Shafi, R. J. Lundgren, L. M. D. Cranswick and M. Bieringer, *J. Solid State Chem.*, 2007, **180**, 3333–3340.

94 B. C. Hernden, J. A. Lussier and M. Bieringer, *Inorg. Chem.*, 2015, **54**, 4249–4256.

95 M. Bianchini, J. Wang, R. J. Clément, B. Ouyang, P. Xiao, D. Kitchaev, T. Shi, Y. Zhang, Y. Wang, H. Kim, M. Zhang, J. Bai, F. Wang, W. Sun and G. Ceder, *Nat. Mater.*, 2020, **19**, 1088–1095.

96 T. Tani and H. Itahara, *Mater. Integr.*, 2004, **17**, 25–31.

97 T. Okada, H. Ogino, J. Shimoyama and K. Kishio, *Appl. Phys. Express*, 2015, **8**, 023102.

98 H. T. D. Nguyen, D. Zhang, T. M. Nguyen, H. Zhang and J. Seidel, *Adv. Opt. Mater.*, 2021, **2100955**, 2100955.

99 J. A. Lussier, F. J. Simon, P. S. Whitfield, K. Singh, V. Thangadurai and M. Bieringer, *Inorg. Chem.*, 2018, **57**, 5607–5614.

100 J. A. Alonso, M. T. Casais and M. J. Martínez-lope, *Dalt. Trans.*, 2004, 1294–1297.

101 L. Pauling, *J. Am. Chem. Soc.*, 1929, **51**, 1010–1026.

102 J. A. Lussier, University of Manitoba, 2018.

103 R. D. Shannon, *Acta Crystallogr. Sect. A*, 1976, **32**, 751–767.

104 W. O. Milligan, L. W. Vernon, H. A. Levy and S. W. Peterson, *J. Phys. Chem.*, 1953, **57**, 535–537.

105 S. Shimono, H. Ishibashi, S. Kawaguchi and Y. Kubota, *J. Solid State Chem.*, 2019, **273**, 37–44.

106 A. Chroneos, B. Yildiz, A. Tarancón, D. Parfitt and J. A. Kilner, *Energy Environ. Sci.*, 2011, **4**, 2774.

107 N. Xu, X. Li, X. Zhao, J. B. Goodenough and K. Huang, *Energy Environ. Sci.*, 2011, **4**, 4942–4946.

108 A. Faes, A. Hessler-Wyser, A. Zryd and J. Van Herle, *Membranes (Basel).*, 2012, **2**, 585–664.

109 T. H. Etsell and S. N. Flengas, *Chem. Rev.*, 1970, **70**, 339–376.

110 A. Lashtabeg and S. J. Skinner, *J. Mater. Chem.*, 2006, **16**, 3161–3170.

111 M. H. Chambrier, A. Le Bail, F. Giovannelli, A. Redjaïmia, P. Florian, D. Massiot, E. Suard and F. Goutenoire, *Inorg. Chem.*, 2014, **53**, 147–159.

112 J. B. Goodenough and P. Singh, *J. Electrochem. Soc.*, 2015, **162**, A2387–A2392.

113 T. Ishihara, H. Matsuda and Y. Takita, *J. Am. Chem. Soc.*, 1994, **116**, 3801–3803.

114 E. Kendrick, M. S. Islam and P. R. Slater, *J. Mater. Chem.*, 2007, **17**, 3104–3111.

115 J. Schuett, T. K. Schultze and S. Grieshammer, *Chem. Mater.*, 2020, **32**, 4442–4450.

116 J. C. Boivin and G. Mairesse, *Chem. Mater.*, 1998, **10**, 2870–2888.

117 J. A. Lussier, G. Devitt, K. M. Szkop and M. Bieringer, *J. Solid State Chem.*, 2016, **242**, 126–132.

118 M. Šimenas, S. Balčiunas, M. MacZka, J. Banys and E. E. Tornau, *Phys. Chem. Chem. Phys.*, 2016, **18**, 18528–18535.

119 R. E. Dinnebier, A. Kowalevsky, H. Reichert and M. Jansen, *Zeitschrift fur Krist.*, 2007, **222**, 420–426.

120 K. Page, M. W. Stoltzfus, Y. Il Kim, T. Proffen, P. M. Woodward, A. K. Cheetham and R. Seshadri, *Chem. Mater.*, 2007, **19**, 4037–4042.

121 W. T. Chen, C. W. Wang, C. C. Cheng, Y. C. Chuang, A. Simonov, N. C. Bristowe and M. S. Senn, *Nat. Commun.*, 2021, **12**, 1–8.

122 B. Chen, Z. Deng, W. Li, M. Gao, Q. Liu, C. Z. Gu, F. X. Hu, B. G. Shen, B. Frandsen, S. Cheung, L. Lian, Y. J. Uemura, C. Ding, S. Guo, F. Ning, T. J. S. Munsie, M. N. Wilson, Y. Cai, G. Luke, Z. Guguchia, S. Yonezawa, Z. Li and C. Jin, *Sci. Rep.*, 2016, **6**, 1–9.

123 A. Simonov and A. L. Goodwin, *Nat. Rev. Chem.*, 2020, **4**, 657–673.

124 S. Westman, *Acta Chem. Scand.*, 1961, **15**, 217.

125 N. Wetchakun, B. Incessungvorn, K. Wetchakun and S. Phanichphant, *Mater. Lett.*, 2012, **82**, 195–198.

126 S. P. Shafi, M. W. Kotyk, L. M. D. Cranswick, V. K. Michaelis, S. Kroeker and M. Bieringer, *Inorg. Chem.*, 2009, **48**, 10553–10559.

127 B. N. Richtik, University of Manitoba, 2021.

128 R. D. Shannon and C. T. Prewitt, *J. Solid State Chem.*, 1970, **2**, 199–202.

129 A. E. Smith, H. Mizoguchi, K. Delaney, N. A. Spaldin, A. W. Sleight and M. A. Subramanian, *J. Am. Chem. Soc.*, 2009, **131**, 17084–17086.

130 S. M. Efendiev, T. Z. Kulieva, V. A. Lomonov, M. I. Chiragov, M. Grandolfo and P. Veccia, *Phys. Stat. Sol.*, 1981, **A**, K17.

131 P. J. Brown, A. G. Fox, E. N. Maslen, M. A. O'Keefe and B. T. M. Willis, in *International Tables for Crystallography*, 2006, vol. C, pp. 554–595.

132 V. K. Pecharsky and P. Y. Zavalij, *Fundamentals of Powder Diffraction and Structural Characterization of Materials*, Springer, New York, 2nd edn., 2009, vol. 5.

133 H. M. Rietveld, *J. Appl. Crystallogr.*, 1969, **2**, 65–71.

134 P. Thompson, D. E. Cox and J. B. Hastings, *J. Appl. Crystallogr.*, 1987, **20**, 79–83.

135 G. Caglioti, A. Paoletti and F. P. Ricci, *Nucl. Instruments*, 1958, **3**, 223–228.

136 J. Rodriguez-Carvajal, 2015.

137 A. A. Coelho, *J. Appl. Crystallogr.*, 2018, **51**, 210–218.

138 J. Roque-rosell, J. Proenza, N. Estaugh, M. Vendrell-saz and F. Mosselmans, in *Instrumental Techniques Applied to Mineralogy and Geochemistry*, eds. M. Suárez, E. Ayuso and E. M. Manchado, Sociedad Española de Mineralogía, Salamanca, 2009, pp. 61–68.

139 A. Gover, *Phys. Rev. Spec. Top. - Accel. Beams*, 2005, **8**, 030701.

140 J. Wang, B. H. Toby, P. L. Lee, L. Ribaud, S. M. Antao, C. Kurtz, M. Ramanathan, R. B. Von Dreele and M. A. Beno, *Rev. Sci. Instrum.*, 2008, **79**, 1–8.

141 P. L. Lee, D. Shu, M. Ramanathan, C. Preissner, J. Wang, M. A. Beno, R. B. Von Dreele, L. Ribaud, C. Kurtz, S. M. Antao, X. Jiao and B. H. Toby, *J. Synchrotron Radiat.*, 2008, **15**, 427–432.

142 U. Ruett, J. Almer, P. Kenesei, J. S. Park, R. Osborn, Y. Ren, D. Robinson, M. Krogstad, S. Rosenkranz, X. Zhang, M. Li and K. M. Wiaderek, *Synchrotron Radiat. News*, 2020, **33**, 44–50.

143 B. H. Toby and R. B. Von Dreele, *J. Appl. Crystallogr.*, 2013, **46**, 544–549.

144 A. A. Yakovenko, 2014.

145 F. Sears, *Neutron News*, 1992, **3**, 26–37.

146 A. Huq, J. P. Hodges, O. Gourdon and L. Heroux, in *Z. Kristallogr. Proc.*, München, 2011, pp. 127–135.

147 A. Huq, M. Kirkham, P. F. Peterson, J. P. Hodges, P. S. Whitfield, K. Page, T. Hugle, E. B. Iverson, A. Parizzia and G. Rennichb, *J. Appl. Crystallogr.*, 2019, **52**, 1189–1201.

148 The Spallation Neutron Source (SNS) at ORNL, https://www.youtube.com/watch?v=LOYmLVIQFyk, (accessed 9 November 2021).

149 S. H. Simon, *The Oxford Solid State Basics*, Oxford University Press, New York, 2013.

150 J. Neuefeind, M. Feygenson, J. Carruth, R. Hoffmann and K. K. Chipley, *Nucl. Instruments Methods Phys. Res. Sect. B Beam Interact. with Mater. Atoms*, 2012, **287**, 68–75.

151 O. Arnold, J. C. Bilheux, J. M. Borreguero, A. Buts, S. I. Campbell, L. Chapon, M. Doucet, N. Draper, R. Ferraz Leal, M. A. Gigg, V. E. Lynch, A. Markvardsen, D. J. Mikkelson, R. L. Mikkelson, R. Miller, K. Palmen, P. Parker, G. Passos, T. G. Perring, P. F. Peterson, S. Ren, M. A. Reuter, A. T. Savici, J. W. Taylor, R. J. Taylor, R. Tolchenov, W. Zhou and J. Zikovsky, *Nucl. Instruments Methods Phys. Res. Sect. A Accel. Spectrometers, Detect. Assoc. Equip.*, 2014, **764**, 156–166.

152 J. Shamblin, M. Feygenson, J. Neuefeind, C. L. Tracy, F. Zhang, S. Finkeldei, D. Bosbach, H. Zhou, R. C. Ewing and M. Lang, *Nat. Mater.*, 2016, **15**, 507–511.

153 G. King, C. M. Thompson, J. E. Greedan and A. Llobet, *J. Mater. Chem. A*, 2013, **1**, 10487–10494.

154 E. C. O'Quinn, J. Shamblin, B. Perlov, R. C. Ewing, J. Neuefeind, M. Feygenson, I. Gussev and M. Lang, *J. Am. Chem. Soc.*, 2017, **139**, 10395–10402.

155 N. Zhang, H. Yokota, A. M. Glazer, Z. Ren, D. A. Keen, D. S. Keeble, P. A. Thomas and Z. G. Ye, *Nat. Commun.*, 2014, **5**, 1–9.

156 S. Billinge, in *Uniting Electron Crystallography and Powder Diffraction*, eds. U. Kolb, K. Shankland, L. Meshi, A. Avilov and W. David, Springer, 2011, pp. 183–193.

157 S. J. L. Billinge, *Philos. Trans. R. Soc. A Math. Phys. Eng. Sci.*, , DOI:10.1098/rsta.018.0413.

158 D. A. Keen, *J. Appl. Crystallogr.*, 2001, **34**, 172–177.

159 C. L. Farrow, P. Juhas, J. W. Liu, D. Bryndin, E. S. Boin, J. Bloch, T. Proffen and S. J. L. Billinge, *J. Phys. Condens. Matter*, 2007, **19**, 335219.

160 R. L. McGreevy, *J. Phys. Condens. Matter*, , DOI:10.1088/0953-8984/13/46/201.

161 M. G. Tucker, D. A. Keen, M. T. Dove, A. L. Goodwin and Q. Hui, *J. Phys. Condens. Matter*, 2007, **19**, 335218.

162 P. F. Peterson, D. Olds, M. T. McDonnell and K. Page, *J. Appl. Crystallogr.*, 2021, **54**, 317–332.

163 K. Momma and F. Izumi, *J. Appl. Crystallogr.*, 2008, **41**, 653–658.

164 A. Stukowski, *Model. Simul. Mater. Sci. Eng.*, 2010, **18**, 015012.

165 M. Newville, *Rev. Mineral. Geochemistry*, 2014, **78**, 33–74.

166 P. W. Atkins, T. L. Overton, J. P. Rourke and M. T. Weller, *Shriver and Atkins' Inorganic Chemistry, Fifth Edition*, 2010.

167 E. R. Aluri and A. P. Grosvenor, *A Review of X-Ray Absorption Near-Edge Spectroscopic Studies of Pyrochlore-Type Oxides Proposed for Nuclear Materials Applications*, Elsevier Inc., 2016.

168 G. B. Bunker, University of Washington, 1984.

169 J. Wong, F. W. Lytle, R. P. Messmer and D. H. Maylotte, *Phys. Rev. B*, 1984, **30**, 5596–5610.

170 A. P. Grosvenor and J. E. Greedan, *J. Phys. Chem. C*, 2009, **113**, 11366–11372.

171 S. Calvin, *XAFS for everyone*, CRC Press, Taylor & Francis Group, Boca Raton, FL, 2013.

172 B. Ravel and M. Newville, *J. Synchrotron Radiat.*, 2005, **12**, 537–541.

173 C. Kittel, *Introduction to Solid State Physics*, 2010.

174 G. A. Bain and J. F. Berry, *J. Chem. Educ.*, 2008, **85**, 532.

175 L. Jansen, L. Chandran and R. Block, *J. Mol. Struct.*, 1992, **260**, 81–98.

176 I. D. Brown and D. Altermatt, *Acta Cryst.*, 1985, **B41**, 244–247.

177 W. Liu and H. H. Thorp, *Inorg. Chem.*, 1993, **32**, 4102–4105.

178 K. H. Tytko, J. Mehmke and D. Kurad, in *Bonding and Charge Distribution in Polyoxometalates: A Bond Valence Approach. Structure And Bonding. Vol. 93*, ed. A. J. Bard, Springer, Berlin, 1999, pp. 1–66.

179 N. E. Brese and M. O'Keeffe, *Acta Crystallogr. Sect. B*, 1991, **47**, 192–197.

180 I. D. Brown, *Chem. Soc. Rev.*, 1978, **7**, 359–376.

181 A. Salinas-Sanchez, J. L. Garcia-Muñoz, J. Rodriguez-Carvajal, R. Saez-Puche and J. L. Martinez, *J. Solid State Chem.*, 1992, **100**, 201–211.

182 A. Ertl, J. M. Hughes, F. Pertlik, F. F. Foit, S. E. Wright, F. Brandstätter and B. Marler, *Can. Mineral.*, 2002, **40**, 153–162.

183 E. Dowty, Shape Software, http://www.shapesoftware.com/00_Website_Homepage/, (accessed 19 November 2021).

184 D. Zagorac, H. Muller, S. Ruehl, J. Zagorac and S. Rehme, *J. Appl. Crystallogr.*, 2019, **52**, 918–925.

185 SciFinder, Chemical Abstract Service, 2017-2022, https://scifinder.cas.org/help/scifinder/R46/index.htm.

186 R. Villars and K. Cenzual, 2021.

187 J. E. Greedan, *Mater. Res. Bull.*, 1979, **14**, 13–19.

188 I. O. Troyanchuk, *Izv. Ak. Nauk. SSSR Neorg. Mater.*, 1990, **26**, 221–222.

189 G. Liu and J. E. Greedan, *JSSC*, 1993, **103**, 228–239.

190 W. Gong, J. E. Greedan, G. Liu and M. Bjorgvinsson, *J. Solid State Chem.*, 1991, **95**, 213–219.

191 V. Havlíček, P. Novák and M. Vichr, *Phys. Stat. Sol.*, 1971, **B44**, K21–K24.

192 I. Veltrusky, *Czech. J. Phys.*, 1978, **B28**, 675–695.

193 W. Yang and W. Zheng, *Spectrosc. Lett.*, , DOI:10.1080/00387010.2010.544359.

194 D. Ball and B. M. Wanklyn, *Phys. Status Solidi*, 1976, **36**, 307–316.

195 D. Ball and J. E. Lowther, 1977, **61**, 333–335.

196 F. J. Torres, M. A. Tena and J. Alarcón, *J. Eur. Ceram. Soc.*, 2002, **22**, 1991–1994.

197 A. Nakatsuka, Y. Ikuta, A. Yoshiasa and K. Iishi, *Acta Crystallogr. Sect. C Cryst. Struct.*

Commun., 2003, **59**, 133–135.

198 J. A. Lussier, K. M. Szkop, A. Z. Sharma, C. R. Wiebe and M. Bieringer, *Inorg. Chem.*, , DOI:10.1021/acs.inorgchem.5b02746.

199 K. Nagasawa, *Mater. Res. Bull.*, 1971, **6**, 853–864.

200 H. Horiuchi, M. Tokonami, N. Morimoto and K. Nagasawa, *Acta Crystallogr. Sect. B Struct. Crystallogr. Cryst. Chem.*, 1972, **28**, 1404–1410.

201 H. Horiuchi, N. Morimoto and M. Tokonami, *J. Solid State Chem.*, 1976, **17**, 407–424.

202 C. E. Rice and W. R. Robinson, *J. Solid State Chem.*, 1977, **21**, 145–154.

203 L. W. Vernon and W. O. Milligan, *Texas J. Sci.*, 1951, 82–85.

204 N. Döbelin, L. Z. Reznitsky, E. V. Sklyarov, T. Armbruster and O. Medenbach, *Am. Mineral.*, 2006, **91**, 196–202.

205 M. Marezio and P. D. Dernier, *J. Solid State Chem.*, 1971, **3**, 340–348.

206 A. Magnéli, N. Hofman-Bang and P. Gjertsen, *Acta Chem. Scand.*, 1948, 2, 501–517.

207 Y. Le Page and P. Strobel, *J. Solid State Chem.*, 1982, **44**, 273–281.

208 T. Armbruster, E. V. Galuskin, L. Z. Reznitsky and E. V. Sklyarov, *Eur. J. Miner.*, 2009, **21**, 885–891.

209 S. Åsbrink, G. N. Greaves, P. D. Hatton and K. Garg, *J. Appl. Cryst.*, 1986, **19**, 331–335.

210 K. Tanaka, T. Nasu, Y. Miyamoto, N. Ozaki, S. Tanaka, T. Nagata, H. Tokoro, A. Namai and S. Ohkoshi, *Cryst. Growth Des.*, 2015, **15**, 653–657.

211 E. Arisi, S. A. Palomares Sánchez, F. Leccabue, B. E. Watts, G. Bocelli, F. Calderón, G. Calestani and L. Righi, *J. Mater. Sci.*, 2004, **39**, 2107–2111.

212 B. Cros and H. Kerner-Czeskleba, *Acta Crystallogr.*, 1980, **B**, 2210–2213.

213 A. J. Browne, C. Lithgow, S. A. J. Kimber and J. P. Attfield, *Inorg. Chem.*, 2018, **57**, 2815–2822.

214 D. S. Cook, M. R. Lees, J. M. Fisher, D. Thompsett and R. I. Walton, *J. Solid State Chem.*, 2020, **288**, 121396.

215 B. Cros, A. Caramel and H. Kerner-Szeskleba, *Rev. Chim. Minérale*, 1977, **14**, 563–571.

216 Y. Singh, R. W. McCallum and D. C. Johnston, *Phys. Rev. B - Condens. Matter Mater. Phys.*, 2007, **76**, 174402.

217 K. Kitayama and T. Katsura, *Bull. Chem. Soc. Jpn.*, 1978, **51**, 1358–1362.

218 E. C. Mayer, *Phys. Rev.*, 1915, **6**, 283–291.

219 M. Schindler, F. C. Hawthorne and W. H. Baur, *Chem. Mater.*, 2000, **12**, 1248–1259.
220 K. Kitayama, H. Sou and T. Katsura, *Bull. Chem. Soc. Jpn.*, 1983, **56**, 3415–3420.
221 E. Levin, *J. Am. Ceram. Soc.*, 1967, **50**, 381–382.
222 M. Piz and E. Filipek, *J. Therm. Anal. Calorim.*, 2017, **130**, 277–283.
223 A. A. Haghighirad, C. Gross and W. Assmus, *J. Cryst. Growth*, 2008, **310**, 2277–2283.
224 K. Kitayama and T. Katsura, *Bull. Chem. Soc. Jpn.*, 1984, **57**, 1222–1226.
225 M. A. Gómez Torres, G. H. Gauthier, A. M. Kaczmarek, M. Huvé, P. Roussel, V. Dupray, L. Yuan, A. Zadoya and M. Colmont, *Inorg. Chem.*, 2020, **59**, 5929–5938.
226 H. Brusset, F. Madaule-Aubry, B. Blanck and A. Deboichet, *Bull. Soc. Chim. Fr.*, 1969, **1**, 15–16.
227 H. Brusset, R. Mahe and J. P. Laude, *Bull. Soc. Chim. Fr.*, 1973, **2**, 496–499.
228 K. Kitayama and T. Katsura, *Bull. Chem. Soc. Jpn.*, 1983, **56**, 1084–1088.
229 Y. Zhang, T. Yamamoto, M. A. Green, H. Kageyama and Y. Ueda, *Inorg. Chem.*, 2015, **54**, 10925–10933.
230 G. Dreyer and E. Tillmanns, *Neues Jahrb. für Mineral. (Journal Mineral. Geochemistry)*, 1981, **4**, 151–154.
231 A. W. Sleight and D. E. Cox, *Mater. Reseacrh Bull.*, 1979, **14**, 1571–1581.
232 M. M. Qurashi and W. H. Barnes, *Am. Mineral.*, 1953, **38**, 489–500.
233 O. Joubert, A. Jouanneaux and M. Ganne, *Mater. Res. Bull.*, 1994, **29**, 175–184.
234 R. N. Vannier, E. Pernot, M. Anne, O. Isnard, G. Nowogrocki and G. Mairesse, *Solid State Ionics*, 2003, **157**, 147–153.
235 R. A. Klein, A. B. Altman, R. J. Saballos, J. P. S. Walsh, A. D. Tamerius, Y. Meng, D. Puggioni, S. D. Jacobsen, J. M. Rondinelli and D. E. Freedman, *Phys. Rev. Mater.*, 2019, **3**, 1–5.
236 F. Abraham, J. C. Boivin, G. Mairesse and G. Nowogrocki, *Solid State Ionics*, 1990, **40**–**41**, 934–937.
237 A. Ramirez, R. Enjalbert, J. M. Rojo and A. Castro, *J. Solid State Chem.*, 1997, **128**, 30–37.
238 A. L. Allred and E. G. Rochow, *J. Inorg. Nucl. Chem.*, 1958, **5**, 264–268.
239 V. . S. Grunin, V. A. Ioffe and Z. N. Zonn, *J. Non. Cryst. Solids*, 1973, **11**, 341–349.
240 J. Livage, *Materials (Basel).*, 2010, **3**, 4175–4195.

241 G. Xu, Y. W. Zhang, X. Sun, C. L. Xu and C. H. Yan, *J. Phys. Chem. B*, 2005, **109**, 3269–3278.

242 H. J. Rossell, *J. Solid State Chem.*, 1976, **19**, 103–111.

243 C. Ma, J. R. Beckett and G. R. Rossman, *Am. Mineral.*, 2014, **99**, 654–666.

244 L. P. Lyashenko, L. G. Shcherbakova, D. A. Belov and A. V. Knotko, *Inorg. Mater.*, 2009, **45**, 543–549.

245 J. A. Valdez, M. Tang and K. E. Sickafus, *Nucl. Instruments Methods Phys. Res. Sect. B Beam Interact. with Mater. Atoms*, 2006, **250**, 148–154.

246 J. Zhang, Y. Wang, M. Tang, J. Won, J. A. Valdez and K. E. Sickafus, *J. Mater. Res.*, 2010, **25**, 248–254.

247 V. P. Red'ko and L. M. Lopato, *Neorg. Mater. (Russian Inorg. Mater.*, 1991, **27**, 1905–1910.

248 D. W. J. Cruickshank, H. Lynton and G. A. Barclay, *Acta Crystallogr.*, 1962, **15**, 491–498.

249 L. P. Lyashenko, L. G. Shcherbakova, E. S. Kulik, R. D. Svetogorov and Y. V. Zubavichus, *Inorg. Mater.*, 2015, **51**, 158–162.

250 D. W. Strickler and W. G. Carlson, in *american Ceramic Society. Basic Science Division Meeting*, Westinghouse Research Laboratories, Washington, D.C., 1963, pp. 63-943-267-P4.

251 O. Knop, F. Brisse and L. Castelliz, *Can. J. Chem.*, 1969, **47**, 971–990.

252 F. Brisse and O. Knop, *Can. J. Chem.*, 1968, **46**, 859–873.

253 G. S. V. Coles, S. E. Bond and G. Williams, *J. Mater. Chem.*, 1994, **4**, 23–27.

254 S. P. Shafi, B. C. Hernden, L. M. D. Cranswick, T. C. Hansen and M. Bieringer, *Inorg. Chem.*, 2012, **51**, 1269–1277.

255 L. D. Sanjeewa, K. A. Ross, C. L. Sarkis, H. S. Nair, C. D. McMillen and J. W. Kolis, *Inorg. Chem.*, 2018, **57**, 12456–12460.

256 A. Ahtee, M. Ahtee, A. M. Glazer and A. W. Hewat, *Acta Cryst.*, 1976, **B**, 3243–3246.

257 D. C. N. Swindells and J. L. Gonzalez, *Acta Crystallogr. Sect. B*, 1988, **44**, 12–15.

258 K. Bernet and R. Hoppe, *Zeitschrift fuer Anorg. und Allg. Chemie*, 1990, **587**, 145–156.

259 M. C. Uribe López, M. A. Alvarez Lemus, M. C. Hidalgo, R. López González, P. Quintana Owen, S. Oros-Ruiz, S. A. Uribe López and J. Acosta, *J. Nanomater.*, ,

DOI:10.1155/2019/1015876.

260 H. D. B. Jenkins, H. K. Roobottom, J. Passmore and L. Glasser, *Inorg. Chem.*, 1999, **38**, 3609–3620.

261 S. Quartieri, G. Antonioli, G. Artioli and P. P. Lottici, *Eur. J. Mineral.*, 1993, **5**, 1101–1110.

262 F. Farges and G. E. Brown, *Phys. Rev. B - Condens. Matter Mater. Phys.*, 1997, **56**, 1809–1819.

263 T. Yamamoto, *X-Ray Spectrom.*, 2008, **37**, 572–584.

264 V. Kunzl, *Collect. Czechoslov. Chem. Commun.*, 1932, **4**, 231–224.

265 P. Chaurand, J. Rose, V. Briois, M. Salome, O. Proux, V. Nassif, L. Olivi, J. Susini, J. L. Hazemann and J. Y. Bottero, *J. Phys. Chem. B*, 2007, **111**, 5101–5110.

266 S. A. A. Sajadi and M. Khaleghian, *J. Therm. Anal. Calorim.*, 2014, **116**, 915–921.

267 D. G. Schulze, S. R. Sutton and S. Bajt, *Soil Sci. Soc. Am. J.*, 1995, **59**, 1540–1548.

268 M. Bieringer and J. E. Greedan, *J. Solid State Chem.*, 1999, **143**, 132–139.

269 L. A. Grunes, *Phys. Rev. B*, 1983, **27**, 2111–2131.

270 T. Glaser, E. Bill, T. Weyhermüller, W. Meyer-Klaucke and K. Wieghardt, *Inorg. Chem.*, 1999, **38**, 2632–2642.

271 M. J. Ward, P. A. Rupar, M. W. Murphy, Y. M. Yiu, K. M. Baines and T. K. Sham, *Chem. Commun.*, 2010, **46**, 7016–7018.

272 R. Belissont, M. Munoz, M. C. Boiron, B. Luais and O. Mathon, *Minerals*, 2019, **9**, 227.

273 A. Paolella, W. Zhu, G. L. Xu, A. La Monaca, S. Savoie, G. Girard, A. Vijh, H. Demers, A. Perea, N. Delaporte, A. Guerfi, X. Liu, Y. Ren, C. J. Sun, J. Lu, K. Amine and K. Zaghib, *Adv. Energy Mater.*, 2020, **10**, 2001497.

274 M. Huang, W. Xu, Y. Shen, Y. H. Lin and C. W. Nan, *Electrochim. Acta*, 2014, **115**, 581–586.

275 G. R. Lumpkin and R. D. Aughterson, *Front. Chem.*, 2021, **9**, 1–12.

276 C. J. Bartel, C. Sutton, B. R. Goldsmith, R. Ouyang, C. B. Musgrave, L. M. Ghiringhelli and M. Scheffler, *Sci. Adv.*, 2019, **5**, 1–10.

277 S. S. Pramana, T. Baikie, T. An, M. G. Tucker, J. Wu, M. K. Schreyer, F. Wei, R. D. Bayliss, C. L. Kloc, T. J. White, A. P. Horsfield and S. J. Skinner, *J. Am. Chem. Soc.*, 2016, **138**, 1273–1279.

278 A. Borowska-Centkowska, M. Leszczynska, F. Krok, M. Malys, W. Wrobel, S. Hull and I. Abrahams, *J. Mater. Chem. A*, 2018, **6**, 5407–5418.

279 L. E. Kalland, S. T. Norberg, J. Kyrklund, S. Hull, S. G. Eriksson, T. Norby, C. E. Mohn and C. S. Knee, *Phys. Chem. Chem. Phys.*, 2016, **18**, 24070–24080.

280 D. Marrocchelli, P. A. Madden, S. T. Norberg and S. Hull, *J. Phys. Condens. Matter*, , DOI:10.1088/0953-8984/21/40/405403.

281 A. West, *Boletín la Soc. Española Cerámica y Vidr.*, 1991, **30**, 461–464.

282 M. Nakayama and M. Manfred, *Phys. Chem. Chem. Phys.*, 2009, **11**, 3010.

283 L. Van Brutzel, A. Chartier and J. P. Crocombette, *Phys. Rev. B - Condens. Matter Mater. Phys.*, 2008, **78**, 1–7.

284 J. Marcial, Y. Zhang, X. Zhao, H. Xu, A. Mesbah, E. T. Nienhuis, S. Szenknect, J. C. Neuefeind, J. Lin, L. Qi, A. A. Migdisov, R. C. Ewing, N. Dacheux, J. S. McCloy and X. Guo, *npj Mater. Degrad.*, 2021, **5**, 34.

285 O. C. Gagné and F. C. Hawthorne, *IUCrJ*, 2020, **7**, 581–629.

286 E. C. O'Quinn, K. E. Sickafus, R. C. Ewing, G. Baldinozzi, J. C. Neuefeind, M. G. Tucker, A. F. Fuentes, D. Drey and M. K. Lang, *Sci. Adv.*, , DOI:10.1126/sciadv.abc2758.

287 S. A. T. Redfern, R. J. Harrison, H. S. C. O'Neil and D. R. R. Wood, *Am. Mineral.*, 1999, **84**, 299–310.

288 J. Shamblin, C. L. Tracy, R. I. Palomares, E. C. O'Quinn, R. C. Ewing, J. Neuefeind, M. Feygenson, J. Behrens, C. Trautmann and M. Lang, *Acta Mater.*, 2018, **144**, 60–67.

289 S. Lijewski, S. K. Hoffmann, J. Goslar, M. Wencka and V. A. Ulanov, *J. Phys. Condens. Matter*, 2008, **20**, 385208 (0–7).

290 P. B. Oliete, V. M. Orera and P. J. Alonso, *Appl. Magn. Reson.*, 1998, **15**, 155–168.

291 Y. Lu, L. Chen, Y. Huang, H. Cheng, S. Il Kim and H. J. Seo, *J. Alloys Compd.*, 2015, **640**, 226–232.

292 P. Singh and M. S. Hegde, *Dalt. Trans.*, 2010, **39**, 10768–10780.

293 F. Shi, J. Meng and Y. Ren, *Solid State Commun.*, 1995, **95**, 745–747.

294 R. J. Lundgren, L. M. D. Cranswick and M. Bieringer, *J. Solid State Chem.*, 2006, **179**, 3599–3606.

295 V. M. Goldschmidt, *Naturwissenschaften*, 1926, **14**, 477–485.

296 M. Touboul and P. Tolédano, *Acta Crystallogr. Sect. B Struct. Crystallogr. Cryst. Chem.*,

1980, **36**, 240–245.

297 H. Yokokawa, N. Sakai, T. Kawada and M. Dokiya, *Solid State Ionics*, 1992, **52**, 43–56.

298 M. L. Sanjuán, C. Guglieri, S. Díaz-Moreno, G. Aquilanti, A. F. Fuentes, L. Olivi and J. Chaboy, *Phys. Rev. B - Condens. Matter Mater. Phys.*, 2011, **84**, 1–18.

299 A. F. Fuentes, S. M. Montemayor, M. Maczka, M. Lang, R. C. Ewing and U. Amador, *Inorg. Chem.*, 2018, **57**, 12093–12105.

300 M. A. Subramanian, G. Aravamudan and G. V. Subba Rao, *Prog. Solid State Chem.*, 1983, **15**, 55–143.

301 V. A. Isupov, *Krist. (A Transl. J. Crystallogr. Acad. Sci. USSR)*, 1957, **3**, 96–97.

302 K. E. Sickafus, L. Minervini, R. W. Grimes, J. A. Valdez, M. Ishimaru, F. Li, K. J. McClellan and T. Hartmann, *Science (80-.).*, 2000, **289**, 748–751.

303 A. F. Reid and T. M. Sabine, *J. Solid State Chem.*, 1970, **2**, 203–208.

304 L. Soderholm and J. E. Greedan, *Mater. Reseacrh Bull.*, 1979, **14**, 1449–1455.

305 A. G. Fox, M. A. O'Keefe and M. A. Tabbernor, *Acta Crystallogr. Sect. A*, 1989, **45**, 786–793.

306 K. P. Loharkar, A. Ingle and S. Jhavar, *J. Mater. Res. Technol.*, 2019, **8**, 3306–3326.

307 J. Sun, W. Wang and Q. Yue, *Materials (Basel).*, 2016, **9**, 231.

308 W. Hume-Rothery, in *Atomic theory for students of metallurgy*, ed. W. Hume-Rothery, The Institute of Metals, London, 4th edn., 1962, pp. 310–341.

309 W. L. Bragg and E. J. Williams, *Proc. R. Soc. A*, 1934, **145**, 699–730.

310 C. I. Hiley, H. Y. Playford, J. M. Fisher, N. C. Felix, D. Thompsett, R. J. Kashtiban and R. I. Walton, *J. Am. Chem. Soc.*, 2018, **140**, 1588–1591.

311 E. Kendrick, J. Kendrick, K. S. Knight, M. S. Islam and P. R. Slater, *Nat. Mater.*, 2007, **6**, 871–875.

Appendix 1. Additional information on t-Sc_2VO_5

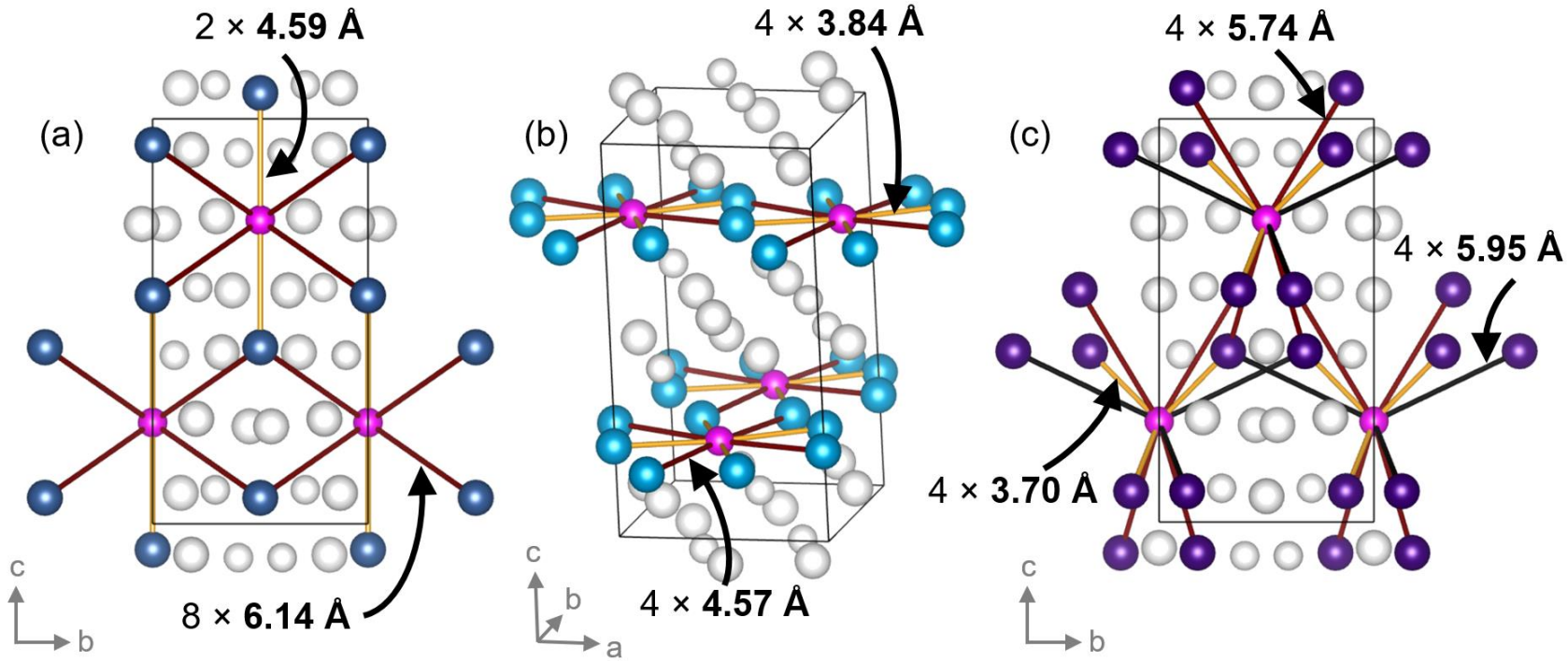

Figure A-1.1. Cationic sublattice of t-$Sc_2VO_{5+\delta}$ with emphasized bonds between V^{5+} in the 2*c* site (magenta) and: (a) – Sc-1 in the 4*f* site (dark-blue); (b) – Sc-2 in the 8*g* site (light-blue); (c) – Sc-3 in the other 8*g* site (purple). Sc-1 forms the longest bonds to V^{5+}.

Appendix 2. Auxiliary information on small-cation oxides V_xO_y and $V_xTi_yO_z$

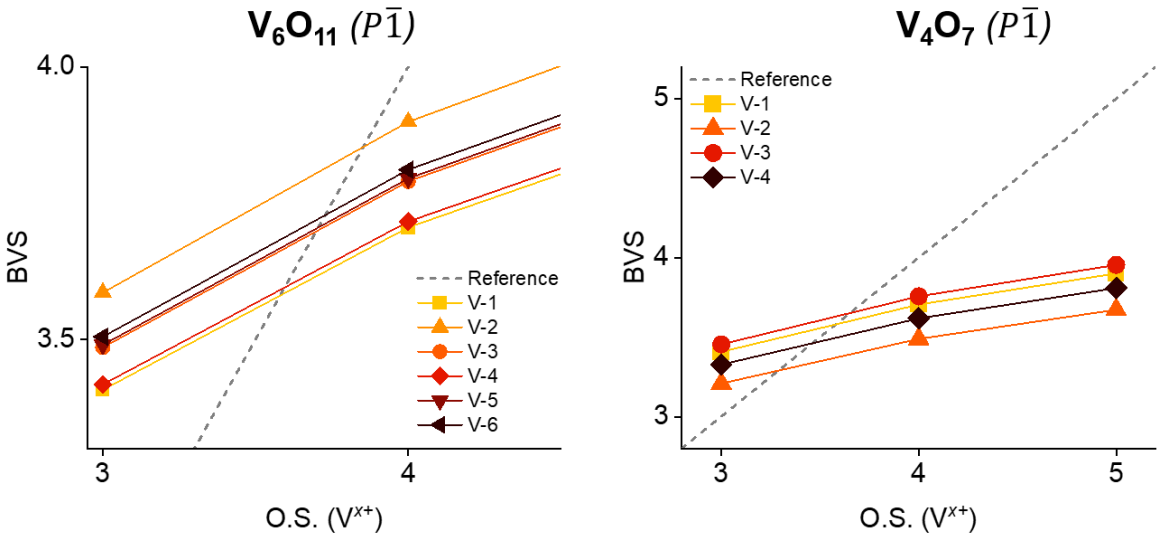

Figure A-2.1. BVS plots for vanadium in V_6O_{11} (left; all six sites are general – 2*i*) and V_4O_7 (right; all four sites are general – 4*i*). Oxidation state of vanadium in each site is in the proximity of the intercepts between the reference line and the corresponding colorful BVS plot. No strong charge-ordering was found from these data. All V-O distances were extracted from ICSD (see text for references).

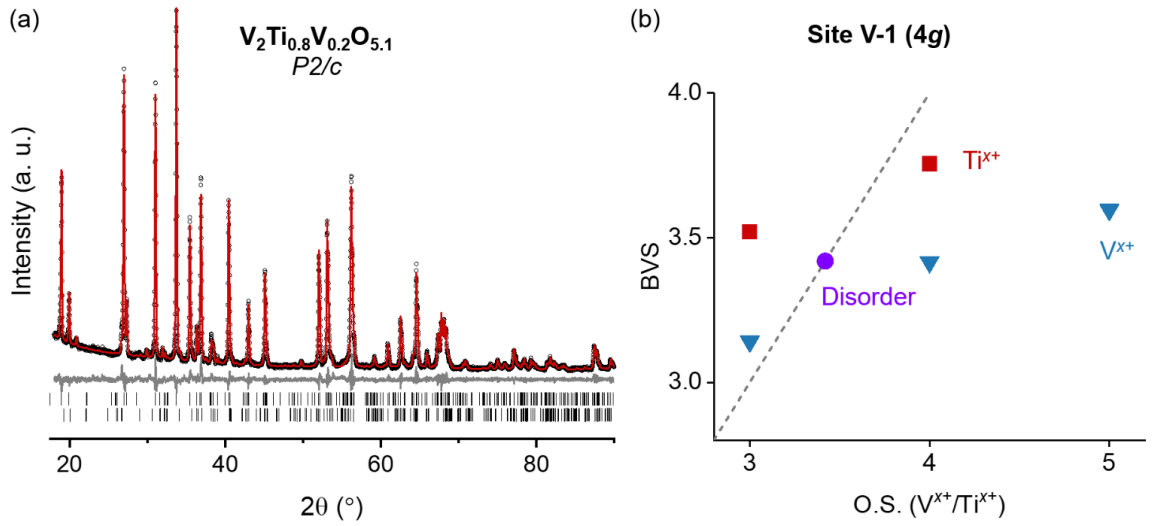

Figure A-2.2. XRD Rietveld (a) and BVS (b) plots of the product of the reaction (static vacuum, 1100 ºC): **V_2O_3 + 0.8 TiO_2 + 0.1 V_2O_5 → $V_2Ti_{0.8}V_{0.2}O_{5.1}$ = $V_{2.2}Ti_{0.8}O_{5.1}$.** The minor impurity was modelled as V_3O_5-type (*P2₁/c*, ~4 mass. %). Rietveld plot: black circles – experimental data, red line – calculated profile, grey line – difference, ticks – Bragg positions of the listed phases. BVS plot describes V-Ti disorder, with one example (out of many) of what the composition of the site V-1 could be: 30% Ti^{3+}, 40% Ti^{4+}, 30% V^{3+}.

Table A-2.1. Structural information on $V_{2.2}Ti_{0.8}O_{5+\delta}$ (SG: *P2/c*, #13, ~96% pure) from a Rietveld refinement against lab XRD data. Thermal parameters for all atoms were fixed at 0.3 $Å^2$. Two special cation sites not in the table: V/Ti-3 (2*a*) (0, 0, 0) and V/Ti-4 (2*b*) (½, ½, 0).

***a* (Å)**	9.93979(194)				
***b* (Å)**	5.062760(80)	**O-1 (4*g*) (*x*, *y*, *z*)**		**O-4 (4*g*) (*x*, *y*, *z*)**	
***c* (Å)**	7.011720(134)	***x***	0.19254(559)	***x***	0.07898(291)
β (º)	109.53408(123)	***y***	0.15151(1264)	***y***	0.65375(953)
***V* (Å³), *Z* = 4**	332.480(11)	***z***	0.03829(1083)	***z***	0.13576(641)
V/Ti-1 (4*g*) (*x*, *y*, *z*)		**O-2 (4*g*) (*x*, *y*, *z*)**		**O-5 (2*e*) (0, *y*, ¼)**	
x	0.36947(223)	***x***	0.30708(561)	***y***	0.30836(1595)
y	0.00458(230)	***y***	0.34376(1254)	**O-6 (2*f*) (½, *y*, ¼)**	
z	0.08943(585)	***z***	0.46443(1076)	***y***	0.18870(1579)
V/Ti-2 (4*g*) (*x*, *y*, *z*)		**O-3 (4*g*) (*x*, *y*, *z*)**		**λ (Å)**	1.54060/1.54443
x	0.13047(220)	***x***	0.59131(297)	**R_{wp} (%) / χ^2**	6.60 / 1.71
y	0.50365(230)	***y***	0.16025(927)	**Step size (º)**	0.0167
z	0.41091(583)	***z***	0.63905(666)	**Range (º)**	18-90

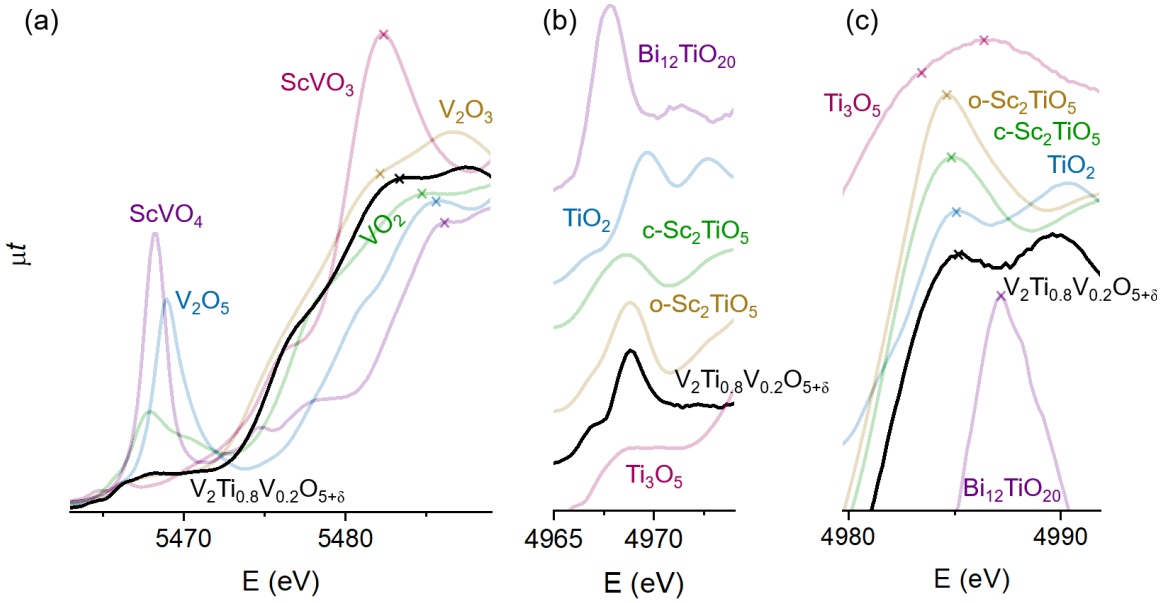

Figure A-2.3. XANES spectra of the compound in **Fig. A-2.2** collected in transmission mode on V (5.465 keV) and Ti (4.966 keV) K edges: (a) – vanadium XANES of the analyte (black) and V standards: yellow V_2O_3 ($V^{3+}{}_{VI}$), red $ScVO_3$ ($V^{3+}{}_{VI+VI}$), green VO_2 ($V^{4+}{}_{VI}$), blue V_2O_5 ($V^{5+}{}_{V}$ or $V^{5+}{}_{dist-VI}$), purple $ScVO_4$ ($V^{5+}{}_{IV}$); (b) – stack plot of pre-edge features of titanium-bearing phases: analyte is black, for standards see ***Section 5.4.2.1***; (c) – stack plot of edge features for the same phases as in (b). Crosses mark the approximate positions of the first edge peaks. The closest description of the V/Ti environment is $(V^{3+},V^{4+})_{VI}Ti^{4+}{}_{VI}$.

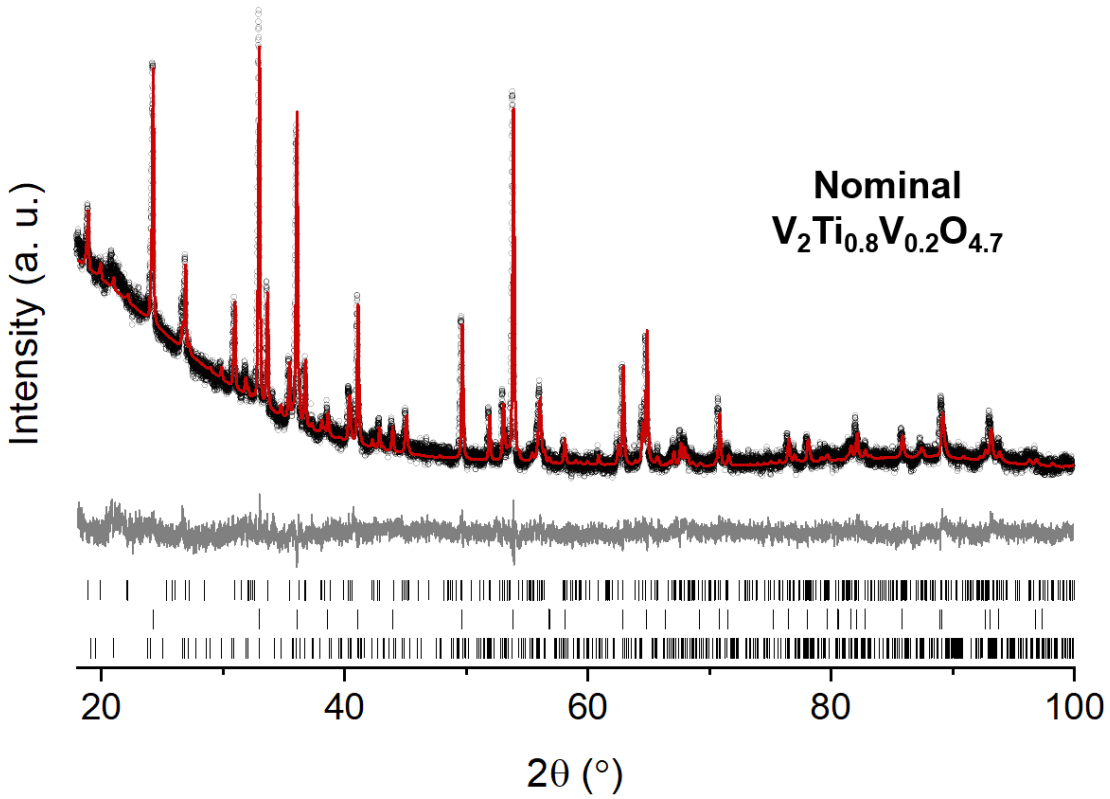

Figure A-2.4. XRD Rietveld plot for the product of the following reaction (vacuum, 1100 ºC): **V_2O_3 + 0.4 Ti_2O_3 + 0.1 V_2O_5 → $V_2Ti_{0.8}V_{0.2}O_{4.7}$ = $V_{2.2}Ti_{0.8}O_{4.7}$**, to be contrasted against **Fig. A-2.2a** with Ti^{4+} in the starting material. The product is a mixture of a V_3O_5-type phase (30.4 mass %), corundum (58.4%), and a Ti_4O_7-type phase (11.2 %). Black circles – experimental data, red line – calculated profile, grey line – difference, ticks – Bragg positions of the listed phases.

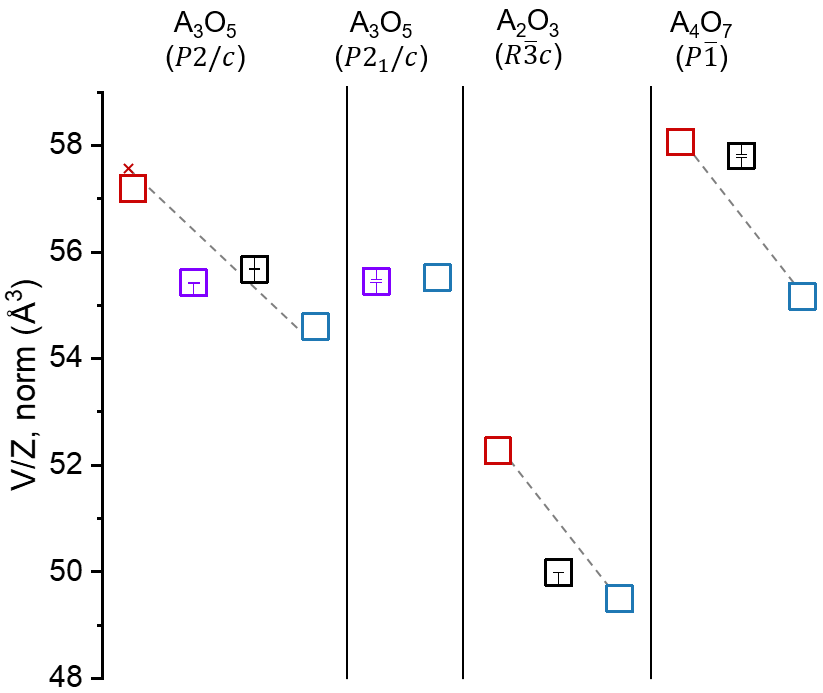

Figure A-2.5. Unit formula volumes (normalized to two cations per unit formula for ease of display) of four phases identified in reactions in **Fig. A-2.2** (purple) and **Fig. A-2.4** (black). It is suggested that the content of V and Ti in each of the phases can be approximated from interpolating a linear trend which connects volumes of the pure Ti (red) and pure V (blue) oxides. *E.g. A_2O_3 is V-rich.*

Appendix 3. Structural information on A_2VO_5-type phases

Table A-3.1. Structural details of $Sc_{1.6}In_{0.4}VO_5$ (t-$Sc_2VO_{5+\delta}$ type) and $Sc_{0.8}In_{1.2}VO_5$ (In_2VO_5 type) from a Rietveld refinement against powder XRD data.

$Sc_{1.6}In_{0.4}O_5$, $I\bar{4}$ (Z = 10)					
unit cell	*a* (Å)	7.81064(6)	O2 8g (*x*, *y*, *z*)	*x*	0.337(2)
	c (Å)	14.6356(2)		*y*	0.108(2)
	V (Å^3)	892.86(2)		*z*	0.159(1)
Sc1 4*f* (0, ½, *z*)	*z*	0.5630(4)	O3 8g (*x*, *y*, *z*)	*x*	0.182(2)
	Occ Sc (%)	90.2(9)		*y*	0.423(2)
	Occ In (%)	9.8(9)		*z*	0.470(1)
Sc2 8*g* (*x*, *y*, *z*)	*x*	0.4476(4)	O4 8g (*x*, *y*, *z*)	*z*	0.364(2)
	y	0.2976(5)	O5 8g (*x*, *y*, *z*)	*z*	0.174(1)
	z	0.2405(3)	O7 8g (*x*, *y*, *z*)	*x*	0.265(2)
	Occ Sc (%)	77.25(60)		*y*	0.199(2)
	Occ In (%)	22.75(60)		*z*	0.330(1)
Sc3 8g (*x*, *y*, *z*)	*x*	0.1309(5)	O8 8g (*x*, *y*, *z*)	*x*	0.159(2)
	y	0.1818(6)		*y*	0.421(2)
	z	0.0784(3)		*z*	0.175(1)
	Occ Sc (%)	77.6(7)	X-ray	λ (Å)	Cu-Kα$_1$, Kα$_2$
	Occ In (%)	22.4(7)		Range (º)	18-120
V1 8g (*x*, *y*, *z*)	*x*	0.1024(7)		Step size (º)	0.01671
	y	0.2111(7)		R_{wp} (%)	7.41
	z	0.4181(4)		χ^2	2.28
O1 8g (*x*, *y*, *z*)	*x*	0.249(3)			
	y	0.399(2)			
	z	0.004(1)			
$Sc_{0.8}In_{1.2}O_5$, *Pnma* (Z = 4)					
unit cell	*a* (Å)	7.1323(2)	O1 4*c* (*x*, ¼, *z*)	*x*	0.082(3)
	b (Å)	3.44742(7)		*z*	0.824(1)
	c (Å)	14.6988(3)	O2 4*c* (*x*, ¼, *z*)	*x*	0.154(3)
	V (Å^3)	361.42(1)		*z*	0.005(2)
In1 4*c* (*x*, ¼, *z*)	*x*	0.342(2)	O3 4*c* (*x*, ¼, *z*)	*x*	0.211(3)
	z	0.763(1)		*z*	0.180(1)
	Occ In (%)	41.3(8)	O4 4*c* (*x*, ¼, *z*)	*x*	0.572(3)
	Occ Sc (%)	58.7(8)		*z*	0.968(1)
In2 4*c* (*x*, ¼, *z*)	*x*	0.3986(6)	O5 4*c* (*x*, ¼, *z*)	*x*	0.332(8)
	z	0.4133(3)		*z*	0.765(5)
	Occ In (%)	78.7(8)	X-ray	λ (Å)	Cu-Kα$_1$, Kα$_2$
	Occ Sc (%)	21.3(8)		Range (º)	18-120
V 4*c* (*x*, ¼, *z*)	*x*	0.388(1)		Step size (º)	0.01671
	z	0.0812(6)		R_{wp} (%)	8.50
				χ^2	2.82

***Notes**:* (1) Sc-V ordering is assumed (idealized structures); (2) 11% impurity of $ScInO_3$ in $Sc_{0.8}In_{1.2}O_5$ is neglected; (3) Oxygen occupancies, if not 100% in the parent structure, and all B_{iso} parameters were taken from *Moller et al. 2007* (for $Sc_{0.8}In_{1.2}O_5$) and *Vrublevskiy et al. 2021* (for $Sc_{1.6}In_{0.4}O_5$).

Table A-3.2. Structural details of $Yb_{7.03(1)}V_{2.97(1)}O_{16.0(2)}$. Space group: *Pccn* (#56).

Structure					
formula	refined (Z = 1)	$Yb_{8.4(1)}V_{3.6(1)}O_{19.1(2)}$	**O1 4*c* (¼, ¼, *z*)**	*z*	0.83162(134)
	$A_7B_3O_{16}$ notation	$Yb_{7.03(1)}V_{2.97(1)}O_{16.0(2)}$		Occ. (%)	73.8(1.8)
	A_2BO_5 notation	$Yb_{2.11(3)}V_{0.89(3)}O_{4.79(6)}$		B_{iso} (Å^2)	1.65(15)
purity (% mass)		90.7(4)	**O2 4*d* (¼, ¾, *z*)**	*z*	0.57104(94)
unit cell	*a* (Å)	11.449981(71)		Occ. (%)	89.0(1.7)
	b (Å)	5.730223(34)		B_{iso} (Å^2)	0.740(76)
	c (Å)	7.150338(39)	**O3 8*k* (*x*, *y*, *z*)**	*x*	0.09306(63)
	V (Å^3) as refined	469.140(5)		*y*	0.50180(175)
Yb 8*k* (*x*, *y*, *z*)	*x*	0.05806(4)		*z*	0.87560(243)
	y	0.74726(32)		Occ. (%)	97.2(1.9)
	z	0.62766(20)		B_{iso} (Å^2)	0.209(34)
	Occ. Yb (%)	88.8(1.6)	**O4 8*k* (*x*, *y*, *z*)**	*x*	0.12151(151)
	Occ. V(%)	11.2(1.6)		*y*	0.53636(379)
	B_{iso} (Å^2)	0.317(8)		*z*	0.38552(517)
V 4*c* (¼, ¼, *z*)	*z*	0.37812(66)		Occ. (%)	61.0(1.7)
	Occ. Yb (%)	33.4(8)		B_{iso} (Å^2)	0.977(118)
	Occ. V(%)	66.6(8)			
	B_{iso} (Å^2)	2.154(41)			

Radiation						
NPD	NPD Bank 1	NPD Bank 2	NPD Bank 3	NPD Bank 4	**XRD**	
Δd/d	0.019	0.0137	0.0069	0.0036	λ (Å)	0.458951
range (μsec)	1400-11000	2200-19000	3500-16000	2500-15200	range (º)	2-50
R_{wp} (%)	3.84	5.59	4.67	4.24	step size (º)	$9.984*10^{-4}$
					R_{wp} (%)	22.6

- Overall Rwp = 10.8%
- χ^2 was forced to ~100 for all 5 banks to achieve equal weighting

Table A-3.3. Selected bond lengths and bond angles in $Yb_7V_3O_{16}$ from Rietveld refinement.

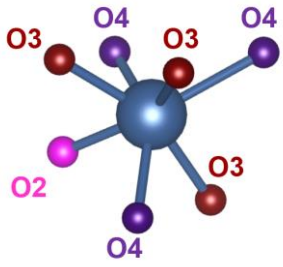

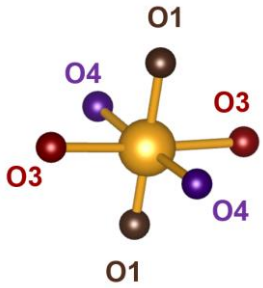

A-O bond length (Å)		B-O bond length (Å)	
A-**O2**	2.272(16)	B-**O1**	1.70(3)
A-**O2**	2.354(12)	B-**O1**	1.88(3)
A-**O2**	2.366(17)	B-**O2**	2.256(12)
A-**O3**	2.2291(19)	B-**O2**	2.256(12)
A-**O4**	2.23(3)	B-**O4**	2.20(2)
A-**O4**	2.34(3)	B-**O4**	2.20(2)
A-**O4**	2.62(2)		
O-A-O bond angle (º)		**O-B-O bond angle (º)**	
O2-A-**O2**	86.1(4)	**O1**-B-**O2**	91.1(6)
O2-A-**O3**	71.3(8)	**O1**-B-**O2**	91.1(6)
O2-A-**O3**	86.7(6)	**O1**-B-**O2**	88.9(6)
O2-A-**O4**	69.7(9)	**O1**-B-**O4**	88.6(1.0)
O2-A-**O4**	69.9(4)	**O1**-B-**O4**	88.6(1.0)
O2-A-**O4**	74.9(5)	**O1**-B-**O4**	91.4(1.0)
O2-A-**O4**	79.7(6)	**O2**-B-**O2**	91.8(5)
O2-A-**O4**	83.8(8)	**O2**-B-**O4**	88.2(5)
O2-A-**O4**	103.2(8)	**O2**-B-**O4**	88.2(5)
O3-A-**O4**	63.5(5)	**O2**-B-**O4**	88.9(6)
O3-A-**O4**	80.2(8)	**O2**-B-**O4**	91.8(5)
O3-A-**O4**	101.5(8)	**O4**-B-**O4**	91.4(1.0)
O4-A-**O4**	77.5(5)		

Table A-3.4. Lattice dimensions of $A_{2.1}V_{0.9}O_{4.8+\delta}$ phases refined from synchrotron powder XRD data. Idealized model was used as described in the text.

A^{3+}	Lu	Yb	Tm
a **(Å)**	11.410344(56)	11.449981(71)	11.491523(57)
b **(Å)**	5.717572(29)	5.730223(34)	5.748386(30)
c **(Å)**	7.124370(34)	7.150338(39)	7.178908(34)
V **(Å^3)**	464.790(4)	469.140(5)	474.222(4)

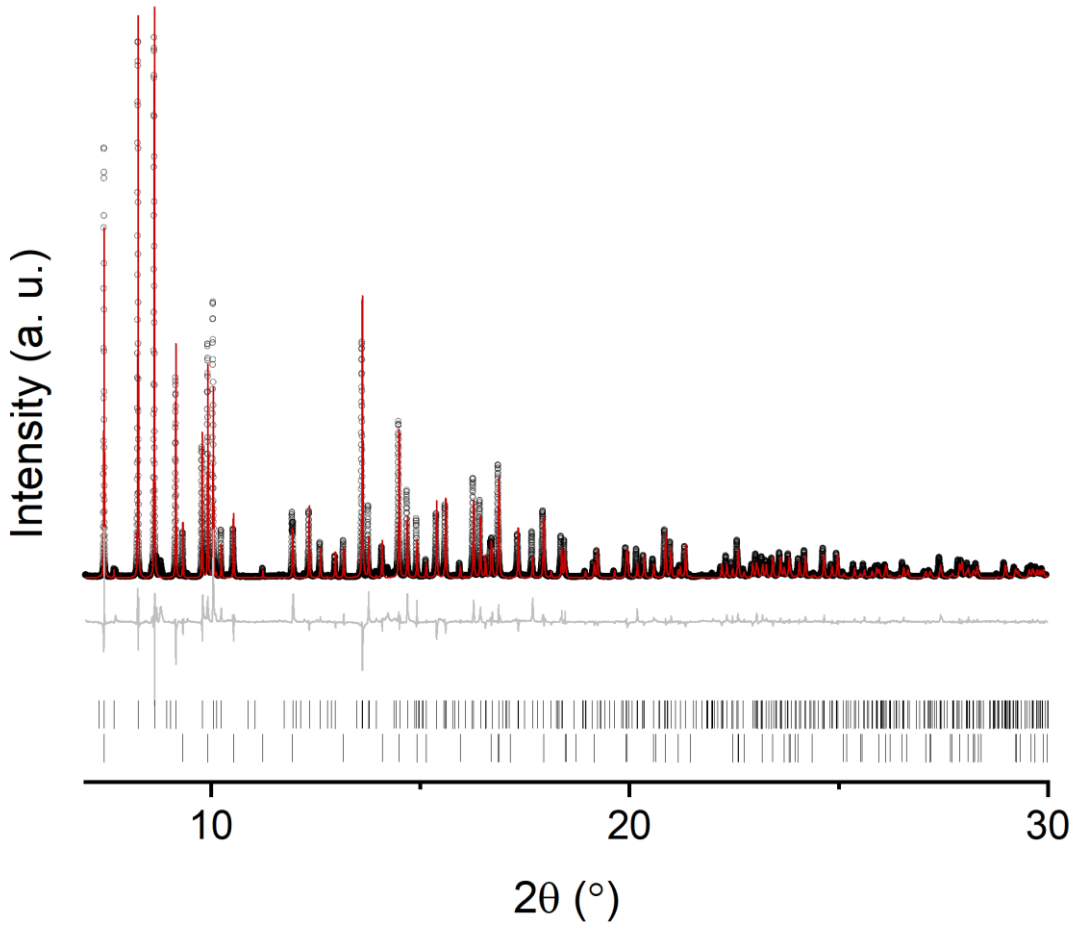

Figure A-3.1. Rietveld refinement of the product of heating the mixture of 3 Tm_2O_3 and 3.5 VO_2 at 1200 ºC under static vacuum. Black – data (λ = 0.458951 Å), red – calculated fit, grey – difference, ticks – Bragg positions: top – $Tu_7V_3O_{16}$ (67 mass %), bottom – $TmVO_4$ (33 %).

Appendix 4. Additional data on $Sc_2V_{1-x}B_xO_{5+\delta}$ series

Table A-4.1. Information on $Sc_2V_{0.8}B_{0.2}O_{5+\delta}$ phases (SG: $I\bar{4}$) from Rietveld refinements.

General					
B		**Ti**	**Ge**	**Cr**	**Sn**
e^- count in O.S.= 4 / b_{coh} (fm)		18 / -3.438	28 / 8.185	20 / 3.635	46 / 6.225
***a* (Å)**		7.781120(21)	7.757673(33)	7.780892(45)	7.810144(54)
***c* (Å)**		14.603449(65)	14.561446(99)	14.592846(108)	14.666555(164)
***V* (Å^3), *Z* = 10**		884.178(6)	876.328(10)	883.489(12)	895.187(23)
O^{2-} per unit formula		4.863(13)	4.828(22)	4.828(16)	4.930(32)
Structural					
Sc1 (4*f*) (0, ½, *z*)	***z***	0.56382(15)	0.56321(24)	0.56588(19)	0.56589(43)
	B_{iso} (Å^2)	1.93(4)	1.67(7)	2.15(6)	2.85(11)
	Occ (Sc) (%)	87.8(6)	87.6(3.6)	87.8(1.2)	87.8(2.0)
	Occ (V) (%)			12.2	
	Occ (B) (%)	0.0(6)	0.2(3.6)	0.0(1.2)	0.0(2.0)
Sc2 (8*g*) (*x*, *y*, *z*)	***x***	0.44999(11)	0.44380(22)	0.448545(14)	0.45088(27)
	y	0.29639(11)	0.29869(20)	0.29694(14)	0.29577(27)
	z	0.24053(6)	0.24001(10)	0.24083(7)	0.24149(16)
	B_{iso} (Å^2)	0.25(2)	0.51(3)	0.40(2)	0.24(4)
	Occ (Sc) (%)	95.4(4)	98.0(2.1)	99.0(8)	93.3(1.3)
	Occ (V) (%)			1.0	
	Occ (B) (%)	3.6(4)	0.1(2.1)	0.0(8)	5.7(1.3)
Sc3 (8*g*) (*x*, *y*, *z*)	***x***	0.13221(12)	0.13154(24)	0.13116(16)	0.13172(31)
	y	0.17961(12)	0.18120(23)	0.18006(16)	0.18100(30)
	z	0.07639(7)	0.07778(12)	0.07643(9)	0.07651(17)
	B_{iso} (Å^2)	0.42(2)	0.84(4)	0.69(3)	0.51(4)
	Occ (Sc) (%)	92.6(1.1)	84.2(3.6)	95.7(1.5)	93.8(2.1)
	Occ (V) (%)			1.6	
	Occ (B) (%)	5.8(1.1)	4.6(3.0)	2.7(1.5)	4.6(2.1)
V1 (8*g*) (*x*, *y*, *z*)	***x***	0.09959(83)	0.09403(165)	0.09856(75)	0.09805(127)
	y	0.21505(87)	0.20940(192)	0.20741(88)	0.21340(147)
	z	0.41436(44)	0.41929(87)	0.41650(42)	0.41930(77)
	B_{iso} (Å^2)	0.07(12)	0.75(0.25)	0.96(9)	0.01(18)
	Occ (Sc) (%)			8.7	
	Occ (V) (%)	78.6(8)	84.6(9)	69.0(1.0)	76.6(1.2)
	Occ (B) (%)	12.7(8)	6.7(9)	22.3(1.0)	14.7(1.2)
V2 (2*c*) (0, ½, ¼)	**B_{iso} (Å^2)**	0.0(3)	0.3(2)	0.17	0.17
	Occ (Sc) (%)			0.0	
	Occ (V) (%)	88.7(2)	50.0(2.1)	100.0(2.0)	100.0(2.1)
	Occ (B) (%)	11.3(2)	50.0(2.1)	0.0(2.0)	0.0(2.1)
O1 (8*g*) (*x*, *y*, *z*)	***x***	0.24925(27)	0.24939(49)	0.24778(22)	0.24814(66)
	y	0.39938(25)	0.40238(46)	0.39910(31)	0.39707(63)

	z	0.00574(15)	0.00453(27)	0.00515(19)	0.00505(38)
	Occ (%)	100.0(7)	96.2(1.2)	100.0(9)	100.0(1.8)
	B_{iso} ($Å^2$)		0.51		
O2 (8*g*) (*x*, *y*, *z*)	***x***	0.33735(28)	0.33683(46)	0.33579(35)	0.33373(72)
	y	0.10887(23)	0.10554(40)	0.11036(29)	0.11151(58)
	z	0.16003(11)	0.16077(19)	0.16106(14)	0.15951(29)
	B_{iso} ($Å^2$)		0.51		
	Occ (%)	100.0(7)	100.0(1.2)	100.0(9)	100.0(1.8)
O3 (8*g*) (*x*, *y*, *z*)	***x***	0.18699(25)	0.18813(43)	0.18876(31)	0.18882(61)
	y	0.42056(22)	0.41971(40)	0.41964(27)	0.42367(57)
	z	0.47332(11)	0.47291(20)	0.47381(14)	0.47451(28)
	B_{iso} ($Å^2$)		0.51		
	Occ (%)	100.0(7)	96.6(1.2)	99.0(8)	100.0(1.7)
O4 (4*e*) (0, 0, *z*)	***z***	0.36114(18)	0.36189(32)	0.36007(23)	0.35962(45)
	B_{iso} ($Å^2$)		0.06		
	Occ (%)	92.6(9)	88.5(1.5)	94.2(1.1)	100.0(2.3)
O5 (4*e*) (0, 0, *z*)	***z***	0.17272(15)	0.17393(27)	0.17321(20)	0.17309(41)
	B_{iso} ($Å^2$)		0.06		
	Occ (%)	100.0(9)	100.0(1.5)	100.0(1.0)	100.0(2.2)
O6 (2*a*) (0, 0, 0)	**B_{iso} ($Å^2$)**		0.9		
	Occ (%)	100.0(1.1)	100(2.1)	100.0(1.4)	100.0(2.9)
O7 (8*g*) (*x*, *y*, *z*)	***x***	0.26305(24)	0.26045(40)	0.26383(30)	0.27037(57)
	y	0.19160(25)	0.19119(42)	0.19072(32)	0.19033(61)
	z	0.32789(14)	0.32884(24)	0.32956(18)	0.33097(35)
	B_{iso} ($Å^2$)		0.51		
	Occ (%)	91.3(6)	93.6(1.0)	90.4(7)	94.6(1.4)
O8 (8*g*) (*x*, *y*, *z*)	***x***	0.16018(24)	0.16530(41)	0.16144(31)	0.16167(59)
	y	0.42078(25)	0.42014(43)	0.42277(33)	0.41973(64)
	z	0.18069(13)	0.17970(22)	0.18107(17)	0.18079(33)
	B_{iso} ($Å^2$)		0.51		
	Occ (%)	95.3(7)	97.9(1.1)	92.1(7)	96.6(1.5)
		Radiation / miscellaneous			
XRD	**λ (Å)**	1.54060	1.54060/1.54443	1.54060	1.54060/1.54443
	R_{wp} (%)	2.81	10.1	3.64	12.47
	χ^2	0.94	2.26	1.35	1.10
	Step size (º)	0.005	0.02	0.005	0.02
	Range (º)	10-100	20-70	10-100	15-90
	Purity (mass %)	97.7(6)	95.6(7)	87.6(4)	94.4(1.0)
NPD (TOF)	**λ_c (Å)**		1.5		
	R_{wp} (%)	5.72	5.49	5.83	1.95
	χ^2	4.58	7.23	5.67	2.68
	Range (μsec)		11500-200000		
	Purity (mass %)	97.2(5)	96.7(1)	92.1(1)	96.0(9)
XRD + NPD	**R_{wp} (%)**	4.59	5.62	5.07	2.12
	χ^2	2.04	5.71	2.69	2.02

Table A-4.2. Legend for **Fig. 5.10b** – an example of a correlation matrix among selected parameters produced by a Rietveld refinement of $Sc_2V_{0.8}Sn_{0.2}O_{5+\delta}$ against NPD and lab XRD data. Asterisk marks an additional, hitherto vacant crystallographic site of oxygen – 8*g* (*x*, *y*, *z*), refined for Sn as *x* = 0.24(4), *y* = 0.45(4), *z* = 0.31(2).

#	Parameter	#	Parameter	#	Parameter
1	B_{iso} of Sc-1, site 4*f*	**10**	B_{iso} of O-6, site 2*a*	**18**	Occ. of O-1
2	B_{iso} of Sc-2, site 8*g*	**11**	B_{iso} of O-7, site 8*g*	**19**	Occ. of O-2
3	B_{iso} of Sc-3, site 8*g*	**12**	B_{iso} of O-8, site 8*g*	**20**	Occ. of O-3
4	B_{iso} of V-1, site 8*g*	**13**	B_{iso} of O-9, site 8*g**	**21**	Occ. of O-4
5	B_{iso} of O-1, site 8*g*	**14**	Occ. of Sn in site 8*g* of V-1	**22**	Occ. of O-5
6	B_{iso} of O-2, site 8*g*	**15**	Occ. of Sn in site 4*f* of Sc-1	**23**	Occ. of O-6
7	B_{iso} of O-3, site 8*g*	**16**	Occ. of Sn in site 8*g* of Sc-2	**24**	Occ. of O-7
8	B_{iso} of O-4, site 4*e*	**17**	Occ. of Sn in site 8*g* of Sc-3	**25**	Occ. of O-8
9	B_{iso} of O-5, site 4*e*			**26**	Occ. of O-9*

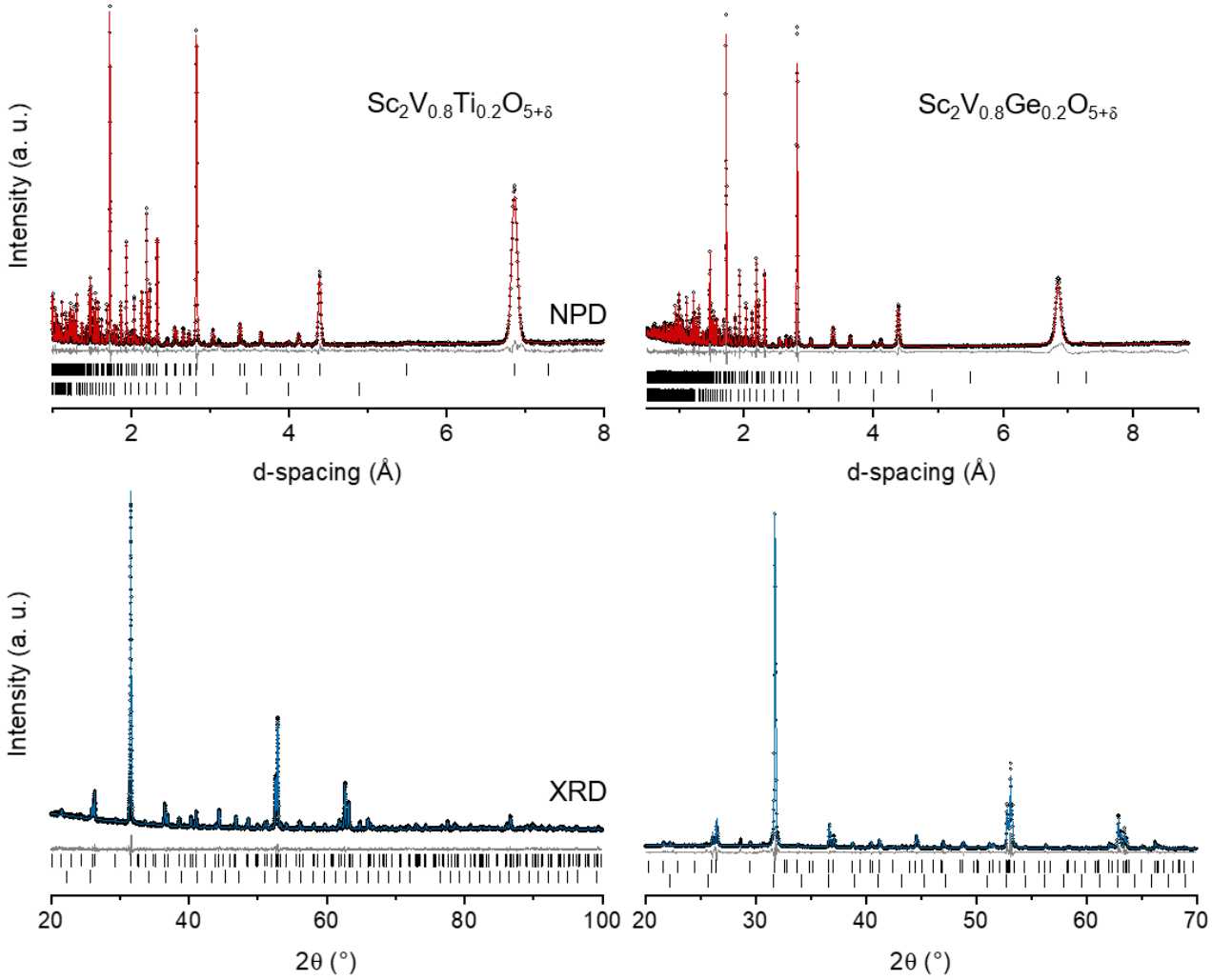

Figure A-4.1. Rietveld refinements against neutron (top) and lab X-ray (bottom) powder diffraction data on $Sc_2V_{0.8}B_{0.2}O_{5+\delta}$ compositions: black circles – data, red line – calculated pattern, grey line – difference, vertical ticks – Bragg peaks of (top to bottom) the main phase ($\boldsymbol{I\bar{4}}$), bixbyite impurity ($\boldsymbol{Ia\bar{3}}$), and for B = Cr – zircon impurity ($\boldsymbol{I4_1/amd}$). Corresponding crystallographic and other data are in **Table A-4.1.** *See the next page for the rest of the figure.*

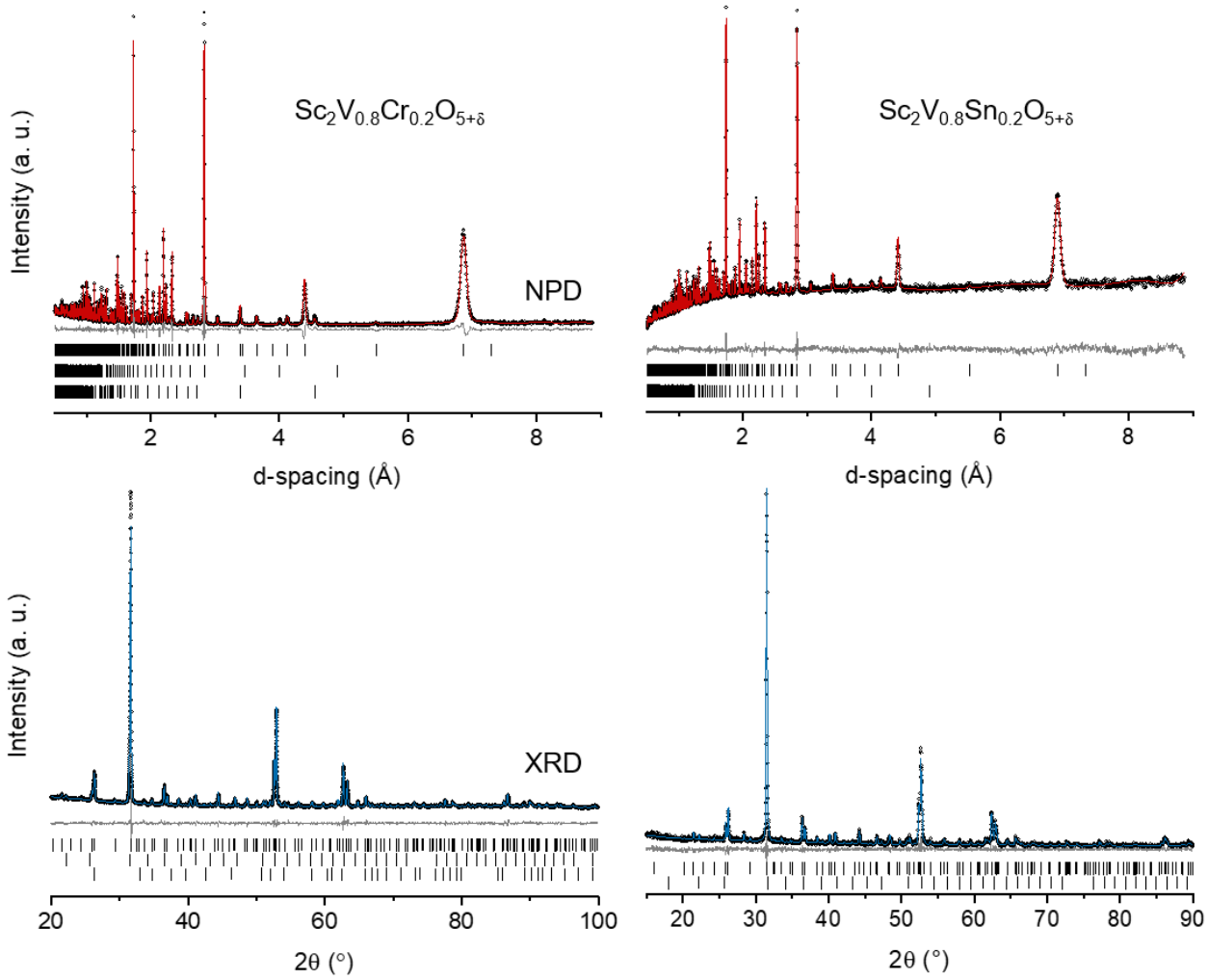

Figure A-4.1. (cont.)

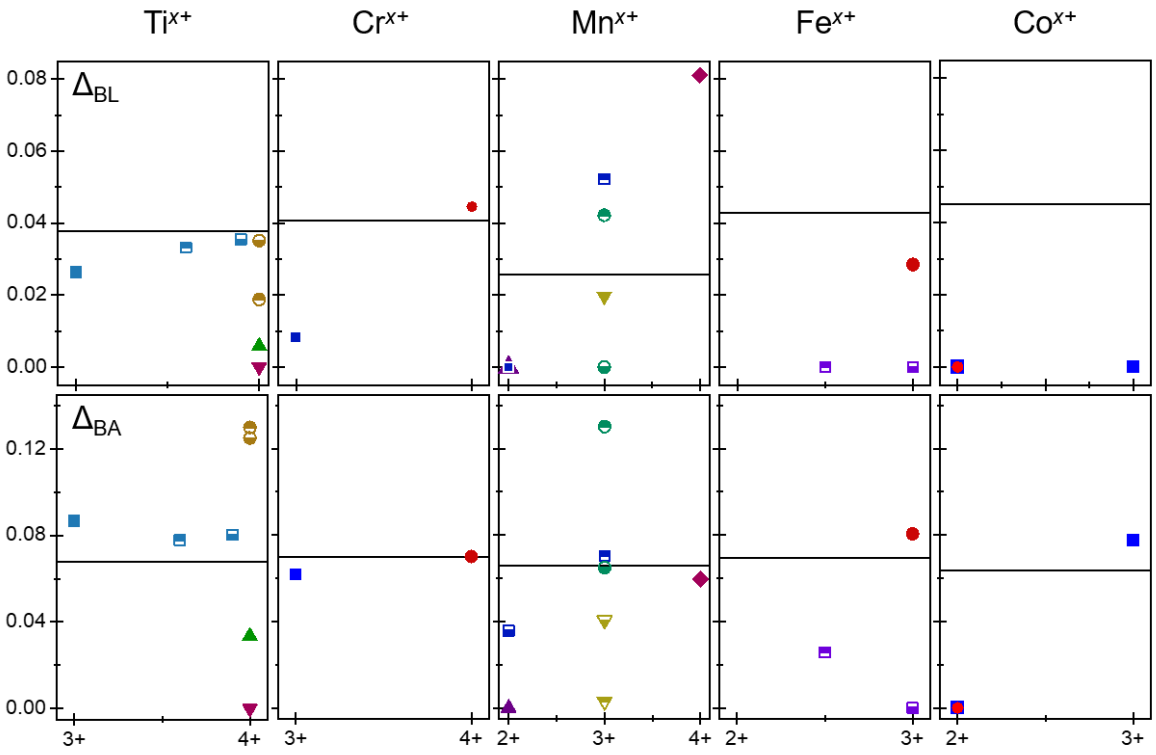

Figure A-4.2. Relative distortions of B-O bond lengths (top) and O-B-O bond angles (bottom) within the 8*g* site of the B-doped solid solutions $Sc_{1.96\pm0.04}V_{0.82\pm0.05}B_{0.255\pm0.035}O_{5+\delta}$ with B = Ti, Cr, Mn, Fe, and Co. Color scheme is similar to that in **Fig. 5.16** with colored markers – standards and black line – the analyte. For the analytes, only the Y axis of the plots matters. Distortions were calculated based on the data from the two-histogram Rietveld refinements against XRD and NPD data.

Appendix 5. The A^{3+}-B^{4+}-O phase diagram

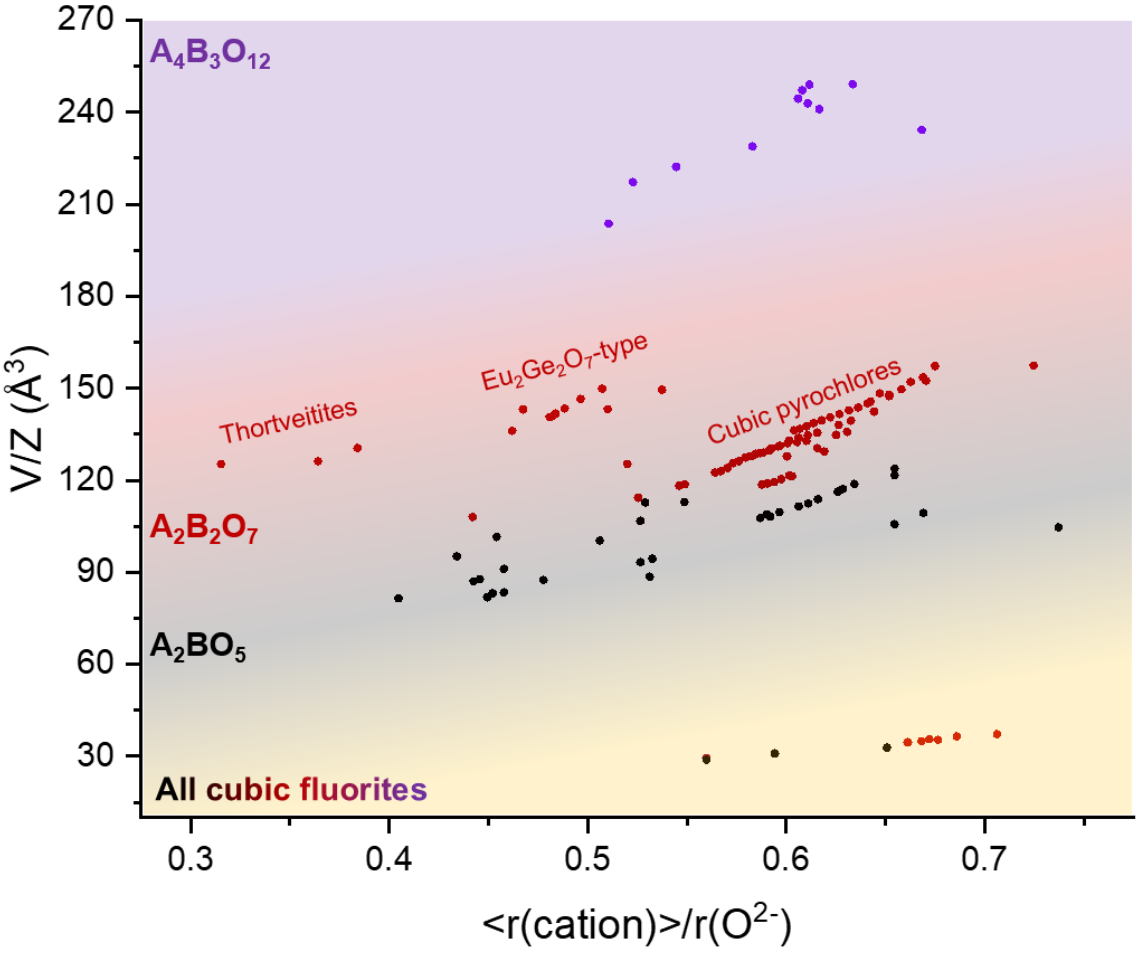

Figure A-5.1. Evolution of the unit formula volume of frequently competing stoichiometries in the A^{3+}-B^{4+}-O phase space. Fluorites were reported in all three mentioned stoichiometries.

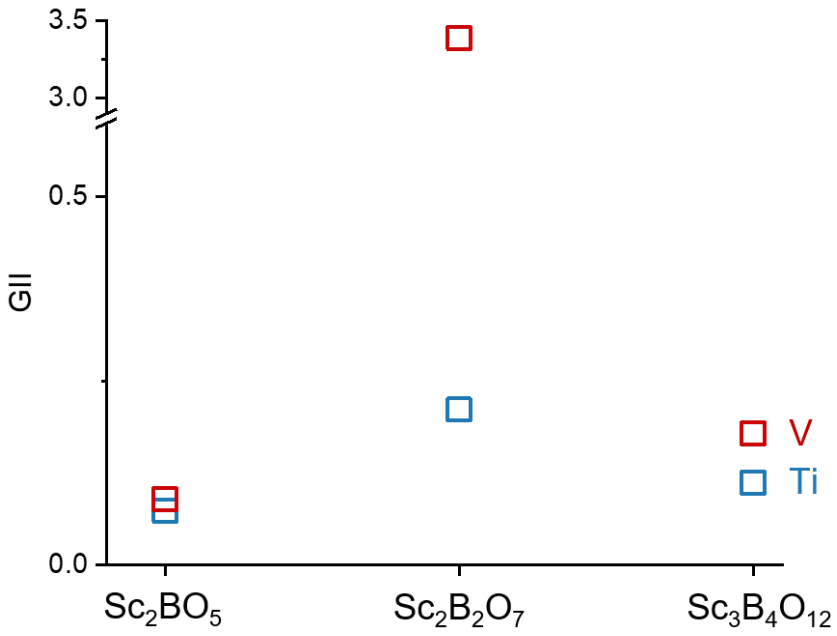

Figure A-5.2. The global instability index for Sc_2BO_5, $Sc_2B_2O_7$, and $Sc_4B_3O_{12}$-type phases with B = V and Ti. All phases but $Sc_4V_3O_{12}$ were reported in literature. Real bond distances and charges in t-$Sc_2VO_{5+\delta}$, Sc_2TiO_5, and $Sc_4Ti_3O_{12}$ phases were used, while for the rest of them the bond-distances were linearly extrapolated from isostructural materials with known or extrapolated unit cell dimensions. The relatively high instability index of $Sc_2V_2O_7$ (note the Y axis values) is consistent with the need to use geological pressure to prepare it.

Appendix 6. Additional data on pseudocubic c-$Sc_2VO_{5+\delta}$

Table A-6.1. Crystallographic data on c-$Sc_2VO_{5+\delta}$ ($\boldsymbol{Fm\bar{3}m}$, product of oxidation of $Sc_2VO_{4.5}$) obtained from a two-histogram Rietveld refinement against synchrotron powder XRD and NPD data. In this refinement, the fluorite notation $Sc_{0.67}V_{0.33}O_{2-\delta}$ was implied (Z = 4).

a (Å)	4.987742(15)
V (Å^3)	124.083(1)
Sc/V-O bond (Å)	2.159756(6)
Sc/V 4*a* (0, 0, 0)	
B_{iso} (Å^2)	4.45(1)
O 8*c* (¼, ¼, ¼)	
B_{iso} (Å^2)	8.93(6)
Occ. (%)	0.861(3) *
X-ray	
λ (Å)	0.412839
Range (º)	5-38
Step size (º)	0.0001
R_{wp} (%)	8.71
χ^2	2.37
Neutron	
λ_c (Å)	2.665
Range (μsec)	24630-140000
R_{wp} (%)	3.20
χ^2	3.09
X-ray + Neutron	
R_{wp} (%)	7.07
χ^2	2.41

*corresponds to $Sc_2VO_{5.17(2)}$. 90% correlation with B_{iso}.

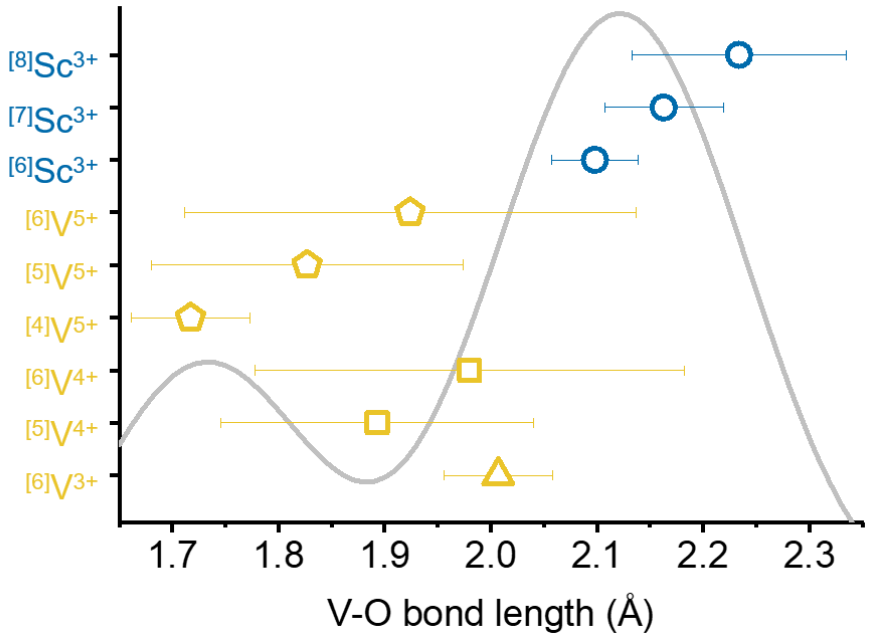

Figure A-6.1. The most common V^{x+}-O and Sc^{3+}-O bond lengths in various coordination environments superimposed upon the first two peaks in X-ray PDF data on c-$Sc_2VO_{5+\delta}$.

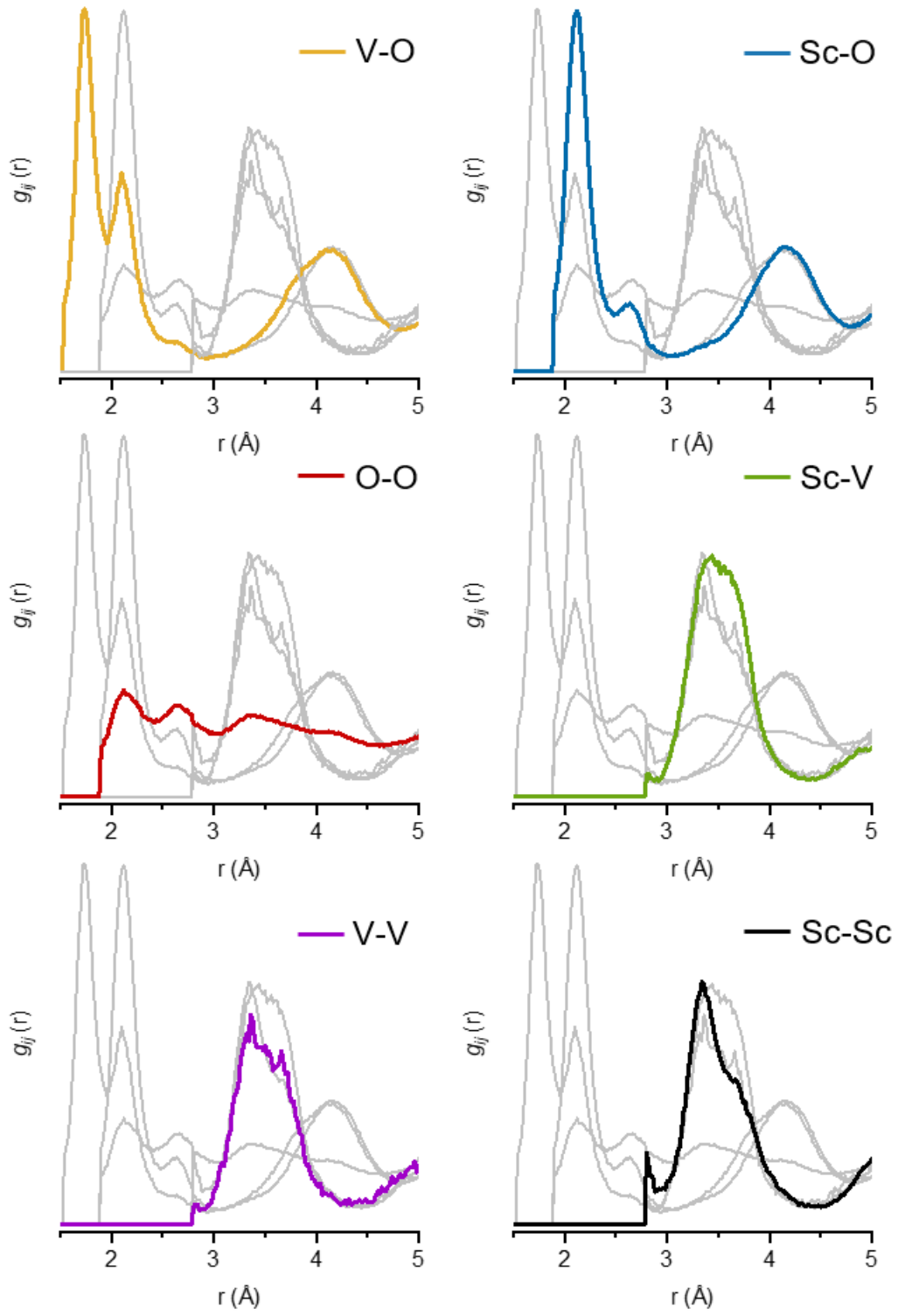

Figure A-6.2. Unnormalized partial $g_{ij}(r)$ contributions from the RMC refinement of c-$Sc_2VO_{5+\delta}$ (obtained from $Sc_2VO_{4.5}$), averaged over 50 independent refinements. Steep features (especially in the metal-metal plots) come from bond length constraints.

Appendix 7. XANES data on $TiVO_{4+\delta}$ ($Ti_{0.5}V_{0.5}O_{2+\delta}$)

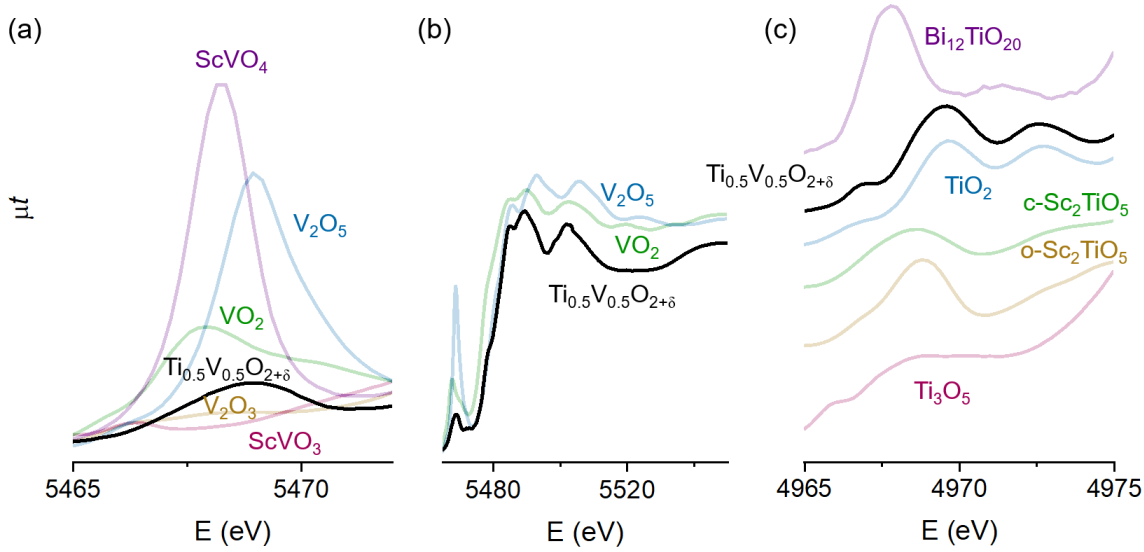

Figure A-7.1. XANES data on the K-edges of V and Ti for selected V and Ti oxides: (a) – K-pre-edge of vanadium; (b) – K-edge and pre-edge of vanadium for three relevant oxides; (c) – K-pre-edge of titanium.

Appendix 8. List of abbreviations

0D (1D, 2D, 3D)	Zero- (one-, two-, three-) dimensional
ANL	Argonne National Laboratory
APS	Advanced Photon Source
BL / BM / ID	Beamline / bending magnet / insertion device
BVS / GII	Bond valence sum(s) / global instability index
CN	Coordination number
DC	Direct current
fcc	Face-centered cubic structure
FWHM	Full width at half-maximum
GOF	Goodness of fit
HT / RT	High temperature / room temperature
ICSD	Inorganic Crystal Structure Database
ID / OD	Inner diameter / outer diameter
LFC	Linear combination fitting
NPD	Neutron powder diffraction
O.S.	Oxidation state
ORNL	Oak Ridge National Laboratory
PDF	Pair distribution function
RMC	Reverse Monte Carlo
SG	Space group
SNS	Spallation Neutron Source
TOF	Time-of-flight
XANES	X-ray absorption near edge structure spectroscopy
XRD	X-ray diffraction

Appendix 9. List of key structure types

Name of the type or group	Example(s) from the text	Space Group
$A_7V_3O_{16}$-type	$Yb_7V_3O_{16}$	$Pccn$ (#56)
Allendeite	δ-$Sc_4Ti_3O_{12}$	$R\bar{3}$ (#148)
Berdesinskiite	V_2TiO_5	$C2/c$ (#15)
Bixbyite	$Sc_2VO_{4.5}$, Lu_2O_3	$Ia\bar{3}$ (#206)
Corundum	V_2O_3	$R\bar{3}c$ (#167)
Fluorite / defect fluorite	c-$Sc_2VO_{5+\delta}$, $ScVO_{3.5}$	$Fm\bar{3}m$ (#225)
"Hydrothermal A_2VO_5"	Yb_2VO_5	$C2/c$ (#15) and $P2_1c$ (#14)
Magnéli phase	V_4O_7	$P\bar{1}$ (#2)
Perovskite of $GdFeO_3$ type	$LuVO_3$	$Pnma$ (#62)
Pseudobrookite	o-Sc_2TiO_5	$Cmcm$ (#63)
Pyrochlore	$Lu_2V_2O_7$	$Fd\bar{3}m$ (#227)
Rutile	α-TiO_2, Sc_2SnO_5	$P4_2/mnm$ (#136)
Thortveitite	$Sc_2Ge_2O_7$	$C2/m$ (# 12)
Zircon	$ScVO_4$	$I4_1/amd$ (#141)